Measuring atmospheric hydrogen cyanide (HCN) from space using the MIPAS-E instrument onboard ENVISAT

Thesis submitted for the degree of
Doctor of Philosophy
at the University of Leicester

by

Manasvi Panchal BSc MSc

Earth Observation Science Group
Department of Physics and Astronomy
University of Leicester, UK

April 2010

Dedicated

to

my teachers

DECLARATION

I hereby declare that no part of this thesis has been submitted to this or any other University as part of the requirements for a higher degree. The work described here was conducted by the undersigned except for the contributions of colleagues indicated in the text.

Manasvi Panchal
April 2010

Measuring atmospheric hydrogen cyanide (HCN) from space using the MIPAS-E instrument onboard ENVISAT

Manasvi Panchal

ABSTRACT

The potential to detect hydrogen cyanide (HCN) spectral signatures and retrieve HCN volume mixing ratios (VMR) in the Upper Troposphere and Lower Stratosphere (UTLS) from a space-borne infrared limb-sounding spectrometer is assessed.

The primary aim of this project is to search for new molecular signatures using the infrared spectrometers and identify a unique tracer of pollution to separate two sources of pollution namely: industrial transport/non-coal emissions and biomass burning. HCN is an important trace gas constituent in the atmosphere and it is suggested as a sensitive tracer of biomass burning. Present knowledge of the sources and sinks of HCN, and its role in atmospheric chemistry and biogeochemistry is highly uncertain. The atmospheric distribution of HCN is variable and previous space-based measurements do not give detailed tropical and sub-tropical distributions of HCN.

Atmospheric limb-emission spectra measured by the Michelson Interferometer for Passive Atmospheric Sounding (MIPAS) onboard the ENVIronment SATellite (ENVISAT) has been successfully used to detect spectral signatures of HCN in MIPAS-E spectra. These signatures were detected in the ranges 744.300–744.525 (HCN_0102) and 746.775–747.825 (HCN_0105) cm^{-1} for a single scan #2 (orbit 08585), for four selected MIPAS-E spectra from different latitude bands and later for the whole month of October 2003 using an automated detection technique.

Retrievals of HCN profiles are also promising, particularly at 12 km MIPAS-E nominal altitude. HCN data have been retrieved for October 2003 in 747.350–747.500 cm^{-1}. The HCN data retrieved at 12 km nominal altitude in the tropics appears to be the most successful. In addition, there is a potential to obtain vertical profiles of HCN on a global basis throughout the UTLS. For more accurate detection and retrieval of HCN, methyl chloride (CH_3Cl) and dinitrogen pentoxide (N_2O_5) need to be fitted well enough in both HCN_0102 and HCN_0105 MW (MW) regions.

ACKNOWLEDGEMENTS

The past four and half years have been a journey to me and I would like to acknowledge many people who have helped me in the completion of this project work. First, I would like to thank my supervisor, Prof. John Remedios, for providing the guidance and constant encouragement to finish my project.

The project would not have been possible without the funding provided by Dorothy Hodgkin Postgraduate Awards (DHPA), the data used for analysis in this thesis from MIPAS-E, AATSR (ESA), ACE-FTS (ACE science team members), EOS MLS (MLS science team), MOPITT and MODIS.

I would like to thank Prof. Paul Monks, Prof. Terry Robinson, Anu Dudhia, Prof. Peter Bernath, Dr. Chris Boone, Sean Mcleod, Gonzalo Gonzalez Abad, and Hugh Pumphrey for their contribution to this project in direct or indirect ways.

I am thankful to my two post docs- Dr. David Moore and Dr. Harjinder Sembhi who have contributed their expertise and valuable time to my research work. Thanks to the members of Earth Observation Science here at University of Leicester, many of whom I have become good friends with. Special thanks to Vijay, Rhian, Anna, Maithili, Rob, Chris, Sam, Roland, Gary, Diane, Catherine, Atousa, Karen, Lizzie to make my stay in Leicester a memorable one.

I would like to thank Prof. Mayank N. Vahia and Mrs. Jyotsana J. Gandhi for their motivational support. Special thanks to my friend Smitha Puthiyadan.

I am indebted to my two housemates and friends, Mobina and Shikha to bear my craziness and saving my sanity.

Finally, I want to thank my parents for their patience and unconditional support to get me where I am today. Special thanks to my sister and little brother.

LIST OF FIGURES

LIST OF TABLES

CONTENTS

CHAPTER 1

1. Introduction

The atmosphere is one of the essential fluid systems of the Earth's climate system. The major constituent is nitrogen (78%), followed by oxygen (21%), argon (0.9%), carbon dioxide (0.03%) with concentrations of trace gases including water vapour (H_2O) and ozone (O_3). Even though the Earth's atmosphere is thin compared to its radius, it is a prerequisite for life on the Earth, for instance, protecting it from the solar ultraviolet radiation and the high-energy particles. The troposphere is the lowest region of the atmosphere, extending from the Earth's surface to the tropopause at 10–18 km. About 90% of the total atmospheric mass resides in the troposphere and the major part of the trace gas burden is found there. The tropopause layer has several definitions; the World Meteorological Organization (WMO) defines it as the lowest level at which the temperature lapse rate decreases to 2 °C/km or less, provided that the average lapse rate between this level and all the higher levels within 2 km does not exceed 2°C/km. In the tropics this corresponds to a 380 K potential temperature surface (θ) which is located at a height between 15 and 18 km [Holton *et al*., 1995]. Towards the poles its height ranges between 6 and 8 km corresponding to a potential temperature of 290–320 K. A tropopause defined by a surface of 2 PVU (potential vorticity units) is often used in the mid-latitudes as the

quantity of potential vorticity emphasizes the material surface nature of the tropopause. This layer acts as an effective boundary to prevent large-scale mixing of the layers above and below due to the inversion of the temperature gradient at this point.

The atmosphere can be categorised into layers defined by their thermal gradient [Figure 1.1]. The primary region of interest for this thesis is the Upper Troposphere and Lower Stratosphere (UTLS) region of the atmosphere at an altitude of approximately 8- to 21-km altitude.

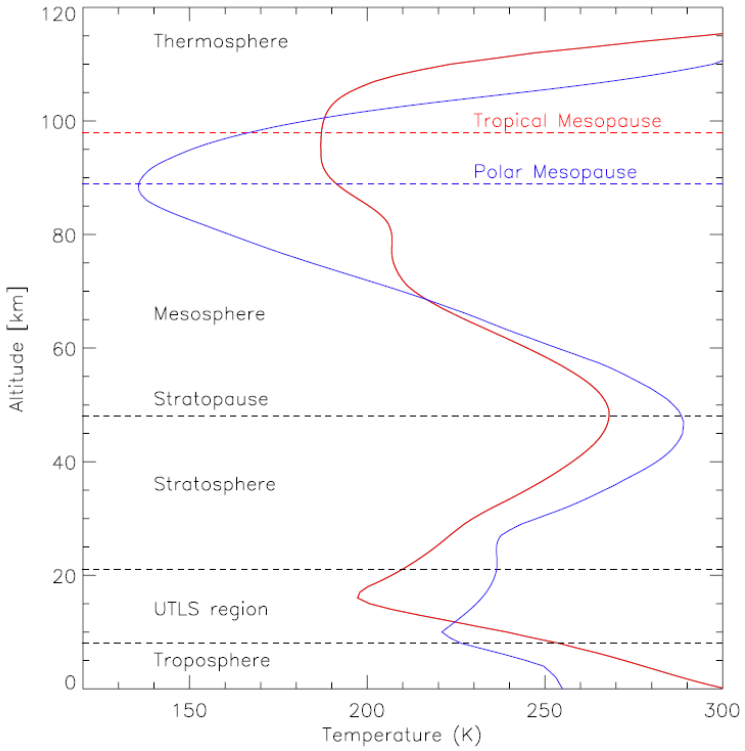

Figure 1.1: The vertical thermal structure of the Earth's atmosphere typical for both tropical (red) and polar (blue) conditions.

Climate change is defined by the Intergovernmental Panel on Climate Change [IPPC, 2007] as 'the change in climate over time, whether due to natural variability or as the result of human activities'.

The Earth's ultimate source of energy is the Sun. The Earth's radiation balance is achieved through a combination of processes as seen in Figure 1.2. About half the incoming solar radiation is in the visible short-wave part of the electromagnetic spectrum, the other half is in the near-infrared region, and the remainder is in the ultraviolet region. A major process is the re-emission of radiation

in the infrared region by the Earth's surface, the so-called 'terrestrial radiation'. In an equilibrium state, the average net radiation flux at the top of the atmosphere is zero (i.e. the solar radiation incident equals the emitted long-wave radiation + reflected short wave radiation). Any change in the magnitude of either the solar or the long-wave radiation causes an imbalance which is called *radiative forcing*.

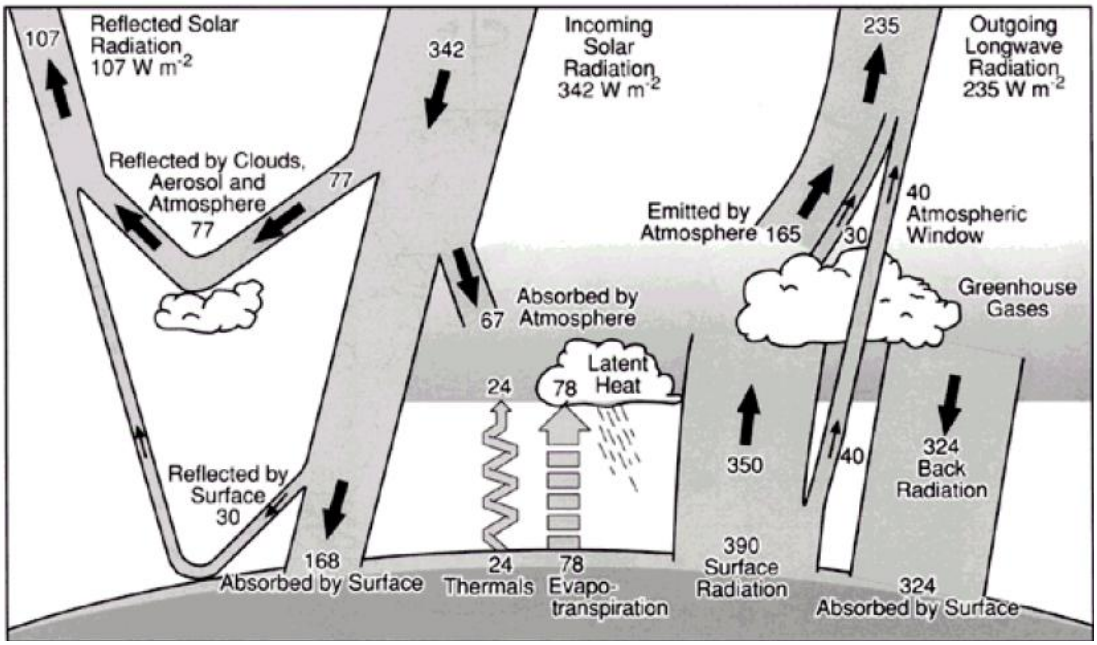

Figure 1.2: The Earth's radiation and energy balance (units in W m^{-2}). The partitioning of the annual global mean energy budget and the accuracy of the values are given in 'Earth's Annual Global Mean Energy Budget' [Kiehl, J. T. and Trenberth, K. E. 1997].

The Earth's radiation balance is essentially in an equilibrium state. There is a small period of changes in the atmospheric temperature such as the diurnal and the seasonal cycles, which relate to the changes in the incoming radiation; it is usually warmer in the day when there is sunlight than it is at the night, and warmer in the summer (the Earth's tilt means that there is more sunlight in the summer than winter). If one looks at the year-to-year changes there is very little change in the annual temperature. Processes such as the El Niño and La Niña make small changes to the outgoing radiation. On decadal timescales, very little change in the radiation balance can be seen because of anthropogenic increases in greenhouse gases. The greenhouse gases absorb primarily in the thermal infrared although also in the near infrared. By increasing these concentrations, more infrared radiation is absorbed in the atmosphere and thus more is re-radiated back towards the Earth rather than

away to the space. The Earth's temperature increases until the equilibrium is restored. At very low concentrations of greenhouse gases the radiative forcing effect is proportional to the increase, however, at higher concentrations saturation occurs and it takes a very large increase in the greenhouse gas concentration to affect radiative forcing (the CO_2 in atmosphere may have doubled from pre industrial levels but change in forcing is much less than that). On very long time scales there are changes seen in the radiation balance (variations in the Earth's eccentricity, axial tilt and precession comprise the three dominant cycles, collectively known as Milkankovich cycles which are related to the ice ages).

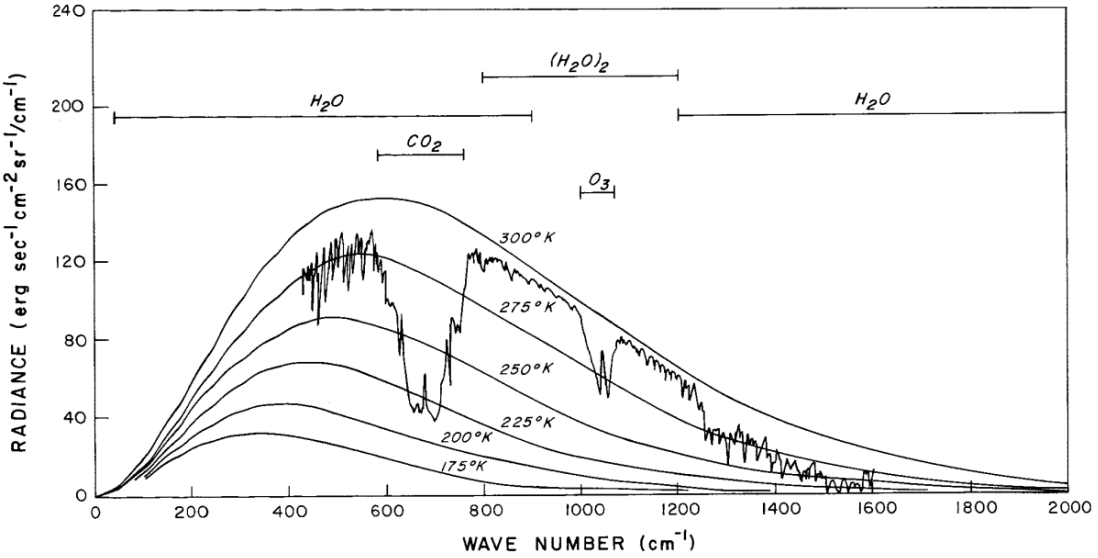

Figure 1.3: Spectrum of outgoing radiation over (215°W, 15°N) observed by the Nimbus 4 satellite as a function of wavenumber ν. Individual absorbing species are indicated and the curves represent the spectrum expected from a black body at different temperatures (Adapted from Liou, [1980]).

Most of the process that affect the Earth's surface occur in the lowest layer extending from the surface to the altitudes between 8 to 21 km (depending on latitude and season) Throughout the atmosphere, greenhouse gases absorb and re-radiate energy [Figure 1.3]. Surface temperature is particularly sensitive to the vertical profile of forcing in the troposphere, UTLS and middle atmosphere. Both natural and anthropogenic (man-made) greenhouse gases are important. An increase in greenhouse gases such as CO_2, O_3, H_2O and many other trace gases, clouds, and aerosol particles alter the radiation balance resulting in a relatively 'warmer troposphere'. Measurements show that certain atmospheric trace gases

have increased significantly since the beginning of the industrial revolution. Most of the observed increase in the global average temperatures since the mid-twentith century is very likely due to the observed increase in this anthropogenic greenhouse gas concentration and human influences now extend to the other aspects of climate, including ocean warming, continental-average temperatures, temperature extremes and wind patterns [IPCC, 2007].

The region above the troposphere is called the stratosphere (extending to altitudes up to approximately 50 km), is heated by the absorption of solar radiation by the ozone layer (that protects the surface from the short-wave ultraviolet radiation), i.e. temperature increases in this layer of the atmosphere. Above the stratosphere is the mesosphere which extends up to altitudes of 90 km. The temperature decreases adiabatically in this layer.

1.1 Pollutants in the atmosphere

Pollutants are substances (including any gaseous, chemical, or organic matter) that have a harmful effect on humans and/or ecosystems when present in sufficiently high concentrations in air, water or soil. The concentration of a pollutant at which it becomes harmful varies between substances; some are only harmful even in large amounts whereas some are harmful in very small amounts.

The chemistry of our atmosphere is considerably altered by transformations during the transport of these pollutants. For example, acid rain arises from the oxidation of SO_2 and NO_2 in the troposphere to form sulphuric (H_2SO_4) and nitric (HNO_3) acid respectively. The process starts with the various sources of anthropogenic and natural emissions and tracks resulting pollutants through their atmospheric transport, transformations and ambient concentrations-on local, regional and global scale-to their ultimate chemical and physical fates, including their impacts on our health and environment [Finlayson-Pitts and Pitts, 2000].

'Natural air pollution' is caused by volcanic eruptions, breaking waves, pollens, dust, terpenes from plants and forest fires. Agricultural practices, in particular, have been a source of additional pollutant species. 'Slash-and-burn' clearing of land adds greatly to the fire source; the removal of the natural vegetation

cover itself increases the rate of dust erosion [Wayne, 2000]. Anthropogenic effects or processes are those that are derived from the human activities. Anthropogenic sources include industry, agriculture, mining, transportation, construction and human habitation.

Primary pollutants are defined as those emitted directly into the atmosphere, e.g., sulphur dioxide, nitrogen dioxide, carbon monoxide, particles, lead, organics (including *Hazardous Air Pollutants* (HAPS)) and combustion-generated particulate matter (PM). Sources may be anthropogenic, biogenic, geogenic or some combination thereof. Once in the atmosphere, they are subjected to dispersion and transport, and simultaneously to chemical and physical transformations into gaseous and particulate secondary pollutants [Finlayson-Pitts and Pitts, 2000].

Air pollution is a serious problem both through direct health effects and through the export of enhanced concentrations of pollutants to the free troposphere. Respiratory disorders are the most common response produced by air pollutants. Air pollutants can be physiologically toxic and may also possess nuisance value [Wayne, 2000].

Localized air pollution can quite often lead to regional pollution by widespread dispersal within the troposphere, for example, the transport of pollutants from the United States to Europe and from Europe to Asia. The regional nature of pollution sources will vary widely depending on industrial emissions or agricultural practices such as biomass burning and cultivation. The exported pollutants contribute to the changes in the tropospheric ozone, altering the lifetime of greenhouse gases and thereby influencing the climate.

Biomass burning and industrial processes release ozone precursors. In addition to a large local effect, pollution can travel large distances. Pollution emissions from tropical biomass burning can reach high altitudes and directly affect the global atmosphere. Due to the long range transport of pollutants, pollution emissions of one country may enhance the trace gas levels in another country and affect the quality of air around the globe. . The lower atmosphere is accurately observed but poorly sampled by the ground and air-based atmospheric instruments. Space-based sensors are a complementary way to carry out effective global

monitoring of pollutants. With the help of satellite measurements, we can verify whether the countries are meeting their targets for controlling air pollution. Thus, to investigate the global air pollution problem one ideally needs to use mobile observing systems such as satellite instruments to detect and measure the concentrations of pollutants globally to understand their impact on the global atmosphere and climate.

1.2 Biomass burning

Biomass burning is the burning of the world's living and dead vegetation for land clearing, land use change and natural burning resulting from lightning-induced fires. It is generally believed that a large fraction of biomass burning is human initiated and biomass burning has increased significantly over the last 100 years.

Biomass burning serves a variety of purposes in agriculture such as:

- clearing of forest and brush land for agricultural use. The burning itself clears large areas of land allowing different types of vegetation to thrive due to increase light/nutrition etc
- control of brush, weeds and litter accumulation on grazing and crop land
- nutrient regeneration in grazing and crop land
- control of fuel accumulation in forest land
- production of charcoal for industrial and domestic use
- energy production for cooking and heating
- burning is also perceived as pest control method because it reduces the population of insects, snakes and so on.

Biomass burning is a significant source of

- greenhouse gases, carbon dioxide and methane, which lead to global warming

- chemically active gases, nitric oxide, carbon monoxide and hydrocarbons, which lead to the photochemical production of tropospheric ozone and acid precipitation (nitric oxide)
- methyl bromide which leads to the photochemical destruction of stratospheric ozone
- atmospheric aerosol, which impact the global climate.

Other impacts of Biomass Burning are

- biogeochemical cycling of nitrogen and carbon compounds from the soil to the atmosphere
- hydrological cycle, i.e., run off and evaporation
- reflectivity and emissivity of the land
- stability of ecosystems and ecosystem biodiversity.

Source of burning	**Biomass burned (Tg dry matter/yr)**	**Carbon released (Tg dry matter/yr)**	**Proportion of Total carbon released (%)**	**CO_2 released (Tg dry matter/yr)**
Savannas	3690	1660	42.1	1494
Agricultural wastes	2020	910	23.1	819
Tropical forests	1260	570	14.5	513
Fuel wood	1430	640	16.2	576
Temperate and boreal forests	280	130	3.3	117
Charcoal	21	30	1.0	27
World Total	**8700**	**3940**	**100.0**	**3546**

Table 1.1: Global estimates of annual amounts of biomass burning and resulting release of carbon and CO_2 into the atmosphere. [Sources: Seiler and Crutzen, 1980; Crutzen and Andreae, 1990; Hao *et al.*, 1990; Andreae, 1991]

Biomass burning occurs in the tropics (tropical rain forests and savanna grasslands), temperate zones and boreal forests. Biomass burning regions include California (chaparral ecosystem), Florida (wetlands), Mexico (tropical rainforests), Canada (boreal forest), Siberia (boreal and taiga forests), South Africa (savanna grasslands), Northern Australia (Bush land) and U.S. and Europe (agricultural wastes after the harvest).

The total mass of burned biomass material on an annual basis according to the source of burning is summarized in Table 1.1. The estimate for carbon released per year, i.e., 3940 Tg/year, includes all carbon species produced by biomass combustion ($C0_2$ + CO + CH_4 + NMHCs + particulate carbon). About 90% of the released carbon is in the form of CO_2 (≈ 3000–4000 Tg/year).

	Biomass burning (Tg element/year)	**All sources (Tg element/year)**	**Biomass burning (%)**
Carbon dioxide (CO_2)	3500	8700	40
O_3	420	1100	38
Carbon monoxide (CO)	350	1100	32
H_2	19	75	25
Non-methane Hydrocarbons (NMHC)	24	100	24
Methyl Chloride (CH_3Cl)	0.51	2.3	22
NO_X	8.5	40	21
NH_3	5.3	44	12
CH_4	38	380	10
Elemental carbon	19	22	86
Particulate organic carbon	69	180	39
Total particulate carbon	140	1530	7

Table 1.2: Estimates of Global emissions from biomass burning and Global emissions from all sources [Levine, 1990].

The burning of the world's forests, grasslands and agricultural land has several distinct impacts on the atmosphere and climate. Burning leads to the

production of the atmospheric greenhouse gases carbon dioxide, methane and tropospheric ozone. Estimates of the atmospheric gases and particulates produced by global biomass burning are given in Table 1.2 [Levine, 1990]. Burning of the world's forests destroys a major sink of atmospheric carbon dioxide and an important source of atmospheric oxygen due to photosynthetic activity. Burning also enhances the biogenic production of the greenhouse gases, nitrous oxide and methane and nitric oxide, the precursor of nitric acid. Global burning has significantly increased over the last century with the bulk of it being human initiated [Levine, 1990; 1991].

	Percentage in burning stage (%)	
	Flaming	**Smouldering**
CO_2	63	37
CO	16	84
CH_4	27	73
NMHC	33	67
NO_x	66	34
NH_3	15	85
HCN	33	67
CH_3Cl	28	72

Table 1.3: Gas production during flaming and smouldering phases of burning based on laboratory experiments. [Lobert *et al.*, 1991]

Nearly 90% of global biomass burning is human-initiated and such burning is increasing with time. Hence, biomass burning may be an important driver of global atmospheric and climatic change.

The flaming phase of fire approximates complete combustion, while the smouldering phase approximates incomplete combustion, resulting in greater production of CO, CH_4 and NMHCs. The percentage production of CO_2, CO, CH_4, NHMCs and carbon ash during the flaming and smouldering phases of burning based

on the laboratory studies is summarized in Table 1.3 [Lobert *et al.*, 1991]. Typically, for forest fires, the flaming phase lasts on the order of an hour or less, while the smouldering phase may last up to a day or more, depending on the type of fuel, fuel moisture content, wind velocity, topography and other parameters. For savanna grassland and agricultural waste fires, the flaming phase lasts a few minutes and the smouldering phase lasts up to an hour.

The presence of biomass burning particles in the atmosphere may also modify the solar radiative balance by changing cloud microphysics. These particles act as cloud condensation and ice nuclei, promoting changes in the cloud drops spectrum and thereby altering the cloud albedo and precipitation.

1.3 UTLS-dynamics and chemistry

The tropics are a source region of heat that drives the global atmospheric circulation by transport processes *through* the UTLS. The tropical biomass burning (in Brazil, Africa and Indonesia) can reach the UTLS and indirectly affect the global atmosphere that releases ozone (O_3) precursors (chemicals contributing to ozone formation). Figure 1.4 shows that pollutants emitted into the UTLS by biomass burning and industrial processes, combined with the downward transport of ozone from the stratosphere, can affect the tropospheric air quality in the middle and higher latitudes resulting in significant upper tropospheric ozone enhancement.

One of the roles of atmospheric radical chemistry, as driven by hydroxyl radical (OH), is to ‘‘cleanse’’ the troposphere of a wide-range of the organic compounds. The primary source of OH radicals in the troposphere is the photolysis of O_3 by UV radiation. The photolysis of O_3 is electronically excited to $O(^1D)$, which reacts with water vapour (H_2O). The OH radical is known to react with most of the trace gases and in many instances it is the first and rate-determining step.

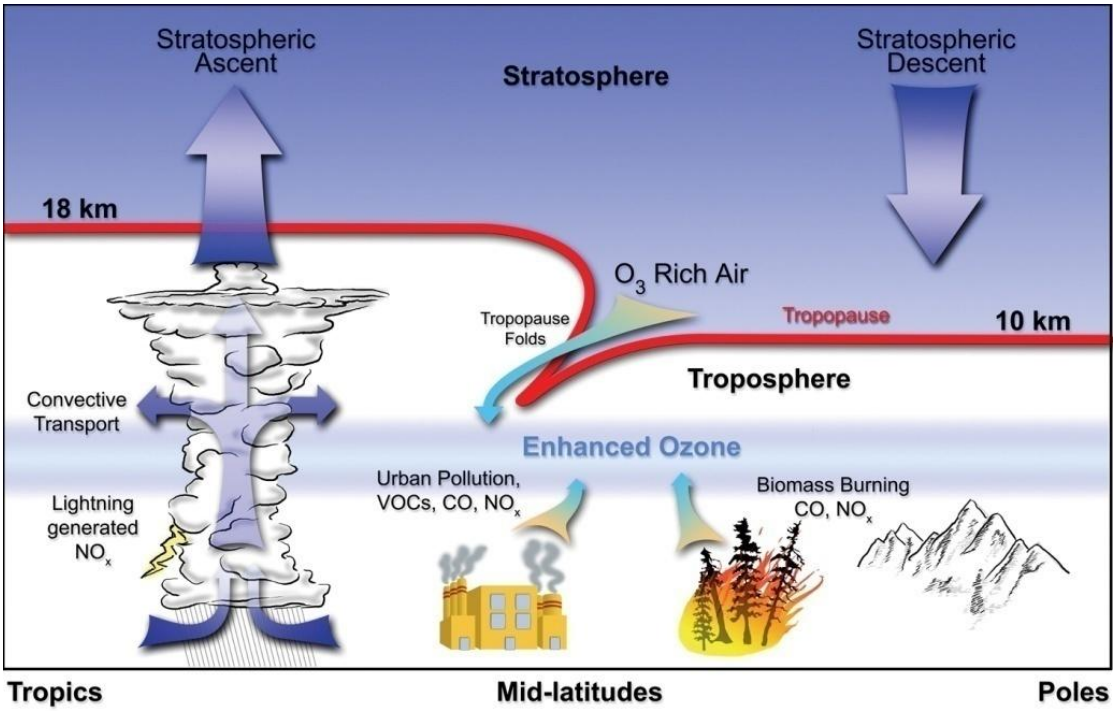

Figure 1.4: Schematic showing global air circulation in northern hemisphere. Air enters the stratosphere through the tropical tropopause layer (TTL-average position shown in red), driven by uplifting tropical clouds. [http://earthobservatory.nasa.gov].

Table 1.4 illustrates the global turnover of a range of trace gases including hydrocarbons and illustrates, for a number of trace gases, the primary role played by OH in their removal [Monks, 2005]. In the troposphere the reaction between CO and OH represents 85% of the CO sink. Approximately 70% of tropospheric OH reacts with CO in the unpolluted troposphere [Wayne, 2000]. Since the OH radical plays an important role in the atmospheric chemistry that influences the climate, carbon monoxide (CO) is one of the important trace gases in the troposphere.

Tropospheric ozone is a pollutant and harmful to living things, including humans. Only 10% of atmospheric ozone is in the troposphere, but despite its low concentrations, it acts as an initiator, reactant and product in much of the oxidation chemistry of the troposphere. Further it is an important source of hydroxyl radical.

Trace gas	Global emission rate/Tg yr^{-1}	Removal by OH [a] (%)
CO	2800	85
CH_4	530	90
C_2H_6	20	90
Isoprenes	570	90
Terpenes	140	50
NO_2	150	50
SO_2	300	30
$(CH_3)_2S$	30	90
$CFCl_3$	0.3	0
[a] Assuming mean global [OH] = 1×10^6 molecules cm^{-3}		

Table 1.4: Global turnover of tropospheric gases and fractions removed by reaction with OH [Monks, 2005].

Ozone plays an integral part in the atmospheric chemistry and CO can provide the mechanisms for the production and destruction of ozone. In areas with sufficient NO_x (oxides of nitrogen, nitrogen oxide (NO) and nitrogen dioxide (NO_2) are collectively known as NO_x), HO_2 produced from the oxidation of CO [reactions 1.1 and 1.2] can initiate the photochemical reactions which result in the *net* formation of ozone [reactions 1.3 to 1.5]. The photolysis of NO_2 and the subsequent reaction of the photoproducts with O_2 is the only known *in-situ* method of producing ozone in the troposphere. In urban and biomass burning areas where large concentrations of CO and other ozone precursors such as NO_x are produced, ozone can be formed in, and downwind of, the source region [Fishman and Seiler, 1983; Cros *et al.*, 1988].

$$CO + OH \rightarrow CO_2 + H \quad (1.1)$$

$$H + O_2 + M \rightarrow HO_2 + M \quad (1.2)$$

$$HO_2 + NO \rightarrow OH + NO_2 \quad (1.3)$$

$$NO_2 + h\nu \rightarrow NO + O \quad (1.4)$$

$$O_2 + O + M \rightarrow O_3 + M \quad (1.5)$$

$$\text{NET: } CO + 2O_2 + h\nu \rightarrow CO_2 + O_3 \quad (1.6)$$

where M is a third body molecule (such as N_2 or O_2), which removes excess kinetic energy in the reaction.

In polluted areas, NO_x > 1ppb alternatively, in non-polluted regions where the NO_x levels are low (<30 pptv), the direct reaction of HO_2 with ozone leading to ozone destruction can dominate [reaction(1.7].

$$HO_2 + O_3 \rightarrow 2O_2 + OH \quad (1.7)$$

$$\text{NET: } CO + O_3 \rightarrow CO_2 + O_2 \quad (1.8)$$

The major source of CO is the oxidation of methane via formaldehyde [reactions (1.9–(1.16]; 30–60% of tropospheric CO levels are estimated to come from the oxidation of non-methane hydrocarbons, biomass burning and incomplete combustion of fossil fuels. Other minor sources include the emissions by vegetation and micro-organisms and the photochemical oxidation of dissolved organic matter in the oceans.

$$CH_4 + OH \ (+O_2) \rightarrow CH_3O_2 + H_2O \quad (1.9)$$

$$CH_3O_2 + NO \rightarrow CH_3O + NO_2 \quad (1.10)$$

$$CH_3O_2 + HO_2 \rightarrow CH_3OOH + O_2 \quad (1.11)$$

$$CH_3OOH + h\nu \rightarrow CH_3O + OH \quad (1.12)$$

$$CH_3O + O_2 \rightarrow HCHO + HO_2 \quad (1.13)$$

$$HCHO + h\nu \rightarrow H_2 + CO \quad (1.14)$$

$$HCHO + h\nu \rightarrow H + HCO \quad (1.15)$$

$$HCO + O_2 \rightarrow CO + HO_2 \quad (1.16)$$

The dominant CO sink is the reaction between CO and OH; approximately 85% of the CO is removed by OH and the rest is transported to the stratosphere [(1.1)]. The reaction of the CO with OH radical is temperature (below ≈300 K) and pressure dependent; roughly, 70% of the OH reacts with CO in the unpolluted atmosphere [Wayne, 2000]. This means that increasing CO levels may lead to lower OH concentrations available for other greenhouse gases such as methane (CH_4), thereby indirectly contributing to the greenhouse gas effect.

1.4 Hydrogen cyanide

Hydrogen cyanide (HCN) has been suggested as a sensitive tracer of biomass burning [Lobert *et al.*, 1990; Holzinger *et al.*, 1999]. The detection of HCN from space would enable us to characterize tropospheric ozone production and loss and furthermore, likely greenhouse gas contributions due to biomass burning on a global scale. An improved understanding of HCN is required because HCN interferes with the measurement of total reactive NO_y {NO_y (total reactive nitrogen) is defined as the sum of NO_X plus the compounds produced from the oxidation of NO_x which include nitric acid. NO + NO_2 + HNO_2 + HNO_3 + HO_2NO_2 + NO_3 + $2N_2O_5$ + $CH_3C(O)O_2NO_2$ (PAN) + other organic nitrates +aerosol nitrate} [Kondo *et al.*, 1997]. Further, it could play a non-negligible role in the biogeochemical cycling of nitrogen.

In this section, we examine the sources and sinks of HCN in the troposphere and discuss the reasons to detect and retrieve HCN using the Michelson Interferometer for Passive Atmospheric Sounding (MIPAS) onboard ENVIronment SATellite (ENVISAT).

1.4.1 Sources and sinks

The atmospheric budget of HCN is still poorly understood. Efforts to determine the various sources and sinks of HCN have been discussed in the articles by many authors [Cicerone and Zellner, 1983; Lobert *et al.*, 1990; Holzinger *et al.,* 1999; Li *et al.*, 2000; Andreae and Merlet, 2001; Li *et al.*, 2003; Singh *et al,.* 2003], and their findings are summarized here.

1.4.1.1 Sources of HCN

The sources of HCN are biomass burning, residential coal burning and biogenic sources. The main sources and sinks of HCN are collected in Table 1.7. Emission ratios for HCN in Table 1.5 are in molar units relative to CO.

1.4.1.1.1 Biomass burning-largest source of HCN

Biomass burning is the largest known source of HCN [Lobert *et al.*, 1990; 1991; Li *et al.*, 2000; 2003; Holzinger *et al.*, 2001; Palmer *et al.*, 2009] and, because of this, is often used as an indicator for biomass burning [Rinsland *et al.*, 1998]. HCN is only emitted in the low-temperature smouldering phase of a biomass burning event, similar to CO [Lobert *et al.*, 1990].

Biomass burning emissions are typically characterised by emission factors. Emission data for HCN from most important types of fire regimes, viz., savannas and grasslands, tropical forest, extratropical forest and many others, show large gaps in the data [Andreae and Merlet, 2001]. A comprehensive list of these regimes can be found in Table 1.5, where adequate data exist for most of the species studied by Andreae and Merlet [2001] in the case of savanna and grassland but for other fire types, data for only the key species was available.

Type of Biomass burning	HCN emission factor (A)	Global emission estimates of HCN (B)
Savanna and grassland	0.025–0.031	0.09
Tropical forest	(0.15) [i]	0.20
Extratropical forest	(0.15) [i]	0.10
Biofuel burning	(0.15) [i]	0.41
Charcoal making	(0.15) [i]	0.02
Charcoal burning	(0.15) [i]	0.0006
Agricultural residues	(0.15) [i]	0.08

Table 1.5: (a) Emission factors (in gram species per kilogram dry matter burned) for HCN emitted from various types of biomass burning. (b) Global emission (in mass of species per year (Tg yr^{-1}) of HCN based on emission factors (column a) and biomass burning estimates. Table taken from [Andreae and Merlet, 2001, Table 1,2].[i] The value is the best guess.

To calculate these emission factors, data from 130 publications was either used directly or results were given as means and standard deviations for the appropriate type of fire (forest, savanna, etc.). Hence estimates have been provided where data are not available for different species and fire types using different

techniques of extrapolation. 'Best guess' estimates were based on the subjective evaluation of the available information, including the results from laboratory burning studies Due to lack of data error, column (b) of Table 1.5 would be a result due to error propagation from emission factor data in column (a) and biomass burning estimates of J. A. Logan and R. Yevich [R. Yevich, personal communication, 2001].

Different fuel types and fire temperatures result in different emission ratios [Lobert *et al.*, 1991]. HCN variability also depends on the nitrogen fuel content in the fires [Goode *et al.*, 2000; Christian *et al.*, 2004]. Past studies have indicated variable emission ratios for HCN [Lobert *et al.*, 1991; Holzinger *et al.*, 1999; Li *et al.*, 2000; Andreae and Merlet, 2001; Singh *et al.*, 2003; Li *et al.*, 2003] listed in Table 1.6.

Rinsland *et al.* [2004] calculated an HCN emission factor of 0.20 ± 0.06 g kg^{-1} from Atmospheric Chemistry Experiment-Fourier Transform Spectrometer (ACE-FTS) measurements which is higher than the 0.15 g kg^{-1} estimated for the extratropical forests [Andreae and Merlet, 2001, Table 1] but lower than the emission factor measurement of 0.43 ± 0.22 g kg^{-1} inferred from the solar absorption measurements through fires at Wollongong, Australia [Paton-Walsh *et al.*, 2005].

1.4.1.1.2 Residential coal burning

Cyanides are also easily formed during high temperature fuel combustion [Equation (1.17] but are instantly converted to NO resulting in nearly zero net emissions [Singh *et al.*, 2003].

$$CH + N_2 \rightarrow HCN + N \qquad (1.17)$$

Direct measurements in automobile exhaust [Lobert *et al.*, 1991; Holzinger *et al.*, 2001] as well as aircraft measurements by Singh *et al.* [2003] support the idea that the source from fossil fuel combustion is negligible.

Conversely, TRAnsport and Chemical Evolution over the Pacific (TRACE-P, a two-aircraft mission over the western Pacific conducted by the Global Tropospheric Experiment (GTE) of the National Aeronautics and Space Administration (NASA) in March–April 2001) observations show a strong enhancement of HCN in Chinese

urban plumes sampled in the Marine boundary layer (MBL) less than two days downwind of the source [Singh *et al.*, 2003]. Asian outflow in the MBL is often advected behind cold fronts and devoid of biomass burning influence [Carmichael *et al.*, 2003; Liu *et al.*, 2003].

The peak mixing ratios of HCN and CO in the Shanghai plume were 1.5 ppbv and1 ppmv, respectively. These peak mixing ratios were associated with high mixing ratios of CH_3Cl and carbonyl sulphide (OCS). Singh *et al.* [2003] further suggested that the enhancements of CH_3Cl and OCS correlated with enhanced HCN in the Chinese urban plumes could indicate a source from hard coal burning. There is a widespread use of biofuel in China, but data from African nitrile emissions from biofuel suggests that this is negligible [Bertschi *et al.*, 2003; Yokelson *et al.*, 2003]. Thus, more work is needed to identify the Chinese source of nitriles.

1.4.1.1.3 Biogenic source

Global estimates of biogenic HCN production are highly uncertain (0.1–3.2 m Tg N yr^{-1}, Li *et al.* [2003]) because the complicated biochemical process is not well understood over the diverse terrestrial ecosystem. A specific metabolic process is cyanogenesis in plants (for example, food crops, clovers and eucalyptus leaves), which is a part of plant defensive activity to fend off herbivores during the growing season. Cyanogenesis (formation or production of cyanogen or hydrocyanic acid) is likely to be a major biogenic process emitting HCN and its by-product, acetone (CH_3COCH_3), from variety of plants [Shim *et al.*, 2007].

Li *et al.* [2003] estimated the global biogenic HCN fractions by ~18% whereas Shim *et al.* [2007] estimated ~41% of global biogenic HCN fractions during the TRACE-P mission. Contributions of biomass burning to HCN (~ 30%) during TRACE-P mission is much smaller than the global estimates (>80%) [Shim *et al.*, 2007].

In the TRACE-P data, a strong correlation was found for HCN with methanol [Li *et al.*, 2003]. Methanol is generally considered a tracer for continental biogenic emissions. The biogenic source for methanol is estimated to be 50–280 Tg yr^{-1} [Heikes *et al.*, 2002]. If the HCN-methanol correlations reflected a common biogenic source, it implies that the biogenic source would be 3-17 Tg N yr^{-1}, too large to agree

with the observed HCN concentrations [Li *et al.*, 2000]. The highest methanol and HCN concentrations were observed in Chinese urban plumes. Methanol and HCN in TRACE-P were strongly correlated with CO, implying an anthropogenic source [Li *et al.*, 2003].

Sources	**HCN (m Tg N yr^{-1})**	***References***
Biomass burning	0.37–1.89	Lobert *et al.* [1990]
	0.64–3.18	Lobert *et al.* [1991]
	0.1–0.3	Holzinger *et al.* [1999]
	1.4–2.9	Li *et al.* [2000]
	0.26	Andreae and Merlet [2001]
	0.7–0.9	Singh *et al.* [2003]
	0.63	Li *et al.* [2003]
Residential coal	0.2	Li *et al.* [2003]
Biofuels	0.21	Andreae and Merlet [2001]
Car exhaust	0.04	Lobert *et al.* [1991]
	<0.02	Singh *et al.* [2003]
Biogenic	0–0.2	Singh *et al.* [2003]

Table 1.6: Literature estimates of global HCN sources [Li *et al.*, 2003]

1.4.1.1.4 Oxidation of CH_3CN by OH as a source of HCN

$$CH_3CN + OH \xrightarrow{Cl^-} HC(O)CN \rightarrow HCN + M \qquad (1.18)$$

Murad *et al.* [1984] and Brassuer *et al.* [1985] had proposed a connection between methyl cyanide (CH_3CN) and HCN. 1D-model study calculations done by Brassuer *et al.* [1985] investigated HCN as progenitor of CH_3CN but concluded that this was unlikely. Measurements of stratospheric HCN [Kleinböhl *et al.*, 2006] using JPL MkIV Fourier transform interferometer (balloon borne infrared solar occultation measurements) were used in a 2-dimensional model with help of newly available reaction rate coefficients for the reactions with OH and $O(^1D)$ [Strekowski, 2001; Sander *et al.*, 2003].

The reaction with OH gave reasonable agreement with the measured and the modeled HCN profiles where it was assumed that HCN loss due to photolysis was negligible. The study concluded HCN yield of 30% from the oxidation of CH_3CN by OH [Equation (1.18); Tyndall *et al.*, 2001] was consistent with the measurements at mid and high latitudes. In this OH-initiated oxidation they report a HC(O)CN yield of (40 ± 20)%, however, no other carbon bearing products could be unambiguously identified.

The study done by Li. *et al.*, [2009] used the new reaction rate coefficients where the HCN-OH rate coefficient was lower by 40% than previous calculations done by Li. *et al.* [2003], also included the additional source of HCN from the CH_3CN oxidation. They considered the sink with $O(^1D)$ as a minor sink and hence ignored it in their model calculations which finally resulted in a HCN lifetime of 6.1 months. This lifetime reproduced the approximate 2 year HCN cycle in the UTLS as observed with EOS MLS and ACE-FTS [Pumphrey *et al.*, 2008]. The atmospheric source of HCN in the troposphere due to oxidation of CH_3CN by OH is low but significant enough in stratosphere particularly at high altitudes.

1.4.1.2 Sinks of HCN

1.4.1.2.1 Reaction with OH

The expected atmospheric sinks of HCN are reactions with OH and $O(^1D)$, photolysis and precipitation scavenging. The reaction of HCN with OH is significant [Cicerone and Zellner, 1983; Li. *et al.*, 2009]. The following chemical equations represent the three main loss processes:

$$HCN + OH \rightarrow HOCN + H \quad (1.19)$$

$$HCN + h\nu \rightarrow H + CN \quad (1.20)$$

$$HCN + O(^1D) \rightarrow OH + CN \quad (1.21)$$

Atmospheric sinks of HCN from reactions by OH and $O(^1D)$ and photolysis yielded lifetime of few years (1–5 years) [Cicerone and Zellner, 1983]. Early photochemical/transport model calculations by Cicerone and Zellner [1983] showed HCN should be relatively well-mixed in the troposphere and its concentration

decreases slowly with altitude in the stratosphere. However, the HCN volume mixing ratios were too low by about 20% for 10–20 km, and showed a rapid decrease above 20 km. Li *et al.* [2003] used rate constants from Wine *et al.* [2002] for HCN, with the monthly mean OH fields from full chemistry simulations [Li *et al.*, 2002]. Wine *et al.* [2002] indicated a lower rate constant by a factor of three for the HCN-OH reaction ($k = 1.0 \times 10^{-13} e^{-773/T}$ cm^3 $molecule^{-1}$ s^{-1} at 600 torr, where T is the temperature measured by Fritz *et al.* [1984]; the reaction of OH-HCN is pressure dependent). The corresponding lifetime against oxidation by OH is 4.3 years for HCN, much longer than the lifetime against the ocean uptake.

Seasonal measurements of an atmospheric column of HCN at northern mid-latitudes indicate factors of 2–3 with maxima in spring and summer [Mahieu *et al.*, 1995, Zhao *et al.*, 2000]. Space-based measurements of HCN mixing ratios in the tropical upper troposphere indicate a range of 200 to 900 pptv [Rinsland *et al.*, 1998]. Such large variations were inconsistent with the conventional view that previously HCN has an atmospheric lifetime of few years with the oxidation of OH providing the main sink. Thus, Li *et al.* [2000] proposed a hypothesis that ocean sinks provide the missing sink for HCN to show that the available observations of atmospheric HCN are consistent with a scenario where biomass burning (1.4–2.9 Tg N yr^{-1}) provides the main source and the ocean provides the main sink. Henry's law constant of HCN (12 M atm^{-1} at 298 K) (i.e. the solubility of HCN) is sufficiently high for the ocean uptake to impose atmospheric lifetimes of few months (2–4 months) if loss in the oceanic mixed layer is sufficiently rapid [Hamm and Warneck, 1990; Li *et al.*, 2000].

1.4.1.2.2 Ocean sink

The first in situ measurements of HCN from the Pacific troposphere (0–12 km) were obtained during the NASA TRACE-P airborne mission [Singh *et al.*, 2003]. Li. *et al.* [2003] analysed these measurements by using a 3D global model to improve the understanding of the atmospheric budget of HCN and confirmed the previous hypothesis of a dominant ocean sink for HCN. The vertical distributions of CO decreased from the boundary layer to the free troposphere, while the opposite was seen in the mixing ratios of HCN and CH_3CN; observed in remote marine air over

the NW Pacific. They concluded that ocean uptake is the dominant sink. Oxidation by OH is an additional major sink and the resulting tropospheric lifetime for HCN is 5.3 months.

Total atmospheric burden (Tg N)	0.423
Atmospheric lifetime	6.1 months
Tropospheric lifetime	5.3 months
Tropospheric burden* (Tg N)	0.38
Sources (Tg N yr^{-1}):	
Biomass burning	0.63
Residential coal burning	0.20
Sinks (Tg N yr^{-1}):	
Ocean uptake	0.73
Reaction with OH	0.1

Table 1.7: Atmospheric budget of HCN [Li *et al.*, 2003; 2009].* Global budget for 1000–10 hPa.

1.5 Measuring HCN in the atmosphere

Hydrogen cyanide was first detected in the stratosphere using a high resolution (0.06 cm^{-1}, apodised) Fourier transform infra-red spectrometer aboard a Sabreliner jet aircraft. By analysing the HCN ν_3-band transitions observed in the infrared solar spectra, an average vertical column above 12 km of $7.1 \pm 0.8 \times 10^{14}$ molecules cm^{-2}, corresponding to an average mixing ratio of 170 parts per trillion by volume (pptv) [Coffey *et al.*, 1981] was reported. Later, mixing ratios of 130–260 pptv in the 20–40 km region were reported by Carli *et al.* [1988] from balloon-borne sub-millimetre emission spectra. Rinsland *et al.* [1982] detected HCN in the troposphere for the first time using IR absorption measurements from Kitt Peak (a high spectral resolution Fourier transform spectrometer operated at the National Solar Observatory (NSO) facility at Kitt peak 31.93°N latitude, 111.63°W longitude, 2.09 km altitude), where HCN mixing ratios of 166 pptv between 2–12 km were detected.

HCN has been detected in the Earth's atmosphere and measured using various methods such as Mass spectrometry [Spreng and Arnold, 1994; Schneider *et al.*, 1997; Holzinger *et al.*, 1999], Gas chromatography [Koppmann *et al.*, 1997] and Fourier transform infrared spectrometry (FTIR) [Zhao *et al.*, 2000, 2002; Rinsland *et al.*, 2001, 2002, 2007; Kasai *et al.*, 2005]. Some of the important measurements are listed in Table 1.8. HCN concentrations in the troposphere have been found to be highly variable, with values ranging from 160–1470 pptv. In the stratosphere, HCN decreases with the increasing altitude.

Measurements of HCN using infrared solar spectra at Rikubetsu (43.5° N, 143.8° E, 370 m a.s.l.) and Moshiri (44.4° N, 142.3° E, 280 m a.s.l.) between 2.09–14 km indicated seasonal variation of HCN over Northern Japan with a maximum of 334±50 pptv to a minimum of 179±30 pptv These variations suggested that HCN lifetime was shorter than one year. Back trajectory calculations showed that biomass burning occurred in China and Mongolia (30°–60° N) from March to November 1997 with intense activities in April to July that resulted in enhanced HCN over Northern Japan [Zhao *et al.*, 2000]. Enhancements of HCN over Northern Japan in the year 1998 were due to biomass burning in eastern Siberia [Zhao *et al.*, 2002] but might as well be related to the 1997–98 El Niño Southern Oscillation (ENSO) period.

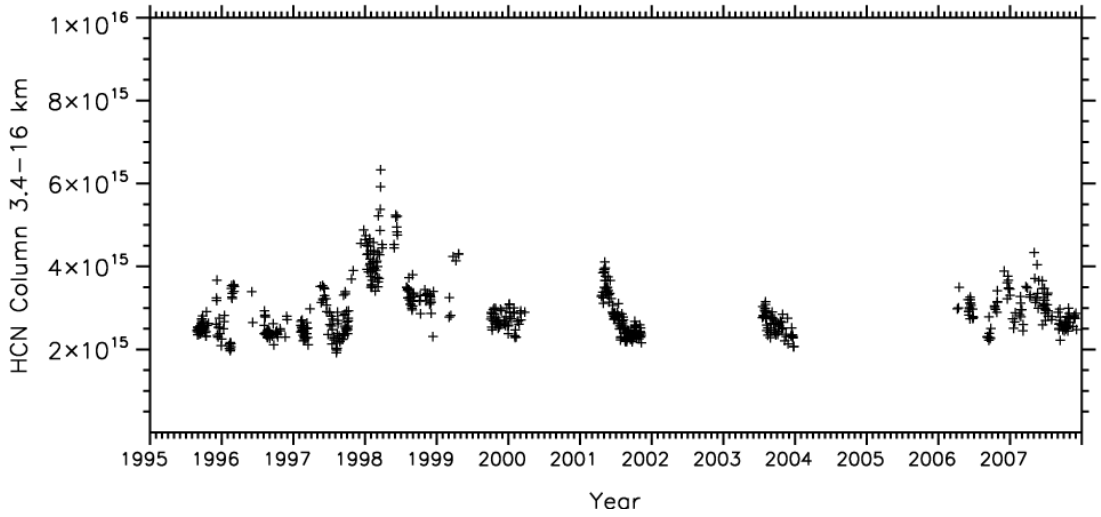

Figure 1.5: Time-series plot of HCN (3.4–16 km) column data. Measurements recorded from August 1995 to December 2007 at the Network for the Detection of Stratospheric Change station on Mauna Loa, Hawaii. Daily mean averages are shown in plus symbols. The data is not fitted due to gaps in the HCN column data.

High spectral resolution (0.003 cm^{-1}) infrared solar absorption measurements of HCN have been recorded at the Network for the Detection of Stratospheric Change station on Mauna Loa, Hawaii. Figure 1.5 shows higher HCN 3.4–16 km column measurements throughout the time period of August 1995 to December 2007. The HCN column data in 1998 (El-Niño year) is strongly enhanced in what was a year of high levels of CO. As seen in the Figure 1.5 no data is recorded in the 2002–2003 El-Niño year but enhancements are not seen in the 2006–2007 El Niño year compared to the 1997–1998 year.

Observations obtained during INTEX-A were analysed by Liang *et al.* [2007] to examine the summertime influence of Asian pollution in the free troposphere over North America. They reported HCN volume mixing ratio (VMR) (>400 pptv) enhancements at 2–4 km altitude compared to the HCN mixing ratio of 243 ± 118 (median 218) pptv measured over the troposphere (0–12 km) during NASA's TRACE-P mission [Singh *et al.*, 2003] and in the upper troposphere (8–11 km) the plume with Asian pollution contained elevated HCN concentration of 320–580 pptv.

In situ measurements of HCN concentrations in the upper troposphere/lower stratosphere were made during the March 2000 deployment of SAGE III-Ozone loss and validation Experiment (SOLVE) campaign. An average HCN VMR of 280 ± 48 pptv was measured from NASA DC-8 aircraft flying at altitudes 10–12.5 km [Viggiano *et al.*, 2003].

Observations in the upper troposphere/lower stratosphere at 15°N to 30°S latitude were recorded by ACE-FTS from 30 September to 3 November 2004 and analysed by Rinsland *et al.* [2005]. They reported HCN VMR as high as 1470 pptv from biomass burning emissions. Further, back trajectory calculations indicated the emissions likely originated near to the surface from tropical regions of intense fire emissions over tropical South America or Africa. ACE-FTS boreal measurements over Alaska and Canada during June–July 2004 recorded HCN VMR of 755 pptv.

Figure 1.6 shows enhancements of HCN VMR inside the Asian monsoon anticyclone [Park *et al.*, 2008] and is roughly coincident with the Carbon Monoxide (CO) enhancements at 16.5 km measured by ACE-FTS (0°–120°E and 10°–40°N). Enhancement of 0.23 ppbv [Coheur *et al.*, 2007] in HCN concentration values was

measured by ACE FTS during a sunset occultation on 8 October 2005 (East Coast of Tanzania, at 6.95°S latitude and 39.42°E longitude).

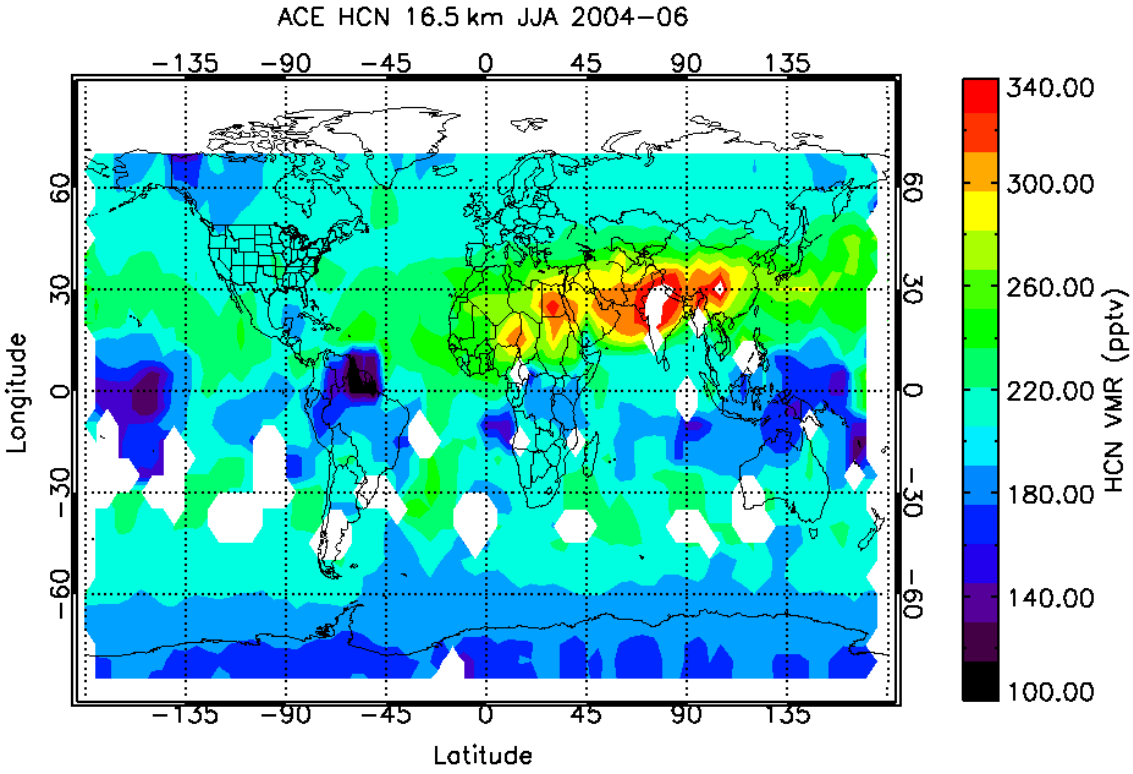

Figure 1.6: Global map of HCN mixing ratios at 16.5 km for June–August (2004–2006).

HCN in the middle atmosphere is measured using the EOS MLS instrument onboard the NASA's Aura satellite [Pumphrey *et al.*, 2006]. In the middle atmosphere HCN is slowly lost due to reactions with OH and O(^{1}D). The HCN VMR over large vertical range (usable retrieved product ≈32–48 km) is retrieved by taking the weekly zonal mean of radiances. The study suggested that HCN mixing ratio in the mesosphere is not greater than 0.1 ppbv unlike the previous measurements done by Kopp [1990] which showed values of 0.2–1.0 ppbv between 70–90 km. Pumphrey *et al.* [2008] concluded that HCN showed a two year tape recorder effect, with the values entering the stratosphere being preserved and carried upwards by the meridional circulation. Also forest fires in the Indonesian region emit a higher proportion of HCN than do fires in other tropical regions with large inter-annual variability.

Method	Platform	Location	Dates	Concentration values
Ground based/Balloon/Aircraft measurements				
Infrared absorption Fourier transform spectrometer (FTS)-0.06 cm^{-1}	Sabreliner jet aircraft	5°N and 50° N latitude-(12–20 km)	1981	170 ± 20 pptv (Avg.)
Infrared solar spectra-FTIR-0.01 cm^{-1}	Ground based	Kitt Peak National observatory (31°57' N , altitude 2095 m)-(2–12 km)	February 23, 1981	166 pptv (Avg.)
Sub millimetre emission spectra	Balloon-borne	20–40 km	1982	180 pptv (Avg.)
Ion-molecule reaction mass spectrometry	Dutch research jet aircraft (Cessna Citation)	62° and 73° Northern Scandinavia-(13–17 km)	9, 18, 21, 24 February 1995	164 pptv (Avg.)
Infrared absorption Fourier transform spectrometer (FTS)-0.0035 cm^{-1} and 0.0020 cm^{-1}	Ground based	Rikubetsu (43.5° N, 143.8° E, 370 m a.s.l.) and Moshiri (44.4° N, 142.3° E, 280 m a.s.l.)-(2.09–14 km)	May 1995–June 2000	Seasonal variations: 333 ± 44 pptv (summer) 195 ± 16 pptv (winter) 334 ± 30 pptv (May–July) 179 ± 30 pptv (Dec–Jan)
Infrared absorption Fourier transform spectrometer (FTS)-0.0035 cm^{-1}	Ground based	Mauna Loa, Hawaii-(3.4–16 km)	August 1995–February 1998	Seasonal variations: 190 pptv–700 pptv

Continued				
Infrared absorption Fourier transform spectrometer (FTS)	Ground based	Kitt Peak, Arizona (31.93° N, 111.63°W, 2.09 km altitude)	May 1978–May 2000	Vertical column abundances: $1–6 \times 10^{-15}$ molecules cm^{-2}
Infrared absorption Fourier transform spectrometer (FTS)	Ground based	Lauder, New Zealand (45.04°S, 169.68°E, 0.37 km altitude)	November 1997–November 2000	Vertical column abundances: $1.77–6.86\times 10^{-15}$ molecules cm^{-2} (0.08–0.35 ppbv)
Infrared absorption Fourier transform spectrometer (FTIR)-0.0019 cm^{-1}	Ground based	Poker Flat, Alaska (65.11°N, 147.42°W) (1–10 km)	2000–2004	Tropospheric column abundances: $2–5 \times 10^{15}$ molecules cm^{-2} (January–April)
SAGE III-SOLVE campaign-Chemical Ionization Mass spectrometry	NASA DC-8 aircraft	Kiruna, 68°N, 20°E, Northern Sweden (Arctic)-(10–12.5 km)	27 February –15 March 2000	280 ± 48 (1σ) pptv
TRACE-P campaign, infrared solar spectra	NASA DC-8 aircraft	Pacific-10°–45° N lat. and 100° E–120° W lon-(0–12 km)	25 February–10 April 2001	243 ± 118 (median 218) pptv
INTEX-A campaign	NASA DC-8 aircraft	United states , Pacific ocean on west and Atlantic ocean on east (6–12 km)	1 July–14 August 2004	290 ± 70 pptv (background) 310 ± 90 pptv (Lower stratosphere) 300 ± 80 pptv (Convection and Lighting) 420 ± 20 pptv (Asian) 1090 ± 850 pptv (Biomass burning)

Continued				
Space based measurements				
Infrared solar absorption spectra-FTS-0.01 cm^{-1}	ATMOS/ Spacelab 3	25.6° and 32.7° N and 46.8° and 49.0° S (12–32 km)	April 30–May 6, 1985	vertical column abundances: $(2.55\pm0.30)\times10^{15}$ molec./cm^2 (S.D.) and $(2.75\pm0.30)\times10^{15}$ molec./cm^2
Infrared absorption Fourier transform spectrometer (FTS)-0.01 cm^{-1}	ATMOS/ ATLAS 3	5.3° and 31.4° N (15–30 km)	3–12 November 1994	200 pptv (stratospheric) 940 ± 190 pptv (~13.9 km-SS98)
ACE FTS-Atmospheric Chemistry Experiment-Fourier Transform Spectrometer, IR solar occultation-0.02 cm^{-1}	ACE-FTS/ SCISAT-1	85°N to 85°S (6–16 km)	launched on 12 August 2003	1470 pptv (~ 10.5 km) 710 ± 30 pptv (11.5 km-ss11607) 160 ± 20 pptv (11.5 km-ss16615) 755 pptv
EOS MLS-Earth Observing System Microwave Limb Sounder, radio telescope	EOS MLS/ NASA's AURA	82°N to 82°S (32–48 km)	launched on 15th July 2004	0.18–0.25 ppbv (24–30 km)

Table 1.8: Measurements of HCN in the troposphere and stratosphere. Many aircraft campaigns and ground based measurements are carried out during a particular season and cover only certain parts of the globe. Measurements of HCN are fairly sparse and satellite based measurements from ACE-FTS do not give detailed distributions of HCN in tropical and sub-tropical latitudes.

HCN is less uniformly distributed in the troposphere than previously indicated by Cicerone and Zellner [1983]. HCN recorded using ground based infrared spectroscopic measurements at the International Scientific Station of the Jungfraujoch (ISSJ) in the Swiss Alps and Kitt Peak shows seasonal trends with enhancement factor of two to three especially during springtime [Rinsland *et al.*, 1998; 1999; 2001].

Total column abundances of HCN have been retrieved from infrared solar spectra observed at Moshiri and Rikubetsu. Sporadic enhancements in the total column HCN data measured over Northern Japan [Zhoa *et al.*, 2000; 2002; 2007] were observed in 1998, 2002 and 2003 and concluded that the enhancements of HCN over Northern Japan during these years were driven by biomass burning in Siberia.

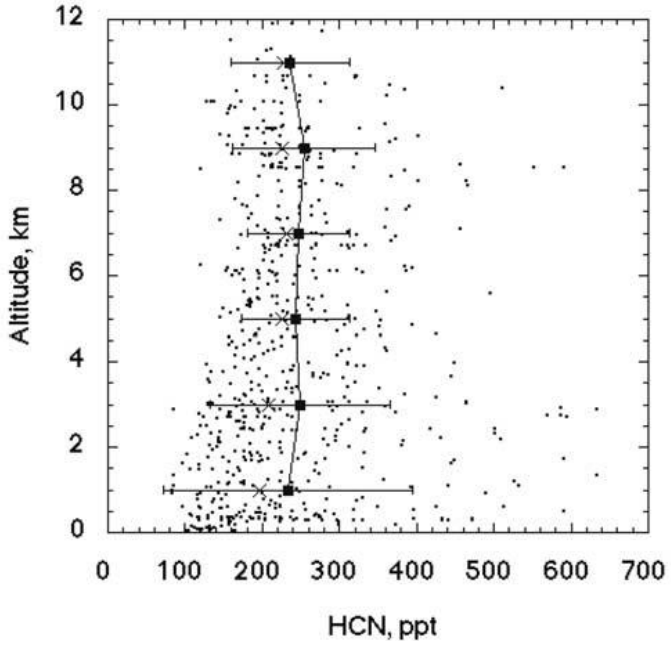

Figure 1.7: Vertical structure of HCN over the Pacific as measured during TRACE-P mission.

The vertical distribution of HCN [Figure 1.7] over the Pacific region show measurements of 200 pptv (background conditions) at altitude levels 0–12 km [Singh *et al.*, 2003]. Under biomass burning conditions, enhancements in the vertical distributions of HCN is seen from 8–15 km altitude levels [Rinsland *et al.*, 2005]. The HCN latitudinal distribution remains variable and can be derived from the fact that

the main source of HCN is biomass burning, with sufficient lifetime to be transported across the different latitude regions.

Lupu *et al.* [2009] investigated the spatial and temporal distribution of HCN in the upper troposphere using the Global Environmental Multiscale Air Quality model (GEM-AQ) simulations and ACE-FTS measurements. HCN biomass burning emissions are based on fire the Global Fire Emission Database (GFED) version 2. In addition, the model results are compared to the total HCN columns measured at Rikubetsu and Moshiri (in Hokkaido, Northern Japan; 2.09–14 km). The Gem-AQ model results show that in the upper troposphere it performs well globally for all seasons, except at the Northern high and the middle latitudes in summer, where the model has large negative bias, and in the tropics it exhibits large positive bias (in winter and spring). The model is able to explain most of the observed variability in the upper troposphere HCN field, including the interannual variations in the observed mixing ratio. The study concluded that more research is needed in order to constrain the ocean sink and to explore and quantify biogenic sources of HCN The injection height of biomass burning plume is also an important parameter for modeling fires in the boreal forest. Better estimation of the biomass burning emissions and further characterization for different ecosystems is required for refinement.

1.6 Summary

The aim is to search for new molecular signatures in the infrared spectrometers and further identifying a molecule that is more likely to be a unique marker of the pollution. Carbon Monoxide (CO) is a good measure of pollution, but we would like to identify a unique marker of biomass burning. By detecting *'signatures'* such as Hydrogen Cyanide (HCN is sensitive tracer) in the biomass burning plume, we could potentially separate the sources of pollution.

As HCN is suggested to have a major biomass burning source in many regions and only coal burning as the other alternative, it is more likely to be a unique marker of the biomass burning pollution and hence a suitable candidate molecule.

The global measurements of HCN should help separate the two sources of pollution namely: the industrial transport/the non-coal emissions and the biomass burning.

The seasonal measurements of HCN [Rinsland 1998, 1999, 2001; Zhoa 2000, 2002, 2007] indicated that main source of HCN is biomass burning. The HCN model study done by Li *et al.* [2001] accepts ocean as the major sink, resulting in a relatively short lifetime of 5.5 months. The present knowledge of the sources, sinks of HCN, and its role in atmospheric chemistry and biogeochemistry is highly uncertain. In this thesis, the HCN study focussed in the UTLS region (8–21 km altitude levels).

Measurements of hydrogen cyanide in the troposphere are extremely sparse. The space-based measurement using ACE-FTS show good coverage at the poles, but is less good at the tropics, due to the measurement viewing geometry. Thus, the main aim of this work is to detect the HCN spectral signature and retrieve accurate HCN profiles using the Michelson Interferometer for Passive Atmospheric Sounding (MIPAS-E) instrument onbaord ENVISAT satellite, a high resolution spectrometer that measures infrared emission spectra using the limb sounding technique. The limb emission technique permits measurements during day and night, with good coverage of all the latitudes.

The structure of following chapters is as follows:

- Chapter two presents introduction to the theory of remote sensing of atmosphere and retrieval theory. A brief description of Oxford's Reference forward model (RFM) that is used to simulate MIPAS-E atmospheric limb radiances is also described here.
- In Chapter three, description of MIPAS-E instrument onboard ENVISAT satellite and data processing is given.
- In Chapter four, detection methodology of HCN spectral signature in biomass burning plume and global scale using MIPAS-E data is given. Questions addressed in this chapter are:
    - Which are the best suitable microwindows (MWs) that can be used for HCN detection purpose in the atmosphere and why?

- What are the instruments' limiting factors to detect HCN?
- Can we detect HCN in a biomass burning plume in the UTLS using MIPAS-E data and if possible further possibility of detection on a global scale?

- In Chapter five, retrieval approach and results of globally retrieved HCN concentration using the Oxford's (MIPAS Orbital Retrieval using Sequential Estimation) MORSE algorithm. is discussed Questions addressed in this chapter are as follows:
  - What can be deduced from the mean profile comparison of non-coincident, ACE-FTS HCN level 2 data with MORSE-retrieved MIPAS HCN data?
  - What are the differences that can be observed in the MORSE retrieved HCN when used to simulate the ACE-FTS HCN transmission micro-windows? Also what is the magnitude of the effects due to presence of CH_3Cl in the HCN retrieval MWs?
  - What can be interpreted from the zonal behaviour of MORSE retrieved HCN when compared to ACE-FTS and EOS-MLS zonal HCN data?
  - What are the differences between the MIPAS HCN retrieved data obtained using the Institut für Meteorologie und Klimaforschung and Instituto de Astrofísica de Andalucía (IMK/IAA) retrieval processor [Glatthor *et al.*, 2009] and those retrieved using the MORSE retrieval algorithm for the month of October 2003? What can be observed from the two sets of global HCN retrieved data?
- Chapter six presents concluding remarks followed by suggestions of future work.

CHAPTER 2

2. Remote sensing of the atmosphere

2.1 Introduction

Remote sensing or indirect measurements of the atmosphere provides one method of measuring atmospheric trace gas concentrations. Remote sensing of the atmosphere has been carried out by a wide variety of instruments using techniques to measure the electromagnetic radiation from regions of the atmosphere. In order to interpret the indirect measurements a complex *inverse* problem must be solved using a mathematical approach to obtain the quantity of interest such as gas concentrations, pressure and temperature. The physical effects exploited may involve refraction, transmission, scattering, thermal emission and non-thermal emission of radiation at all wavelengths from radio to the ultraviolet. The major advantage of remotely sensed measurements from satellite instruments is their ability to provide global coverage from only one sensor system over a period of time.

The radiation will be modified by absorption and scattering processes out of the beam as it passes through the atmosphere. The intensity, or radiance, of a beam of energy originating from a point can be defined as the flux of energy in a given direction per second per unit frequency (or wavelength) range per unit solid angle per unit area perpendicular to the given direction. All molecules interact with electromagnetic radiation and either emit or absorb the radiation at discrete frequencies and this information is used to provide information on their atmospheric concentration.

2.2 Thermal emission limb sounders

The satellite instrument scans the Earth's atmosphere either in nadir or limb sounding mode. The nadir sounding technique looks at the atmosphere at 90° to the vertically downwards Earth's surface and total column measurements of the trace gases can be inferred. There is a possibility of measuring at good horizontal spatial resolution; however the vertical resolution is limited to several kilometres except for the temperature and water vapour (H_2O). The limb sounding technique looks through the edge of the atmosphere 'horizontally' at the horizon using cold space as a background (MIPAS on ENVISAT, EOS MLS on NASA's AURA satellite). When sun (stellar) or moon (lunar) measurements are used as a background source to measure the absorption of the atmosphere, it is known as the occultation method (solar occultation- ACE-FTS, ATMOS). These techniques give good vertical resolution.

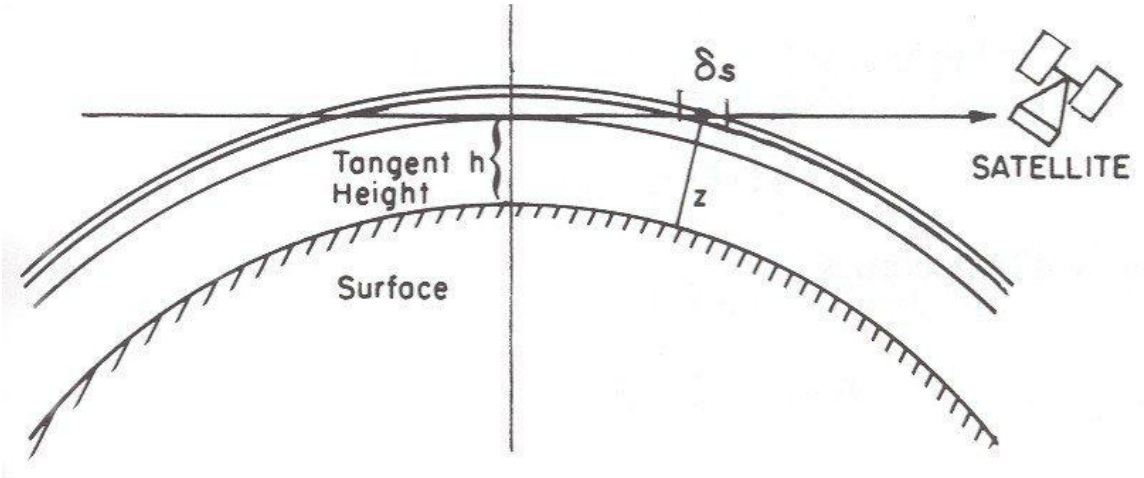

Figure 2.1 : The MIPAS-E limb viewing geometry [Stephens, 1994]

The limb viewing geometry is shown in Figure 2.1. By scanning vertically, measurements of the Earth's atmosphere at general tangent height *h* are made. The radiance is received from the section δs of the path at the height *z*. As per the geometry, the radiation from the lower tangent altitudes will have a longer path length compared to measurements at the upper atmosphere. As the viewing geometry is in the horizontal mode or Earth's 'limb' mode, the horizontal resolution is limited and can be between a few hundred kilometres (> 500 km) along the line of sight (LOS). However, the vertical resolution can be as high as 1-3 km compared to nadir sounding (usually > 5 km).

Instrument	**Platform**	**Launch**	**Measurement technique**	**Spectral range**
MIPAS-E	ENVironmental SATellite (ENVISAT)	03/2002	Limb emission	4.15–14.6 μm
ATMOS	NASA space shuttle	Four missions from 1985 to 1994	Solar occultation	2.1–16.6 μm
ACE-FTS	The Canadian Space Agency SCISAT-1 satellite	08/2004	Solar occultation	2.2–13.3 μm
EOS MLS	The EOS AURA satellite (NASA)	07/2004	Limb emission	118–2250 GHz

Table 2.1: Selected list of important limb sounding instruments, used in this thesis, those capable of measuring trace gases in the upper troposphere and lower stratosphere (UTLS) region.

It is important to know the pointing knowledge of the instrument as precisely as possible in order to retrieve the potential quantities using Earth's radiance. The total radiance signal contribution is affected both by the radiance measured at a particular tangent height *h* and by signal coming from above the tangent point. Thus the measured upper tropospheric radiances are also due to contributions from higher layers in the tangent path. In limb geometry, the signal below the line of sight (and associated field of view (FOV)) at the tangent height does not contribute to the measured spectra, thus ignoring emission from the lower atmosphere and from the

surface (no scattering effects). At the upper tropospheric levels, the radiance signals are affected by the presence of clouds as well as trace gases. A list of limb sounding instruments is listed in Table 2.1 used in this thesis.

2.3 Radiative transfer theory

The fundamental concept used to interpret the remotely measured atmospheric radiances and how the atmospheric matter interacts with the Earth's radiation is based on radiative transfer theory. The radiation leaving the Earth's atmosphere is attenuated by the atmospheric constituents throughout the atmosphere. For limb sounding, the radiation sensed by the satellite instrument is a total of radiation entering the FOV of the instrument. The radiation is modified by absorption processes and scattering out of the beam of the radiation. The monochromatic intensity or radiance, in a given direction, is a measure of intensity of this radiance in units of energy per unit cross sectional area per time per wavelength and per steradian.

The radiation interacts in two ways; by absorption and scattering (resulting in a decrease in intensity of the radiation beam) and by emission and scattering (resulting in an increase in intensity of the radiation beam). The radiation beam of wavelength λ, passing through the absorbing medium along path *ds*, the net decrease in the intensity is given as

$$dI_\nu = -e_\nu n_a I_\nu ds \tag{2.1}$$

where I_ν is the radiance, e_ν is the molecular extinction coefficient constant, n_a is the number density of absorbing atoms or molecules. The negative sign denotes loss of radiation.

In emission, the same beam of radiation has an increase in intensity travelling through path *ds* given by

$$dI_\nu = j_\nu n_a ds \tag{2.2}$$

where j_ν is the emission coefficient constant, which characterises the emission properties of the molecules in the path.

When the atmospheric layers are considered to be in local thermodynamic equilibrium (LTE) [Goody and Yung, 1989], Kirchhoff's law states the emission and absorption coefficients are related by a universal function depending on temperature T and given by

$$\frac{j_\nu}{e_\nu} = f_\nu(T) = J_\nu \tag{2.3}$$

where J_ν is the defined source function.

Thus combining equations (2.1) and (2.2)],

$$dI_\nu = e_\nu n_a J_\nu ds \tag{2.4}$$

The radiative transfer equation formally known as Schwarzchild's equation is given by

$$\frac{dI_\nu(P,\boldsymbol{s})}{ds} = -e_\nu j_\nu [I_\nu(P,\boldsymbol{s}) - J_\nu(P,\boldsymbol{s})]ds \tag{2.5}$$

where $I_\nu(P,\boldsymbol{s})$ defines the radiance at point P in an arbitrary direction $\boldsymbol{s}$. This is Schwarzchild's radiative transfer equation, originally derived in the early 20th century.

The effects of simple scattering are ignored (usually negligible in infrared atmospheric limb sounding) thus implying the extinction coefficients are the same as the absorption coefficients; $e_\nu = k_\nu$.

The monochromatic optical thickness (optical depth) of the layer of the medium, with points s' and s along the direction $\boldsymbol{s}$, is given by

$$\tau_\nu = \int_{s'}^{s} k_\nu(s'')n_a(s'')ds'' \tag{2.6}$$

The intensity of radiation at point P' at a distance s' can be written as:

$$\frac{dI_\nu(s',\boldsymbol{s})}{d\tau_\nu} = [I_\nu(s',\boldsymbol{s}) - J_\nu(s',\boldsymbol{s})] \tag{2.7}$$

Multiplying by necessary integral factor results in:

$$\frac{d[I_\nu(s', \boldsymbol{s}) exp(-\tau_\nu)]}{d\tau_\nu} = \exp(-\tau_\nu)\, J_\nu(s', \boldsymbol{s}) \tag{2.8}$$

Integrating this equation from s ($where\ \tau_\nu = 0$) to the origin s_0 gives

$$I_\nu(s, \boldsymbol{s}) = I_\nu(s_0, \boldsymbol{s}) \exp[-\tau_\nu(s_0, s)] + \int_0^{\tau(s_0,s)} J_\nu(s', \boldsymbol{s}) \exp[-\tau_\nu(s', \boldsymbol{s})] d\tau_\nu \tag{2.9}$$

Under local thermodynamic conditions the source function at a point *P'* and direction **s**, is given by the Planck function, $B_\nu(T)$,

$$B_\nu(T) = \frac{2h\nu^3}{c^2} \frac{1}{\exp(h\,\nu/kT) - 1} \tag{2.10}$$

where *h* is the Planck constant and *k* is the Boltzmann constant.

At a given temperature, the source function depends only on temperature, T, if the gas is in thermodynamic equilibrium.

For thermal limb measurements, $I_\nu(s_0, \boldsymbol{s})$ is the emission of cold space (negligible in infrared). Thus equation (2.9)] can be rewritten as

$$I_\nu(s, \boldsymbol{s}) = \int_0^{\tau_\nu(s_0,s)} B_\nu(s', \boldsymbol{s})\, exp[-\tau_\nu(s', s)] d\tau_\nu \tag{2.11}$$

2.4 Infrared molecular spectroscopy

Molecular energy is exchanged in transitions between quantum states and this is accompanied by the absorption or emission of photons (quanta of electromagnetic radiation energy). Radiance emissions in the mid-infrared region related to photon energies transitions between energy levels corresponds to simultaneous molecular vibrational and rotational transitions. In the atmosphere, the result is infrared bands centred on a vibrational transition frequency, displaying rotational lines or a rotational fine structure. In addition, various physical mechanisms can cause overlap or broadening of the spectral lines, by collisions or Doppler effects.

2.4.1 Molecular vibrations

The number of degrees of freedom of the molecule determines the number of fundamental vibrations of a molecule. A molecule comprising of N atoms will have 3N degrees of freedom of which three are needed to describe the translational motions of the molecule. For non-linear molecules a further three are required to describe their rotational motion and this is reduced to two for linear molecules. Ultimately for non-linear molecules there are 3N-6 and 3N-5 for linear molecules vibrational degrees of freedom.

In the infrared, vibrational transitions occur and if the motion can be assumed to be simple harmonic, then the energy levels of each vibrational state are:

$$E_v = hc\left(v_i + \frac{1}{2}\right)\tilde{\nu}_i \qquad (2.12)$$

where $\tilde{\nu}_i$ is the wavenumber (defined as the reciprocal of wavelength) of the normal vibrational mode and v_i is the vibrational quantum number (greater than or equal to zero). The usual vibrational transition selection rule at lower temperatures is given by $\Delta v = \pm 1$ (where +1 represents absorption and −1 emission). In the ground state only absorption by the molecule (a positive transition) is permitted. The strongest band is between the transition from the ground state ($v = 0$) and $v = 1$ due to the fact that relative populations of the levels decrease towards higher energy states according to the Boltzmann distribution:

$$\frac{N_v}{N_0} = exp\left(-\frac{E_v}{kT}\right) \qquad (2.13)$$

where N_v describes the population of higher vibrational states relative to the ground state population, N_0 at a temperature T. Spacing between vibrational levels is large and the majority of molecules occupy the ground state at standard atmospheric temperatures. With a temperature increase, the population of higher energy states increases, allowing transitions between higher vibrational states ($v > 0$); these are known as 'hot' bands. Additionally, each vibrational state may have other harmonics or overtones associated with it and so $\Delta v = \pm 2, 3, 4$, *etc*. leading to overtone bands ($2\nu_1$, $2\nu_2$), combination bands (e.g. $v_1 + v_3$) and difference bands (e.g. $v_3 - v_1$), which can be seen in the mid-infrared.

2.4.2 Rotation of molecules

All molecules can be segregated into types depending on their moments of inertia about three perpendicular axes through their centre of gravity. These are conventionally labelled I_A, I_B and I_C where $I_A \leq I_B \leq I_C$. Molecules are divided into one of four groups depending on their symmetry:

- Linear molecules have one moment of inertia equal to zero, whilst the other two are equal ($I_A = 0$ and $I_B = I_C$). One example is carbon dioxide (CO_2).
- Symmetric top molecules usually have two equal moments of inertia and a third moment that is not equal to zero. ($I_A = I_B$ and $I_C \neq 0$). Further subdivision of this group leads to the prolate symmetric top ($I_A < I_B = I_C$) and the oblate symmetric top ($I_A = I_B < I_C$). An example of a symmetric top molecule (or rotor molecules as they are sometimes called is ammonia (NH_3)).
- Spherical tops have all three moments of inertia equal ($I_A = I_B = I_C$). An example is sulphur hexafluoride (SF_6) or methane (CH_4).
- Asymmetric tops have none of the three moments of inertia equal ($I_A \neq I_B \neq I_C$). Many halocarbons are of this type and the majority of molecules belong to this fourth class.

2.4.3 Vibration-rotation bands

Vibrational energy levels in a rotating molecule are split into rotational energy levels a fact described by the Born-Oppenheimer approximation. This assumes energy associated with the vibrational and the rotational (and also the electronic and the nuclear) states are independent and the total energy of a molecule is the sum of energies of the vibrational and the rotational motion. Interactions between the two motions are not insignificant, meaning that this is only an approximation. Rotational transitions require much smaller amounts of energy than the vibrational ones and so occur simultaneously with the vibrational transitions.

Selection rules for the vibration-rotation bands are molecule dependent, and are defined by whether vibration causes a parallel or perpendicular change in the

electric dipole moment to the axis of symmetry. For the linear molecules, the dipole moment change occurs parallel to the major axis of symmetry (parallel bands) with the selection rules of ΔJ = ±1. If the change occurs perpendicular to the axis of symmetry (perpendicular bands), which happens for many halocarbons, ΔJ = 0 is allowed in addition to ΔJ = ±1. Since all the three types of rotational transitions are allowed for asymmetric top molecules (of which many halocarbons are included), the most common form of a vibration-rotation band is the 'PQR' band. In this situation, the P-branch corresponds to ΔJ = −1, the Q-branch to ΔJ = 0 and the R-branch to ΔJ = +1. The Q-branch is usually the most intense feature of the band in the mid-infrared and corresponds to the purely vibrational transition energy. The P-branch is observed at lower frequencies to the Q-branch and the R-branch is observed at higher frequencies compared to the Q-branch.

2.4.4 Line intensities

The intensity of each spectral line (S) is as important to know as the position of the line itself. S is calculated by:

$$S = \int k(\tilde{\nu}) d\,\tilde{\nu} \tag{2.14}$$

where $k(\tilde{\nu})$ is the absorption coefficient. For a vibration-rotation line for a state i to $k(\tilde{\nu})$ state j transition, the line intensity of a single molecule is given by:

$$S_{line} = \frac{8\pi^3 \nu_{ij}}{4\pi\varepsilon_0 3hcQ} \exp\left(\frac{-E_i}{kT}\right)\left(1 - \exp\left(\frac{-hc\tilde{\nu}_{ij}}{kT}\right)\right) S_{ij} \tag{2.15}$$

where Q is the partition function, T is the temperature in Kelvin, E_i is the energy of the lower state, and S_{ij} is the line strength, defined as the square of the transition moment relative to a fixed an axis fixed in space.

2.4.5 Line widths

Spectral lines can be broadened (that is the line width increased) by many physical mechanisms including natural, Doppler and collisional broadening. Natural broadening is the smallest of the three mechanisms and is a direct result of the

Heisenberg Uncertainty Principle. In the atmosphere both Doppler [defined by equation (2.16)] and collisional broadening [defined by equation (2.17] are important where the lineshape may involve a combination of the two effects. Doppler broadening is caused by the particles moving towards or away from the point of measurement inducing a frequency shift of the spectral line emitted by the particle. The net result is broadening of the line as observed in the atmosphere. This is most important in the atmosphere at altitudes above 80 km. Collision broadening is the most important line-broadening mechanism below 30 km in the atmosphere.

$$f_D(\nu - \nu_0) = (\pi\alpha_D)^{-\frac{1}{2}} exp\left(\frac{-(\nu - \nu_o)^2}{{\alpha_D}^2}\right) \tag{2.16}$$

$$f_L(\nu - \nu_0) = \frac{\alpha_L \pi}{(\nu - \nu_0)^2 + \alpha_L^2} \tag{2.17}$$

2.4.6 Voigt lineshape

In the mid infrared, spectral line widths due to Doppler and pressure broadening become equal at around 30 km. The Voigt lineshape [Armstrong, 1967] adequately describes the combined behaviour of both mechanisms in atmospheric applications. This provides a convolution of the Doppler and pressure-broadened (Lorentz) lineshapes:

$$k(\tilde{\nu}) = \frac{S}{\alpha_D\sqrt{\pi}} \frac{y}{\pi} \int_{-\infty}^{\infty} \frac{e^{-t^2}}{y^2 + (x - t)^2} dt \tag{2.18}$$

where $k(\tilde{\nu})$ is the absorption coefficient at some wavenumber $\tilde{\nu}$. S is the line intensity at some reference line centre, and t is the ν_0 duration of emission. Also, x and y are defined as:

$$\begin{aligned} x &= \frac{\alpha_L}{\alpha_D} \\ y &= \frac{\tilde{\nu} - \tilde{\nu_0}}{\alpha_D} \end{aligned} \tag{2.19}$$

where α_L and α_D are the Lorentz and Doppler half-widths respectively.

2.4.7 Spectroscopy of the HCN molecule

The HCN ($H-C\equiv N$) molecule is a linear triatomic molecule which has four normal modes of vibration [Keedy, 1988]. The spectrum of HCN is very simple where the bending mode of HCN is of particular interest because of the large amplitude of motion for the light hydrogen.

The modes of vibration are ν_3 (C-N stretch) at 2089 cm^{-1}, ν_2 (a doubly degenerate bending) at 712 cm^{-1}, ν_1 (C-H stretch) at 3312 cm^{-1}. The ν_1 mode is not IR active but Raman active due to the little change in the molecular dipole moment during the C-N stretch. The other features of the spectrum include the absorption bands at 1412 and 2117 cm^{-1}, which are $2\nu_2$ and $3\,\nu_2$ overtones of the ν_2 fundamental.

A number of high-resolution studies have been reported for the fundamental, overtone and combination bands of HCN and its isotopomers. Measurements were performed on the infrared emission spectrum (spectral resolution-0.006 cm^{-1}) of three isotopologues of hydrogen cyanide (ν_2 region of $H^{12}C^{14}N$, $H^{12}C^{15}N$ and $H^{13}C^{14}N$) at high temperatures of the order of 1370 K [Maki *et al.*, 1996; 2000] to measure the bending vibrational levels. The room temperature measurements of $H^{13}C^{14}N$ are also reported in the 1200–1500 cm^{-1} and 2500–3700 cm^{-1}. Absolute intensity measurements of the ν_2 bending mode of HCN are reported. The intensities of the $2\nu_2$ overtone band of HCN are reported by Smith *et al.* [1981].

The previous measurements are based on lower spectral resolution and high pressure samples to reduce errors arising from spectrum saturation effects. Also only a few measurements are devoted to absolute line intensity measurements and very few measurements have reported of the self-broadening and self-shift coeffcients of any HCN band [Foley *et al.*, 1946; Pine *et al.*, 1993; Lemaire *et al.*, 1996]. The three vibrational bands ν_2, ν_1, $2\nu_2$ of $H^{12}C^{14}N$ isotopomer were measured by Rinsland *et al.* [2003]; Devi *et al.* [2004; 2005] at high spectral resolution in the infrared spectral regions (spectral resolution of the Fourier transform spectrometer/s) 3150–3450 cm^{-1} (0.005 and 0.008 cm^{-1}), 1200–1600 cm^{-1} (0.005 cm^{-1}) and 610–810 cm^{-1} (0.005 cm^{-1}).

The line parameters are calculated for the lines belonging to the P and R branches of the ν_2 band where due to the presence of several unresolved Q-branches [ν_2 band of $H^{12}C^{14}N$, $H^{13}C^{14}N$ and also the Q-branch of the $2\nu_2$-ν_2 hot band of $H^{12}C^{14}N$] limited the analysis of the ν_2 band. Details of spectral parameters in this band can be found in Section 4.2.4.5. The HCN line parameters in this band that are available from two primary spectroscopic databases GEISA and HITRAN are compared.

Absolute intensity measurements and the first extensive high-resolution experimental measurements of self-broadening and self-induced shift coeffcients of HCN ν_1 fundamental band ($H^{12}C^{14}N$) along with weak hot band $\left[\nu_1 + \nu\frac{1}{2} - \nu\frac{1}{2}\right]$ transitions ($H^{13}C^{14}N$) are reported [Rinsland *et al.*, 2003].

The absolute accuracy of the positions of the ν_1 lines of $H^{12}C^{14}N$ is better than ± 0.0001 cm^{-1}.

The mean and the standard deviation in the line position differences of ν_1 (64) lines of $H^{12}C^{14}N$ between the Devi *et al.* [2003] and Maki *et al.* [2000] is +0.00002 ± 0.00007 cm^{-1}. Uncertainty of measured self-broadening coeffcients for the ν_1 lines is estimated to be ~2%.

The precision in the self-shift coeffcients in the ν_1 band is about ±0.0002 cm^{-1} atm^{-1} (except for the weak lines at large J) and the absolute uncertainty to be ±0.002 cm^{-1} atm^{-1}.

Temperature dependence of the self-broadening and the self-induced shift coeffcients for ν_1 and the hot bands could not be determined from the measured spectra.

The integrated band intensity (S_{band}) determined for ν_1 band is 225.73 ± 0.19 cm^{-2} atm^{-1} measured at 296 K. The ratios of absolute intensities measured to values determined by Maki *et al.* [1995(a); 1995(b)] was found to be 0.97 ± 0.10 and 0.99 ± 0.18 for hot band and ν_1 band respectively.

The air-broadened half-width parameters have been recalculated using a polynomial expression derived by fitting together parameters from ν_1 [Rinsland *et al.*, 2003], ν_2 [Devi *et al.*, 2005] and pure rotational [Yang *et al.*, 2008] bands to

provide better prediction of γ_{air} for the lines involving higher-lying rotational states (|m|≤40).

2.5 The Oxford Reference Forward Model (RFM)

A radiative transfer model can be used to calculate the MIPAS-E atmospheric limb radiances for different atmospheric scenarios that can incorporate both instrument parameters of the observing system and relevant physics of the Earth's atmosphere. The Oxford Reference Forward Model (RFM) is a GENLN2 [Edwards, 1996] based line-by-line radiative transfer model developed by University of Oxford [http://www.atm.ox.ac.uk/RFM/] under an European Space Agency (ESA) contract to provide reference spectral calculations for the MIPAS-E instrument. The basic purpose of RFM is to solve the radiative transfer equation for a given observation geometry and the atmospheric model. The RFM model requires a driver table which contains a user defined atmosphere to calculate limb emission/transmission spectra that are subsequently used in the retrieval process of atmospheric constituents. The RFM model works in the infrared region.

2.5.1 The reference forward model features

The section describes the basic method used by the RFM model to compute the solution of the radiative transfer equation within the context of the MIPAS-E measurement scenarios. The inhomogeneous atmosphere along the radiation path is treated by sub-dividing the atmosphere into series of layers [Figure 2.2]. The integration over z becomes summation over the constituent layers. In the spherical geometry relevant for the MIPAS-E measurement, the layers may be thought of as concentric shells. The RFM calculates the optical depths for each of the single gas paths within each layer and then combines them monochromatically in spectral space to obtain the multi-gas optical depths of each layer, such that the gas within the layer is considered to be homogeneous.

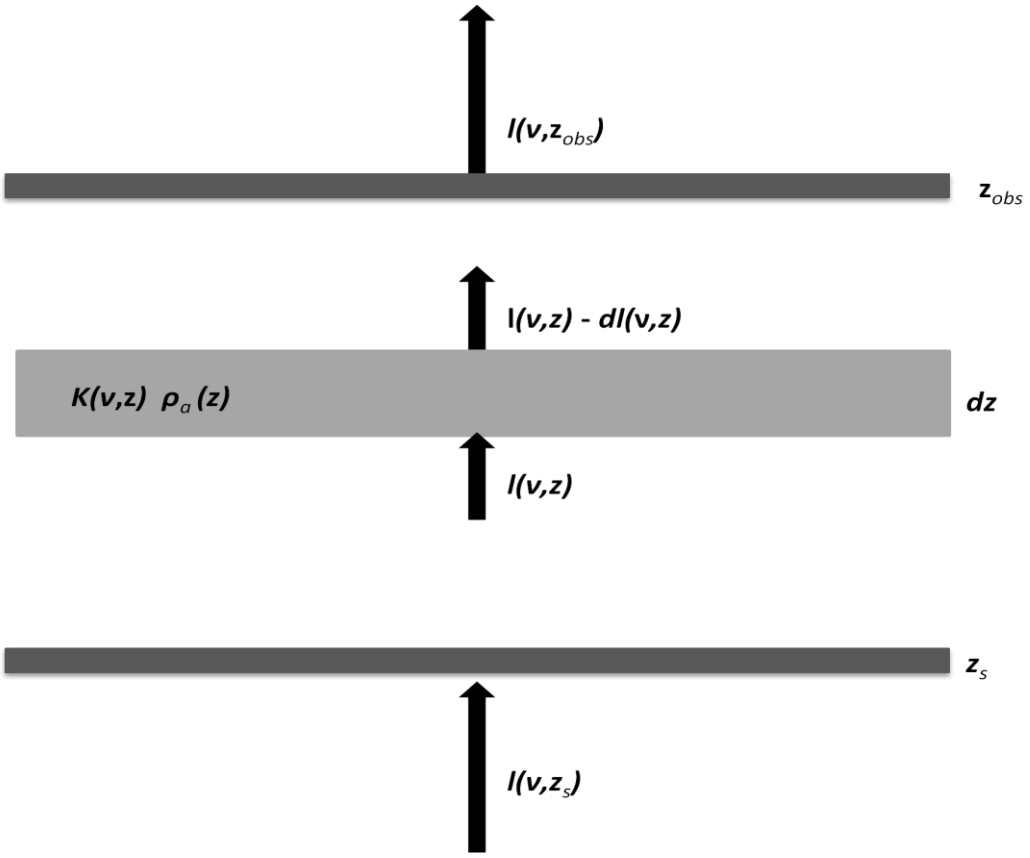

Figure 2.2: Transmission of radiation through a slab of absorbing material. [Edwards, 1996].

The parameters required to define paths (l) for each of the required gases are the lower boundary altitudes and local zenith angle θ at the lower boundary altitude determined by Snell's law

$$C = n(r)r \sin\theta \,, \tag{2.20}$$

where C is a constant along the ray path and n(r) is the refractive index of air at the Earth's radius of curvature r ('Refractivity' N = (n−1) × 10^6). Once the ray paths are defined, the Curtis-Godson absorber weighted mean temperature T_{CG} and pressure P_{CG} values are calculated for each path and are assumed to be constant within a given layer.

The line-by-line calculation involves calculating transmittances over spectral ranges of interest. Spectral calculations in wavenumber space for each gas in several atmospheric layers are performed using a two-pass system that first calculates lines on fine 0.0005 cm^{-1} grid followed by a triangular interpolation onto the same grid calculated on a coarse 0.5 cm^{-1} grid. This ensures that the narrowest lines are

adequately sampled; although a user defined irregular grid can also be defined. All spectral calculations are performed at a user defined resolution and a wavenumber range. The RFM has options for using the Lorentz, Doppler and Voigt line shapes (modified in the case of CO_2). The continuum absorption of certain molecules, in particular water vapour (which has large seasonal and zonal variations in the upper troposphere) must be considered as the H_2O continuum is responsible for most of the absorption in the infrared atmospheric windows and leads to a wide range of calculated attenuations.

2.5.2 Atmospheric profiles

The RFM model requires atmospheric profiles of the height (km), pressure (mb), temperature (K) and the gas concentrations (ppmv) that are used for calculating the total radiance contributions in a particular spectral region. The reference atmosphere is (RAMSTAN) version 3.1 [Remedios *et al.*, 2007(b)], a climatological database which contains zonal and seasonally averaged model profiles for four different latitude bands, including the tropical, the polar summer, the polar winter and the mid-latitudes (day and night to represent the diurnal behaviour of species in the stratosphere). In addition, a current version 4.0 comprises a four season, six latitude climatology database (the 'IG2 climatology' or 'Initial Guess 2 climatology') [Remedios *et al.*, 2007(a)]. The atmospheric profiles can be updated subsequently by using retrieved species information from other instrument measurements.

2.5.3 The Spectroscopic database

The importance of the laboratory and the atmospheric measurements has increased and are periodically updated to make available to the line-by-line radiative transfer codes. The RFM model accepts the much widely used spectroscopic database known as HIgh-resolution TRANsmission (HITRAN) in following three options:

- HITRAN line data [Rothman *et al.*, 2005]
- HITRAN cross section data for heavy molecules.

- Look up tables compressed by the Single Value decomposition (SVD).

The HITRAN data base is first processed by the GENLN2 routine [Edwards, 1996] HITLIN to prepare an input line list compatible with the RFM. This routine extracts the required line information either by the gas species or the spectral interval and stores the lines of interest in a binary file format.

2.5.4 Instrumental effects

The MIPAS-E instrument is an interferometer with finite spectral resolution and finite FOV at the limb; these effects have to be accounted for in the forward model calculations. The calculated radiance spectrum at the instrument resolution is convolved with an instrument line shape (ILS) function in spectral dimension which is provided externally and the FOV in the vertical dimension. The ILS function for an interferometer has to be in the form of a *sinc* function and for MIPAS-E the ILS function is wavenumber dependant. The function can later be apodised, using for example the Norton-Beer apodisation function [Norton and Beer, 1976]. The instrument's FOV is accepted in terms of altitude or elevation angle terms. It is assumed that the FOV is not wavenumber dependant hence only one FOV file is supplied for all wavenumber range. In RFM, the FOV has a form of a trapezium with a width equal to the FOV and is centred on the calculations for the nominal tangent height.

Under the AMIL2DA project [von Clarmann *et al.*, 2003]; the RFM model output was compared to other radiative transfer models such as Rutherford Appleton Laboratory's 2-Dimensional Forward Model (FM2D) and the Optimised Forward Model (OFM), also used to model MIPAS-E radiances. Line mixing, ILS and continuum effects in specified spectral regions at tangent altitudes 10, 15, 40 and 100 km were examined. Relatively small spectral differences were observed between RFM model outputs compared to other model output results, typically in order of 0.1 nW/(cm^2 sr cm^{-1}). The RFM does not account for multiple scattering in the radiative transfer calculations where it computes the Plank function only.

2.5.5 RFM Output files

The output files can be radiance, transmission, absorption or optical depth spectra. For MIPAS-E measurements, the level 1b data are in radiance form and for ACE-FTS measurements the level 1 data is in transmission form. The line-by-line calculations are convolved with ILS and FOV with respect to the instrument data in order to compare radiative transfer modelled data to the atmospheric measurements.

The RFM model calculates the jacobians that represent the difference in radiance caused by perturbating the atmospheric profiles and these are 1% for volume mixing ratios, 1 K for temperature and 1×10^{-4} ext/km for aerosol extinction. For a set of tangent altitudes, the perturbations for each jacobian are effectively triangular centred on each altitude and decreasing linearly to 0 (in K or %) at adjacent altitudes.

2.6 Retrieval theory

The radiance at the top of the atmosphere sensed by the satellite instrument at wavenumber ν in clear sky conditions is defined by the equation (2.11. In order to obtain pressure, temperature and gas VMR, the radiative transfer equation has to be solved which is an *inverse* problem. The problem of retrieving an atmospheric profile from an indirect measurement using remote sounding is often ill-posed and ill-conditioned and thus for example the retrieval of temperature profile may result in more than one solution which may not be consistent with what is observed in the 'real' atmosphere.

The retrieval problem requires a method to find an appropriate, constrained solution from the measurements [Section 2.6.2]. Most of the real inverse problems are non-linear and do not have a unique solution unless *a-priori* knowledge is used to identify a probable solution; *a-priori* data and covariances are intended to encapsulate prior knowledge of the atmosphere. The section follows the retrieval theory from Rodgers [2000] and Carlotti *et al.* [2001] for the retrieval method used to retrieve atmospheric constituents from the Earth's atmosphere.

2.6.1 Definitions

Consider the MIPAS-E instrument makes m, total radiance measurements at different limb altitudes. The main aim of the retrieval is to obtain as much information of $\boldsymbol{x}$ given $\boldsymbol{y}$ as possible. The relation between the measurements and the parameters to be retrieved is defined as:

$$\boldsymbol{y} = \boldsymbol{f}(\boldsymbol{x}, \boldsymbol{b}) + \boldsymbol{\varepsilon} \tag{2.21}$$

where each term is defined as follows:

- The state vector $\boldsymbol{x}$ is (set of n parameters to be retrieved) that describes the state of the atmosphere.
- The measurement vector $\boldsymbol{y}$ used to determine the state vector $\boldsymbol{x}$.
- The forward function $\boldsymbol{f}(\boldsymbol{x}, \boldsymbol{b})$ that describes the relation between the measurement and state vectors.
- The forward function parameters $\boldsymbol{b}$, describes any other factor that can affect the measurement, but which are not retrieved (which may not be known exactly).
- The random error associated with the measurements or with the instruments noise is denoted by vector $\boldsymbol{\varepsilon}$.

In practise, the forward function is represented by the Forward model $\boldsymbol{F}(\boldsymbol{x})$ that approximates the atmospheric physics and incorporates the knowledge of how the instrument works, coupled with how the measured quantity (radiances from MIPAS-E) is related to the desired quantity. Thus the equation (2.18 can be rewritten as

$$\boldsymbol{y} = \boldsymbol{F}(\boldsymbol{x}) + \boldsymbol{\varepsilon} \tag{2.22}$$

2.6.1.1 The weighting function matrix

By simplifying the general retrieval problem i.e. linearization of forward model with respect to some reference state $\boldsymbol{x_0}$, one can write

$$\boldsymbol{y} - \boldsymbol{F}(\boldsymbol{x_0}) = \frac{\partial \boldsymbol{F}(\boldsymbol{x})}{\partial \boldsymbol{x}}(\boldsymbol{x} - \boldsymbol{x_0}) + \boldsymbol{\varepsilon} \quad (2.23)$$

The equation (2.21 describes the $m \times n$ weighting function matrix $\boldsymbol{K}$ where $\partial \boldsymbol{F}(\boldsymbol{x})/\partial \boldsymbol{x}$ is the partial derivative of an m forward model element with respect to the n state vector element (usually represented by $\boldsymbol{K}$) that denotes the sensitivity of the forward model (change in radiances). Thus, equation (2.20 is rewritten as

$$\boldsymbol{y} - \boldsymbol{F}(\boldsymbol{x_0}) = \boldsymbol{K}(\boldsymbol{x} - \boldsymbol{x_0}) + \boldsymbol{\varepsilon} \quad (2.24)$$

The weighting function $\boldsymbol{K}$ which gives information about the sensitivity of each element of $\boldsymbol{F}$ to each state element may also be called the Jacobian matrix or sensitivity kernel.

2.6.2 Solution using *a-priori* information

The retrieval problem is often non-linear and ill-posed which can lead to unstable solutions with large errors. If m = n than it makes the simultaneous equations solvable unless $\boldsymbol{K}$ turns out to be singular. If $m < n$ i.e. fewer measurements than unknowns and hence the equations are under-constrained (or ill-posed or under-determined). Conversely if $m > n$ i.e. more measurements than unknowns and hence the equations are over-constrained (or ill-conditioned or over-determined).

The aim is to find the 'best' (optimal) solution or estimate of the desired quantity from the measurement y. Often, a Bayesian approach is used that allows possible states to be constrained using the information about the measurement, the forward model and all associated errors. Using this information, and for mathematical simplicity assuming a normal Gaussian distribution of the states, a probability density function for all possible states can be defined. To have a well-posed solution the '*a-priori* information' can be used to constrain the retrieval problem. This often comes from previous measurements collated with the climatology of a former state expressed as prior pdf.

If $P(\boldsymbol{x})$ is the Probability density function (pdf) of the state, $\boldsymbol{x}$, and $P(\boldsymbol{y})$ is the pdf of measurement state vector $\boldsymbol{y}$, a conditional pdf of $\boldsymbol{x}$ given $\boldsymbol{y}$ is $P(\boldsymbol{x}|\boldsymbol{y})$. Bayes theorem states:

$$P(\boldsymbol{x}|\boldsymbol{y}) = \frac{P(\boldsymbol{y}|\boldsymbol{x})P(\boldsymbol{x})}{P(\boldsymbol{y})} \tag{2.25}$$

where $P(\boldsymbol{y}|\boldsymbol{x})$ can be calculated using forward model and known noise of the instrument. The most likely state (i.e. the mean state averaged over the pdf) from an ensemble of all possible states corresponds to

$$\hat{\boldsymbol{x}} = \int \boldsymbol{x}\, P(\boldsymbol{x}|\boldsymbol{y}) d\boldsymbol{x} \tag{2.26}$$

where $P(\boldsymbol{x}|\boldsymbol{y})$ is the pdf and $\hat{\boldsymbol{x}}$ is the 'solution'. The $pdfs$ are assumed to have a Gaussian distribution symmetric about its maximum, although this is not always true for real atmospheric climatologies. The mean state averaged over the pdf corresponds to the solution and the width, or variance of the *pdf*, is an estimate of the associated error.

The best solution can be found using a non-linear least square fitting technique where the fit to real observed measurements is found using a forward modelled state. One way is to use the maximum likelihood estimation (MLE) theory that looks for a solution by minimising some function χ^2 that is defined as the square summation of the differences between observations and simulations weighted by the measurement error. The method looks for a solution by minimising the cost function χ^2 given by

$$\chi^2 = (\boldsymbol{y} - \boldsymbol{K}\boldsymbol{x})^T \boldsymbol{S}_y^{-1} (\boldsymbol{y} - \boldsymbol{K}\boldsymbol{x}) + (\boldsymbol{x} - \boldsymbol{x_a})^T \boldsymbol{S}_a^{-1} (\boldsymbol{x} - \boldsymbol{x_a}) \tag{2.27}$$

where $\boldsymbol{S}_a$ is the *a-priori* error covariance and $\boldsymbol{S}_y$ is the measurement error covariance. The χ^2 value depends on the difference between measured, $\boldsymbol{y}$, and the modelled radiances $\boldsymbol{F}(\boldsymbol{x})$, and also the difference between the solution $\hat{\boldsymbol{x}}$ (found in next iteration step) and *a-priori* state $\boldsymbol{x_a}$.

Another approach is to find the profile $\hat{\boldsymbol{x}}$ for which $P(\boldsymbol{x}|\boldsymbol{y})$ has the largest possible value. In turn, this is the most probable value of $\boldsymbol{x}$. The technique that finds such a value is called maximum $a\ posterior$ (MAP) method. An *a-priori* profile is one that provides the best independent estimate of the quantity being measured and is used alongside the measurement itself to obtain a best estimate of the solution. Typically, the *a-priori* corresponds to a climatology profile and variance profile of the desired quantity or a previous measurement of the quantity.

2.6.2.1 The Gain matrix

The measurement gain matrix (also known as the contribution function matrix) or $\boldsymbol{G}$ is defined as

$$\boldsymbol{G} = \frac{\partial \hat{\boldsymbol{x}}}{\partial \boldsymbol{y}} \tag{2.28}$$

The gain matrix describes how the solution is affected by the change in the measurement, $\boldsymbol{y}$ and relates the unknowns to all of the measured quantities.

$$\boldsymbol{G} = \boldsymbol{S}_a \boldsymbol{K}_T \left(\boldsymbol{S}_y + \boldsymbol{K}\boldsymbol{S}_a\boldsymbol{K}_T\right)^{-1} \tag{2.29}$$

where $\boldsymbol{S}_a$ is the covariance matrix of prior estimate $\boldsymbol{x}_a$ about the exact state, and the $\boldsymbol{S}_y$ is the covariance matrix of measurement $\boldsymbol{y}$.

In terms of $\boldsymbol{G}$, the solution $\hat{\boldsymbol{x}}$ is given as

$$\hat{\boldsymbol{x}} = \boldsymbol{G}\boldsymbol{y} \tag{2.30}$$

2.6.2.2 The Averaging kernel matrix

As an important part of diagnostics, one important output of the retrieval is the averaging kernel matrix which describes the sensitivity of the retrieval of the true space and is defined as

$$\boldsymbol{A} = \frac{\partial \hat{\boldsymbol{x}}}{\partial \boldsymbol{x}} = \boldsymbol{G}\boldsymbol{K} \tag{2.31}$$

The retrieved profile is combination of both *a-priori* climatology and the true atmospheric state. The solution can be expressed as

$$\hat{\boldsymbol{x}} = \boldsymbol{A}\boldsymbol{x} + (\boldsymbol{I} - \boldsymbol{A})\boldsymbol{x}_a \tag{2.32}$$

The rows of the matrix $\boldsymbol{A}$ are the 'smoothing functions' or averaging kernels with the width representing the vertical (spatial) resolution of the instrument. Where the area under the averaging kernel curve is one, the retrieval uses more measurement information and is less biased to the *a-priori* values. The columns in the matrix describe how a perturbation in one of the state vector elements, will affect all the retrieved parameters. Ideally, the averaging kernel matrix will be $\boldsymbol{A} = \boldsymbol{I}$.

2.6.2.3 Degrees of Freedom

The degrees of freedom for the signal d_s, is the trace of the averaging kernel matrix:

$$d_s = tr(\boldsymbol{A}) \tag{2.33}$$

Therefore the diagonal of the matrix *A* is a measure of the number of degrees of freedom per height level, in the case of the MIPAS-E, and its reciprocal is the number of levels per degree of freedom, a measure of height resolution.

2.6.3 Iteration approach

If the retrieval problem is not too non-linear, then the Gauss-Newton iteration is used to find the 'best' estimate of the state $\hat{\boldsymbol{x}}$ and is given by

$$\boldsymbol{x}_{iter} = \boldsymbol{x}_{iter-1} + \left(\boldsymbol{K}_{iter-1}^{T}\boldsymbol{S}_{y}^{-1}\boldsymbol{K}_{iter-1}\right)^{-1}\boldsymbol{K}_{iter-1}^{T}\boldsymbol{S}_{y}^{-1}\boldsymbol{R}_{iter-1} \tag{2.34}$$

where $\boldsymbol{x}_{iter}$ is the new estimate of $\boldsymbol{x}$ and $\boldsymbol{x}_{iter-1}$ is the result of the previous iteration. As an initial guess, to initiate the iteration process, for *iter* = 0, *a-priori* state $\boldsymbol{x_0}$ is used where $\boldsymbol{x}_{iter-1} = \boldsymbol{x_0}$. $\boldsymbol{K}_{iter-1}^{T} = \partial(\boldsymbol{p}, \boldsymbol{x}_{iter-1})/\partial\boldsymbol{x}_{iter-1}$ is the jacobian relative to the previous iteration and $\boldsymbol{R}_{iter-1} = \boldsymbol{y} - \boldsymbol{F}(\boldsymbol{p}, \boldsymbol{x}_{iter-1})$is the difference between the measurement and the simulation. After each iteration, the cost function χ^2, can be evaluated under certain convergence criterion. In this method, sometimes the true solution is far from the current iteration where further iterations either do not change the residual or in fact make the residual larger.

In such cases, the Levenberg-Marquardt iteration technique can be used which is not dissimilar to the Gauss-Newton iteration but with an added constant term, γ, which aids convergence [Marquardt, 1963]. The matrices $\boldsymbol{S}_a$ and $\boldsymbol{S}_y$ are inverted using the Gauss-Jordan Elimination technique with full-pivoting, based on the routine GAUSSJ [Pages 28–29, Numerical recipes, Press *et al.*, 1992]. The Gauss-Newton iteration now becomes

$$\boldsymbol{x}_{iter} = \boldsymbol{x}_{iter-1} + \left(\boldsymbol{K}_{iter-1}^{T}\boldsymbol{S}_{y}^{-1}\boldsymbol{K}_{iter-1} + \gamma\boldsymbol{I}\right)^{-1}\boldsymbol{K}_{iter-1}^{T}\boldsymbol{S}_{y}^{-1}\boldsymbol{R}_{iter-1} \tag{2.35}$$

where $\boldsymbol{I}$ is the unit matrix and the term γ is initialised by the user that either increases or decreases depending on whether chi-square (χ^2) increases or

decreases. If the γ value obtained from the iteration reduces the χ^2 parameter, the new estimate, $\boldsymbol{x}_{iter+1}$ is accepted and is divided by ten. If the error increases on $\boldsymbol{x}_{iter+1}$ however, then is multiplied by ten and equation (2.32] is solved again until an increment is obtained that reduces the χ^2 below a pre-defined threshold of t_1 and the difference between consecutive χ^2 values is less than t_2.

2.6.3.1 Retrieval convergence

The retrieval problem employing the Gauss-Newton or Levenberg-Marquardt iteration method is stopped once a suitable convergence criterion is satisfied. Usually, there are two methods used to set convergence criteria in the retrieval process are:

1. $\boldsymbol{F}(\boldsymbol{x}_{iter+1})$ is compared with $\boldsymbol{F}(\boldsymbol{x}_{iter})$.

   The difference $\boldsymbol{F}(\boldsymbol{x}_{iter+1}) - \boldsymbol{F}(\boldsymbol{x}_{iter})$ is usually a good indicator of the retrieval convergence error in $\boldsymbol{y}_{iter}$, so it is useful overestimate of the convergence error in $\boldsymbol{y}_{iter+1}$.

2. $\boldsymbol{x}_{iter+1}$ is compared with $\boldsymbol{x}_{iter}$.

   The difference $\boldsymbol{x}_{iter+1} - \boldsymbol{x}_{iter}$ is usually a good indicator of the retrieval convergence error in $\boldsymbol{x}_{iter}$, so it is useful overestimate of the convergence error in $\boldsymbol{x}_{iter+1}$.

To limit the computing time, it is also sensible to assume that convergence has not been reached if the number of iterations exceeds a predetermined number.

The estimation of $\hat{\boldsymbol{x}}$ in optimal estimation represents the minimisation of the cost function, χ^2, a value dependent on the difference between measured, $\boldsymbol{y}$, and modelled radiances, $\boldsymbol{F}(\boldsymbol{x}_{iter})$, and also the difference $\hat{\boldsymbol{x}}$ and $\boldsymbol{x}_{\boldsymbol{a}}$:

$$\chi^2 = (\mathbf{y} - \mathbf{K}\boldsymbol{x})^{\mathrm{T}}\mathbf{S}_{\mathrm{y}}^{-1}(\mathbf{y} - \mathbf{K}\boldsymbol{x}) + (\boldsymbol{x} - \boldsymbol{x}_{\mathbf{a}})^{\mathrm{T}}\mathbf{S}_{\mathrm{a}}^{-1}(\boldsymbol{x} - \boldsymbol{x}_{\mathbf{a}}) \quad (2.36)$$

The size of the cost function χ^2 can be used to determine how well the solution fits to the measurements. An example of such a test is:

$$\chi^2 = (\hat{\boldsymbol{x}}_{\boldsymbol{n}} - \hat{\boldsymbol{x}}_{\boldsymbol{n+1}})^T \boldsymbol{S}_y^{-1}(\hat{\boldsymbol{x}}_{\boldsymbol{n}} - \hat{\boldsymbol{x}}_{\boldsymbol{n+1}}) \ll n \quad (2.37)$$

where if χ^2 is too large, meaning that the retrieval does not fit the measurements. Numerous explanations exist for this scenario. The measurements themselves could be poorly calibrated or the measurement errors could be underestimated. The forward model itself may have incorrect physics incorporated within it and may not represent the system well or even that the *a-priori* may be inapt (i.e. it may be too tightly constrained). Conversely, if is χ^2 too small the measurement noise may be overestimated or the *a-priori* could be too loosely set.

2.6.4 Error analysis

The total retrieval error has two main error components: systematic and random error. The error in the solution $\hat{x}$ can be written as:

$$\hat{\boldsymbol{x}} - \boldsymbol{x} = \boldsymbol{G}_y\boldsymbol{\varepsilon} + \boldsymbol{G}_y\boldsymbol{K}_b\left(\boldsymbol{b} - \hat{\boldsymbol{b}}\right) + \boldsymbol{G}_y\Delta\boldsymbol{f}(\boldsymbol{x}, \boldsymbol{b}, \boldsymbol{b}') + (\boldsymbol{A} - \boldsymbol{I})(\boldsymbol{x} - \boldsymbol{x}_a) \qquad (2.38)$$

In this section, four major sources of error in the retrieval are considered. They are: Retrieval noise (first term)-a total random quantity, no correlation with time. Measurement noise, $\boldsymbol{\varepsilon}$, is usually random, generally unbiased, often uncorrelated between the channels. It has a known covariance matrix defined as:

$$\boldsymbol{S}_m = \boldsymbol{G}_y\boldsymbol{S}_\varepsilon\boldsymbol{G}_y^T \qquad (2.39)$$

Forward model parameter error (second term)-may be truly systematic (i.e. in the spectral data) or could vary from day to day (i.e. calibration parameters). But even the random component of the model parameter error may be constant over minutes or hours. The error in the retrieval due to the forward model parameters is given by the $\boldsymbol{G}_y\boldsymbol{K}_b\left(\boldsymbol{b} - \hat{\boldsymbol{b}}\right)$. Evaluation of $\boldsymbol{G}_y$ and $\boldsymbol{K}_b$ can be performed by perturbations in inverse method and forward model respectively. If the forward model parameters have been estimated properly and assuming that the model is linear, then the individual errors will be unbiased and the expected error will be zero.

Forward model error (third term)-estimates how well the model represents the physics of the atmospheric system. It is defined as

$$\boldsymbol{G}_y\Delta\boldsymbol{f} = \boldsymbol{G}_y[\boldsymbol{f}(\boldsymbol{x}, \boldsymbol{b}, \boldsymbol{b}') - \boldsymbol{F}(\boldsymbol{x}, \boldsymbol{b})] \qquad (2.40)$$

It can be difficult to evaluate the modelling error as it requires a model for $\boldsymbol{f}$ which includes all of the correct physics. If this is possible (which is rarely the case for atmospheric physics due to the complex nature of the processes in the atmosphere) and the physics can be modelled accurately, and $\boldsymbol{F}$ is simply a numerical approximation then evaluating model error is straightforward. The forward model error source is likely to be systematic.

Smoothing error (fourth term)-loss of fine structure in the retrieval due to the observing system. This error term arises when it is assumed that the retrieval is an estimate of the true state rather than an estimate of the state that has been smoothed by the averaging kernel. The true state will not be known in general (which is why the measurement is being made in the first place) thus the actual smoothing error cannot be estimated. Instead, the statistics of the error can be investigated from looking at the mean and covariance from an ensemble of states. To estimate the smoothing error covariance, the covariance matrix of a real ensemble of states must be known.

2.7 Summary

This Chapter focuses mainly on the principles of the infrared limb sounding technique. The theory behind the process of transmission of radiation leaving the top of the Earth's atmosphere and the interaction of atmospheric constituents with it is described in detail. The principles relating to the spectroscopy of HCN in the infrared spectrum to measure its spectral features in the emission spectrum is described.

An absorption/emission only radiative transfer forward model (only in clear sky conditions) capable of accurately modelling limb emission spectra, the reference forward model (RFM) is introduced which is part of the retrieval process in Chapter 5. The forward model is used in Chapter 4 and 5 to simulate emission spectra measured by the MIPAS-E instrument and the ACE-FTS transmission spectra.

The last section describes the method (optimal estimation) to invert the measurements from infrared limb sounding instrument into meaningful profiles. The method described forms the basis of the retrieval scheme used in Chapter 5;

MIPAS Orbital Retrieval using Sequential Estimation (MORSE) algorithm, an inverse model developed by University of Oxford. Details of the operational MIPAS processor is described in detail in following chapter along with the description of the MIPAS-E instrument. Further a brief description of retrieval error is also described in this Chapter.

CHAPTER 3

3. The MIPAS instrument onboard ENVISAT

3.1 The ENVISAT satellite

The ENVISAT (ENVIronment SATellite) is the largest spacecraft built by the European Space Agency. It was launched aboard Ariane-5 on March 1st, 2002, carrying ten optical and radar instruments that continuously monitor the Earth's atmosphere, land, ocean and ice caps. The ENVISAT mission's intention is to continue to improve measurements initiated by ERS (European Remote Sensing)-1, 2 satellites. Continuous and coherent data sets can help the scientific community to understand the Earth's environment and climatic changes.

The ENVISAT is in a sun-synchronous polar orbit at a mean altitude of 799.8 km with an orbital speed of 7.45 km/second. The time period per orbit is 100.59 minutes, resulting in 14.3 orbits per day. The repeat orbit cycle is 35 days to pass over specific Earth location, thus providing continuous monitoring and global coverage of the Earth system. The satellite's orbit is at an inclination of 98.55°, thus

it maintains a constant position with respect to the sun and crosses the Earth's equator at 10:00 am Mean Local Solar Time (MLST) in the descending node and 10:00 pm in the ascending node.

The ENVISAT's orbit is controlled to a maximum deviation of ± 1 km from the ground track and ± 5 minutes on the equator crossing MLST [http://envisat.esa.int/m-s/mission/operations.html]. To maintain synchronous timing, in-plane manoeuvres are used to compensate for effects due to air drag. Out-of-plane corrections are used to correct the steady drift of inclination mainly caused by solar and lunar gravity perturbations.

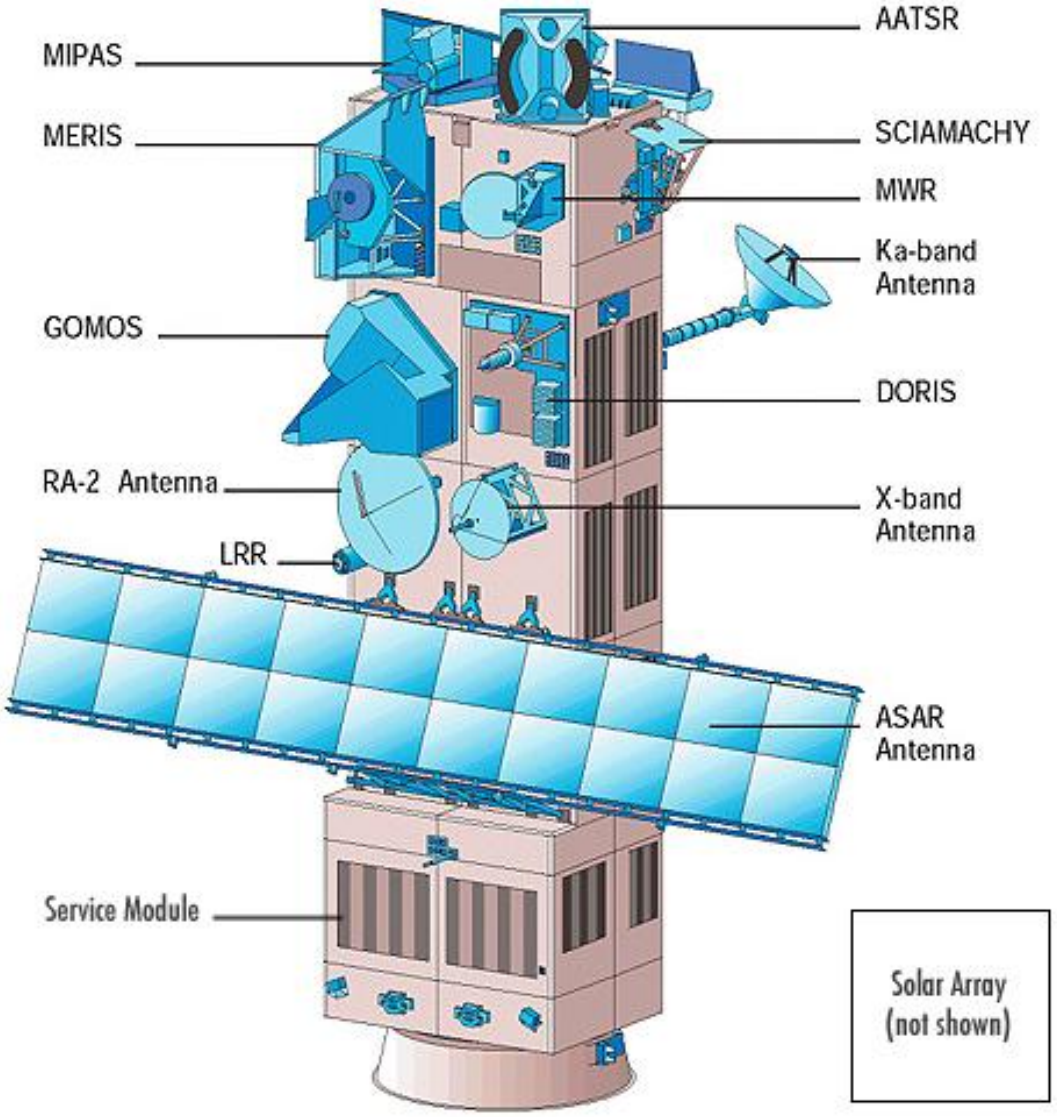

Figure 3.1: Instruments onboard ENVISAT satellite. [Image courtesy ESA, website-http://envisat.esa.int/instruments/tour-index/]

The Envisat's payload module consists of instruments [Figure 3.1; Table 3.1] that provide measurements of the Earth's atmosphere, ocean, land and ice. There are two radar instruments, three spectrometers, two radiometers and two instruments to track ENVISAT's position. These instruments cover a wide range of the electromagnetic spectrum, ranging from centimetre waves to the ultraviolet.

ENVISAT instruments		Application
AATSR	Advanced along track scanning radiometer	Precise sea and land surface temperature, vegetation indices, aerosol, cloud parameters.
ASAR	Advanced synthetic aperture radar	Study of ocean waves, sea ice extent and motion and land surface studies (deforestation, desertification).
DORIS	Doppler orbitography and radio positioning integrated by satellite	Precise satellite positioning
GOMOS	Global ozone monitoring by occultation of stars	Monitoring and understanding of ozone depletion in the stratosphere.
LRR	Laser retro-reflector	Precise orbit determination, calibrate the radar altimeter RA-2 range, verify stability of positioning system.
MERIS	Medium resolution imaging spectrometer	Ocean colour monitoring (chlorophyll, yellow substance, suspended matter) and vegetation status.
MIPAS	Michelson interferometer for Passive atmospheric sounding	Ozone chemistry, monitoring of global distribution of major greenhouse gases, atmospheric dynamics, clouds (including polar stratospheric clouds)
MWR	Microwaves radiometer	Total atmospheric water column measurements for correction of RA measurements
RA-2	Radar altimeter 2	Ocean topography, marine geoid characteristics, wind speed and wave height
SCIAMACHY	Scanning imaging absorption spectrometer for atmospheric cartography	Global distribution of trace gases, air pollution, aerosols, clouds and stratospheric ozone chemistry.

Table 3.1: The nine instruments and Laser Retro-Reflector (LRR) onboard the ENVISAT satellite including the MIPAS-E instrument.

3.2 The MIPAS-E instrument

The Michelson Interferometer for Passive Atmospheric Sounding (MIPAS) is a high resolution Fourier Transform Infrared (FT-IR) spectroradiometer designed to observe radiation emitted by the Earth's atmosphere in the limb-viewing mode. Spectral radiances in the mid-infrared region from 14.6μm to 4.15μm (685–2410 cm^{-1}) of the electromagnetic spectrum are measured with a unapodised spectral resolution of 0.025 cm^{-1}, using a passive remote sensing technique. The instrument is well described in Endemann *et al.* [2000], MIPAS product handbook [ESA 2007], Fischer *et al.* [2008].

Radiance measurements are made for all seasons, during both day and night and since the Earth's infrared radiation acts as a measurement source. This is one advantage limb emission measurements have over limb occultation instruments that only obtain trace gas profiles when there is a solar or lunar or stellar event (when viewing the sun/moon). The spectral resolution of MIPAS-E is sufficiently high to allow the simultaneous measurement of more than 25 important trace gases, including the complete NO_y family [Section 1.4] and several CFC's. It scans down to 6 km (3 km in optimized resolution mode) enabling the measurement of upper tropospheric trace gases where the absence of clouds permits.

The primary objectives of MIPAS-E focus on studying [Endemann *et al.*, 2000; Fisher *et al.*, 2008]:

1. Stratospheric chemistry and dynamics-understanding stratospheric ozone depletion, role of anthropogenic emission of Chlorofluro-carbons (CFCs) in the lower stratosphere [Moore 2005; Moore *et al.*, 2006], OH radical chemistry.
2. Atmospheric dynamics and stratosphere-troposphere exchange-accurate measurements of long lived trace gases to understand the processes that are involved between troposphere and stratosphere on the global scale.

3. Chemistry and physics of the UTLS-transport of natural and anthropogenic greenhouse gases between the regions, the impact of biomass burning and industry on ozone levels in upper troposphere and other trace gases. [Waterfall 2003; Allen G. *et al.*, 2005(a), 2005(b)]

4. Chemistry and physics of the upper atmosphere (mesosphere and lower thermosphere-MLT)-the temperature structure and energy balance, the chemistry, the dynamics and the interaction between the middle and the upper atmosphere.

5. Climatology study and weather forecasting-global distribution and occurrence frequency of polar stratospheric clouds (PSCs) and thin cirrus clouds as well as cloud top height, temperature and formation of the clouds can be studied. [Höpfner *et al.*, 2002, 2004, 2006; Spang *et al.*, 2003, 2005(a), 2005(b)]

6. Chemical weather forecast and forecast of ozone fields-global measurements of trace constituents for the operation of numerical models.

Scientific investigations using MIPAS-E will lead to the improved understanding of the upper tropospheric chemistry, the stratospheric chemistry and the atmospheric dynamics. The atmospheric distribution of the aerosol particles, the tropospheric cirrus clouds and stratospheric ice clouds (including Polar Stratospheric Clouds) can also be derived from MIPAS-E observations.

3.2.1 Scanning geometry

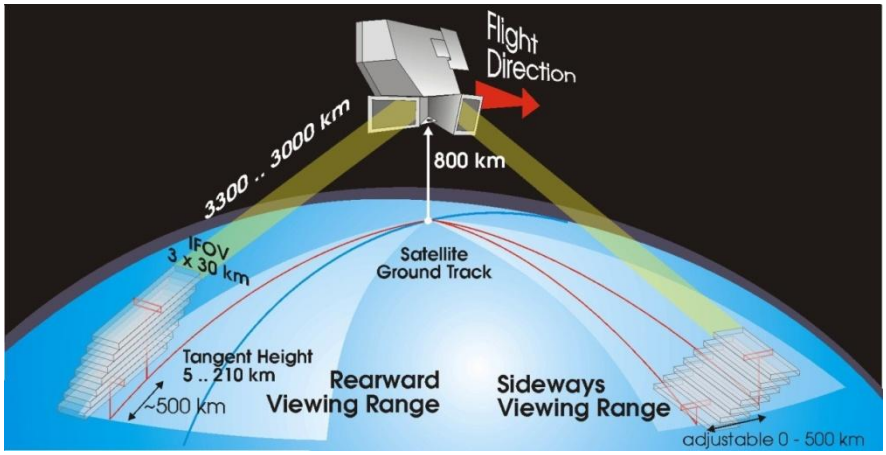

Figure 3.2 : Scanning Geometry (rear looking and sideways looking).

As a limb sounder the MIPAS-E instrument observes at a specific tangent point to resolve the spectral emissions of many trace gases in the atmosphere. Each altitude measurement is selected by an elevation mirror and the viewing mode is selected by an azimuth mirror. Operational measurements in 'nominal mode' are made in the rear-ward viewing direction (within 35° wide range around anti-flight direction) through an IFOV of 3 km × 30 km wide [Figure 3.2]. In special mode, MIPAS-E measures in sideways viewing range (within 30° range on the anti-Sun side of satellite).

A single limb sequence is performed by changing the orientation of the elevation mirror (instrument's line of sight (LOS)) with discrete steps in tangent altitude. A nominal mode limb scanning sequence consists of 17 spectra, measured at tangent altitudes from 6–68 km with spacing of 3 km at low altitudes and larger spacing of 8 km above. The MIPAS-E will acquire about 72 limb scans of full resolution spectra per orbit with typical sweep measurement time of 4.45 seconds. Each day about 14 orbits are obtained for a total of 1000 limb sequences or profiles per day.

The vertical and horizontal spacing [Table 3.2] of the limb measurements depends on the mode of observation, direction of view and angle of elevation. Horizontal spacing of the single measurement is 100–800 km (upper troposphere to lower mesosphere) with a vertical spacing of 1.5–10 km. The ground track is limited to the latitude region between about 80° S and 80° N (due to inclination of the orbit) and thus azimuth angle is occasionally changed during the orbit in order to perform observations from pole to pole, thus providing global measurements. MIPAS-E is also capable of pointing perpendicularly to the flight track in the range 80° to 110°; this allows diurnal changes to be detected and special events to be observed.

3.2.2 Observation modes

Typically during full resolution mode (0.025 cm^{-1}, unapodised), the MIPAS-E instrument spends 80% of the operation time in nominal mode and the remaining 20% of the operation time is accredited to the special modes that are focused on

special research study that includes polar winter chemistry, study of the upper atmosphere, or troposphere-stratosphere exchange [Table 3.2].

The nominal mode has been the standard mode for stratospheric chemistry and dynamics though it has been extended down into the upper troposphere and up into the lower mesosphere to allow the study of stratosphere-troposphere and stratosphere-mesosphere exchange.

To cover the various scientific objectives, several modes of observation were planned for MIPAS-E:

Observation Mode	**Scientific Objective**	**Pointing direction**	**Coverage**	**Altitude range (km)**	**Vertical Spacing (km)**	**Horizontal spacing (km)**
Nominal	Stratospheric chemistry and dynamics	rear	Global	6–68	3–8	530
Polar Winter Chemistry	Polar chemistry and dynamics	rear	Regional or occasional	8–55	2–10	450
Tropospheric-Stratospheric Exchange	Exchange between stratosphere and troposphere, troposphere chemistry	rear	Regional or occasional	5–40	1.5–10	400
Upper Atmosphere	Upper atmosphere	rear	Regional or occasional	20–160	3–8	800
Dynamics	Small-scale structures in the middle atmosphere	rear	Regional or occasional	8–50	3–8	500
Diurnal Changes	Diurnal changes near the terminator	side	Regional or occasional	15–60	3	100
Impact of Aircraft	Study of major air traffic corridor	side	Regional or occasional	6–40	1.5–10	500

Table 3.2: The eleven observation modes of MIPAS-E instrument in reduced resolution mode.

The MIPAS-E instrument was switched off in March 2004 due to increasing data anomalies caused by problems with the motion of retro reflectors in the

interferometer. As a result, it was proposed to reduce the spectral resolution to about 40% of prior value (corresponding to 0.0625 cm^{-1}) and the duty cycle of MIPAS-E was restricted in 2005 by 35%. Due to reduced resolution, a single interferometer sweep takes 1.64 seconds which allowed more full elevation scans to be acquired. The profiles are oversampled with a 1.5 km resolution in the Upper Troposphere Lower Stratosphere (UTLS), within the 3 km IFOV. By December 2007, the duty cycle has been increased step-by step to 100%.

In this thesis, measurements from the full spectral resolution nominal mode are investigated to study the behaviour of hydrogen cyanide (HCN) in the UTLS region only.

3.2.3 Instrument design

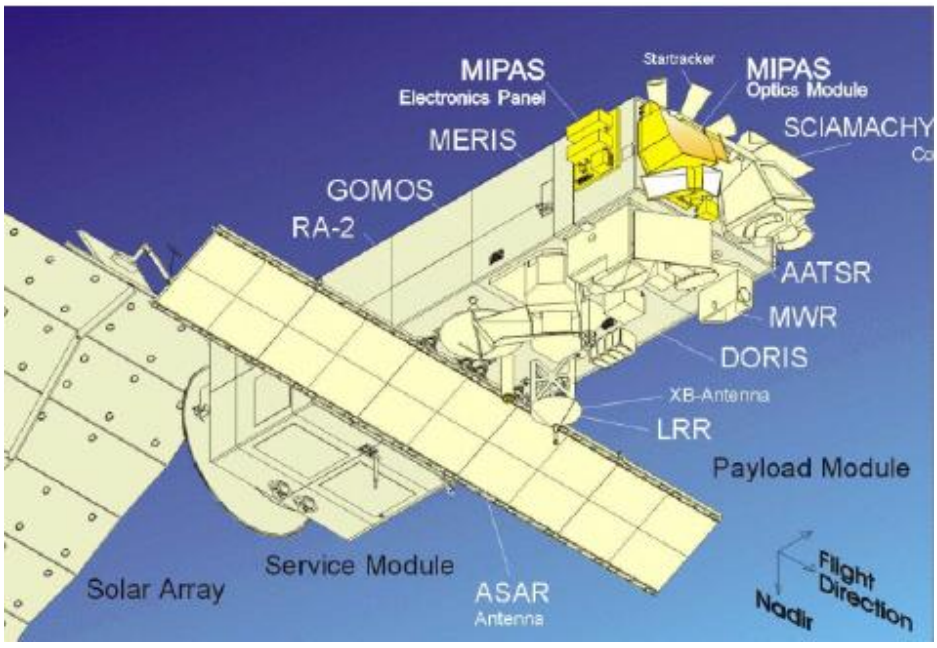

Figure 3.3 : ENVISAT in flight showing location of MIPAS-E. (Note the flight direction).

The MIPAS-E instrument is located on the rear corner of the ENVISAT platform between MERIS and AATSR as shown in [Figure 3.3]. The instrument has a total mass of 320 kg, with power consumption of 210 W. The space segment of MIPAS-E is divided into two modules: The MIPAS-E Optic module (MIO) and the MIPAS-E Electronics module (MIE).

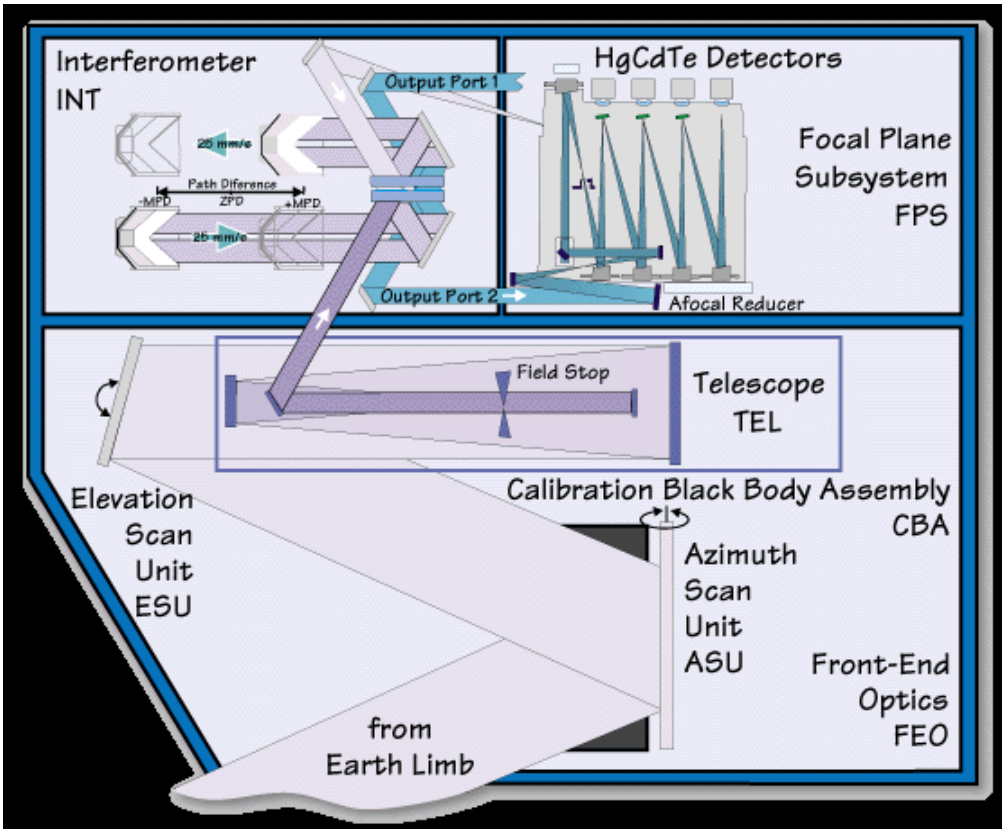

Figure 3.4: Schematics of MIPAS-E MIO module.

The MIO [Figure 3.4] has the following major parts: Front End Optics, Interferometer and Focal Plane Subsystem. The Front End Optics consists of Azimuth Scan Unit, Elevation Scan Unit, telescope and calibration blackbody. Earth's atmospheric radiation enters through the Front End Optics where it is reflected at an azimuth and an elevation scan mirror [Section 3.2.1]. The Azimuth Scan Unit (ASU) helps to select the line of sight and the Elevation Scan Unit (ESU) determines the actual limb height of the measurements. The incoming radiation is collimated to one of the input ports of the interferometer. The detectors record the varying intensity of the interference pattern produced by the interferometer [described in detail in section 3.2.4]. The spectral distribution of radiation is obtained by post processing of the interferograms. During a calibration sequence, the azimuth mirror is pointed towards an internal calibration blackbody which acts as a reference source to calibrate the measured signal. The internal Calibration Blackbody Assembly (CBA) has an emissivity greater than 99.6% to achieve high accuracy gain calibration. The instrument control unit houses the electronics to drive the front end optics mirrors and interferometer subsystems such as the laser diode and the corner cube

actuators. The MIO module needs multi-layered insulation to protect the instrument and measurements against Sun and Earth's shine. It is necessary to reduce the amount of heat produced by the instrument itself so that it does not mask the infrared radiation of the atmosphere. A large radiator keeps the entire optics module at 210 K. Below the MIO are two baffles that reduce the amount of stray light.

The MIE comprises of electronic support plate (ESP), the instrument control electronics (ICE) boxes, the MIPAS-E power distribution unit (MPD), the digital bus unit (DBU) and the signal processing electronics subsystem (SPE).

3.2.4 The interferometer

The MIPAS-E interferometer is a Fourier transform infrared (FTIR) spectroradiometer based on the Michelson-Morley interferometer. In principle, the FTIR has two mirrors located at right angles to each other and oriented perpendicularly. The beamsplitter is placed at the vertex of the right angle, oriented at 45° angle relative to the mirrors. By smoothly translating the movable mirror, the optical path difference between the beams reflecting off the two mirrors is continuously varied producing an interferogram. The resulting interferogram is encoded; mathematically the interferogram is a Fourier Transform of the required spectrum. Three main advantages of Fourier transform Spectrometers are:

1) Throughput advantage-A large beam of radiation can be accepted, so even the faint sources can be detected.

2) Multiplex advantage-It requires only one detector and not one detector per spectral interval.

3) Precision advantage-It uses a laser to control the velocity of the moving mirror and to time the collection of data points throughout the mirror stroke.

The MIPAS-E interferometer [Figure 3.5] is based on a variant of the Michelson interferometer and is designed with few modifications to count for spectroscopic, radiometric, continuity and size requirements for the MIPAS-E instrument. For radiometric and spectroscopic performance requirements, a dual

slide interferometer with dual input and dual output ports is selected. With this configuration the interferometer will provide highest detectable signal at the outputs, least uncertainties in design, the highest degree of redundancy and most compact design. Using corner cubes, the radiation path is folded, allowing more compact arrangements and thus longer optical path differences resulting in finer spectral resolution. The incident angle of the radiation onto the beamsplitter is 30° to reduce polarization effects by the beamsplitter. The MIPAS-E interferometer is 0.58 m long, 0.36 m wide and has a mass of 30 kg. Major subassemblies include the interferometer optics, the drive units and the optical path difference sensor. The following section describes how MIPAS-E measures the interferograms.

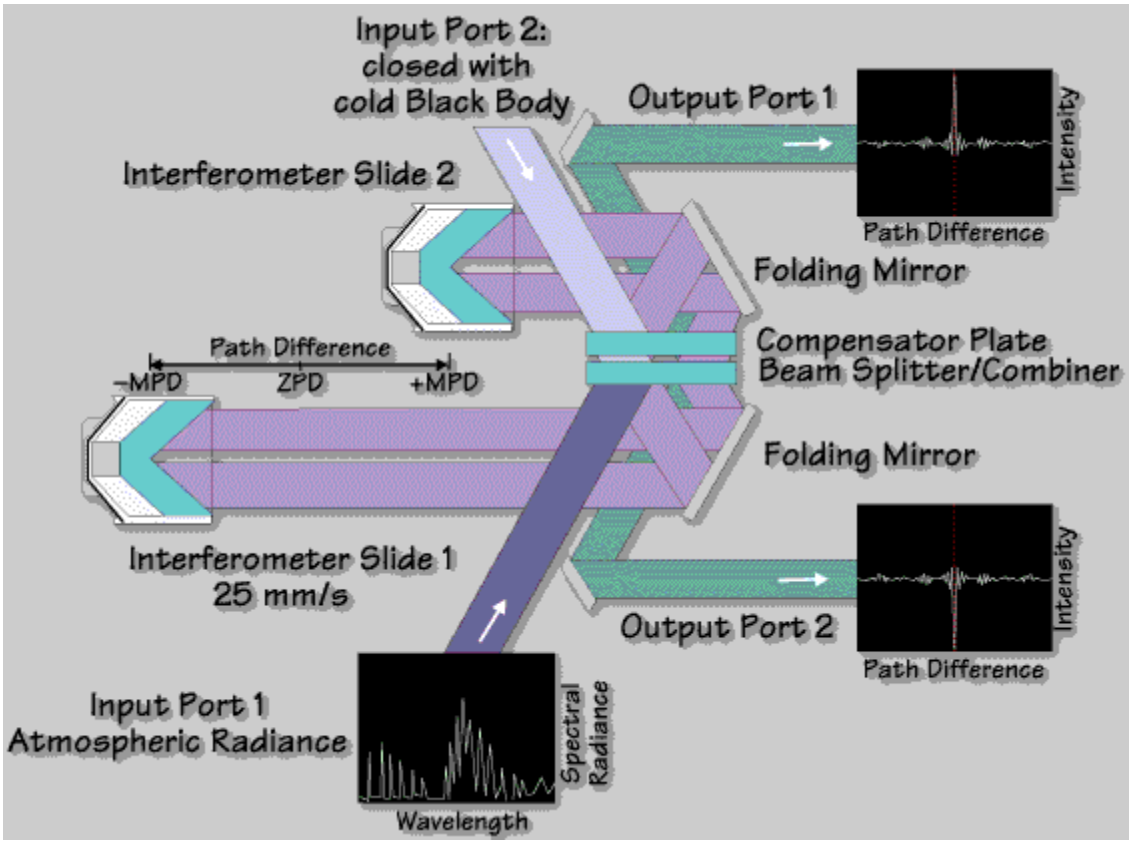

Figure 3.5 : Schematics of MIPAS-E interferometer.

The interferometer optics consist of a beamsplitter assembly, flat steering mirrors and the corner cubes on the slides. The beam is reflected by the elevation scan unit, which is designed for very high pointing stability as it determines the tangent height and collimated to the input port of the interferometer. Only one input port is required to acquire data from a given space, the second input port is designed

to look at a cold target (cold plate of high emissivity cooled at 70 K) in order to minimise its contribution to the signal. The incoming radiation beam is divided into two components by the beamsplitter. Approximately 50% of the incident radiation is reflected and the remaining 50% transmitted towards the two sliding cube corner retro-reflectors. The beamsplitter coatings themselves are quite critical, as they have to provide a reflectance near 50% throughout the broad spectral range. The beamsplitter assembly has to compensate for the phase delays caused by the varying refractive index throughout the spectral range which is attained with a second substrate of the same thickness as the beamsplitter itself and mounted with a narrow gap to the beamsplitter coatings. The corner cubes are designed such that the incident and reflected rays do not overlap as they travel to and from the beamsplitter. The corner cube slides are guided by mechanical bearings (dry-lubricated ballbearings) that are driven by force generated by linear motors in (two identical) Interferometer Drive Units (IDUs). Once more the beams are reflected by the retro-reflectors back to the beamsplitter where they recombine. The recombined beam is divided again by the beamsplitter into two beams and each is directed to one output port. The phase difference of the radiation depends on the distance between the mirrors with respect to the beamsplitter resulting in constructive and destructive interference patterns. Behind the interferometer, the output beams are collected by a series of eight detectors.

An interferogram is obtained when this interference-modulated signal is recorded as a function of optical path difference. The generated interference pattern is collected by infrared detectors. In principle a fine spectral resolution can be achieved by a long path difference since the resolution depends on the maximum optical path difference between the two mirrors. The longer the optical path difference, the finer the spectral resolution. The MIPAS-E interferometer provides two-sided interferograms with a maximum optical path difference (MPD) of 20 cm. This is achieved by independently moving the two cube corners by 5 cm backward and forward. The spectral resolution is approximately 0.6/MPD; 0.035 cm^{-1}. To convert this interferogram from spatial to spectral domain, a computational algorithm called a Fast Fourier Transform (FFT) can be performed which applies a

discrete Fourier transform (DFT) to each point of the interferogram reconstructing a spectrum as a function of energy and frequency [Griffiths, 1975].

3.2.5 Interferogram sampling

As the corner-reflectors are moved, the interference pattern moves over the detectors. To record a set of useful interferograms, the modulated output has to be sampled at a regular optical path difference. This is done with help of a laser interferometer in the same optical set up that triggers the sampling of the detector output at very precise intervals of optical path values (the required sampling accuracy for MIPAS-E is about 30 nm). The built-in laser interferometer makes use of a single-mode 1.3 micron diode laser whose output is guided by a single mode polarizing optical fibre to the interferometer.

The interferogram of the monochromatic laser is pure sine wave. A dedicated metrology detector and fringe counter detects the interferogram. The fringe counter forms the 'clock signal' that is sent to the Analogue to Digital Converter (ADC) in the signal processer electronics (SPE). The fringes trigger the sampling of the interferometer.

3.2.6 Detectors and spectral ranges

The two output beams of the interferometer are reduced in size by two small off-axis Newtonian telescopes and directed into the cold focal plane subsystem which houses the signal detectors with their interfaces to the active coolers, as well as the associated optics required for spectral separation and beam shaping.

At each output port, four detectors are placed to record the interferograms. The data recorded by the eight detectors are co-added to increase the signal to noise ratio. The set up provides redundancy of measurements, whereby if the detector on one of the output points fail, then the corresponding detector in second output port still provides useful data (but not in case of bands AB and B).

Photoconductive Mercury Cadmium Telluride (HgCdTe) detectors (PC-CMT) meet the requirement of low noise contribution and electronics bandwidth to cover

the long wave spectral range (14.6–7 μm) whereas photovoltaic HgCdTe detectors (PV-CMT) are preferred to cover the shorter wave (7–4 μm) range where they are more linear. The detectors are cooled at 70 K by a Stirling cycle cooler to reduce internal noise contribution.

The four detectors are named A, B, C and D with common detectors in the two ports for bands A, C, D. Detectors B1 and B2 are different having different spectral coverages giving bands AB and B respectively. These eight detectors are combined in five spectral bands [Table 3.3].

Detector	Band	Spectral range (cm^{-1})
A1, A2	A	685–970
B1	AB	1020–1170
B2	B	1215–1500
C1, C2	C	1570–1750
D1, D2	D	1820–2410

Table 3.3: The five spectral bands covered by MIPAS-E.

3.2.7 MIPAS electronics (MIE) module

After pre-amplification, the eight signals enter the analogue part of the Signal Processing Electronics (SPE) which generates the associated digital bit streams. The digitized data is separated in to five nominal bands by complex filtering and are formatted to source packets and sent to the platform bus for transmission to ground. The controlling functions of the MIPAS-E instrument are performed by the Instrument Control Electronics (ICE). There are two boxes (ICE1 and ICE2) for redundancy. The main functions of ICE include control of MIPAS-E operation and its operational modes, recoding of the instrument events, commanding and monitoring of MIPAS-E equipments, monitoring and processing of MIPAS-E housekeeping data and initiation of corrective actions in case of instrument failures.

3.3 Calibration measurements

To provide useful measurements, MIPAS-E has to meet certain performance requirements. Any emission arising from noise sources within the detectors and thermal emissions will be added to the instrument signal. Thus, MIPAS-E performs two step calibrations using 'cold' and 'warm' targets to compensate for temperature variations along the orbit. Pointing calibration very rarely is performed to compensate for slow drifts of the satellite pointing.

3.3.1 Noise equivalent spectral radiance (NESR)

The Noise Equivalent Spectral Radiance (NESR) quantifies the noise level of the data. The $NESR_t$ is defined as the standard deviation of the measured single sweep spectral radiance taken over *N* measurements for the input signal of a blackbody at temperature T assuming stationary conditions. The $NESR_0$ is defined as $NESR_t$ with T sufficiently small that the noise contribution from the input signal becomes negligible to the noise contributions from the instrument itself. The $NESR_0$ is evaluated from deep space measurements at 210 km tangent-point altitude.

Spectral band	Wavelength cm^{-1}	NESR (nW /(cm^2 sr cm^{-1})
A	685–970	50
AB	1020–1170	40
B	1215–1500	20
C	1570–1750	6
D	1820–2410	4.2

Table 3.4: MIPAS-E $NESR_0$ requirement as per each spectral band. [Kleinert *et al.*, 2007]

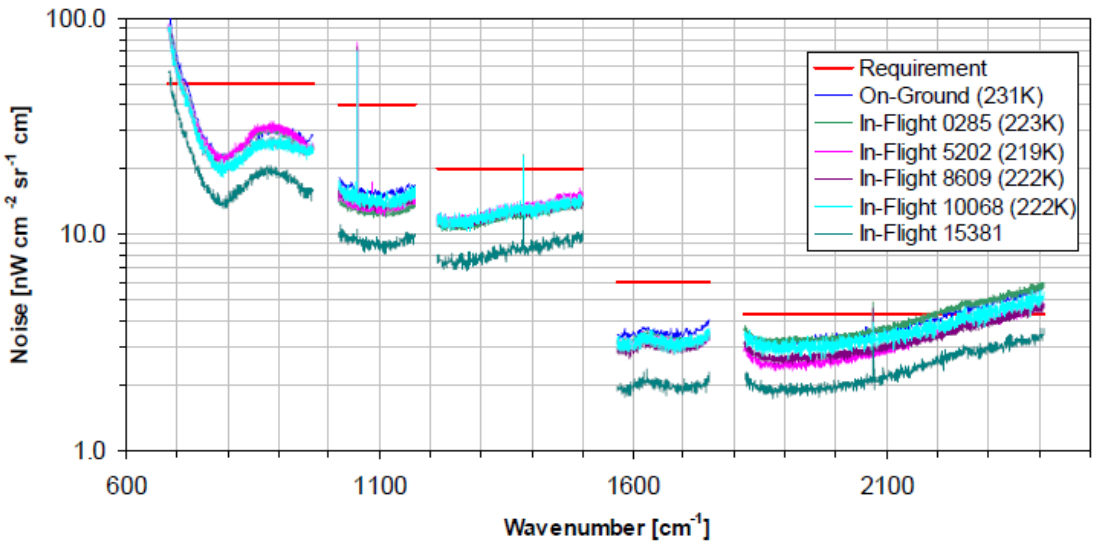

Figure 3.6 : $NESR_0$ of MIPAS-E on ground and in-flight.

The pre-flight required NESR, for each MIPAS-E band, is shown in Table 3.4 and Figure 3.6. Recently, Kleinert *et al.* [2007] reported that the NESR has not degraded in any systematic way since MIPAS-E has been in the orbit and has remained well within the required limits. The most important factor affecting the NESR is ice accumulation on the detector system, which may temporarily degrade the NESR by up to 20% with respect to an ice free detector.

Figure 3.7 and Figure 3.8 shows the distribution of NESR from level 1b MIPAS-E data with CI > 1.8 and represents NESR in HCN_0102 MW at average altitudes 8.30–19.71 km (MIPAS-E nominal altitude range 9–18 km) and HCN_0105 MW at average altitudes 8.30–28.39 km (MIPAS-E nominal altitude range 9–27 km) respectively for October 2003. From figures we observe the noise level of data in both HCN MWs for October 2003 is between 30 and 40 nW/(cm^2 sr cm^{-1}) which is well below the required limit of 50 nW/(cm^2 sr cm^{-1}) [Kleinert *et al.*, 2007].

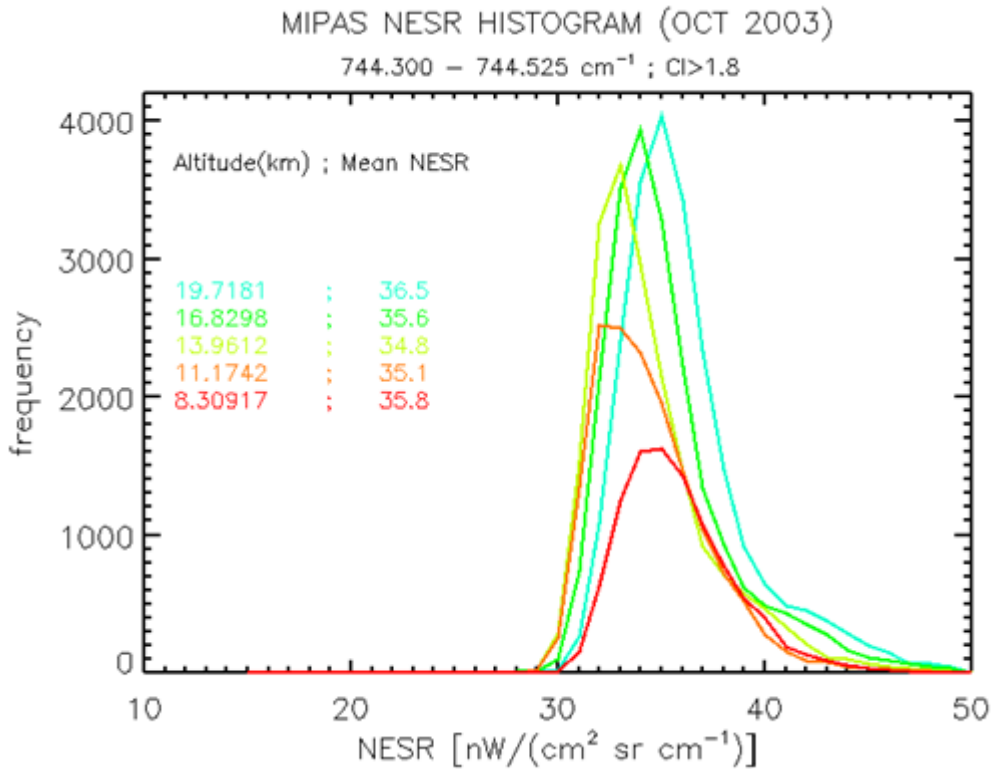

Figure 3.7: MIPAS-E NESR distribution for 744.300–744.525 cm^{-1}; apodised (spectral region defined as HCN_0102 in Chapter 4, Table 4.2).

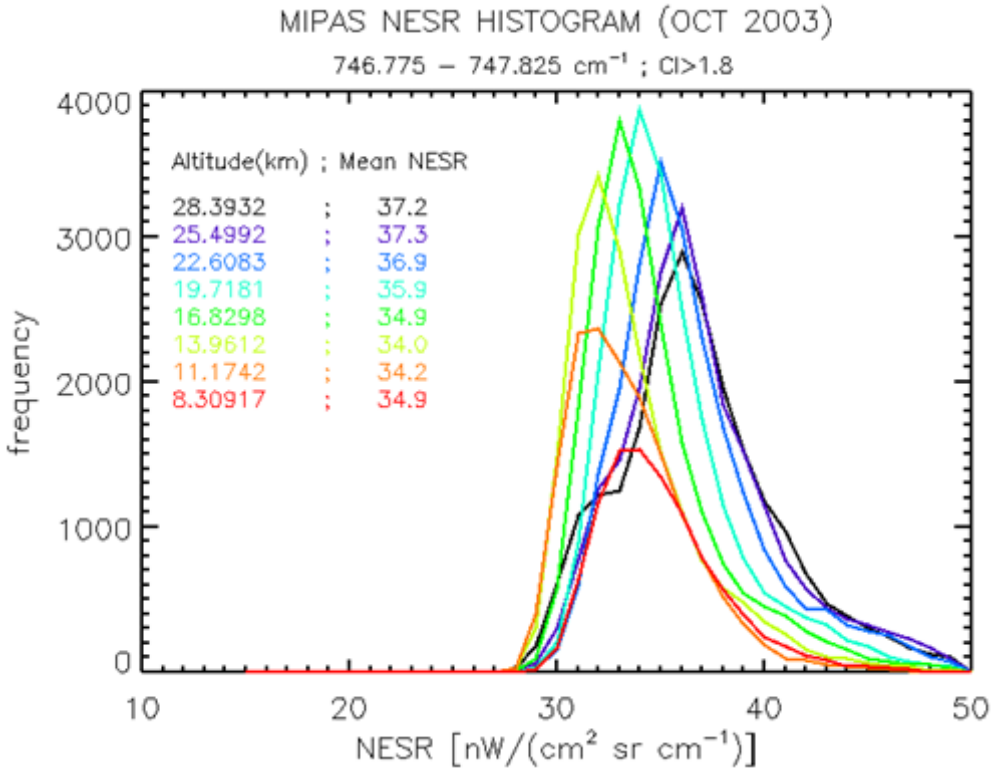

Figure 3.8: MIPAS-E NESR distribution for 746.775–747.825 cm^{-1}; apodised (spectral region defined as HCN_0105 in Chapter 4, Table 4.2).

3.3.2 Radiometric calibration

Radiometric calibration is the process of assigning absolute values in radiance units, (noted (r.u.) expressed in $W/(cm^2\ sr\ cm^{-1})$)) to the intensity axis (y-axis) with specified accuracy. The radiometric calibration implies the knowledge of a certain spectral calibration. Radiometric calibration characterises the instrument's self emission and is performed using two known radiation sources ('hot' and 'cold') to the spectra. The hot source is the internal calibration blackbody, while the deep space serves as a cold source. Any emission arising from noise sources within the detectors or thermal emission from the optical components will contribute to the instrument's signal. Each interferometer sweep that corresponds to a calibration measurement is performed at a low spectral resolution ($1/10^{th}$ the nominal spectral resolution) taking 0.4 seconds and requires an ensemble of measurements that are co-added to increase the signal-to-noise (SNR) ratio.

3.3.2.1 Offset measurement

A deep space measurement, in which radiance is measured at a tangent altitude of 250 km constitutes the offset calibration and accounts for the instrument's self-emission. There are about 20 offset measurements per orbit performed frequently (once every four scans) in order to account for changing self-emission of the instrument due to temperature variations along the orbit. In order to improve the signal to noise ratio, the offset calibration is obtained from 6 successive deep space measurements (3 forward and 3 reverse). The baseline scenario uses 300 sweeps at low resolution in both forward and reverse directions, requiring a total duration time of 16.15 seconds. The offset is measured about every 7 minutes and offset change between two consecutive measurements is below 10% of the NESR.

3.3.2.2 Gain calibration

Internal Blackbody (BB) measurements are performed after deep space measurements to calculate the radiometric gain function. Typically the BB is kept at

a maximum temperature of 230 K with an emissivity above 99.6% is used to test the instrument's response in each channel at a temperature corresponding to high radiance emissions. In order to reduce noise many measurements are made and co-added on the ground. The baseline scenario uses 300 sweeps at low resolution in both forward and reverse direction. The gain function is more stable than the instrument's offset and thus it is sufficient to generate a gain calibration function once per week. Changes in the gain function are mainly due to ice contamination of the detector system. The radiometric gain stability is typically better than 1.5% per week [Kleinert *et al.*, 2007].

3.3.3 Spectral calibration

Spectral calibration is the process of assigning absolute values in cm^{-1} to the wavenumber axis (x-axis) with a specified accuracy. The goal of spectral calibration is to correct the Doppler shift caused by the relative motion of the satellite and the atmosphere. It also corrects the shift of the diode laser used to sample the interferograms.

Particular spectral lines are retrieved in the observed spectrum and the known values of their wavenumbers [Table 3.5] acts as reference spectral lines that are used to establish the spectral shift in the measured spectrum. Four spectra are chosen at a tangent altitude (geo-located) of 32 km and are co-added in order to determine the spectral shift. The measured spectra are shifted in groups so that the spectral position of the compared lines matches the theoretical reference lines. For spectral stability and accuracy better than 0.001 cm^{-1} throughout the spectral range, spectral calibration is performed every four limb sequence (or 320 s).

Spectral calibration is based on few assumptions:

- Spectral calibration includes the spectral shift and no ILS function is applied.
- A minimum of 4 limb sequence spectral data are used at tangent altitude from 29–35 km.
- The spectral calibration shift function is applied throughout the spectral range. This assumes that there is a common optical axis for all 8 detectors.

Further residual misalignment between two output ports is low enough such that the difference in wavenumber is negligible.

Reference spectral lines are based on ground processing values, i.e. the correct spectral location is obtained by appropriately shifting the measured spectra to match the theoretical spectra.

Band	Target gas	Peak position (cm^{-1})	Spectral interval (cm^{-1})	Tangent altitude (km)	Used in spectral calibration
A	O_3	802.5074	802.40–802.62	30	Yes
AB	O_3	1125.2085	1125.10–1125.30	30	No
B	H_2O	1409.9689	1409.85–1410.08	50	Yes
C	H_2O	1672.4750	1672.40–1672.55	50	Yes
D	H_2O	1966.2615	1966.00–1966.50	50	Yes

Table 3.5: Spectral lines and intervals used for MIPAS-E ILS and spectral calibration. Source adapted from [ESA, 2007]

3.3.3.1 Instrument line shape (ILS) function

The ILS is a function that describes the unapodised instrumental response to the negligible spectral width. The ILS is directly related to the maximum path difference (MPD) of an instrument. The longer the MPD, the narrower the ILS arising from the boxcar truncation and finer spectral resolution obtained.

Selection of specific microwindows (MWs) containing precisely one reference peak of well-known wavenumber is made. It is followed by generation of the reference theoretical spectral line corresponding to this MW. Using an iterative process the residuals between reference line and the parameter ILS are minimised in order to fit the ILS to the incoming radiometrically calibrated spectrum. The ILS retrieval is processed per orbit and is part of the MIPAS-E level 1B (L1B) product. The reference spectra that are used for the ILS retrieval and spectral calibration are listed in Table 3.5.

3.3.4 Line of sight (LOS) calibration

The Line of sight calibration is the process of assigning a calibrated LOS pointing angle to a given atmospheric spectrum with a specified accuracy. These calibrated angles combined with the spacecraft position are used to determine the geo-location of the tangent point. LOS calibration is performed weekly.

For MIPAS-E, LOS pointing relies on the ENVISAT orbit and attitude control system which uses a star tracking system as reference. The angular calibration of the MIPAS-E scan mirror relative to the platform is inferred from the observation of stars moving through the IFOV of MIPAS-E. Any difference in expected and measurement in time of star passing indicates pointing errors and thus implies the accuracy of pointing measurements is strictly related to the accuracy achieved in the determination of the time at which a given star crosses the IFOV.

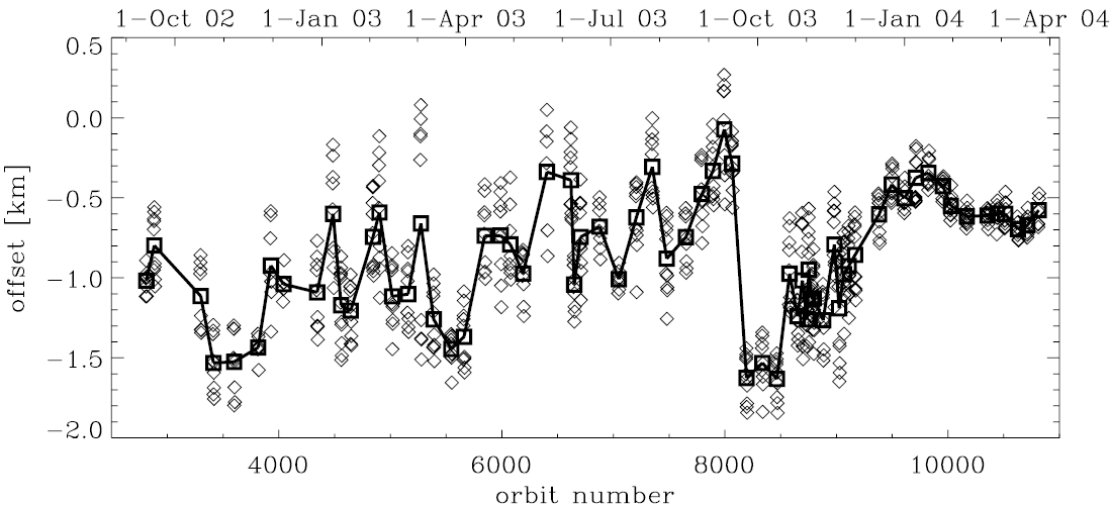

Figure 3.9: Offset between IMK LOS retrieved altitude and engineering tangent altitude drawn over orbit number. Only days with at least 500 processed geolocations have been taken. Each diamond represents a value of a single orbit. The daily average is marked by thick lines connecting squares [Kiefer *et al.*, 2007].

The MIPAS-E engineering tangent altitudes are too high by 0–1.8 km with conspicuous variation in this range in time [Kiefer *et al.*, 2007] and there are systematic differences in the mis-pointing between the poles which amounts to 1.5 to 2 km. A major trend is observed [Figure 3.9] in the offset data (November 2002 to

early September 2003) and the daily mean of the offset in this time span changes from −1.3 to −0.4 km which corresponds to a trend of 80 m/month. An offset down to −1.6 km at orbits 8100–8500 and −1.1 km at orbits 8600–9200 is seen.

3.3.5 MIPAS field of view

The MIPAS-E FOV response and the co-alignment of the detector channel has been analysed both prior to launch and post-launch. Co-alignment of detector channels was also verified post-launch. Prior-launch characterization of the FOV width, based on optical measurements, yielded a value of 52 mdeg (FWHM) in the elevation direction.

Verification measurements were carried out at IR wavelengths for individual detector channels, with the instrument collimated input beam viewing a hot blackbody source equipped with a circular aperture. By active scanning of the instrument's line of sight across an infrared bright, 'point-like' source while raw mode interferograms were acquired simultaneously in all 8 detectors. Mercury was chosen as the target which provided sufficiently high flux density across the wavelength band of interest. Prior to actual measurement the scan angles of the LOS were adjusted such that the IR source would pass through centre of the FOV while the elevation scan angle is scanned at constant velocity (≈ 23.5 mrad/s). The overall timing was chosen such that the expected passage of the planet Mercury through the FOV occurred ≈ 1 s after the start of an appropriate interferometer sweep. The settings ensured the actual passage occurred well before reaching the zero path difference peak and sufficiently high tangent altitudes (>80 km) to avoid perturbations through atmospheric broadband emission. The response of individual detectors as a function of elevation and azimuth offset can be attained by estimating the spectrally integrated signals from each channel. Kleinert *et al.* [2007] reports absolute points of inflection positions agree within 0.023 mrad for all channels and that FOV half width varies between 0.788 mrad for detectors A1 and A2 and 0.811 mrad for detectors D1 and D2.

3.4 MIPAS-E data

The detector signal before being transmitted to the ground the detected signal is amplified and the analogue filtered, digitized, numerically filtered and decimated, equalized and combined, bit truncated and finally packetized. The level 0 (L0) product is received by ground stations at Kiruna (Sweden) and Esrin (Italy). At the intermediary Level 1A (L1A) the data packets are extracted and sorted into time sequenced atmospheric measurement and calibration measurement interferograms. The MIPAS-E data processing flowchart is shown in Figure 3.10.

The two operational data products from MIPAS-E are:

1. L1B data product that provides the calibrated atmospheric measurements radiometrically, spectrally and geo-located. These spectra are intensity measurement as a function of wavenumber (cm^{-1}) and units are ($nW/(cm^2\ sr\ cm^{-1})$).
2. Level 2 data that are the vertical profiles of temperature (T), pressure (p) and six target species: water vapour (H_2O), ozone (O_3), methane (CH_4), nitric acid (HNO_3), nitrogen dioxide (NO_2) and nitrous oxide (N_2O).

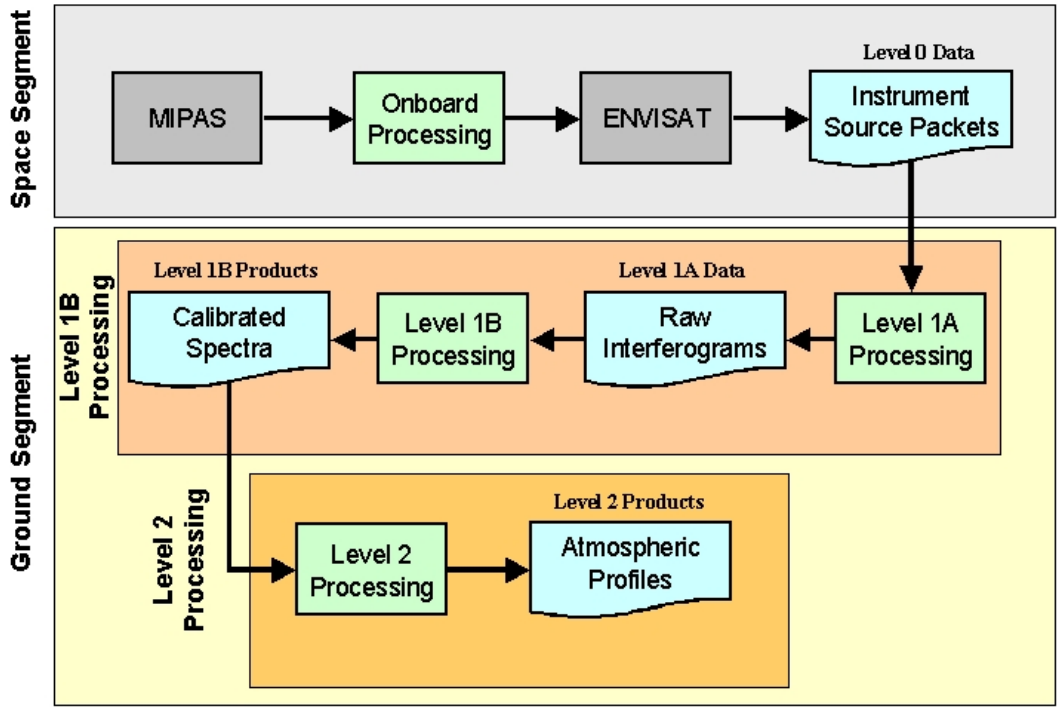

Figure 3.10 : Flow chart of MIPAS-E data processing. (Source by ESA).

3.4.1 Level 1b (L1b)-MIPAS-E calibrated spectra

For MIPAS-E, Level 1B output is calibrated, geolocated atmospheric spectra showing radiance as a function of wavenumber. The goal of L1b processing is to transform the interferograms generated at the end of the level 1A processing into calibrated and corrected spectral radiance spectra. The Level 1B processing requires auxiliary data files that contain the information of instrument status, instrument level and platform parameters such as pointing and timing information.

Specific functions are applied to the data in following order:

- Offset Calibration function which performs spike detection, sorts offset data according to the interferometer sweep direction, detects and corrects for the detectors non-linearity, coadds interferograms in each band (3 forward/3 reverse). It determines the NESR performance and checks validity of incoming offset measurements.
- Gain Calibration function performs spike detection, sort's blackbody and deep space measurements according to the interferometer sweep direction, detects and corrects for detector non-linearity, calculates coarse spectra for blackbody and deep space interferograms, calculates theoretical blackbody radiance from temperature readings corresponding to the blackbody measurements and calculates the complex gain ratio. Finally checks for radiometric accuracy of the blackbody and deep space measurements.
- Spectral Calibration is applied every 4 elevation scans. The function computes the spectral calibration factor based on the known values of the reference line positions and the measured line positions.
- Calculate Radiance function performs the processing scene measurements and generates a radiometrically calibrated spectrum. The function performs spike detection, sorts scene measurements according to the interferometer sweep direction, detects and corrects for fringe count errors, corrects for detector non-linearity, equalize and combines interferograms in band A, subtracts offset due to contribution of the instrument. It computes spectra

using the Fast Fourier transform (FFT) algorithm applied on the zero-padded interferograms. It corrects the spectral axis for Doppler shift and performs spectral interpolation onto a predefined uniform spectral axis. The function interpolates spectrum over a pre-determined users grid, multiplies the scene spectra by most recent gain and reports NESR.

- The ILS Retrieval function generates once per orbit the ILS retrieval from the radiometrically and spectrally calibrated spectra. A theoretical ILS is modelled using a limited number of parameters, convolved with the theoretical line and iteratively fits the results onto the experimental data.
- Calculate pointing function performs line of sight (LOS) pointing calibration which includes correcting elevation pointing angle and correcting pointing of actual scene. Specific objectives achieved are computing the actual pointing error at time of Zero Path Difference (ZPD) crossing, actual azimuth pointing angle, correction of elevation angle and actual elevation pointing angle.
- Calculate geolocation function computes tangent height of actual scene, RMS error of tangent height of actual scene, longitude/latitude of actual scene, orbital position of spacecraft at ZPD time, estimated error on computed tangent height.

The geo-located, spectrally and radiometrically calibrated spectra, calibration data and auxiliary data, corresponding to 75 elevation scans per orbit, are output into single L1b orbit files.

3.4.2 Level 2 (L2)-MIPAS-E operational data

The operational level 2(L2) retrieval code is based on the Optimized Retrieval Model (ORM) [Ridolfi *et al.*, 2000] that was developed by an international consortium in the frame of an ESA study. The Near Real Time (NRT) operational data product is distributed within three hours from the measurement time. For re-analysis of MIPAS-E data, Off-line (OL) measurements with improved geo-location are computed. In the OL analysis, time constraint is relaxed by factor of 2 and more iteration per retrieval and extended height range are employed. Data were

nominally processed in the NRT mode from July 2002 until March 2004 when the MIPAS-E instrument was switched off due to mechanical problems. The OL processing has been used to re-process all data from July 2002 to March 2004. The main challenge of the ORM has been the requirement of performing the complex operation of mathematical inversion in near real time (NRT) for a large number of data. The ORM uses the Optimized Forward Model (OFM) that was developed for application in the operational near-real time processing of MIPAS-E spectra which involves minimization of computational requirements. For reasons of computational efficiency, the OFM does not include effects such as non-local thermodynamic equilibrium (N-LTE) or scattering of radiation by the clouds [Raspollini *et al.*, 2006].

In the pre-launch phase, besides the operational MIPAS-E level-2 data processor there exist six retrieval codes that were developed and cross-validated within the 'Advanced MIPAS-E Level-2 Data Analysis' (AMIL2DA) project [von Clarmann *et al.*, 2003]. Most of these processors involve modelling aspects of radiative transfer not included in the ORM or use a retrieval strategy of higher sophistication. These are the extended scientific versions of the OFM/ORM by IFAC [Ridolfi *et al.*, 2000], the Retrieval Control Program (RCP) by IMK/IAA, two distinct data processors by DLR (Deutsches Zentrum für Luft- und Raumfahrt) - D-PAC (German Processing and Archiving Centre) processor and Istituto di Fisica Applicata ''Nello Carrara'' (IFAC) , the RET2D code by the Rutherford Appleton Laboratory and the Oxford University Processor to Invert MIPAS-E Measurements (OPTIMO), which meanwhile has been replaced by the MORSE software [Dudhia *et al.*, 2005]. Further MIPAS-E data processors are the one coded and applied by Forschungszentrum Jülich [Hoffman *et al.*, 2005], the OPERA code of the University of Leicester [Moore *et al.*, 2006] and the GMTR code by Bologna University [Carlotti *et al.*, 2006].

All these scientific processors required forward modelling of radiative transfer through the Earth's atmosphere which plays a key role to retrieve atmospheric parameters. Five line-by-line radiative transfer models were compared under AMIL2DA project specifications: The Karlsruhe Optimized and Precise Radiative transfer code (KOPRA) of the Forschungszentrum Karlsruhe [Stiller *et al.*, 2000, 2002], the Reference Forward Model (RFM) of Oxford University [Dudhia,

2002(b)], Modular Infrared Atmospheric Radiative Transfer (MIRART) by DLR [Schreier *et al.*, 2002], the Optimized Forward Model (OFM) by IFAC (formerly IROE) [Ridolfi *et al.*, 2000], an enhanced version of the OFM (IROE1) and a radiative transfer code by Rutherford Appleton Laboratory, called FM2D.

The conclusions of the AMIL2DA study show that the results of OFM and ORM agree within the predicted error margins with those provided by the other processors considered in the AMIL2DA project. Moreover, the blind test retrieval experiment highlighted that the retrieval codes are capable of producing reliable results, in the sense that the discrepancies between the retrieved and the true (assumed) profiles were found to be statistically consistent with the profile error bars determined on the basis of analytical error propagation.

3.4.2.1 The Operational level 2 retrieval

The operational L2 retrieval algorithm is based on a non-linear least squares fitting and consists of the global fit of a theoretical forward model calculations $\mathbf{F}(\mathbf{p},\mathbf{x})$ to the observations $\mathbf{y}$. $\mathbf{F}(\mathbf{p},\mathbf{x})$ simulates the observations starting with a known instrument, geophysical and spectral parameters $\mathbf{p}$ to retrieve the unknown quantity $\mathbf{x}$. A solution based on iterative procedure is obtained using the Gauss-Newton method, modified according to the Levenberg-Marquardt criterion, for minimization of cost (χ^2) function.

Three main optimizations are made in the L2 retrieval code [Raspollini *et al.*, 2006] to handle the multiplicity of unknowns and the redundancy of the data. They are described in detail as follows:

1. Global fit of the limb sequence

   A global fit approach is used for retrieval of each vertical profile, in this all the spectral data of a complete limb sequence are fitted simultaneously. The Levenberg-Marquardt method is used to calculate the vector residual term which is the difference of the observations and the simulations from all altitudes in the MIPAS-E elevation scan measurement.

$$\boldsymbol{R} = \boldsymbol{y} - \boldsymbol{F}(\boldsymbol{p}, \tilde{\boldsymbol{x}}) \qquad (3.1)$$

The global fit provides a full exploitation of the measurements and a rigorous determination of the correlation between the atmospheric parameters at different altitudes

2. Use of 'microwindows'

A set of narrow spectral intervals less than 3 cm^{-1} width, called 'microwindows' [Dudhia *et al.*, 2002], contains the best information on target parameters and are least affected by forward model errors (such as the uncertain spectroscopic data, interference of non-target species, Non-Local Thermal Equilibrium (N-LTE) and line mixing effects) are used.

Microwindows are selected such that the total error defined as the sum of the measurement error $\mathbf{V}_x$ (due to random noise) and various model errors:

$$\boldsymbol{V}_x^{tot} = \boldsymbol{V}_{\boldsymbol{x}} + \sum_i \boldsymbol{V}_x^i \qquad (3.2)$$

where each $\boldsymbol{V}_x^i$ represents an independent forward model error. For each error spectrum $\delta\mathbf{y}_i$ is computed as the difference between forward model calculations obtained for a nominal value of the parameter and for the parameter perturbed by 1σ. The error for each error $\delta\mathbf{y}_i$ is related to the variance covariance matrix of the forward model as follows:

$$\boldsymbol{V}_y^i = (\delta \boldsymbol{y}_i)(\delta \boldsymbol{y}_i)^T \qquad (3.3)$$

The final MWs are chosen when the information content cannot increase further (growing MWs) or when the maximum 3 wavenumber width is reached.

3. Sequential retrieval of the species

Defining a sequence of operations avoids the repetition of the same calculations and minimizes the number of memorized quantities. A hierarchy of operations is followed to retrieve different unknowns. Firstly, temperature

and pressure (pT retrieval) are retrieved simultaneously, then VMR profiles of the target species are individually retrieved following the order of their reciprocal spectral interference, i.e., : H_2O first, followed by O_3, HNO_3, CH_4, N_2O and NO_2 and lastly a retrieval of continuum-like emission effects and the zero-level offset. The pT retrieval [Carlotti and Ridolfi, 1999] uses CO_2 spectral features and assumes the hydrostatic equilibrium that provides a relationship between temperature, pressure and geometrical altitude.

The altitude is determined by the engineering measurement of the pointing direction. Tests performed showed that in first few months of operations, MIPAS-E engineering altitude had a bias of up to 3 km [von Clarmann *et al.*, 2003]. The bias was reduced within accuracy specification, i.e. 900 m after an upgrade of the MIPAS-E pointing system. The short term pointing stability, during one interferometer sweep of 4 s duration was verified to be better than 80 m [Kiefer *et al.*, 2007]. The short term pointing stability is used to improve pT retrieval and the retrieval of tangent pressure is estimated to have an accuracy of about 1% which corresponds to an altitude uncertainty of about 70 m.

L2 processing involves simultaneous retrieval of pressure and temperature (pT) followed by sequential retrieval of VMR of the L2 products H_2O, O_3, HNO_3, CH_4, NO_2 and N_2O. In nominal measurement scenario MIPAS-E measurements extend from 68–6 km, but the L2 retrieval can be limited to a selected molecule dependent on altitude range. The retrieval begins with a Level 2 pre-processor that assesses the quality of the chosen L1b elevation scan using a quality filter or PCD flag. Any corrupt L1b data are flagged as 'false' and not used in any part of the L2 retrieval.

The operational processor requires a pre-retrieval cloud detection scheme which filters any 'corrupt' level 1B spectral data to remove effects due to strong clouds. If the L1B data is flagged as cloudy, it is removed from the analysis and the profile retrieval begins from the tangent height above the cloud corrupt measurement. The scheme used for cloud detection in infra-red remote sensing instruments involves computing the ratio of integrated signals in cloud MW pairs [Spang *et al.*, 2004] with one pair defined in each of three MIPAS-E (A, B and D). The

scheme incorporated into the MIPAS-E L2 operational retrieval processor was originally designed for Cyrogenic Infrared spectrometers and telescopes for the Atmosphere (CRISTA) mission [Spang *et al.*, 2002] which verified that cloud features are present in infra-red emission instruments and thus needs to be included in analyses of limb datasets.

An index value, called CI-A for MIPAS-E band A is defined by calculating the ratio of mean radiances from two different wavelength regions (MW1/MW2). The first wavelength region MW1, 788–796 cm^{-1} is mostly dominated by CO_2 and ozone shows weak emission features and slight changes in the presence of optically thin clouds. On the other hand, the second wavelength region MW2, 832–834 cm^{-1} is mainly dominated by aerosol and cloud emissions with some weak emissions by ozone and CFC11. This method was extended to include cloud indicators for MIPAS-E bands B and D. For cloud free conditions (non-polar regions), cloud index (CI > 4.0) is large.

Cloud index MIPAS-E band	**MW1 (cm^{-1})**	**MW2 (cm^{-1})**	**Cloud index Threshold value**	**CRISTA defined altitude range (km)**	**Preliminary in-flight altitude range (km)**
CI-A	788.20–796.25	832.3–834.4	1.8	8–60	10–45[a]
CI-B	1246.3–1249.1	1232.3–1234.4	1.2	8–50	10–40[a]
CI-D	1929.0–935.0	1973.0–1983.0	1.8	8–32	12–30[a]

Table 3.6: Cloud detection settings for MIPAS-E [Spang *et al.*, 2004][a]. The height range will be extendable to lower altitudes for mid and high latitudes.

The CI [Table 3.6] was found close to unity for optically thick cloud presence and values between 2.0 and 4.0 for transition from optically thick to optically thin cloud presence or when MIPAS-E FOV was partially filled with cloud presence. Cloud detection methodology is mainly limited due to the effect of extreme upper tropospheric H_2O concentrations on the cloud index [Greenhough *et al.*, 2005] below 12 km. Test results based on the reference atmosphere database [Remedios *et al.*, 1999] suggested CI-A values ≤ 1.8 cannot differentiate between cloud and high H_2O

concentrations below 8 km. Further, above 12 km, no dependence of calculated CI-A values was observed.

The Optimized Forward Model (OFM) built-in the ORM simulates the L1B good quality, cloud-free spectra. The 'best' MWs are selected and linearly interpolated on a fine spectral grid (irregular grid). The radiative transfer model also takes into account for the effect of the refractive index in the ray of the optical path, Voigt profile of the atmospheric line shape, use of a fine grid (5×10^{-4} cm^{-1}) in the spectral domain for monochromatic modelling of radiative transfer. The forward model convolves the atmospheric spectrum with the ILS and IFOV of the instrument. Effects due to Non-LTE, line mixing and pressure shifts are not taken in the forward model, but accounted for in the MW selection and error budget.

The forward model is the most time consuming and computationally expensive part of the retrieval process. Hence, the retrieval assumes that the atmosphere is horizontally homogeneous and in local thermodynamic equilibrium.

The retrieval process is iterative and hence the L2 processor requires minimizing the χ^2 value which is computed after each iteration and tested against the convergence criteria.

$$\chi^2 = n_{iter}^T S_n^{-1} n_{iter} \tag{3.4}$$

n_{iter} is the vector 'residual' at the iteration 'iter' and S_n is the variance covariance matrix. The retrieval process stops when three convergence criteria are fulfilled:

1. The maximum relative difference of the χ^2 value from the previous iteration to the current χ^2 value must be less than threshold T1. Raspollini *et al.* [2006] state typical T1 values of less than 0.02 for OL processing.

2. The maximum relative difference of the fitted parameters between two consecutive iterations must be less than threshold T2. In OL processing T2 is found to be less than 0.2 [Raspollini *et al.*, 2006].

3. The maximum number of allowed iterations is limited due to general computer time constraints (typically no. of iterations = 8).

The performance of the MIPAS-E level 2 processor strongly depends on the auxiliary data used.

1. Spectroscopic database:

   High-Resolution Transmission molecular absorption database (HITRAN)-a spectroscopic database contains spectral line information and infrared cross section measurements of up to 37 atmospheric constituents. The original dedicated database mipas_pf2.0 built on first version (HITRAN 1996) was replaced by database mipas_pf3.1 containing updated and improved spectral data for molecules CO_2, HNO_3, CH_4, NO_2, O_3 and COF_2 with most significant improvement of HNO_3 molecule [Flaud *et al.*, 2003; Mencaraglia *et al.*, 2006]. Version 'mipas_pf3.2' included changes to molecules NO, OCS, NH_3, H_2O_2 and HNO_3 [Flaud *et al.*, 2006; 2007]. Further updates for C_2H_6 and NO^+ line parameters were included both in mipas_pf3.2 and mipas_pf3.3 version [Flaud and Ridolfi, 2007].

2. Reference atmosphere database:

   The processing requires a climatology of profiles that are used to define the VMR of those species that interfere with the analysed spectrum, but not currently retrieved (interfering gases), which acts as the initial guess for the retrieved parameters. The reference atmosphere database [Remedios *et al.*, 2007(a, b)], as explained in detail in Chapter 4, has two components that are the standard and the initial guess (IG2) profiles. The IG2 seasonal climatologies provide the initial guess for retrieved parameters. The standard atmospheres were used to develop cross-section look-up tables, for MW selection and for error estimation.

3.5 Use MIPAS-E data to detect the HCN molecular signature

To characterize Hydrogen cyanide (HCN) behaviour we need geo-located, calibrated, high resolution spectral data. High resolution spectra are of importance

as detection and retrieval of HCN is complicated by the presence of many other major gaseous spectral features that either completely or partially overlap the HCN spectral feature. Band A (685–970 cm^{-1}) of MIPAS-E is rich in many interesting emission features of many gases where the signal to noise ratio is comparatively low which makes the detection of particular gas emission feature feasible. Significant knowledge of interfering gases in the HCN spectral range of interest is also necessary to quantify the presence of HCN in the Earth's atmosphere.

Even though MIPAS-E measurements are made over the whole globe, there are limitations such as interfering clouds and thus these data-points are contaminated. The measurement geometry of MIPAS-E has an advantage of making thousands of measurements; near global when compared to ACE-FTS/SCISAT which typically obtains 30 profiles per day. On the other hand the HCN signal is too low in MLS/AURA measurements and thus averaged over large number of data points to make HCN detection possible.

3.6 Summary

An overview of the nine instruments and Laser Retro-Reflector (LRR) onboard ESA's ENVISAT is described in this chapter. A detailed explanation of measurement and operation of Michelson Interferometer for Passive Interferometer (MIPAS) is presented. The chapter also covers the measurement geometry, the working of the main components of the MIPAS-E instrument, including the interferometer and the detectors. Section 3.4 describes the process of converting the raw interferograms into emission spectra and later into VMR profiles. The section details how MIPAS-E measurements are processed into useful geophysical data.

For both detection and retrieval of HCN using MIPAS-E limb measurements from level 1b and level 2 are selected (full resolution mode only-0.025 cm^{-1}). The following chapters describe detection of HCN emission spectral feature using L1B data, retrieval of HCN profile concentration using MORSE algorithm [Section 5.1] and comparison of data to pre-existing measurement data.

CHAPTER 4

4. Detection of hydrogen cyanide in MIPAS-E spectra

As discussed in Chapter 3, MIPAS-E is capable of measuring high-resolution atmospheric spectra in the range 685–2410 cm^{-1} over the altitudes of 6–68 km (MIPAS-E nominal altitudes) on a global scale. In the mid-infrared region, changes in the molecular vibrational and rotational energy of many important trace gases, including HCN, take place under certain conditions because of the interaction of infrared radiation with matter. The Earth's atmospheric signals are generally higher in this region as the maximum of the Planck function is at 11 μm (909.09 cm^{-1}) and it is thus potentially easier to detect HCN spectral signals in MIPAS-E spectra. To determine HCN distributions on a global scale, it is essential to detect the HCN emission feature prior to retrieval of the HCN profiles; the easiest case is that of biomass burning plumes where HCN is expected to be enhanced. Advantages of using a detection process are as follows:

a) It can provide the evidence of HCN emission signature in MIPAS-E spectral data.

b) It can provide confidence in the chosen HCN MWs and furthermore, allows better representation of the spectra from which accurate HCN VMR profiles can be retrieved.

c) It is computationally less expensive; it is faster than a retrieval scheme.

d) It is important to understand how well other interfering gases are modelled.

4.1 Detecting residual signatures in MIPAS-E spectra

The technique used to detect HCN emission signatures in MIPAS-E spectra is based on the search for HCN *residual* signatures. In this work, the method of Remedios *et al.* [2007(c)] is followed.

The measured residual spectrum, ΔY, is a function of wavenumber (ν) and is defined as the difference between the real measured MIPAS-E spectrum R_Y and a simulated spectrum $R_{x\,-HCN}$. R_{x-HCN} represents a simulation of MIPAS-E spectra that excludes HCN representation in the atmospheric calculations.

$$\Delta Y\,(\nu) = R_Y\,(\nu) - R_{X-HCN}\,(\nu) \qquad (4.1)$$

A 'reference' residual spectrum, ΔX, is also required and is defined as the difference between a simulated spectrum including HCN (R_x) and a simulated spectrum excluding HCN ($R_{x\,-HCN}$).

$$\Delta X\,(\nu) = R_X\,(\nu) - R_{X\,-HCN}\,(\nu) \qquad (4.2)$$

In an ideal world, ΔY = ΔX, where a perfect measurement would have no associated errors and perfect spectra calculation would have accurate spectral reference data and prior information of all other influencing gas concentrations. In reality, this cannot be true as there are many sources of measurement errors and errors in the forward model calculations. Furthermore, ΔX will not be perfect due to reasons such as errors in spectroscopic information, uncertainties in the profiles of other gases and also approximations in the forward model calculations. For

detection purposes from the atmospheric MIPAS-E emission spectra, the following detection criteria need to be satisfied:

1) Depending on the concentration of HCN in the atmosphere, the HCN spectral feature must contribute to a specific spectral region of interest for different altitudes.
2) The peak value of the HCN spectral feature must be greater than twice the NESR to distinguish the HCN feature from the instrument's noise.
3) The shape of the measured HCN spectral feature must be similar to a reference shape calculated at a specified VMR.

Once these criteria are satisfied, we can substantiate the presence of the HCN emission feature in MIPAS-E spectral data. Otherwise, the feature would not be distinguishable from the instrument's noise.

Thus, the detection of HCN from atmospheric spectra will depend on the factors related to the measuring instrument, such as the instrument's noise level (MIPAS-E NESR), spectral resolution and instrument's ILS.

4.2 Detection methodology

The detection method requires some preliminary steps to pre-select suitable MIPAS-E emission spectra to which the residual method can be applied. Selection of location and time period is described in Steps 1–3. The selection of the emission spectral MW is described in Step 4. Step 5 describes the effects of the ILS, spectral resolution and apodisation of the HCN spectral emission feature.

4.2.1 Step 1-Biomass burning as a lead to detection of HCN spectral signature [Chapter 1]

To ensure the detection of HCN spectral signatures in the atmospheric emission spectra, we need to select a time period when the HCN signature is expected to be enhanced e.g., active fire regions. Using a fire map one can locate the

'hot spots' around the globe. A 10-day Moderate Resolution Imaging Spectroradiometer (MODIS) fire map is shown below in Figure 4.1, which maps out the fires for 18–27 October 2003.

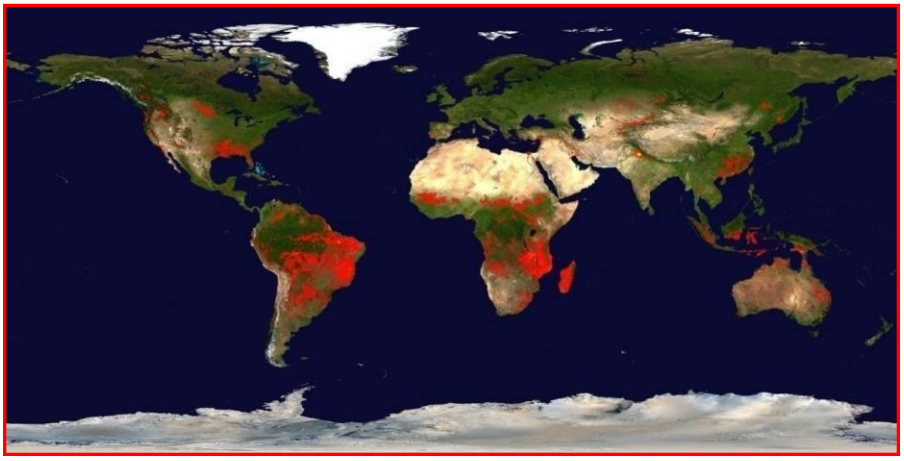

Figure 4.1 : 10-day MODIS fire map (18–27 October 2003).

The red colour indicates the fire counts and it can be noticed that fires are active in the tropical regions such as South America and South East Africa during the month of October. The selection of time period and region is further based on work by Glatthor *et al.* [2007], which covers the end of the biomass burning season in South America and South and East Africa, where large amounts of pollutants are released in the atmosphere and transported across large distances in the southern hemisphere.

4.2.2 Step 2-Carbon monoxide (CO) as a lead to detection of HCN emission feature in biomass burning plume

Carbon monoxide (CO) is a marker of large-scale influences of pollution on regional and global scales. CO concentration amounts are strongly enhanced by both biomass burning and industrial pollution. By studying the transport and distribution of CO in the atmosphere on spatial and temporal scales, one can investigate the likelihood of determining 'new' molecular signatures. A study by Rinsland *et al.* [2005] using the ACE-FTS data has shown a high correlation between enhanced CO and HCN VMR values [Figure 4.2] in biomass burning plumes in the free

troposphere. Identifying biomass burning regions with high mixing ratios of CO can be used to identify areas where HCN is most likely to be present, making it easier to detect the HCN spectral feature.

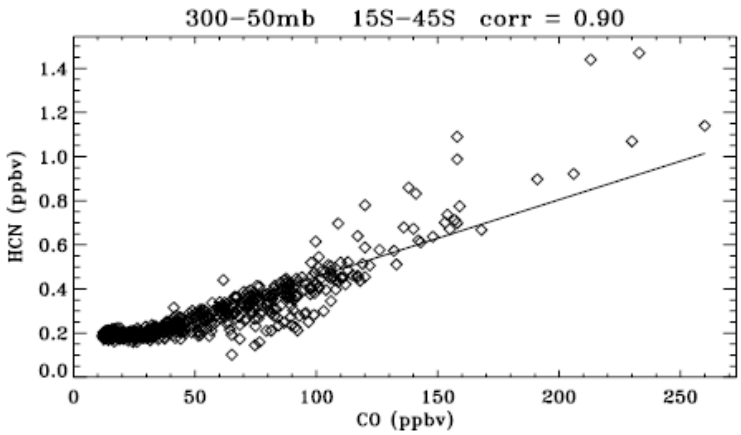

Figure 4.2: Correlation between the volume mixing ratios of CO and HCN derived from the ACE-FTS version 2.2 measurements between 30 September and 3 November 2004. A correlation coefficient of 0.90 was derived from 56 occultations recorded during that time period [Rinsland *et al.*, 2005].

The Measurement of Pollution in the Troposphere (MOPITT) instrument onboard NASA's Terra satellite has mapped CO concentrations on a global scale since March 2000. A 5 day CO plot (19–23 October 2003) using MOPITT version 3 of level 2 data [Figure 4.3] shows enhanced levels of CO plume over the East African region at 250 hPa.

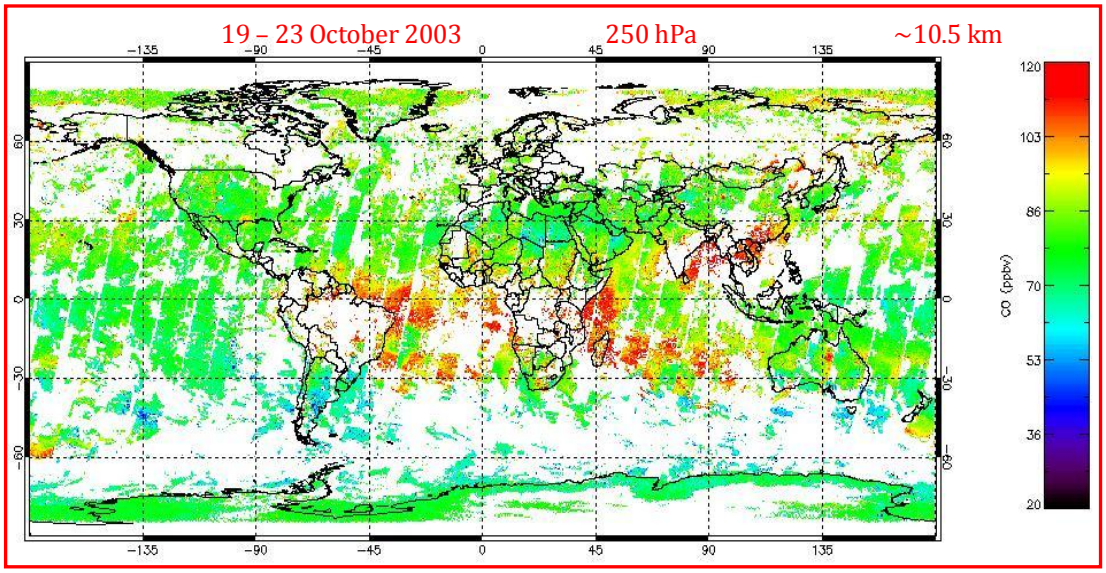

Figure 4.3: MOPITT (level 2-version 3) 5 day CO plot (19–23 October 2003) at 250 hPa. An enhanced CO plume can be seen near the East African region.

4.2.3 Step 3-Co-locating regions of MIPAS-E measurements

Co-locating the regions of enhanced CO measurements with MIPAS-E orbit tracks will further help select MIPAS-E spectral data to detect the feature of HCN emissions in the biomass burning plumes. Figure 4.4 shows the MIPAS-E orbit for 21 October 2003.

The MIPAS-E orbits 08577 and 08585 pass over the South and East Africa and the Madagascar region, which are all identified as biomass burning regions and enhanced CO measurements have been observed by MOPITT in this region on 21 October 2003. The 1-day orbit track plot [Figure 4.4] itself shows the availability of MIPAS-E spectral data around the globe at one particular MIPAS-E nominal altitude level.

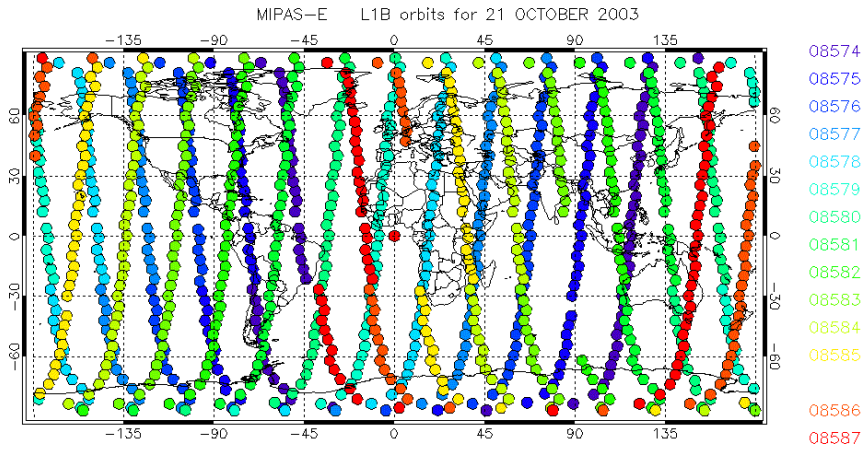

Figure 4.4 : Map of MIPAS-E l1b orbit data for 21 October 2003 at 12 km nominal altitude.

4.2.4 Step 4-Forward modelling with Oxford RFM

The retrieval of trace gas concentration information, as well as pressure and temperature, requires an analysis of spectra simulated to represent the true atmosphere from which the measured spectra were recorded. The accuracy of fit between the measured and simulated spectra ultimately determines the accuracy of parameters used in the simulation, within the limitations of measurement error. The accuracy of the simulation and hence the accuracy of retrieved parameters are also limited by the accuracy of reference spectral data used for each gas included in the

simulation. In addition, care must also be taken to simulate an atmosphere that includes all gases that are expected to influence the spectral region of interest.

To simulate atmospheric spectra, the Oxford RFM is used. This line-by-line radiative transfer model allows the simulation of atmospheric spectra using input parameters of pressure, temperature and gas VMR values using a specified viewing geometry. It also includes the feature to simulate the instrument's FOV and ILS and to use a number of other spectral and numerical approximations.

4.2.4.1 Reference data

To provide a reasonable first guess approximation of the true atmosphere, a simulated atmosphere was constructed using appropriate sources for gas VMR profiles, pressure and temperature.

4.2.4.1.1 Atmospheric profiles

The MIPAS reference atmospheres (RAMSTAN) constructed by Remedios *et al.* [2007(c)] provide an initial guess for contaminant gas profile data. These atmospheres contain quantitative descriptions of the mean state of the atmosphere and the likely deviations from the mean state.

MIPAS reference atmospheres are a set of standard atmospheres covering five atmospheric states encompassing broad latitudinal and seasonal variability (tropical, mid-latitude day/night, polar summer and polar winter); version v3.1 of the standard atmospheres were used. The standard atmospheres were constructed to cover 36 species (N_2, O_2, C_2H_2, C_2H_6, CO_2, O_3, H_2O, CH_4, N_2O, CFC-11, CFC-12, CFC-13, CFC-14, CFC-21, HCFC-22, CFC-113, CFC-114, CFC-115, CH_3Cl, CCl_4, HCN, NH_3, SF_6, HNO_3, HNO_4, NO, NO_2, SO_2, CO, HOCl, ClO, H_2O_2, N_2O_5, OCS, $ClONO_2$, COF_2) on a common altitude, pressure and temperature grid from 0 to 120 km. It further includes both means and estimates of variability (maximum, minimum and one sigma values).

The current version v4.0 has the further addition of a seasonal climatology comprising a 4-season, 6-latitude climatology database (the 'IG2 climatology' or Initial Guess 2 climatology) [Remedios *et al.*, 2007(a)].

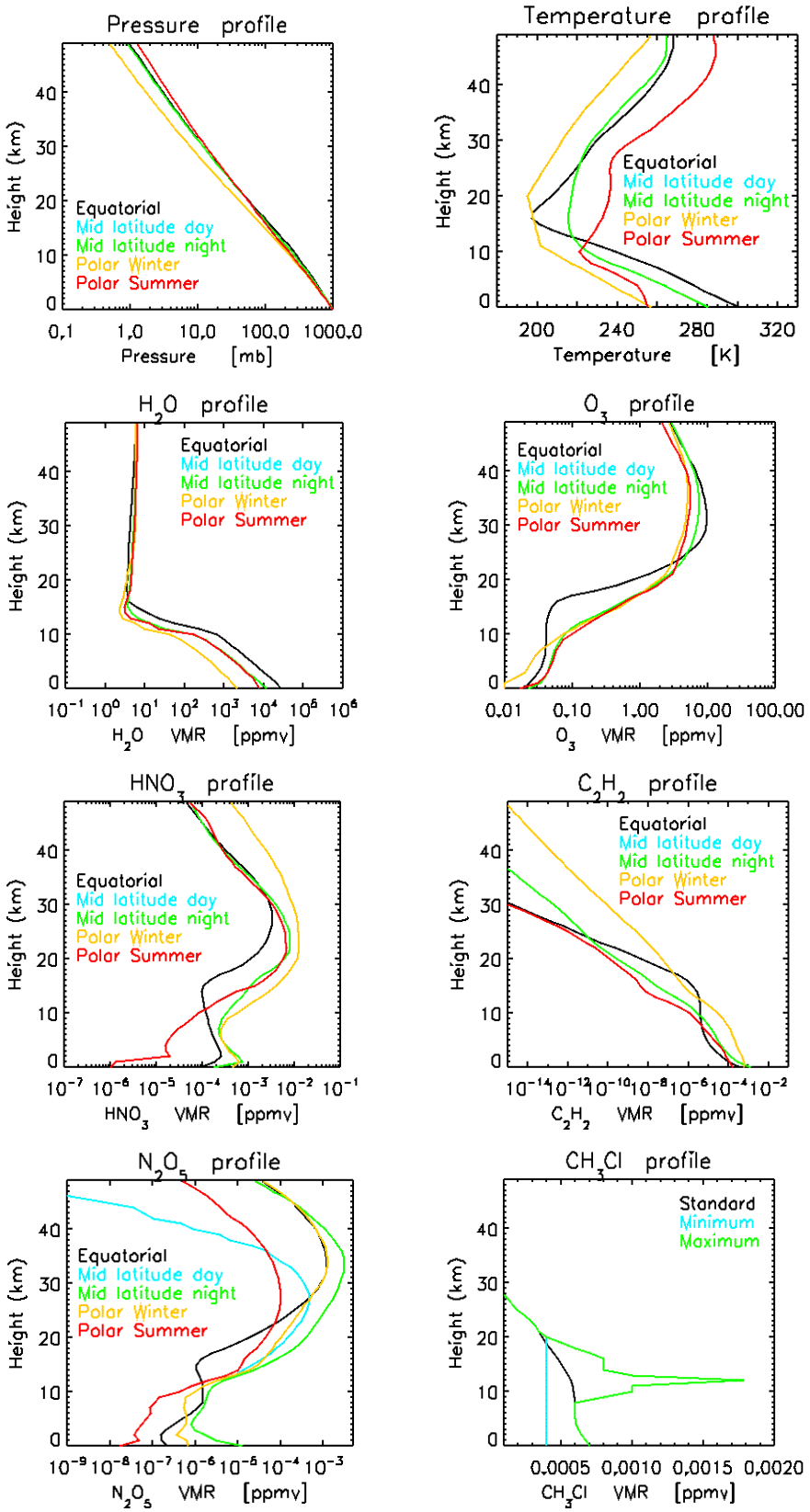

Figure 4.5: Pressure, temperature, H_2O, O_3, HNO_3, C_2H_2, N_2O_5 profiles based on standard MIPAS reference atmosphere (v3.1, 5 latitude bands, 0–50 km) and CH_3Cl based on extra_species_v3_1.dat, minimum and maximum cases.

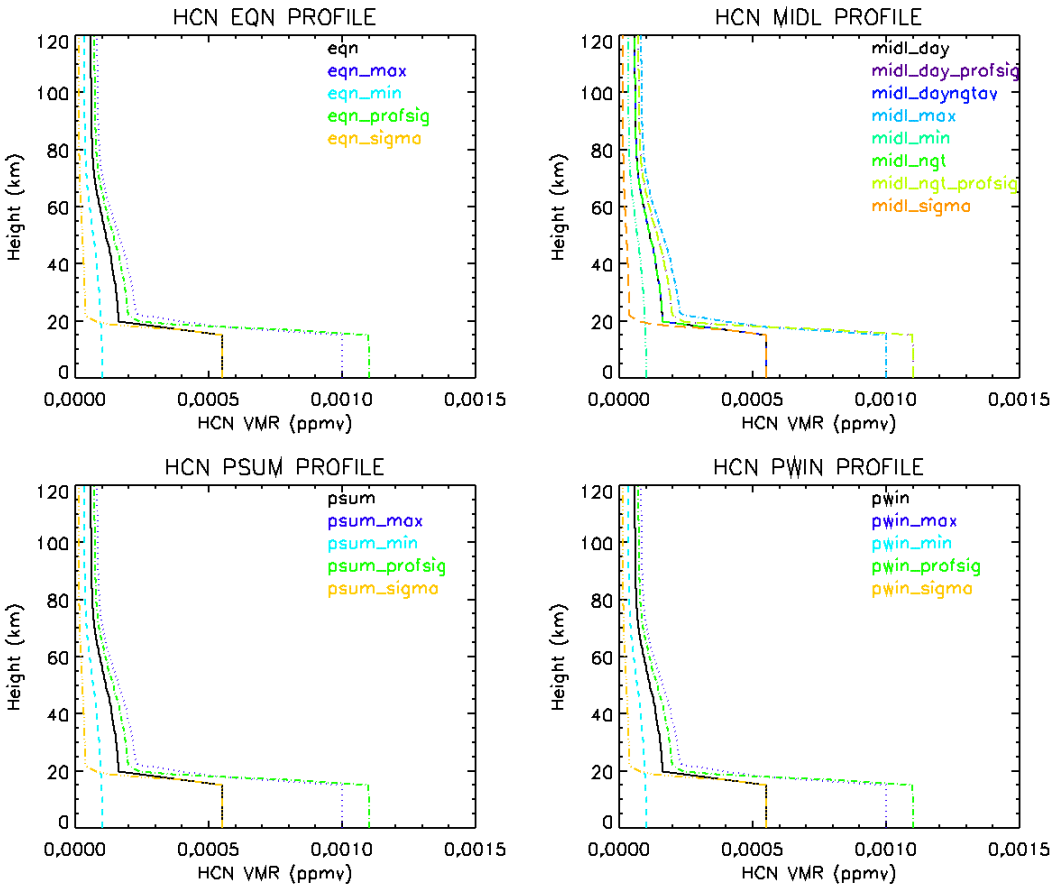

Figure 4.6: HCN profile plots using MIPAS reference atmosphere (v3.1, 5 latitude bands, 0–120 km).

The Figure 4.5 shows profiles for pressure, temperature and interfering gases such as H_2O, O_3, HNO_3, C_2H_2 and N_2O_5 to show the behaviour in different latitude bands that are used to simulate the atmospheric spectra based on MIPAS climatology values; CH_3Cl profiles standard, minimum and maximum case represent general, background and biomass burning case. Figure 4.6 shows HCN profiles plotted based on MIPAS climatology values [Remedios *et al.*, 2007(c)].

4.2.4.2 Searching for candidate spectral regions for HCN detection

The MWs used by ACE-FTS/SCISAT-1 (except for 1438.7 and 1444.76 cm^{-1} line centres) and MLS/EOS Aura to retrieve HCN concentrations are not covered by MIPAS-E spectral bands and thus not useful for HCN detection. However, the MWs

used by ATMOS/SPACELAB-3 and ATMOS/ATLAS-3 can be used to detect the HCN emission feature and are listed in Table 4.1.

Instrument	Altitude range (km)	HCN line centre/MW (cm^{-1})
ATMOS/SPACELAB-3	12.5–30	1438.6686 1444.8572
ATMOS/ATLAS-3	11–16	753.05–753.60 761.95–762.30
ACE-FTS/SCISAT-1	10–28 15–25	1438.70 1444.76

Table 4.1: List of HCN MWs based on previous infrared measurements useful for detection of HCN limb emission spectral lines.

As the previous studies on HCN were based on absorption spectra, in this analysis the spectra are simulated in the same spectral region as in MIPAS-E limb emission spectral data. The simulations begin on a broader spectral region approach i.e. simulation of MIPAS-E limb emission spectra in the spectral range of 685–970 cm^{-1} and later refines the HCN spectral MW regions depending on detection criteria.

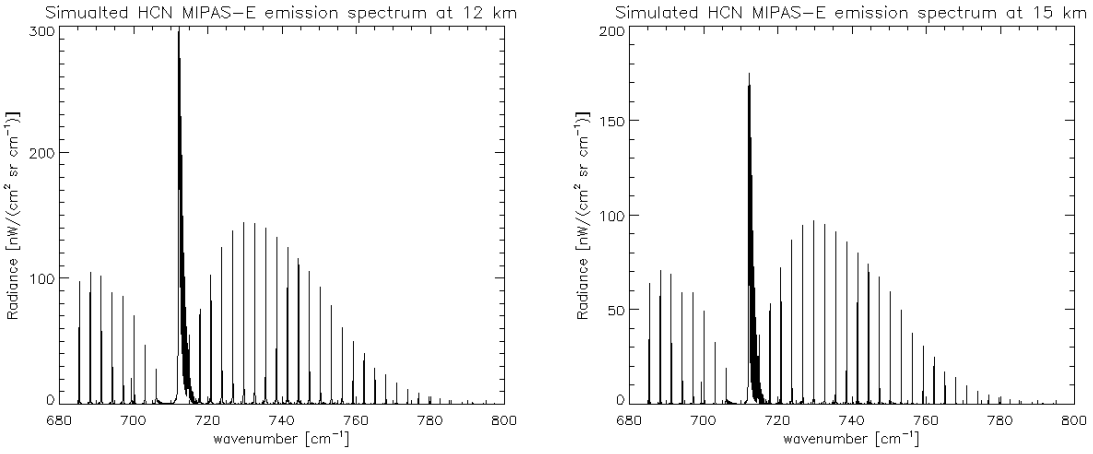

Figure 4.7: Simulated HCN MIPAS-E band A (685–970 cm^{-1}) limb emission spectrum where HCN background concentration was set to 220 pptv for 12 and 15 km (only HCN).

A simulated spectrum for HCN at 12 and 15 km is shown in the Figure 4.7. The HCN concentration is set to a value of 220 pptv at 12- and 15-km. The minimum

HCN concentration value is based on flight measurements performed during spring 25 February–10 April 2001 by the NASA Transport and Chemical Evolution (TRACE-P) mission [Singh *et al.*, 2003]. The HCN emission spectral feature exceeds the MIPAS-E NESR which is typically 40 nW/(cm^2 sr cm^{-1}) for the spectral region of band A if it is the only trace gas present in the atmosphere.

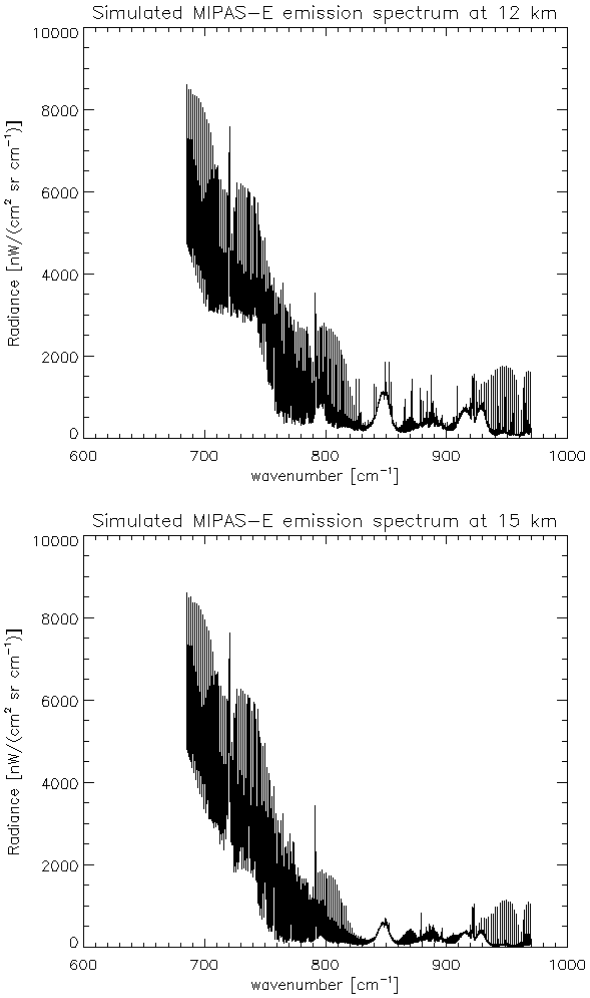

Figure 4.8: Simulated MIPAS-E band A (685–970 cm^{-1}) limb emission spectrum using standard reference profiles for major gases, HCN concentration was set to a 220 pptv for 12- and 15-km.

A simulated MIPAS-E spectrum at 12- and 15-km tangent altitudes is shown in Figure 4.8. Simulated profiles for all other gases are based on a standard reference atmosphere compiled by Remedios *et al. [*1999; 2007(c)]. Detection of the HCN emission feature is complicated by the presence of many other major gases, such as CO_2, O_3 and H_2O and many other molecules that either completely or partially

overlap the HCN spectral feature in the 685–970 cm^{-1} spectral region. Aerosol extinction must also be considered at tropospheric levels. With typically low mixing ratios of ≈ 220 pptv in the atmosphere, the detection of HCN becomes more complex. Thus, in order to detect the HCN spectral feature in the atmospheric spectrum, the effects due to other gaseous spectral features and aerosols should be removed.

For trace gas species with small contributions to the total observed infrared emission radiance, it is possible to linearly approximate the radiance contribution for a particular gas by calculating the difference between simulated spectra with and without the gas of interest in the simulated atmosphere [Grant, 2005]. Equation (4.2 is used to calculate the HCN residual radiance contribution due to HCN emission signatures with values set to 220 pptv at 12 and 15 km in the MIPAS-E band A [Figure 4.9].

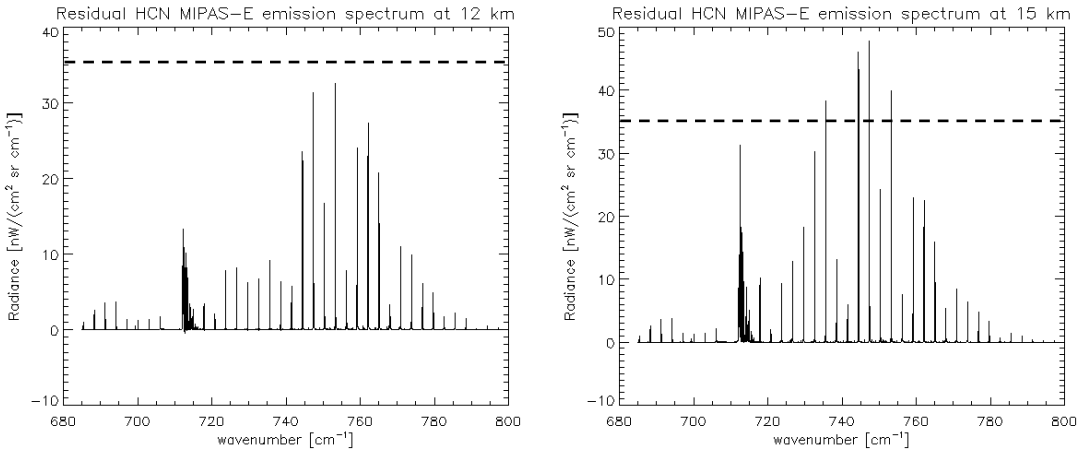

Figure 4.9 Simulated residual HCN radiance contribution in MIPAS-E band A emission spectrum, with HCN background concentrations set to 220 pptv at 12 and 15 km. The black dashed line represents NESR in the 680–800 cm^{-1} MW region.

The HCN emission spectral feature can be detected at 15 km in the 744.300–744.525 744.525 and 746.775–747.825 cm^{-1} MW regions as the two HCN emission lines exceed the MIPAS-E band A mean NESR value of 35.6 and 34.9 nW/(cm^2 sr cm^{-1}) at 15-km nominal altitude [

Figure 3.7 and Figure 3.8] respectively even when the HCN VMR was set to a low value of 220 pptv. The HCN residual radiance contribution at 12 km does not

seem to exceed the NESR value but the emission features may exceed the NESR value with higher concentration levels of HCN at 12 km altitude.

From these results, two MWs 743.000–745.000 and 746.000–748.000 cm^{-1} are chosen for detection purposes. Further refinement of these MWs is based on the MIPAS-E MW selection technique [Dudhia *et al.*, 2002(a)] and more accurate wavenumber regions are listed in the Table 4.2 (described further in Chapter 5). This will help in reducing the computing time for simulations in the automated detection process for HCN emission line signatures.

HCN region	**Start wavenumber (cm^{-1})**	**End wavenumber (cm^{-1})**	**Detection Altitude range (km)**	**Contribution due to other gases**
HCN_0102	744.3000	744.5250	12–24	H_2O(1), CO_2(2), O_3(3), HCN(23), N_2O_5(62), CH_3Cl(24), C_2H_2(26), HNO_3(12), NH_3(11), NO_2(10), CH_6(27), COF_2(29)
HCN_0105	746.7750	747.8250	12–27	H_2O(1), CO_2(2), O_3(3), HCN(23), N_2O_5(62), HNO_3(12), C_2H_2(26), NH_3(11), NO_2(10), COF_2(29), C_2H_6(27)

Table 4.2: Target MWs for HCN emission feature for detection in MIPAS-E emission spectra. Gases that contribute in the MW region are also listed (Numbers in the brackets represent HITRAN-04 molecule ID number). The detection altitude range assumes a higher value of HCN VMR, 550 pptv at 0 to 15 km altitude range.

4.2.4.3 Contribution spectra due to contaminants

This section describes the importance of other trace gases that contribute to the total atmospheric radiance. All the molecules that either emit or absorb radiation contribute to the total atmospheric radiance and thus have specific signatures in the spectral region at a particular altitude level. To understand the influence of other major radiatively active gases in the chosen HCN MW regions, equation (4.2 is applied to plot the contribution radiances due to the interfering gases. Equation (4.2 also provides a good way of understanding the (non-linear) contributions of the interfering gases to the total measured spectrum. Three sets of simulated radiance contribution plots are shown in Figure 4.10-Figure 4.14 based on the tropical extreme minimum, the tropical standard and the tropical extreme maximum climatology conditions respectively.

The Figure 4.10, Figure 4.12 and Figure 4.14 represent the contribution of O_3, CH_3Cl, N_2O_5, HCN and C_2H_2 in the 710–780 cm^{-1} region at 9-, 15- and 21-km levels. The Figure 4.11, Figure 4.13 and Figure 4.15 show individual plots for total radiance and interfering gases such as H_2O, CO_2, O_3, HCN, N_2O_5, CH_3Cl, HNO_3, C_2H_2 and NO_2 in the 710–780 cm^{-1} region at 15 km level. For the minimum case, CH_3Cl and HCN profiles are set to a background concentration values of 400 and 220 pptv (0 to 20 km) respectively. For the extreme maximum case, a CH_3Cl profile was created using ACE-FTS upper tropospheric measurements [Rinsland *et al.*, 2007] of Boreal forest over Alaska and Canada during June–July 2004 and a C_2H_2 profile was created using ACE-FTS upper tropospheric measurements [Rinsland *et al.*, 2005] of tropical fire emissions in South America and Africa during September–November 2004.

HCN emission signatures cannot be detected at the 9 km level since there is either no contribution (tropical standard and extreme maximum) or the contribution is below the noise level (tropical minimum). The contribution plots show the importance of fitting the radiance contributions of the interfering gases in order to detect the HCN spectral signature. The contribution of HCN suggests that the maximum occurs at the 15 km level and decreases with altitude. The major contribution is due to O_3 in the HCN MWs.

Thus, a good knowledge of the VMR profiles of atmospheric parameters is needed in order to detect and retrieve the HCN emission feature in the chosen MWs.

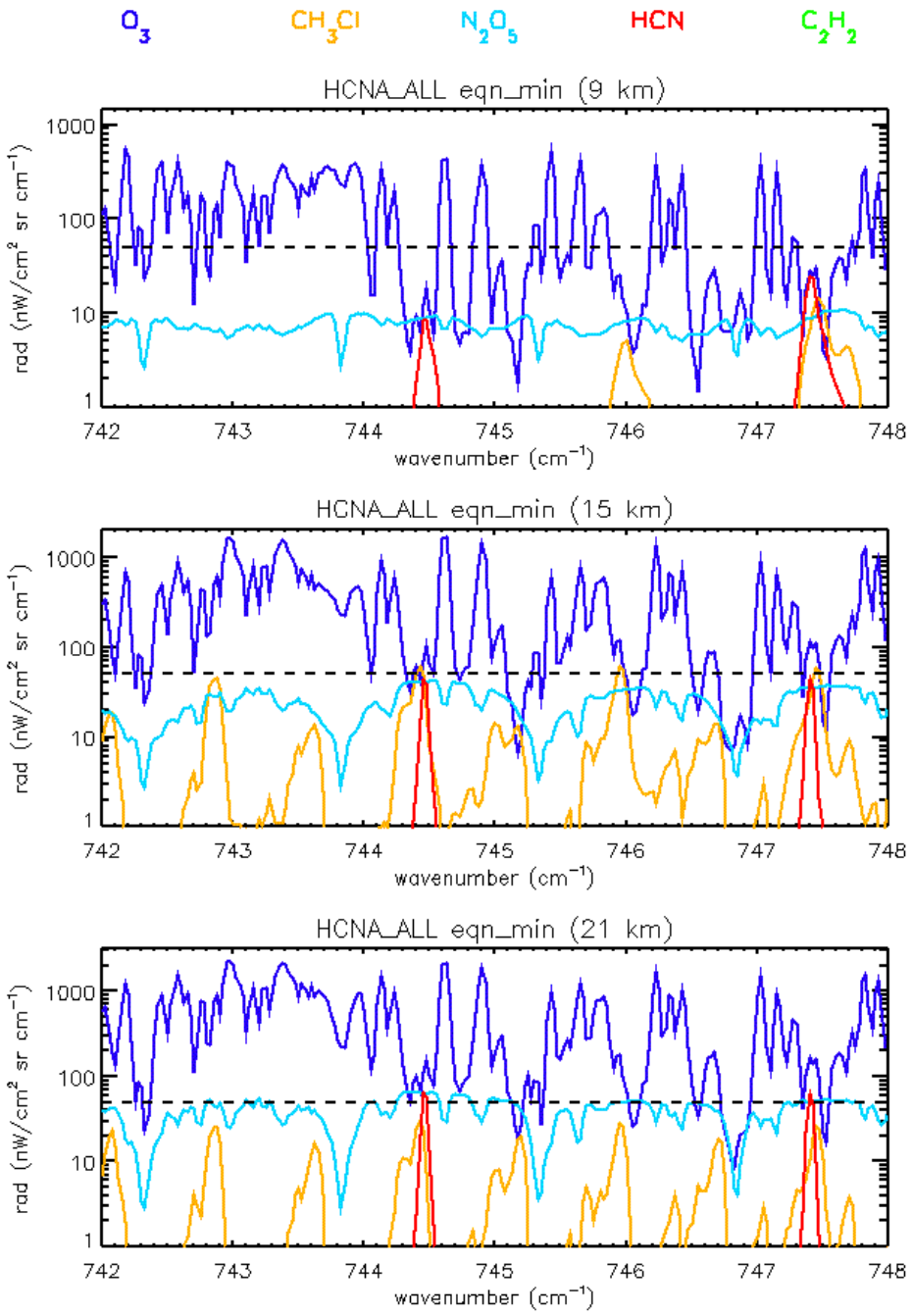

Figure 4.10: Plot of RFM modelled radiances (RFM(all)−RFM(without gas)) for major interfering gases in the 742–748 cm^{-1} region in the tropics (30°N–30°S) using extreme minimum climatology values. The black dotted line represents the expected noise equivalent to the spectral radiance (NESR) of the MIPAS-E, which is based on pre-flight estimates of 50 $nW/(cm^2\ sr\ cm^{-1})$ for band A.

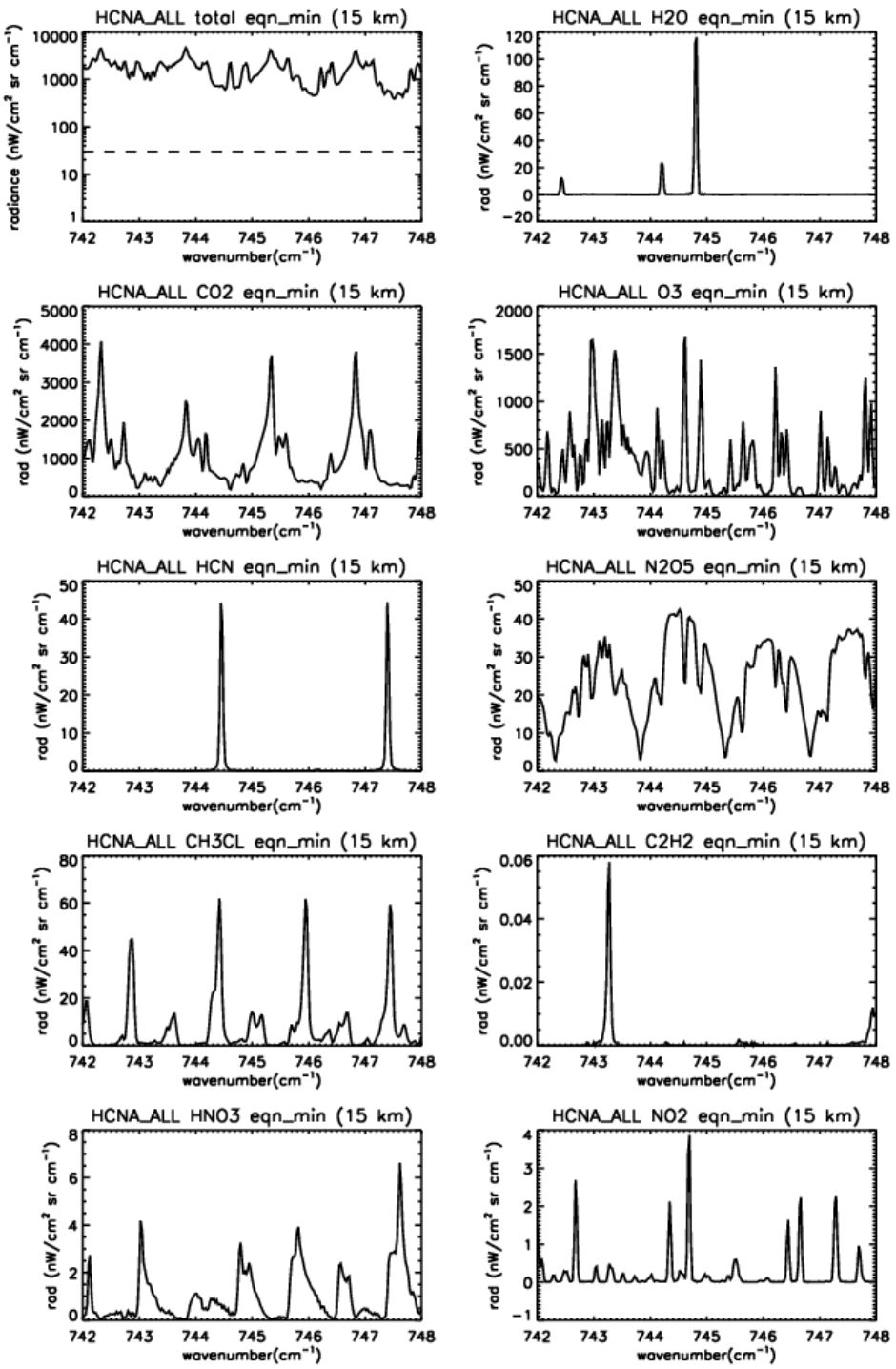

Figure 4.11: Plots of RFM modelled radiance contribution of each gas in the 742–748 cm^{-1} region in the tropics (30°N–30°S) using the extreme minimum climatology values.

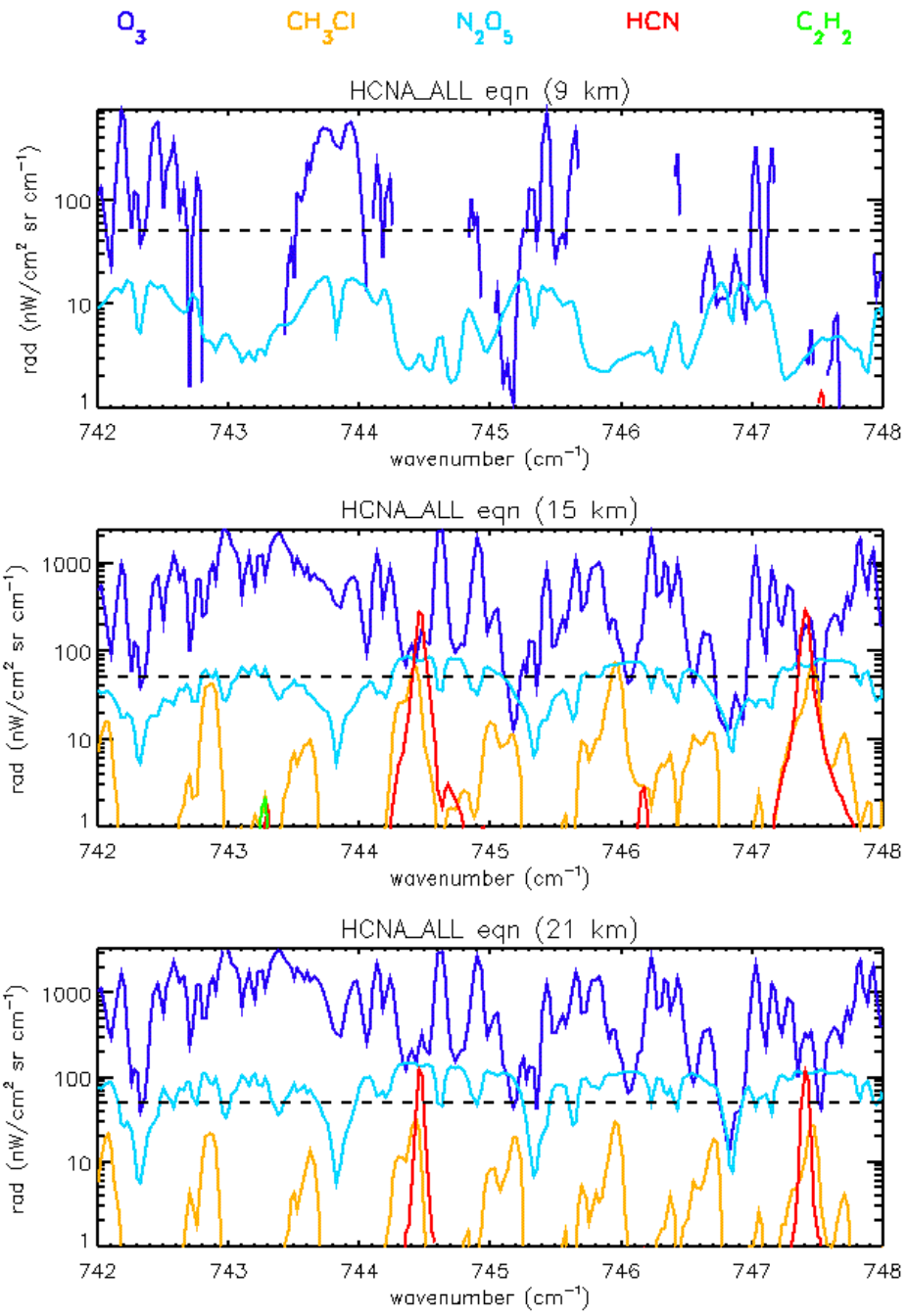

Figure 4.12: Plot of RFM modelled radiances (RFM(all)−RFM(without gas)) for dominant radiatively active gases in the 742–748 cm^{-1} region in the tropics (30°N–30°S) using standard climatology values. The black dotted line represents expected noise equivalent to spectral radiance (NESR) of the MIPAS-E which is based on pre-flight estimates of 50 $nW/(cm^2\ sr\ cm^{-1})$ for band A.

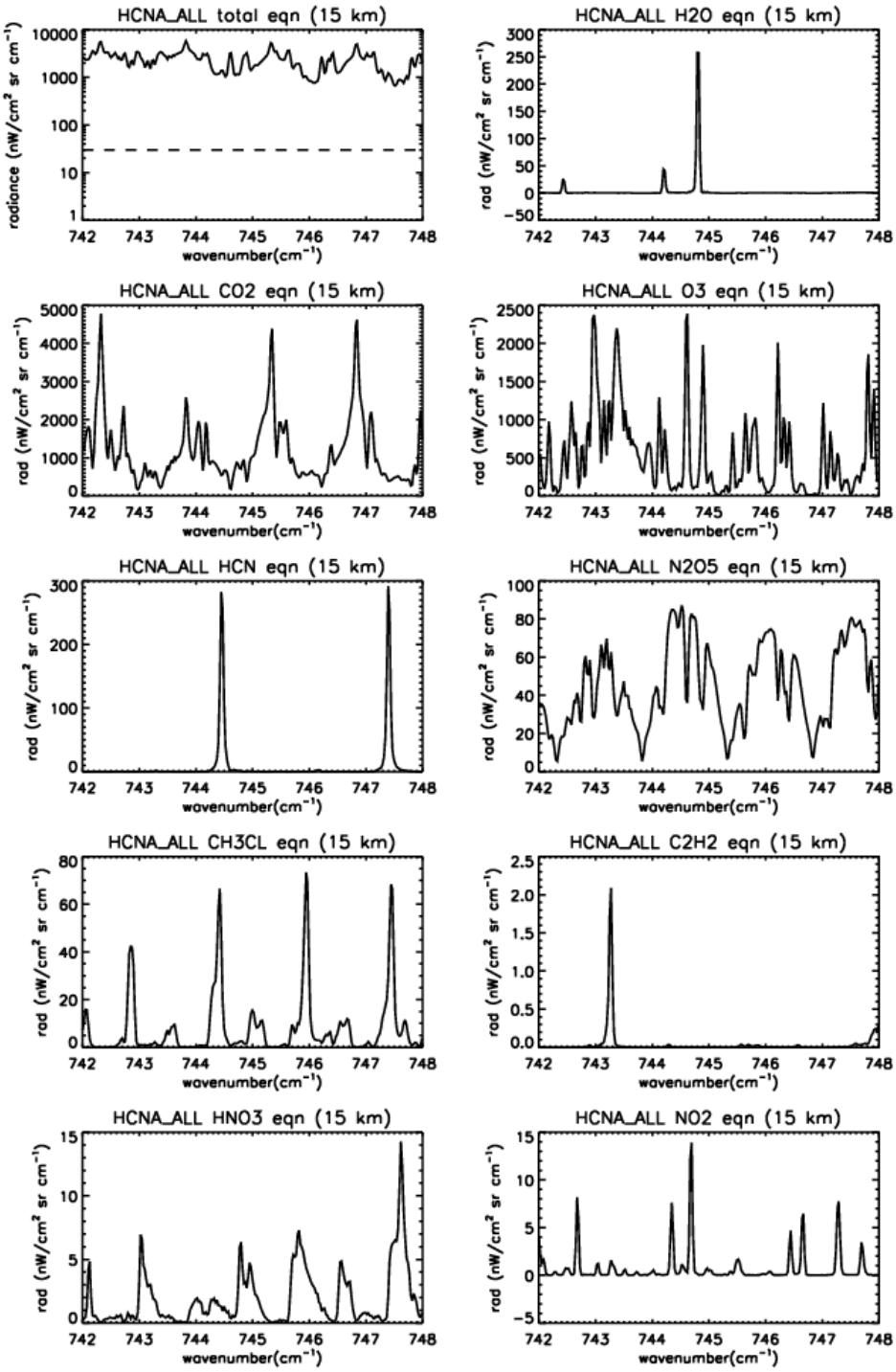

Figure 4.13: Plots of RFM modelled radiance contribution of each gas in the 742–748 cm^{-1} region in the tropics (30°N–30°S) using standard climatology values. (The CH_3Cl profile remains the same for the minimum and standard profile cases)

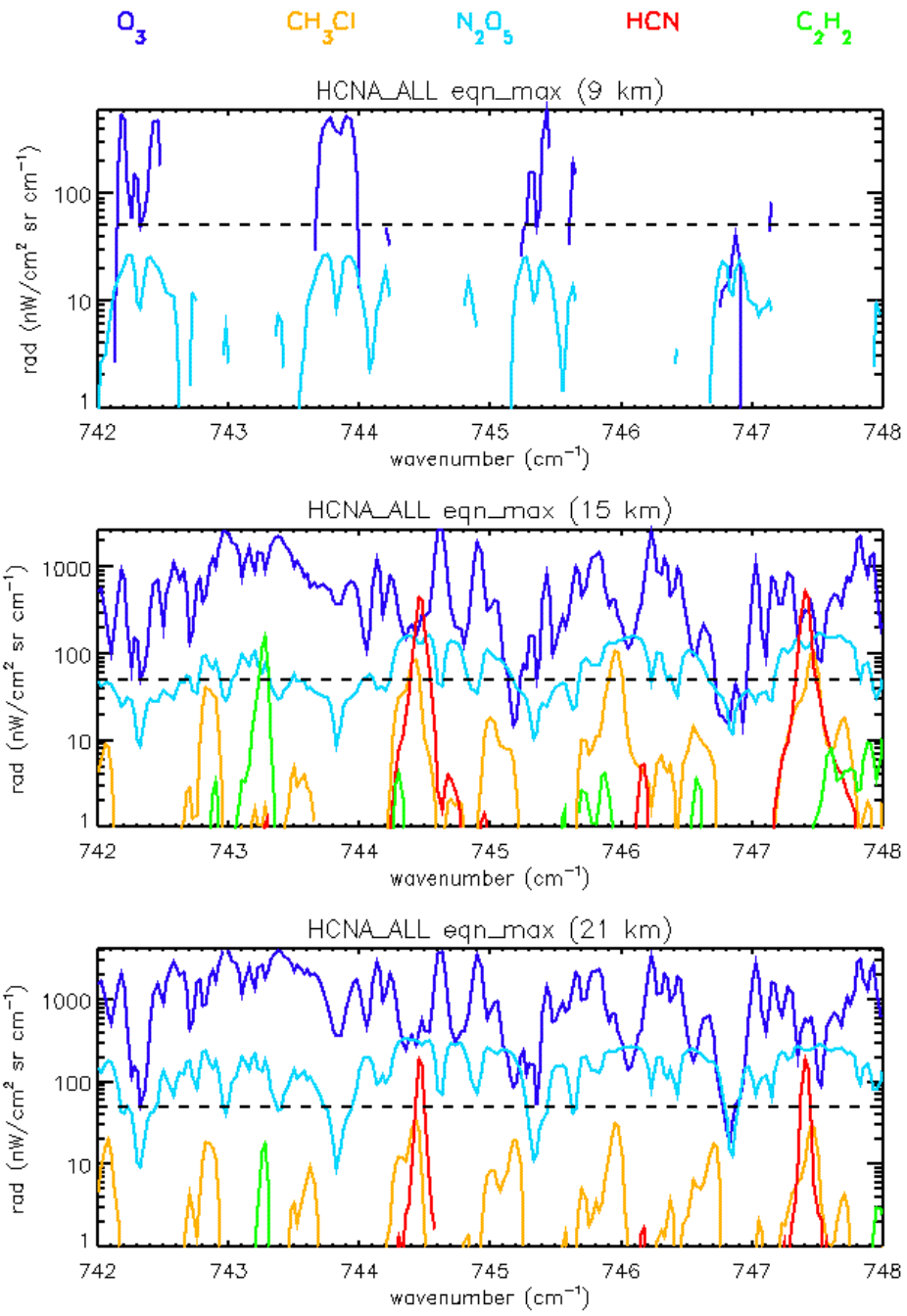

Figure 4.14: Plot of RFM modelled radiances (RFM(all)−RFM(without gas)) for major interfering gases in the 742–748 cm^{-1} region in the tropics (30°N–30°S) using extreme maximum climatology values. The black dotted line represents expected noise equivalent to spectral radiance (NESR) of the MIPAS-E which is based on pre-flight estimates of 50 $nW/(cm^2\ sr\ cm^{-1})$ for band A.

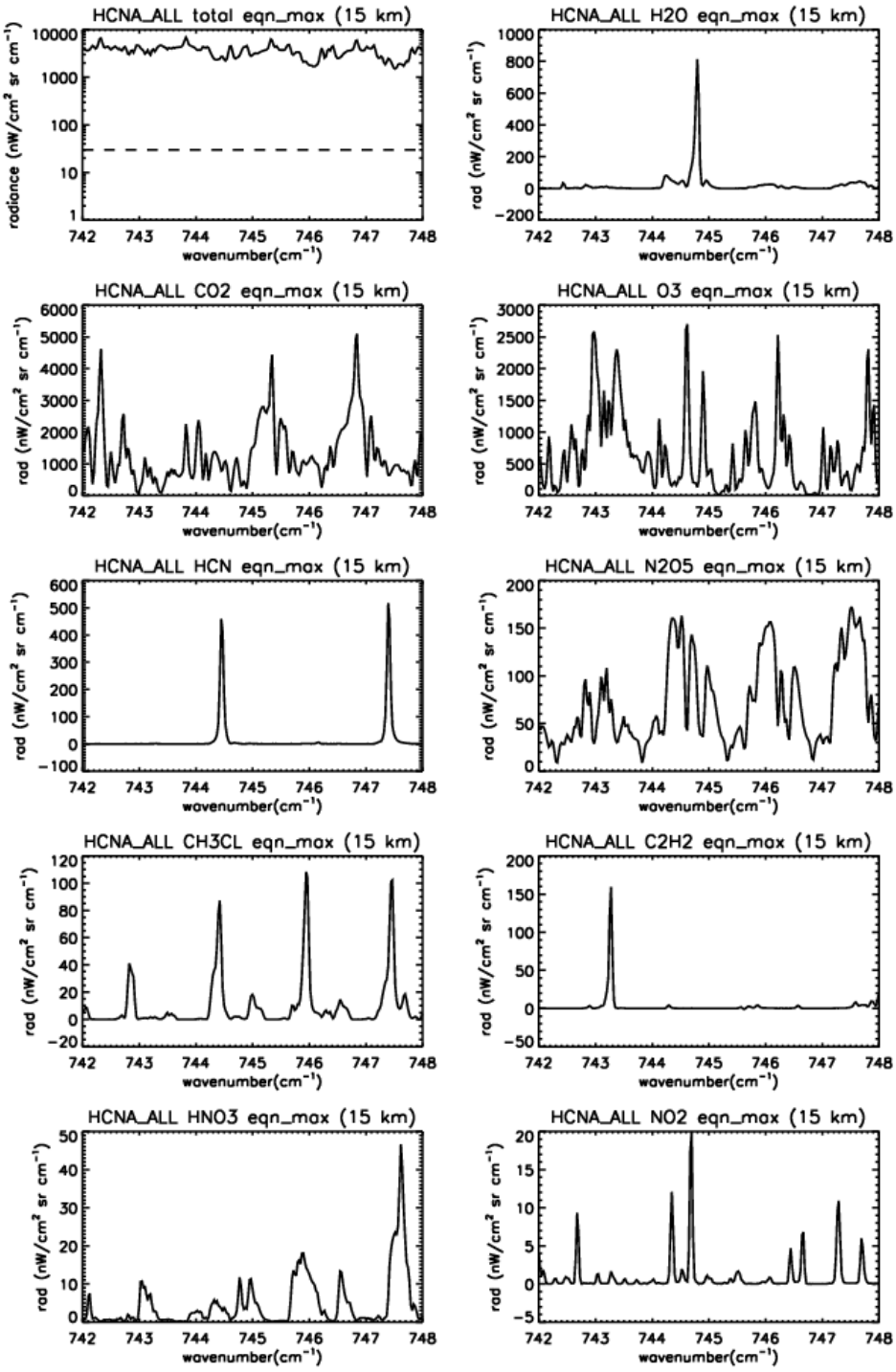

Figure 4.15: Plots of RFM modelled radiance contribution of each gas in the 742–748 cm^{-1} range in the tropics (30°N–30°S) using the extreme maximum climatology values.

4.2.4.4 Weighting functions for HCN candidate regions

The sensitivity of an atmospheric gas relative to altitude and wavenumber can also be studied with the aid of Jacobian spectra simulations; in this study the sensitivity of interfering gases such as H_2O, O_3, HNO_3, N_2O_5, CH_3Cl, N_2O and C_2H_2 are studied in the chosen HCN MWs.

Jacobian spectra are calculated as a difference spectrum at a specified tangent altitude calculated for a change of ±1% in the gas concentration at a specified profile altitude. For pressure and temperature, such Jacobian spectra represent a ±1 mb and ±1 K change respectively, whilst for aerosols, such spectra represent a change of $\pm 1 \times 10^{-4}$ km^{-1} in the extinction coefficient.

The Jacobian plots for the contaminant gases listed in Table 4.2 for HCN_0102 and HCN_0105 are plotted in Figure 4.16 to Figure 4.19. The Jacobian plots in Figure 4.16 and Figure 4.18 are based on standard equatorial profiles. The Jacobian plots in Figure 4.17 and Figure 4.19 are based on the set of extreme maximum values for equatorial profiles.

The Jacobian spectra analysis for the interfering gases O_3 and N_2O_5 show an increase in radiance with the increase in altitude and hence fitting radiances due to these molecules become important with increasing altitude. H_2O perturbations are negligible unless extreme values are present at 12 km for both HCN_0102 and HCN_0105 MW regions.

The CH_3Cl emission line overlaps the HCN feature in both the MW regions and the CH_3Cl peak is very close to the HCN peak at all altitudes. Furthermore, perturbations due to ±1% change in CH_3Cl gas concentration are significant enough to mask the HCN emission feature in both the HCN detection MW regions. Thus, it is important to fit the CH_3Cl line in HCN_0102 and HCN_0105 well enough to detect and retrieve the HCN VMR profiles.

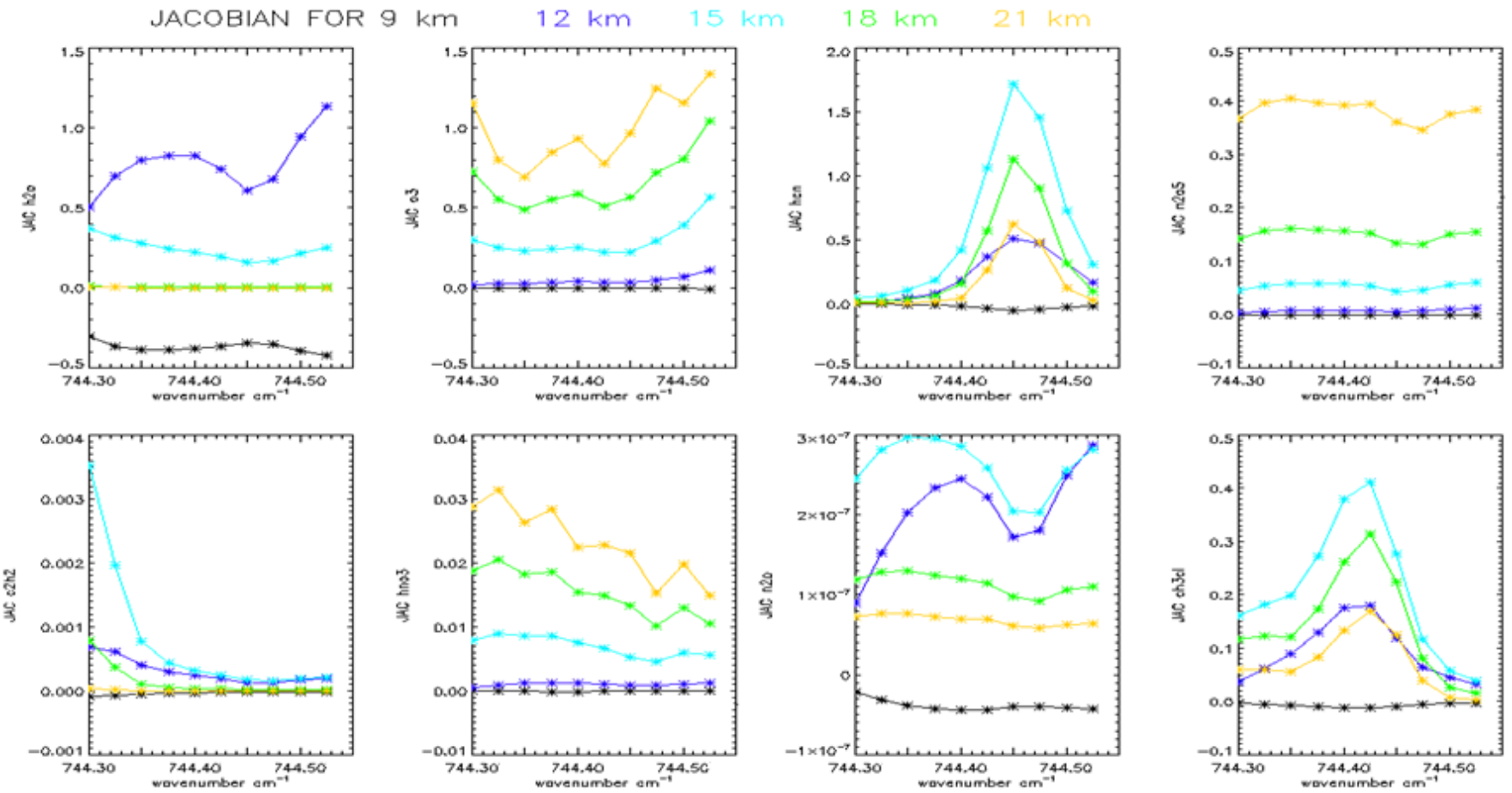

Figure 4.16 : Simulated Jacobian plots for contaminant gases in HCN_0102 spectral region using standard equatorial profiles.

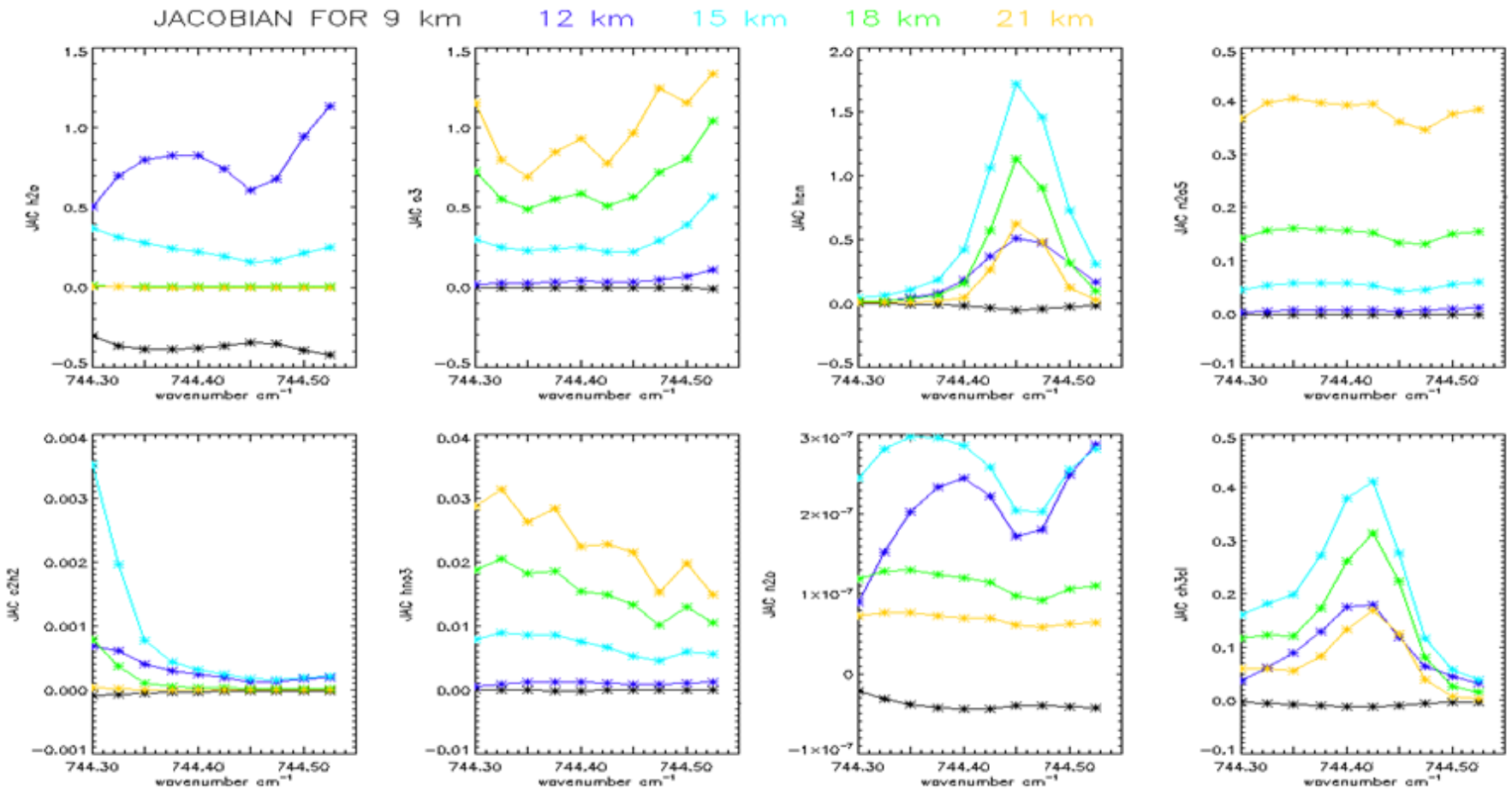

Figure 4.17: Simulated Jacobian plots for contaminant gases in HCN_0102 spectral region using the extreme maximum values for equatorial profiles.

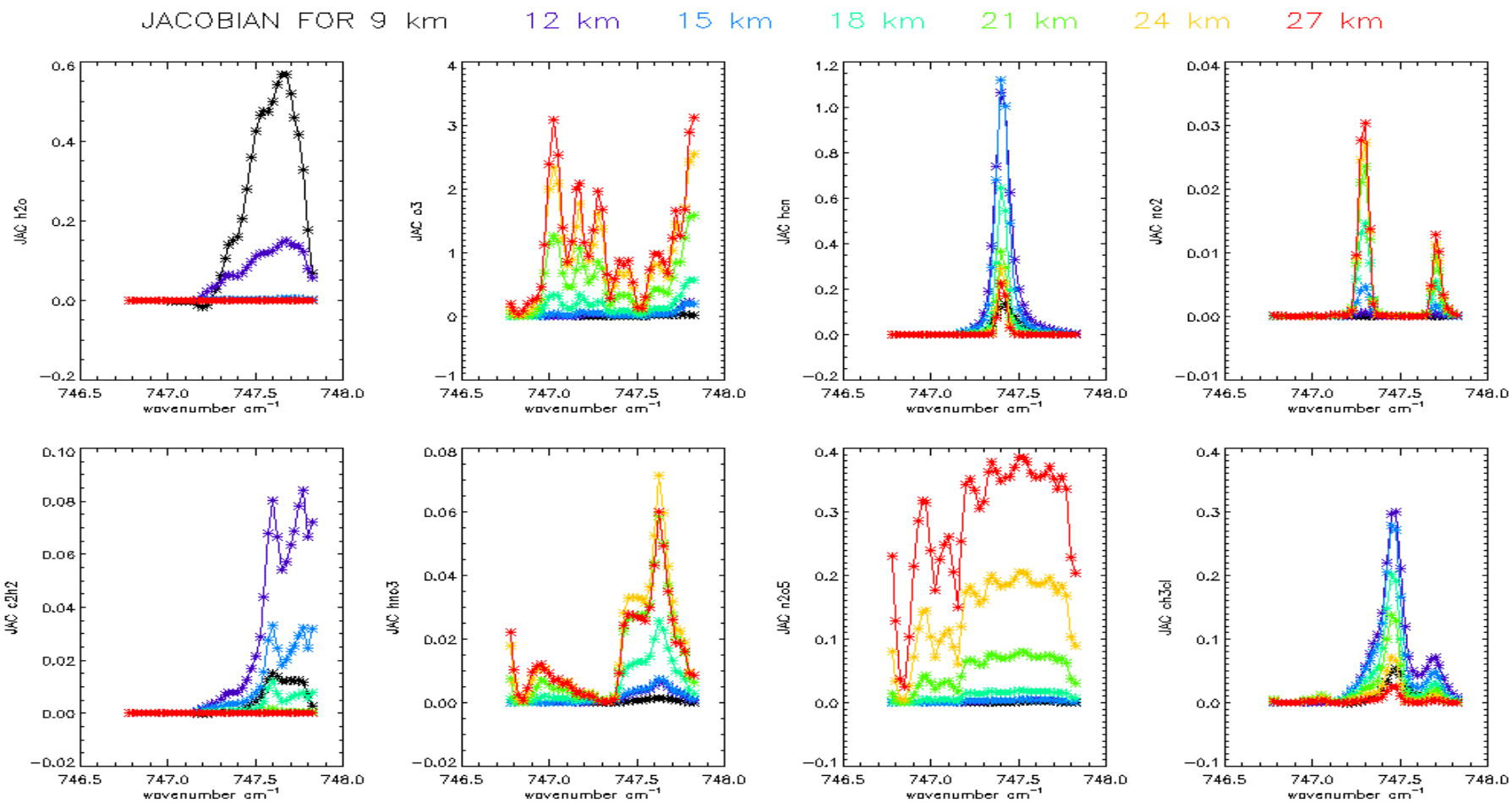

Figure 4.18: Simulated Jacobian plots for contaminant gases in HCN_0105 spectral region using standard equatorial profiles.

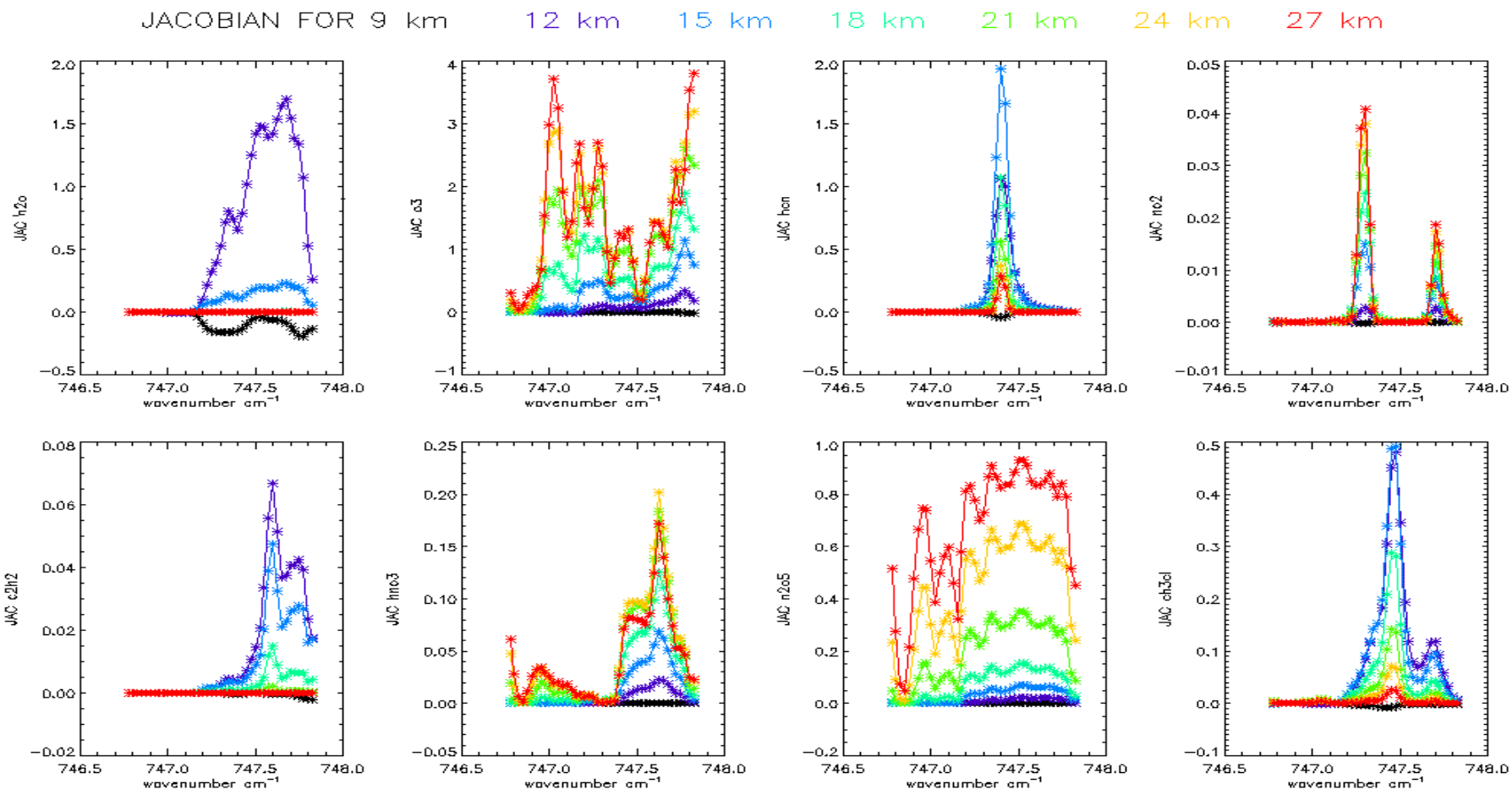

Figure 4.19: Simulated Jacobian plots for contaminant gases in HCN_0105 spectral region using the extreme maximum values for equatorial profiles.

4.2.4.5 Spectroscopy of HCN molecule in the selected regions

There are two primary databases for spectral parameters, HITRAN and GEISA that provide distinctly different results in terms of both line strengths and positions as shown in the Figure 4.20–Figure 4.24. The accuracy of retrieved atmospheric properties depends on the quality of any available spectral databases. There may be inadequate reference spectral data as there are many problems encountered in the laboratory when trying to measure the atmospheric species. The Table 4.3 explains the difference between the two databases for HCN molecule line parameters.

Spectral database	HCN ID	# of bands	Isotopologue	# of lines	Total # of lines	Spectral coverage	
						Minimum wavenumber (cm^{-1})	Maximum wavenumber (cm^{-1})
GEISA-03	27	41	124 134 125	2250 185 115	2550	2.956 2.880 2.870	18407.973 9627.961 9671.953
HITRAN-04	23	30	124 134 125	2955 652 646	4253	0 2 2	3424 3405 3420

Table 4.3: Comparison between GEISA-03 and HITRAN-04 spectral database for HCN molecule.

Gestion et Etude des Informations Spectroscopiques Atmosphériques (GEISA): The management and study of atmospheric spectroscopic information were developed in 1974. The entries are spectroscopic parameters required to describe adequately the individual spectral lines belonging to 42 molecules (96 isotopic species) and located between 0 and 22,656 cm^{-1}. The GEISA database [Jacquinet-Husson N *et al.*, 2008] will update the 2008 edition by replacing the whole content for HCN molecule line parameters.

The HIgh-resolution TRANsmission molecular spectroscopy (HITRAN) database was created in response to the need of an agreed and consistent database to be used by the scientific community for detailed infrared properties of the Earth's atmosphere. It was first published in 1973 and provides fundamental spectroscopic parameters for atmospheric radiance calculations used in the simulation and retrieval processes. The line-by-line portion of the database contains spectroscopic parameters for 39 molecules, including many of their isotopologues. The results in this thesis require cross-section information that is used from HITRAN 2004 edition [Rothman *et al.*, 2004].

The work of Rinsland *et al.* [2003], Devi *et al.* [2004; 2006] and Rinsland *et al.* [2003] led to the improvements of spectral data for the three HCN isotopologues which were applied to the HITRAN 2004 database in the pure-rotation region and the infrared from 500 to 3425 cm^{-1}, ignoring transitions appearing at wavenumbers larger than 3425 cm^{-1}. The amount of HCN data was increased from 772 transitions [Maki *et al.*, 1996] in HITRAN 2000 to 4253 transitions in HITRAN 2004 [Devi *et al.*, 2005].

Air-broadened half-widths, self-broadened half-widths, the exponent in the formula for the temperature dependence of the air-broadened half-width and air pressure-induced line shifts were updated using polynomials to fit the 54 P- and R-branch transitions in the ν_2 band of $H^{12}C^{14}N$ centred at 712 cm^{-1}. No Q branch lines were included in the study done by Devi *et al.* [2005].

Line positions for the ν_2 band of HCN reported in HITRAN 2000 differ by 0–0.0025 cm^{-1} from previous calculations done by Maki *et al.* [1996] and measurements reported in HITRAN 2004. The absolute uncertainty in line intensity measurement (HITRAN 2004) is about 2% and the maximum intensity difference (%) between HITRAN 2004 and HITRAN 2000 is about 30%. The vibrational band intensity (S_ν) and the integrated band intensity (S_{band}) determined for ν_2 band is 264.4 ± 0.1 and 259.59 cm^{-2} atm^{-1} respectively, measured at 296 K. The integrated band intensity in HITRAN 2004 is 10% higher than the previously computed value of 156 cm^{-2} atm^{-1} [Maki *et al.*, 2000; 2002].

Self- and air-broadening coefficients were determined by fitting 54 HCN transitions in the P and R branches (Q branch lines remained unresolved and, hence, were excluded from the study). The air-broadening coefficients vary from 0.08 to 0.14 cm^{-1} atm^{-1} at 296K; the self broadening coefficients range between 0.2 and 1.2 cm^{-1} atm^{-1} at 296K as a function of the rotational quantum number index |m|. To calculate these coefficients the RMS (observed-calculated) difference used to fit the three bands (ν_1, ν_2 and $2\nu_2$) of HCN was 1.2% and 0.6% for air-broadening and self-broadening coefficients respectively. Air pressure induced line shift has been set to zero as calculations were not made and new measurements were needed in the ν_2 band. The measured values of the temperature-dependence exponent for air-broadening in HITRAN 2004 range from ~0.85 to 0.70, whereas HITRAN 2000 assumed a value of 0.5 for all HCN lines.

The air-broadened half-width parameters were recalculated by fitting together parameters from ν_1, ν_2 and pure rotational bands of HCN [Yang *et al.*, 2008] since the constant air-broadened half-width with a value of 0.088 cm^{-1} atm^{-1} was overestimated for higher rotational quantum numbers (|m| > 30). The standard deviation calculated by the polynomial fit for air- and nitrogen-broadened half-widths is 0.0024 and 0.00313 respectively. For |m| > 40, a constant air-broadened half-width of 0.0518 cm^{-1} atm^{-1} is assigned (HITRAN 2008).

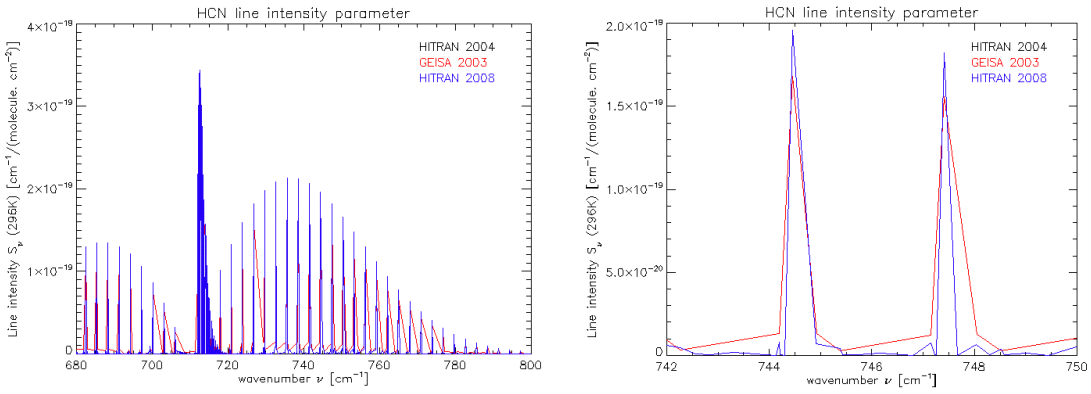

Figure 4.20: Comparison of HITRAN 2004, GEISA 2003 and HITRAN 2008 data for HCN spectral line intensity parameters in MIPAS-E band A (left) region and for individual lines in 742–750 cm^{-1} (right) region. HITRAN-08 data (blue) overlaps HITRAN-04 data (black) and no difference is observed.

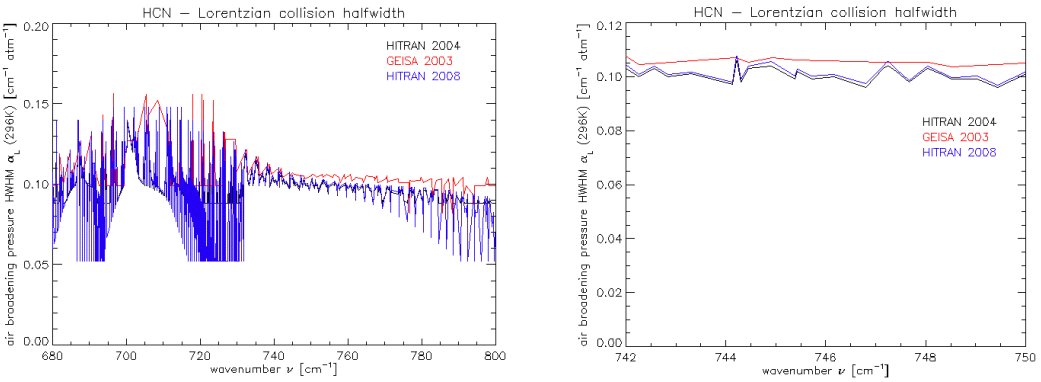

Figure 4.21: Comparison of HITRAN 2004, GEISA 2003 and HITRAN 2008 data for Lorentzian collision halfwidth parameter of HCN in MIPAS-E band A (left) region and for individual lines in 742–750 cm^{-1} (right) region.

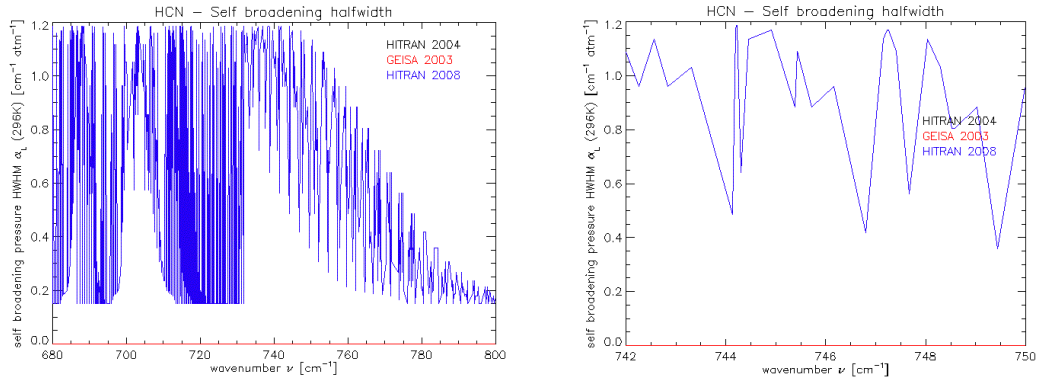

Figure 4.22: Comparison of HITRAN 2004, GEISA 2003 and HITRAN 2008 data for Self broadening halfwidth parameter of HCN in MIPAS-E band A (left) region and for individual lines in 742–750 cm^{-1} (right) region. HITRAN -08 data (blue) overlaps HITRAN-04 (black) and no difference is observed.

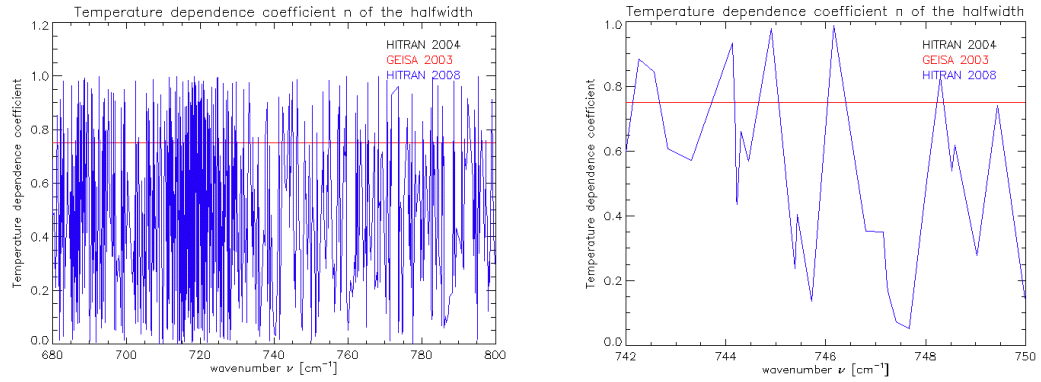

Figure 4.23: Comparison of HITRAN 2004, GEISA 2003 and HITRAN 2008 data for temperature dependence coefficient n of air broadened halfwidth in MIPAS-E band A (left) region and for individual lines in 742–750 cm^{-1} (right) region. HITRAN -08 data (blue) overlaps HITRAN-04(black) and no difference is observed. GEISA-03 data is set to a constant value of 0.75.

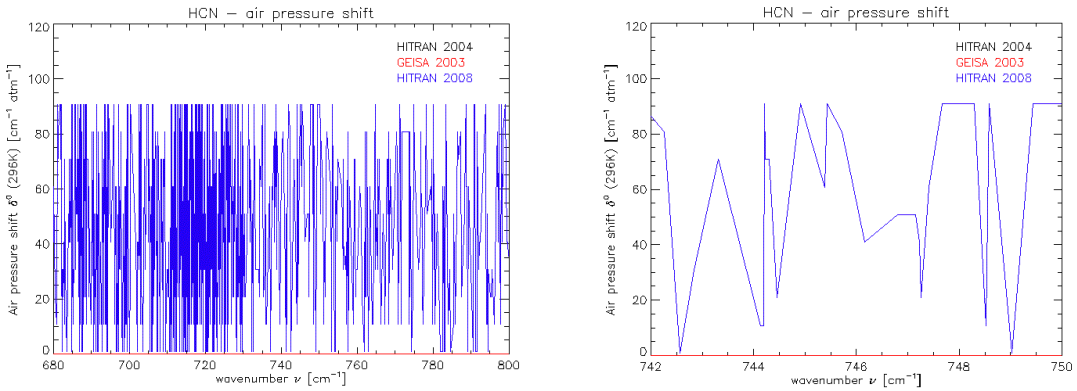

Figure 4.24: Comparison of HITRAN 2004, GEISA 2003 and HITRAN 2008 data for air pressure shift in MIPAS-E band A (left) region and for individual lines in 742-750 cm^{-1} (right) region. HITRAN -08 data (blue) overlaps HITRAN-04 (black) and no difference is observed in 742–750 cm^{-1} between HITRAN-04 and HITRAN-08 data. Data for air pressure shift in GEISA-03 database does not exist.

To reduce errors in radiative transfer calculations, one requires accurate and precise measurements of spectral parameters related to a particular gas. For very small HCN VMR values in the atmosphere (0.18 pptv) the self-broadening and self-shift coefficients are not critically important for atmospheric studies. However, for the detection purposes, the intensity parameters are necessary for interpreting the Earth's atmospheric data acquired from remote sensing instruments.

Figure 4.20 to Figure 4.24 show the difference between the spectral parameters of HCN in the two primary databases, HITRAN [2004; 2008] and GEISA [2003]. The measured intensity parameter is lower in the case of the GEISA-03 database when compared to the HITRAN-04 and HITRAN-08 databases, as shown in Figure 4.20. The positions of the two line centres of HCN in desired MWs remain the same for all the three databases. A difference can be observed in the Lorentzian collision halfwidth parameter, but no significant difference can be seen in the HCN_0102 and HCN_0105 MWs.

Self-broadening half-width, temperature dependence coefficient n of air-broadened half-width, air-pressure-shift parameters remain the same for both the HITRAN-04 and HITRAN-08 databases [Figure 4.21 to Figure 4.23]. No data is available for the self-broadening halfwidth, temperature dependence coefficient n of air-broadened half-width and air-pressure-shift parameters in GEISA-03 database.

The temperature dependence coefficient n of air-broadened half-width in GEISA-03 database is set to 0.75.

The temperature dependence of self-broadening, self-inducedshifts and air-induced shifts is not currently available in the HITRAN-04 database. This study includes data from HITRAN-04 for performing simulations to detect the HCN emission feature and retrieve HCN VMR profiles.

4.2.5 Step 5: Instrument's limiting factors for HCN feature detection

4.2.5.1 Instrument line shape (ILS)

Figure 4.25 shows the comparison of the effects due to ILS on simulated radiances and the MIPAS-E spectrum. The black spectra represent simulated radiance calculations with no ILS information included, red spectra represent simulated radiance calculations with apodised ILS information computed for the spectral band A of MIPAS-E and blue spectra represent the MIPAS-E spectrum with the apodised ILS function. The spectral lines are truncated as a result of convoluting the atmospheric spectrum with an ILS function and loss of spectral features and spectral resolution can be seen in the spectral bands. In addition, the apodised ILS (AILS) degrades the measured spectrum.

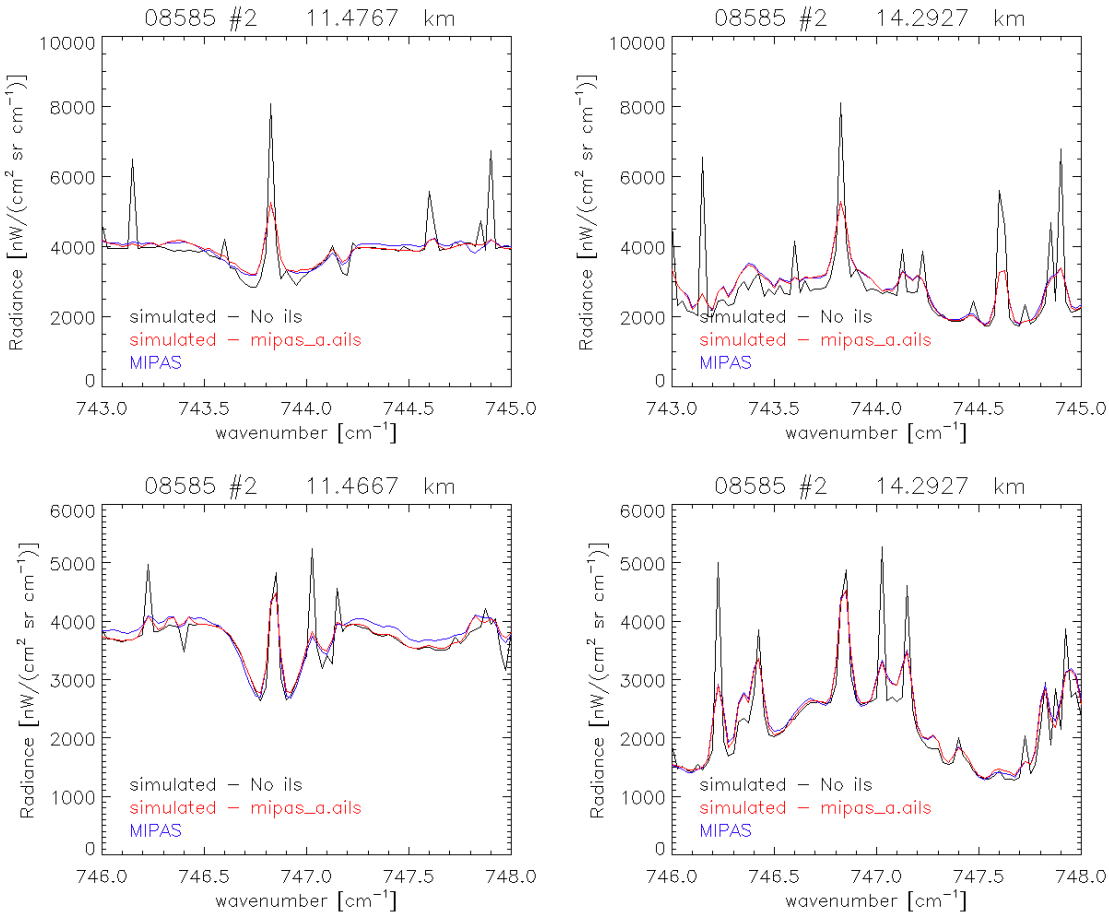

Figure 4.25: Comparison of MIPAS-E emission spectrum and simulated spectrum calculated with and without MIPAS-E ILS for the two MW regions HCN_0102 (top) and HCN_0105 (bottom) Blue-MIPAS-E emission spectrum obtained from 08585 orbit scan#2; Black-Simulated radiance using no ILS information; Red-Simulated radiance including ILS information for MIPAS-E band A at 12 km nominal altitude (left) and 15 km nominal altitude (right).

4.2.5.2 Instrument's spectral resolution

Figure 4.26 shows the effect on HCN spectral feature due to the spectral resolution of the instrument. The black spectra represent simulated radiances based on the MIPAS-E full resolution of 0.025 cm^{-1}, and blue spectra represent simulated radiances based on a higher resolution of 0.01 cm^{-1}. The ILS is not included in the simulated radiance calculations. Figure 4.26 shows that MIPAS-E cannot resolve many lines in the HCN_0102 and HCN_0105 MW regions and the same is true for all the five spectral bands of MIPAS-E.

Thus, in effect, one can say that instruments such as ACE-FTS with a high spectral resolution of 0.02 cm^{-1} have better resolving power than MIPAS-E. At the same time, we can say that the MIPAS-E full spectral resolution mode has higher resolving power when compared to the MIPAS-E optimized spectral resolution of 0.0625 cm^{-1} mode as well as the Infrared Atmospheric Sounding Interferometer (IASI) instrument with a spectral resolution of 0.35–0.5 cm^{-1}.

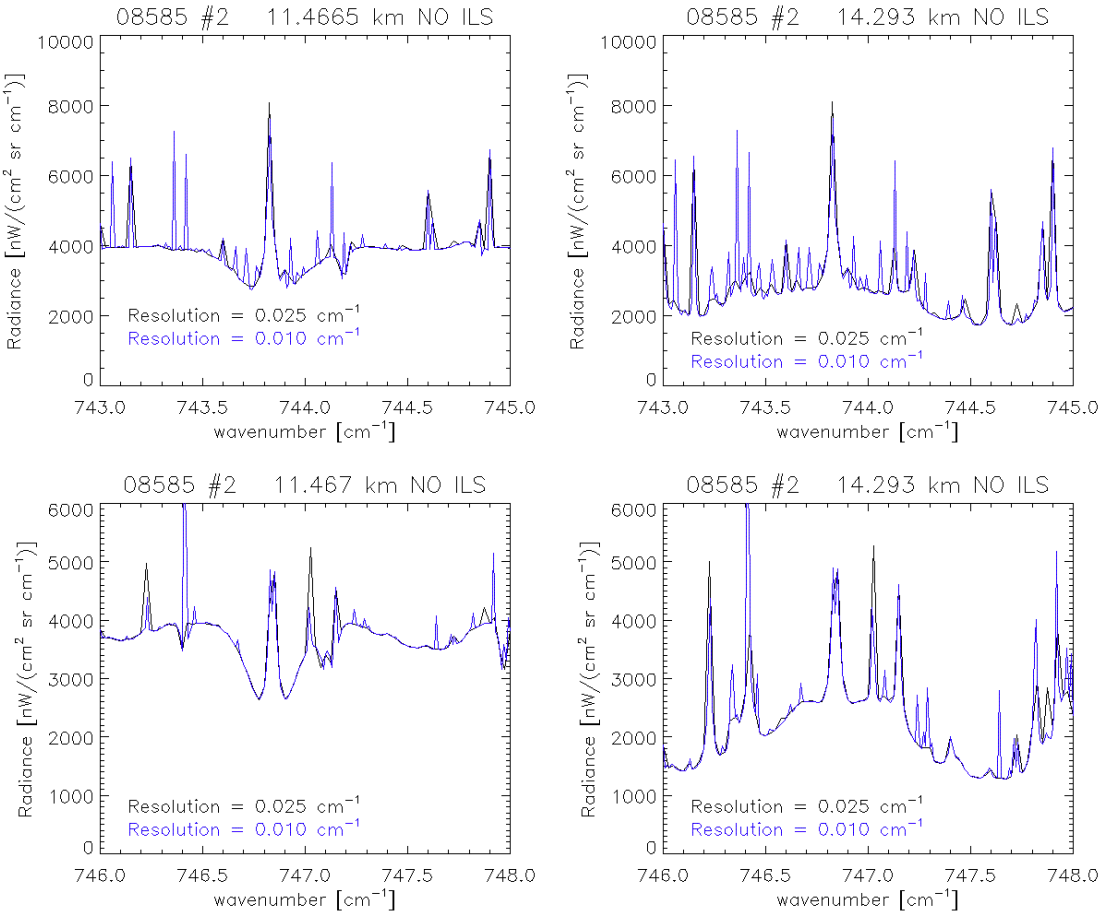

Figure 4.26: Comparison of simulated spectra calculated using low and high spectral resolutions. No ILS is included for the two MW regions HCN_0102 (top) and HCN_0105 (bottom). Black-Simulated radiance using 0.025 cm^{-1} spectral resolution; Blue-Simulated radiance using 0.010 cm^{-1} spectral resolution at 12 km nominal altitude (left) and 15 km nominal altitude (right).

4.2.5.3 Apodisation function

Figure 4.27 and Figure 4.28 show the effects on the HCN emission feature as a result of the apodisation function. The black spectra represent MIPAS-E

unapodised spectra and red spectra, apodised spectra. The MIPAS-E spectra are plotted in the range 685–970 cm^{-1} at 12- and 15-km tangent altitudes as shown in Figure 4.27: the unapodised and apodised spectra differ in spectral intensity. Figure 4.28 shows finer effects of apodisation in the HCN_0102 and HCN_0105 MW regions at 12- and 15-km nominal altitudes.

Effects of the apodisation function can be seen in Figure 4.27. It can be easily noted that many spectral features are lost, and the amplitude of each spectral feature is further reduced. The apodisation effects are true for each spectral band of MIPAS-E. The spectral features due to the weak absorbing molecules in any particular MIPAS-E wavenumber will be lost and, thus, detection of such molecules will be difficult. The MIPAS-E L1B spectral data used in this thesis are apodised by applying the Norton-Beer function before the detection of HCN spectral signature and the retrieval of HCN VMR profiles.

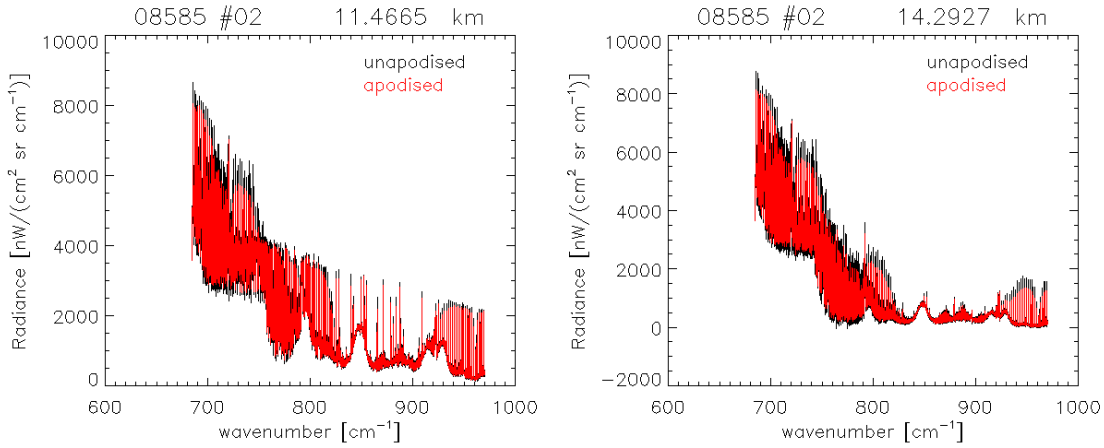

Figure 4.27: Comparison of unapodised and apodised MIPAS-E emission spectra at 12- and 15-km nominal altitudes for MIPAS-E orbit 08585 scan#2.

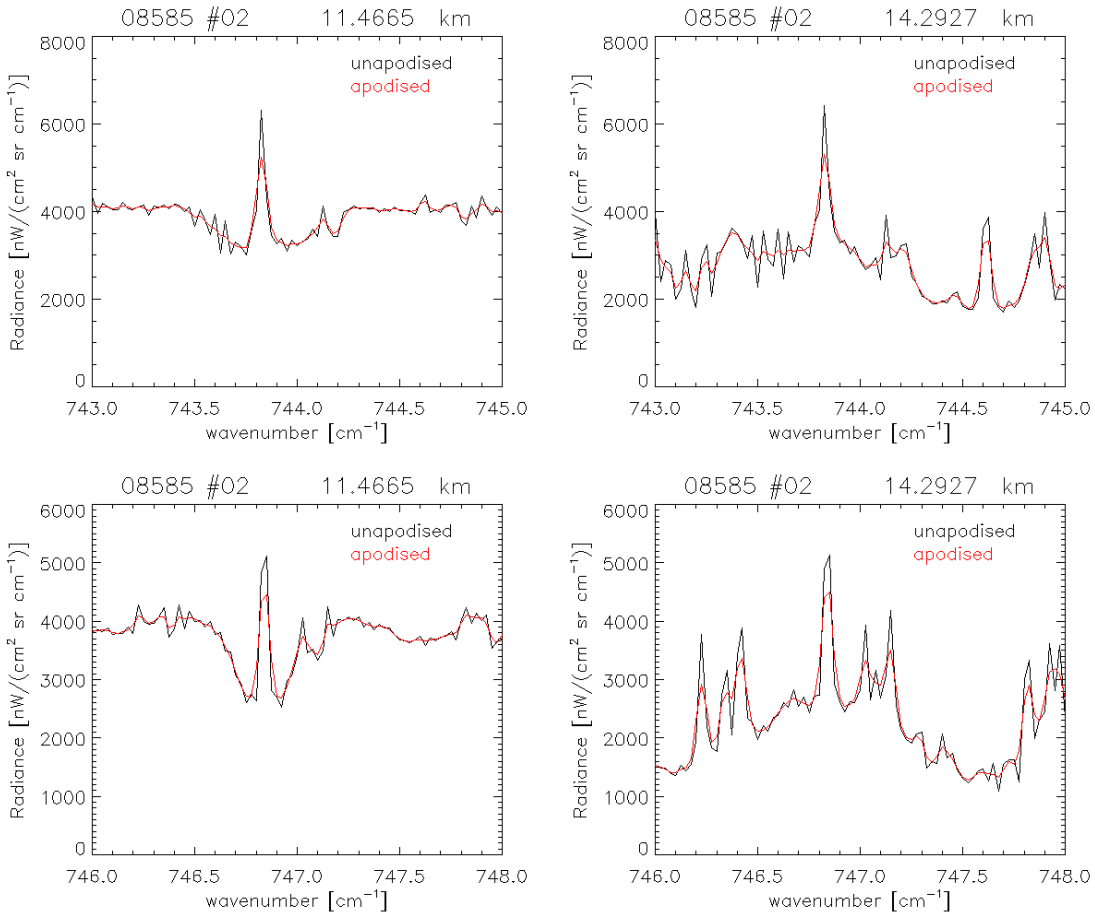

Figure 4.28: Comparison of unapodised and apodised MIPAS-E emission spectra at 12- and 15-km nominal altitudes for MIPAS-E orbit 08585 scan#2 in HCN_0102 and HCN_0105; magnified view for HCN_0102 region-744.300–744.525 cm^{-1} (top) and HCN_0105 region-747.350–747.500 cm^{-1} (bottom).

4.2.6 Step 6: Detection results of HCN limb emission signature in biomass burning plume

This section first presents the results of HCN emission feature detection in biomass burning plume using MIPAS-E level 1 data from orbit 08585-scan #2 at 11.5-,14.3- and 17.2-km over East Africa (11.7410°S, 36.8764° E) on 21 October 2003. This allows the deduction of further evidence of HCN emission signatures from MIPAS-E spectral data for the month of October 2003.

Previous sections have shown that in order to detect the HCN spectral features, we will have to reduce the effects of major interfering gases in both

HCN_0102 and HCN_0105 MW regions. The residual method described in section 4.1 is used to carry out the detection. Simulations are carried out with and without the presence of HCN in both HCN_0102 and HCN_0105 MW regions at 9-, 12- and 15 km MIPAS-E nominal altitudes. The residual features were compared to detect HCN spectral features.

To simulate the atmospheric spectrum for MIPAS-E orbit 08585 scan#2 level 2 retrieved MIPAS-E parameters such as H_2O, O_3, HNO_3, along with pressure, temperature are used as inputs in the forward model radiative transfer calculations. For MIPAS-E, level 2 profiles provide a good initial guess to the simulated atmosphere. Other interfering gases were not operationally retrieved and profile information for all these gases is obtained from reference atmospheres. C_2H_2 VMR profile data were retrieved using Oxford's MORSE retrieval algorithm to provide an initial guess which was fed in the forward model calculations. For rest of the atmosheric parameters or profiles for the other interfering gases are specified in Section 4.2.6.2.

4.2.6.1 Comparison of measured and simulated spectra

The detection of HCN depends on the clear observation of a distinguishable HCN spectral signature in the residual spectrum. A measured residual spectrum (ΔY) is calculated as the difference of the measured spectrum from the simulated spectrum without HCN. ΔX is compared with the residual spectrum (ΔY), which is calculated as a difference of the simulated spectrum with HCN and the simulated spectrum without HCN. The comparison yields the quality of spectral fitting as well as the level of confidence in detection of HCN. The quality of spectral fit depends on the accuracy of atmospheric profiles of infrared species which represents the true state of the atmosphere.

Tangent altitudes between nominal altitudes of 12- and 15-km are most likely to be of interest for HCN detection. Simulated spectra are calculated at tangent altitudes from level 1b data for the corresponding profile. Before automating the detection technique, examples of simulated MIPAS-E spectra at 9-, 12- and 15-km MIPAS-E nominal tangent altitude for 710–780 cm^{-1} in five different latitude bands

are taken into consideration; these are plotted in Sections 4.2.6.3.1 to 4.2.6.3.5 together with simulated the residual spectra for HCN at a concentration of 550 pptv.

4.2.6.2 Simulated spectra

The success of HCN detection is based on the comparison of measured (ΔY) residual spectra and simulated (ΔX) residual spectra. Simulations are carried out using the Oxford RFM. The RFM driver table set up is as follows:

1. An altitude grid is constructed for 0–120 km in steps of 3 km, substituted with the retrieved level 2 altitude values where they are operationally retrieved for MIPAS-E.
2. Standard reference atmosphere profiles are used for other spectrally important gases listed in Table 4.2.
3. MIPAS-E operational level 2 data for pressure, temperature and H_2O, O_3 and HNO_3 VMRs were used for the 6–68 km MIPAS-E nominal altitude ranges.
4. MORSE retrieved C_2H_2 VMR profiles are used as inputs.
5. Additional profiles for species that are not included in reference atmospheres are available using Fast Atmospheric Signature Code (FASCODE; [Smith et al., 1978]) for species such as F13, F21, F113, F114, F115 and CH_3Cl.
6. Tangent altitude selection is based on MIPAS-E 9-,12- and 15-km nominal altitudes for the detection of HCN.
7. A trapezium-like FOV 2.8-/4-km (top/base) at 5 pt resolution is used for MIPAS-E radiance simulations. The FOV is not dependent on spectral points and one FOV is used for each RFM simulation.
8. Spectral parameters for contributing gases in the 710–780 cm^{-1} and the HCN_0102 and HCN_0105 MWs were based on the HITRAN 2004 database.
9. Voigt lineshapes are used for all the absorbers (interfering gases in HCN_0102 and HCN_0105 MWs). Currently, the chi-factor (CHI) lineshape is used for CO_2, which represents sub-lorentzian wings of CO_2.
10. Simulations are performed, one with HCN gas included and the other without HCN in the 710–780 cm^{-1} spectral range with a spectral resolution of 0.025

cm^{-1}. Similarly simulations are repeated for H_2O, CO_2, O_3, N_2O_5, CH_3Cl, HNO_3 and C_2H_2 and aerosol extinction.

11. The simulated (ΔX) residual spectrum acts as the expected residual signature of HCN i.e. the difference between the simulated spectrum with HCN and the simulated spectrum without HCN.
12. The atmospheric radiance is convolved using an AILS specific to MIPAS-E spectral bands. The Norton-Beer strong function is used as the apodising function.

4.2.6.3 Detection results

In this section, results of the comparison of measured and simulated atmospheric limb emission spectra for MIPAS-E are shown. The following results are based on the availablity of the MIPAS-E level 1b spectral data as wide range of spectral range is required along with matching MIPAS-E operational level 2 data products (pressure, temperature and H_2O, O_3 and HNO_3 VMRs) and the MORSE retrieved C_2H_2 VMR profiles. To ensure the consistency of MIPAS-E data used in the simulations, the MIPAS-E level 1b, level 2, cloud index files and MORSE retrieved C_2H_2 VMR profiles are matched using the unique time ID attached to each measurement. The data is cloud filtered using the Spang *et al.* [2004] cloud detection technique for the MIPAS-E data.

The quality of the MIPAS-E operational level 2 parameters such as pressure, temperature, and H_2O, O_3 and HNO_3 VMR profiles are tested against the quality flag set that are used in the simulations. The MORSE retrieved data products are sequentialy retrieved after jointly retrieving pressure and temperature. Thus, the MORSE retrieved parameters such as pressure and temperature and C_2H_2 VMR profiles, are quality tested at the lowermost altitudes in the UTLS region. The MORSE retrieval process and testing the quality of the MORSE retrieved data are described more in detail in Chapter 5 [Section 5.1 to 5.4]

The spectral fits and corresponding residual fits, for five different latitude bands (viz.: tropics, mid-latitude day, mid-latitude night, polar summer and polar winter) are plotted for the three tangent altitudes in the UTLS region. Simulated and

residual spectral fits are shown in these figures for 710–780 cm^{-1} spectral range to find the evidence for the detection of HCN spectral signature in the MIPAS-E measurements.

The top panel in the Figure 4.29 to Figure 4.55 (odd numbered figures) shows the measured spectrum (black) with the RFM simulated fit (red). Ideally, the two spectra should remain unresolved which will indicate 'best' quality RFM simulated fit, with the difference between them approaching the MIPAS-E NESR level at all altitudes (plotted as blue dashed in the middle and lower plots). The MIPAS-E NESR is 34.2, 34.0 and 34.9 $nW/(cm^2\ sr\ cm^{-1})$ at 9-,12- and 15-km MIPAS-E nominal tangent altitudes.

Residual spectra for the HCN spectral lines, plotted in the central and lower panel of the same figures, show the comparison of ΔY (black) with ΔX (red) at each altitude for the 710–780 cm^{-1} and 744–748 cm^{-1} spectral range. At all altitudes in the UTLS region (except for troposphere levels), ΔY should agree with ΔX within certain acceptable limits set for the successful detection of the HCN spectral signature. The measured residual ΔY can be compared to ΔX using the following filtering criteria:

1) The HCN peak strength has to be greater than twice the MIPAS-E NESR.
2) The standard deviation in the non-HCN peak regions has to be less than the NESR.
3) For the shape of the HCN spectral feature, the standard deviation calculated for the difference in the measured and simulated residual spectrum should to be less than half the NESR.

Similarly, in the Figure 4.30 to Figure 4.56 (even numbered figures), the residual spectra show the comparison of ΔY (black) with ΔX (red) at each altitude for other interfering gases such as H_2O, CO_2, O_3, N_2O_5, CH_3Cl, HNO_3 and C_2H_2 and aerosol extinction.

4.2.6.3.1 Tropics: Orbit 08585 scan #2

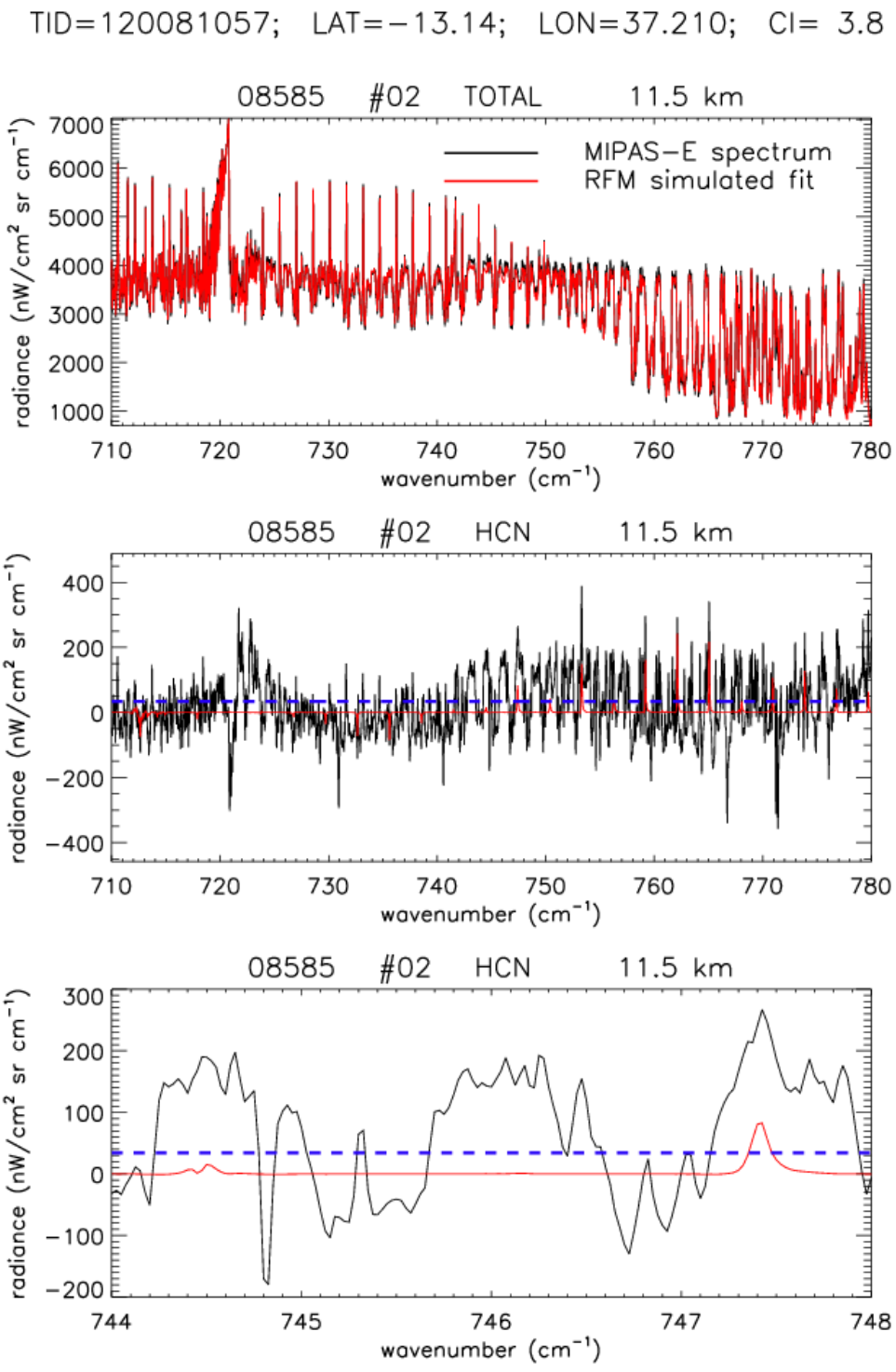

Figure 4.29: Comparison of measured MIPAS-E spectrum with simulated total at 11.5 km tangent altitude (top); measured residual ΔY (black) with reference residual ΔX (red) spectra (middle); and close-up of ΔY and ΔX residual spectra in the 744–748 cm^{-1} region (bottom). The MIPAS-E NESR is 34.0 nW/cm^2 sr cm^{-1} (blue dashed line).

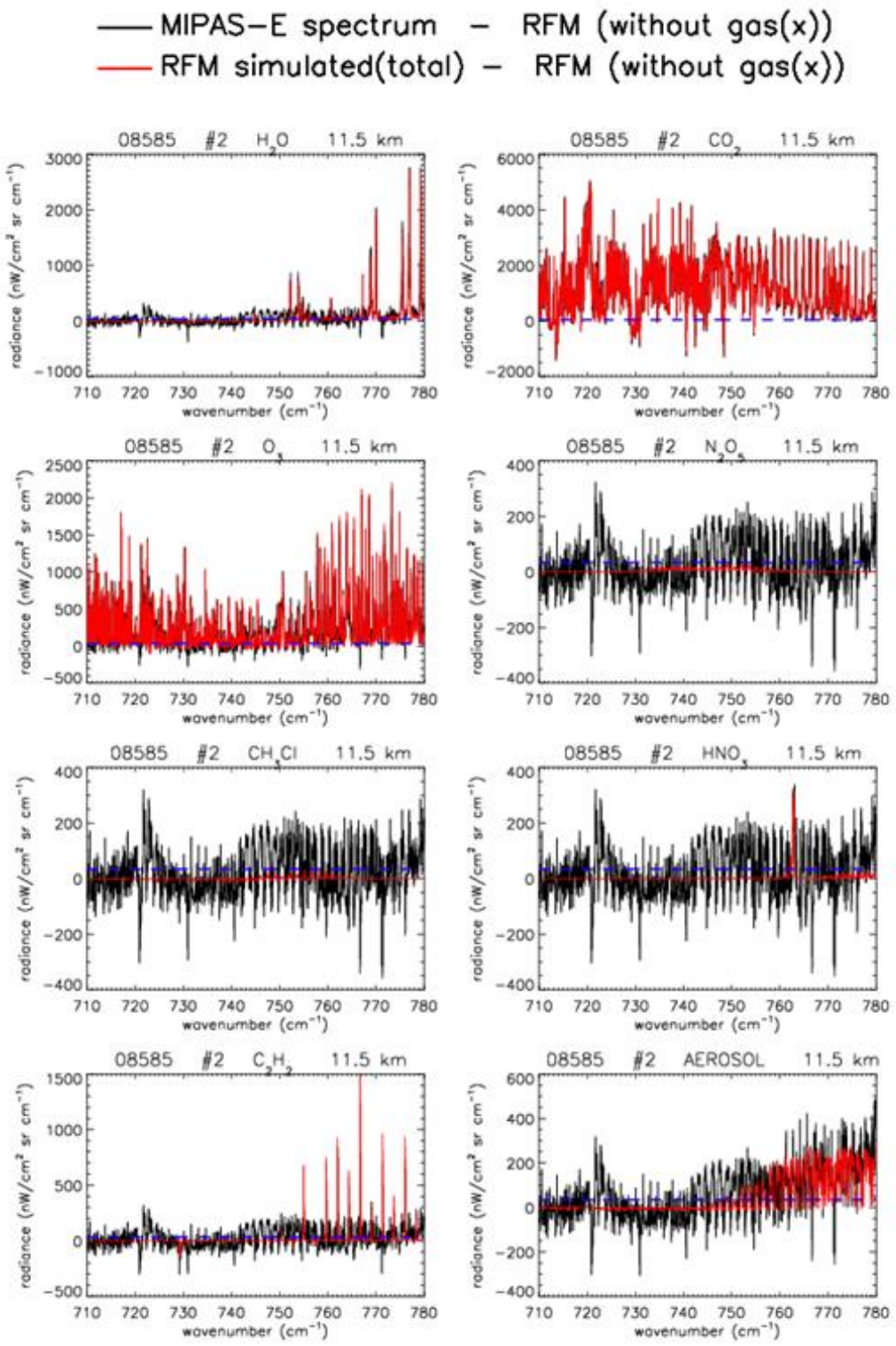

Figure 4.30: Comparison of measured residual ΔY with reference residual ΔX spectra for major interfering gases and aerosol extinction at 11.5 km tangent altitude. The MIPAS-E NESR is 34.0 nW/cm² sr cm⁻¹ (blue dashed line).

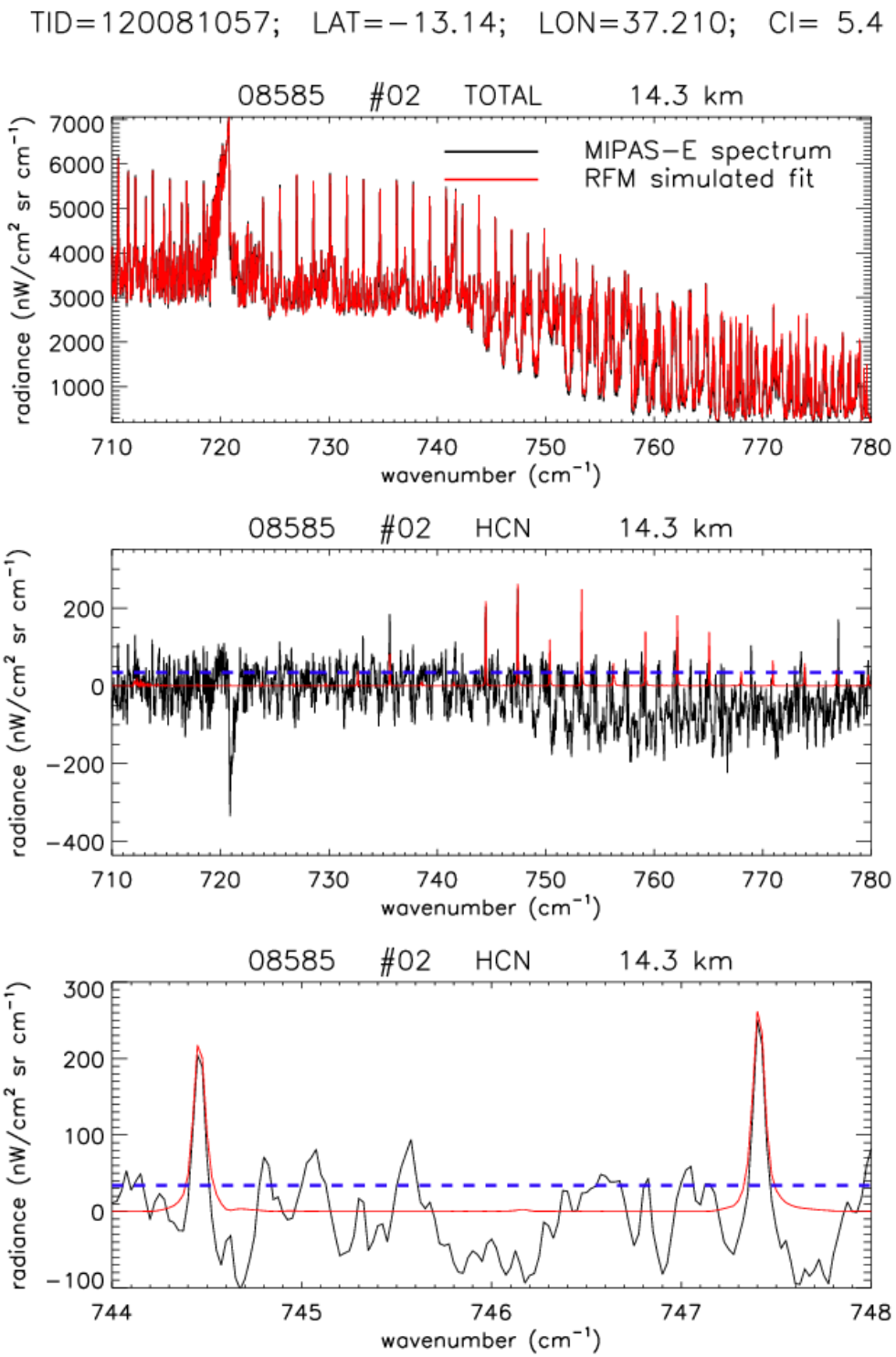

Figure 4.31: Comparison of measured MIPAS-E spectrum with simulated total at 14.3 km tangent altitude (top); measured residual ΔY (black) with Reference residual ΔX (red) spectra (middle); and close-up of the ΔY and ΔX residual spectra in the 744–748 cm^{-1} region (bottom). The MIPAS-E NESR is 34.2 nW/cm^2 sr cm^{-1} (blue dashed line).

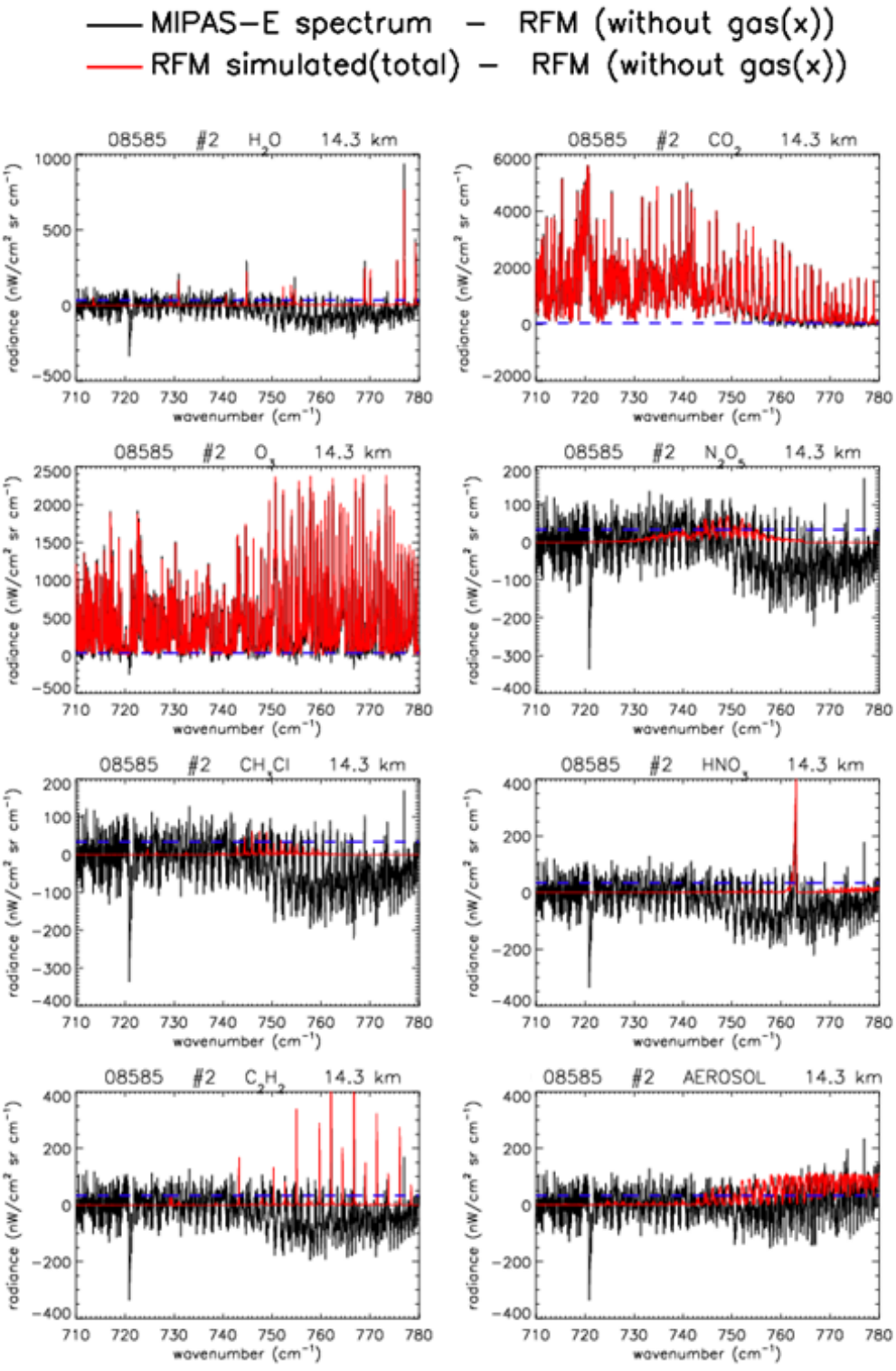

Figure 4.32: Comparison of measured residual ΔY with reference residual ΔX spectra for major interfering gases and aerosol extinction; at 14.3 km tangent altitude. The MIPAS-E NESR is 34.2 nW/cm² sr cm⁻¹ (blue dashed line).

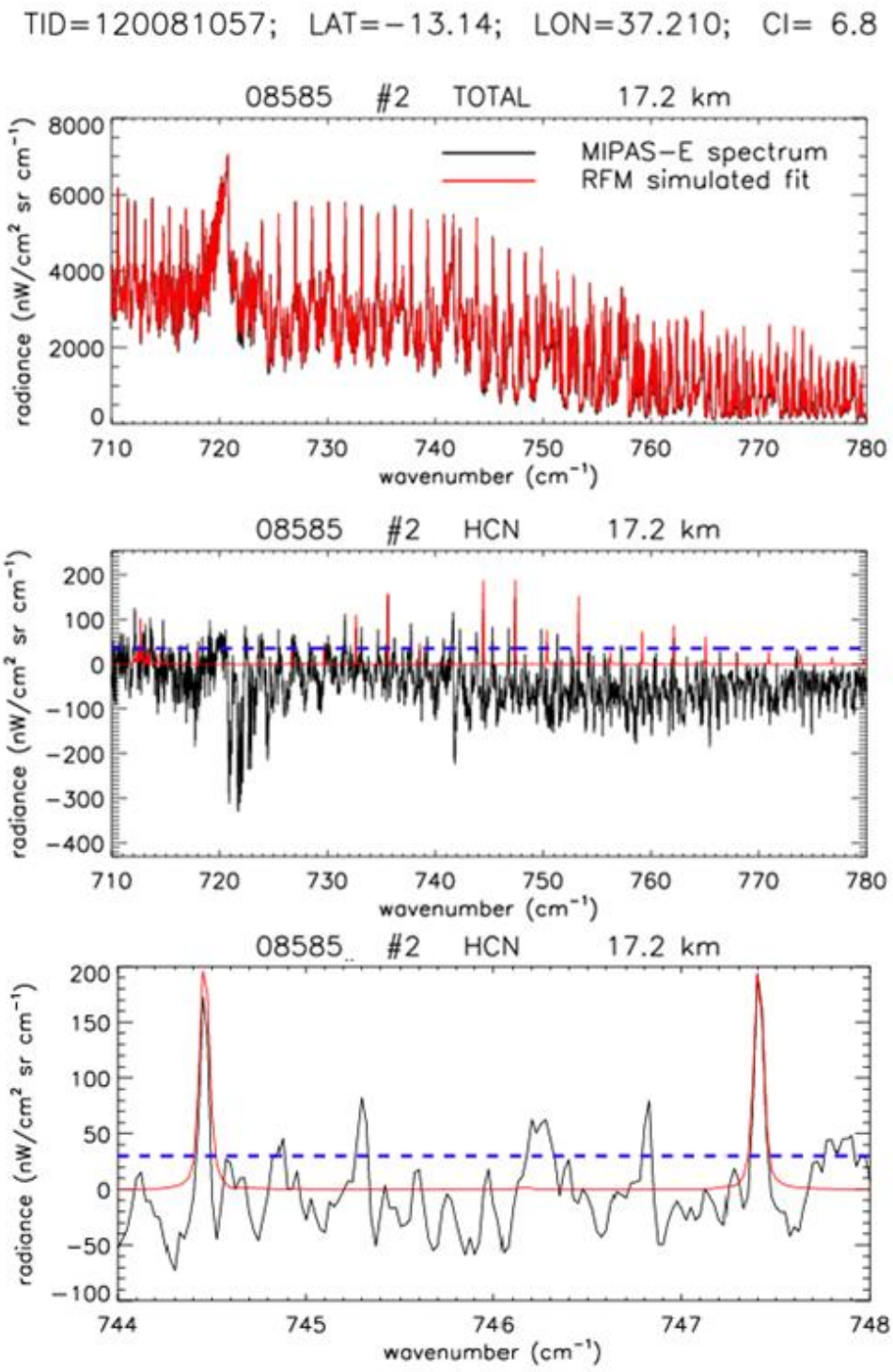

Figure 4.33: Comparison of measured MIPAS-E spectrum with simulated total (top); measured residual ΔY (black) with Reference residual ΔX (red) spectra (middle); and close-up of the ΔY and ΔX residual spectra in the 744–748 cm^{-1} region, at 17.2 km tangent altitude (bottom). The MIPAS-E NESR is 34.9 nW/cm^2 sr cm^{-1} (blue dashed line).

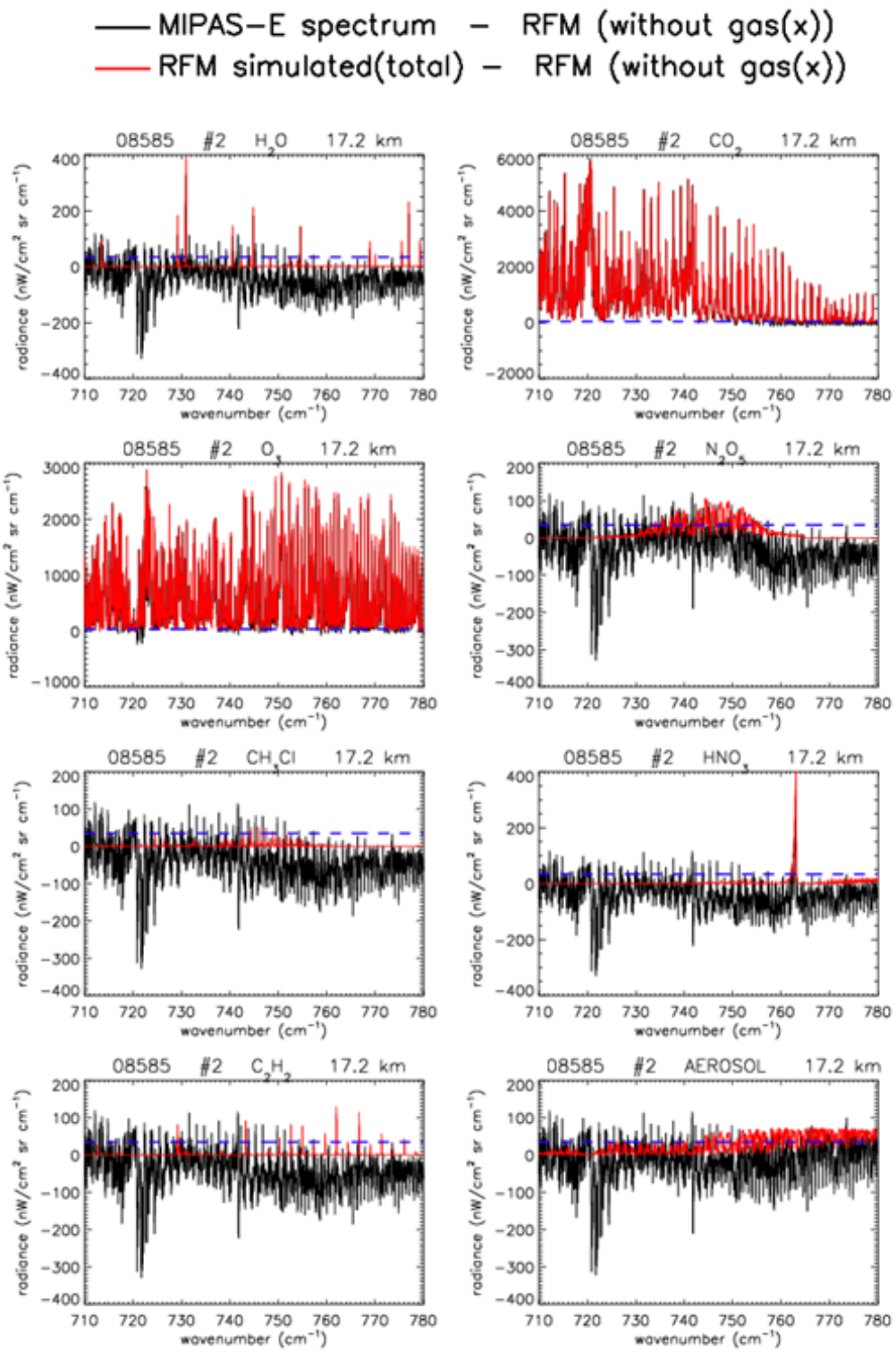

Figure 4.34: Comparison of measured residual ΔY with reference residual ΔX spectra for major interfering gases and aerosol extinction; at 17.2 km tangent altitude. The MIPAS-E NESR is 34.9 nW/cm² sr cm⁻¹ (blue dashed line).

4.2.6.3.2 Mid-latitude day: Orbit 08494 scan#49

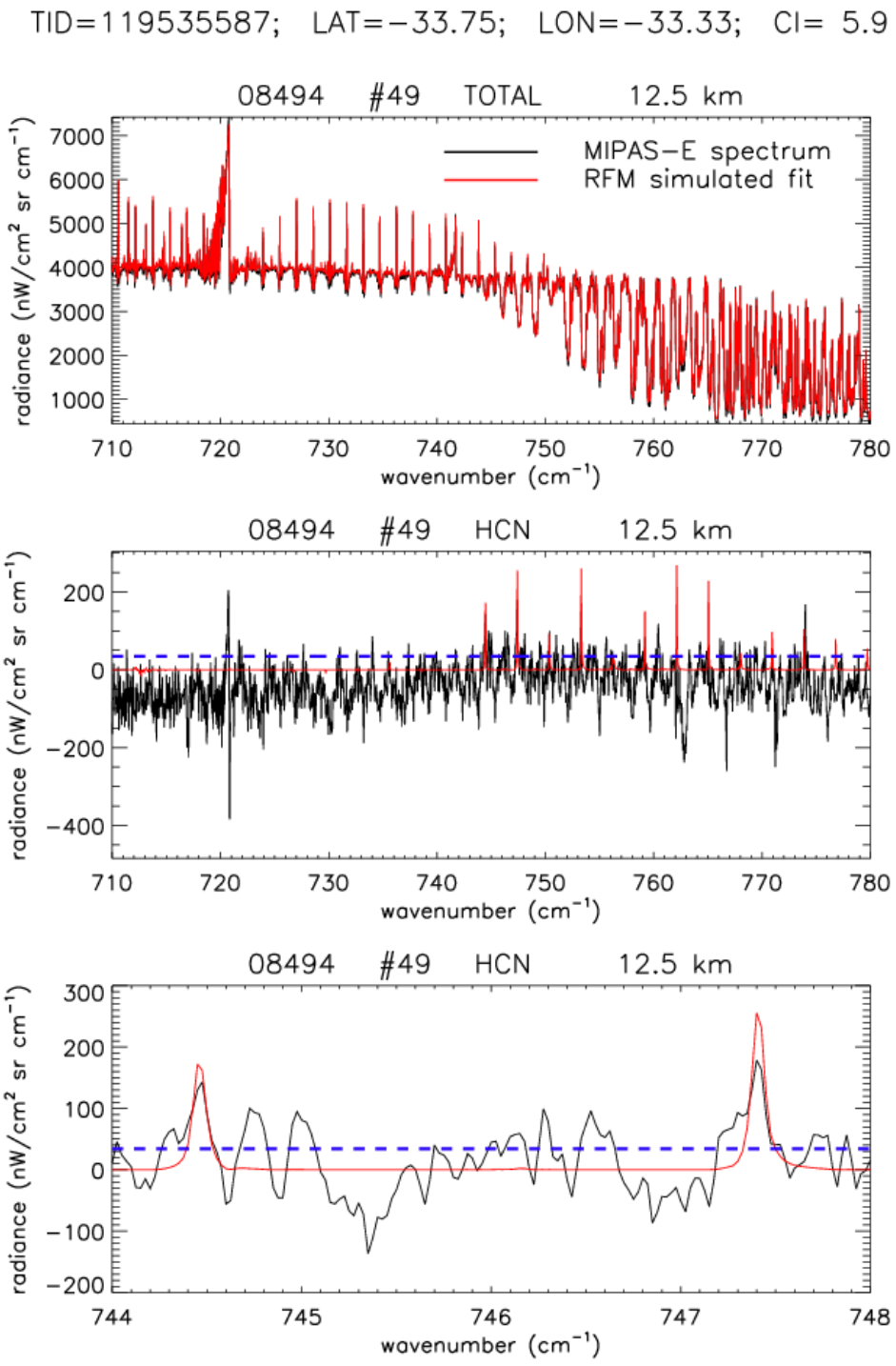

Figure 4.35: Comparison of measured MIPAS-E spectrum with simulated total at 12.5 km tangent altitude (top); measured residual ΔY (black) with reference residual ΔX (red) spectra (middle); and close-up of ΔY and ΔX residual spectra in the 744–748 cm^{-1} region (bottom). The MIPAS-E NESR is 34.0 nW/cm^2 sr cm^{-1} (blue dashed line).

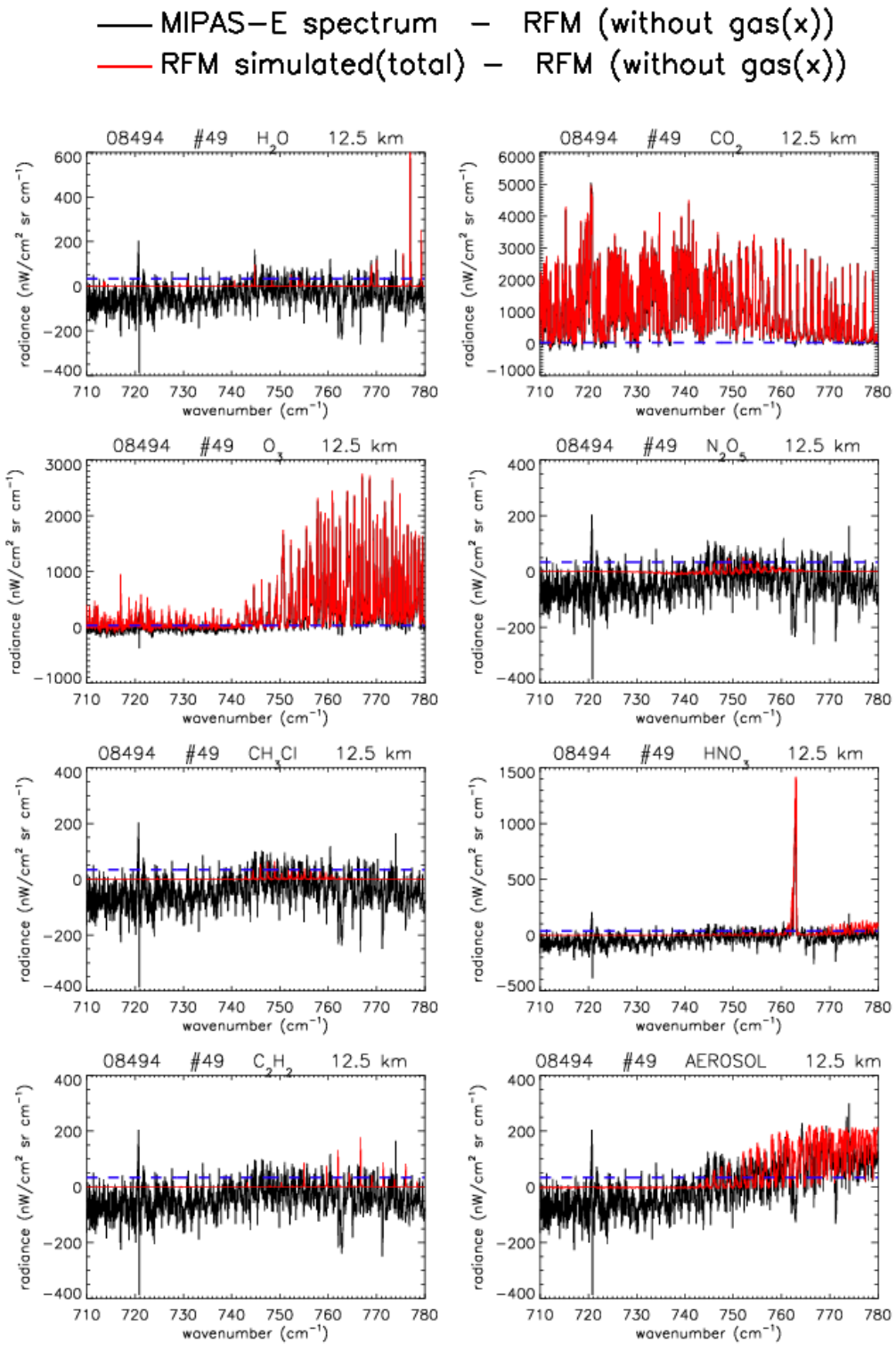

Figure 4.36: Comparison of measured residual ΔY with reference residual ΔX spectra for major interfering gases and aerosol extinction at 12.5 km tangent altitude. The MIPAS-E NESR is 34.0 nW/cm² sr cm⁻¹ (blue dashed line).

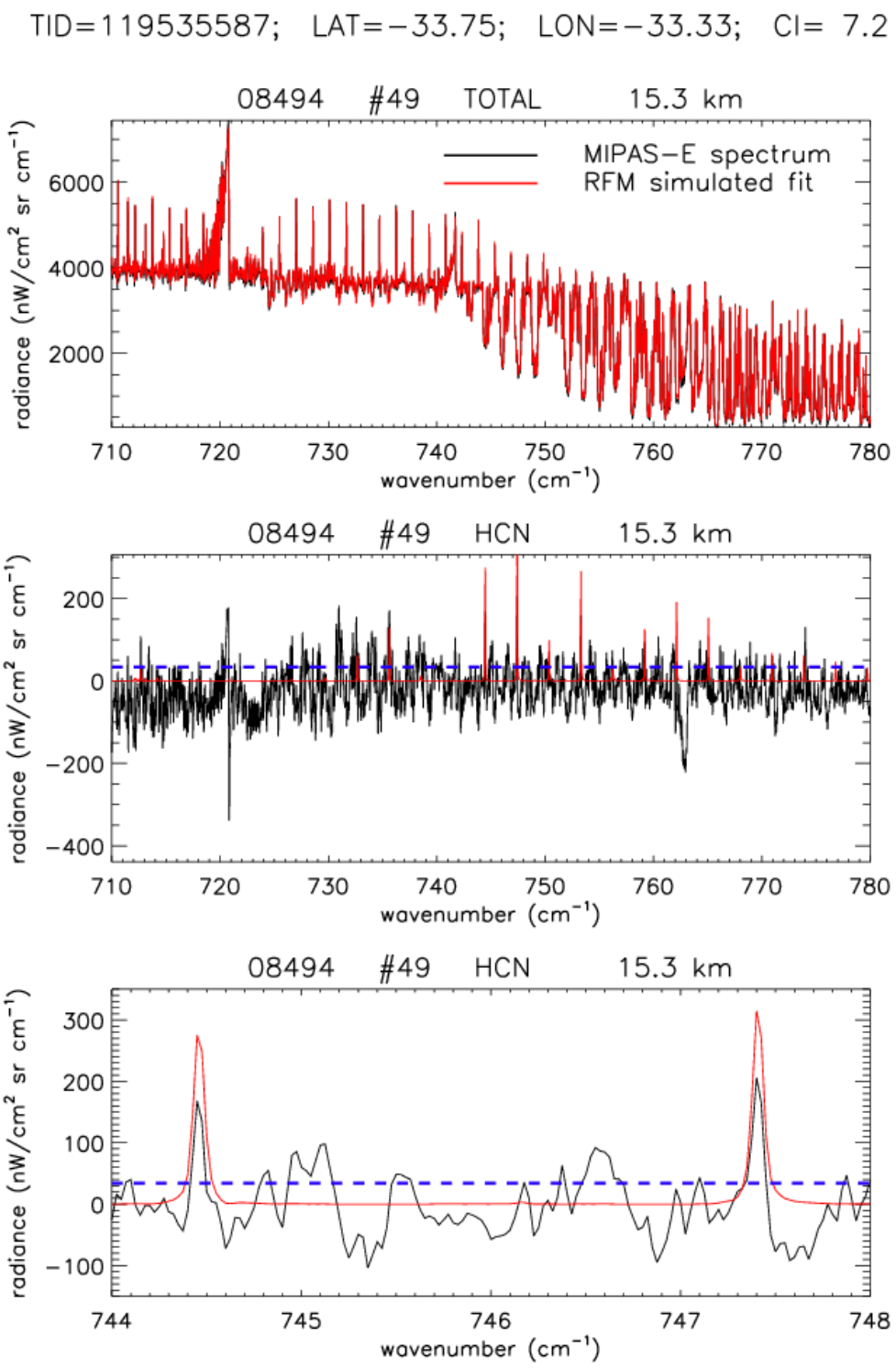

Figure 4.37: Comparison of measured MIPAS-E spectrum with simulated total at 15.3 km tangent altitude (top); measured residual ΔY (black) with reference residual ΔX (red) spectra (middle); and close-up of ΔY and ΔX residual spectra in the 744–748 cm^{-1} region (bottom). The MIPAS-E NESR is 34.2 nW/cm^2 sr cm^{-1} (blue dashed line).

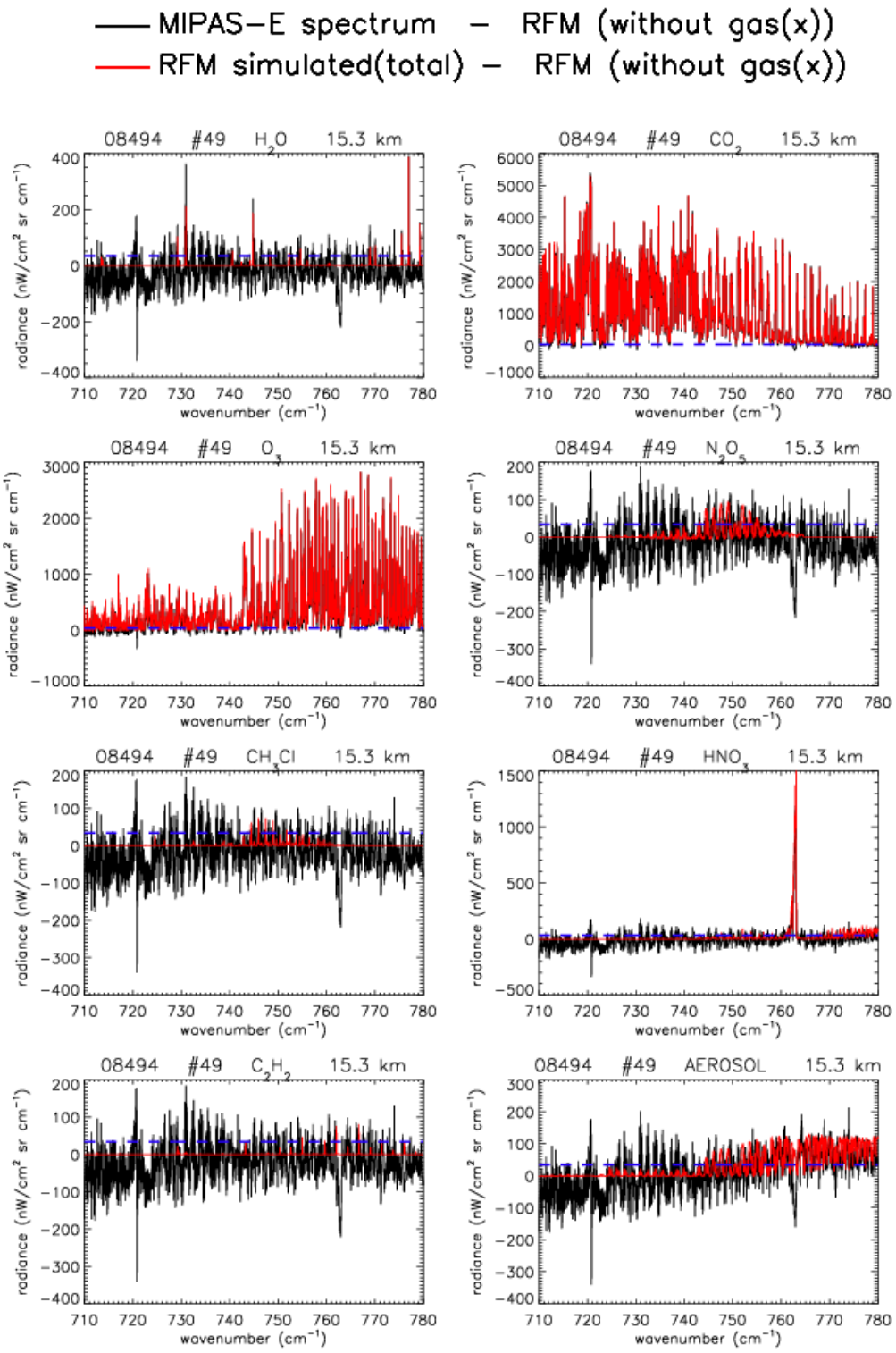

Figure 4.38: Comparison of measured residual ΔY with reference residual ΔX spectra for major interfering gases and aerosol extinction at 15.3 km tangent altitude. The MIPAS-E NESR is 34.2 nW/cm² sr cm⁻¹ (blue dashed line).

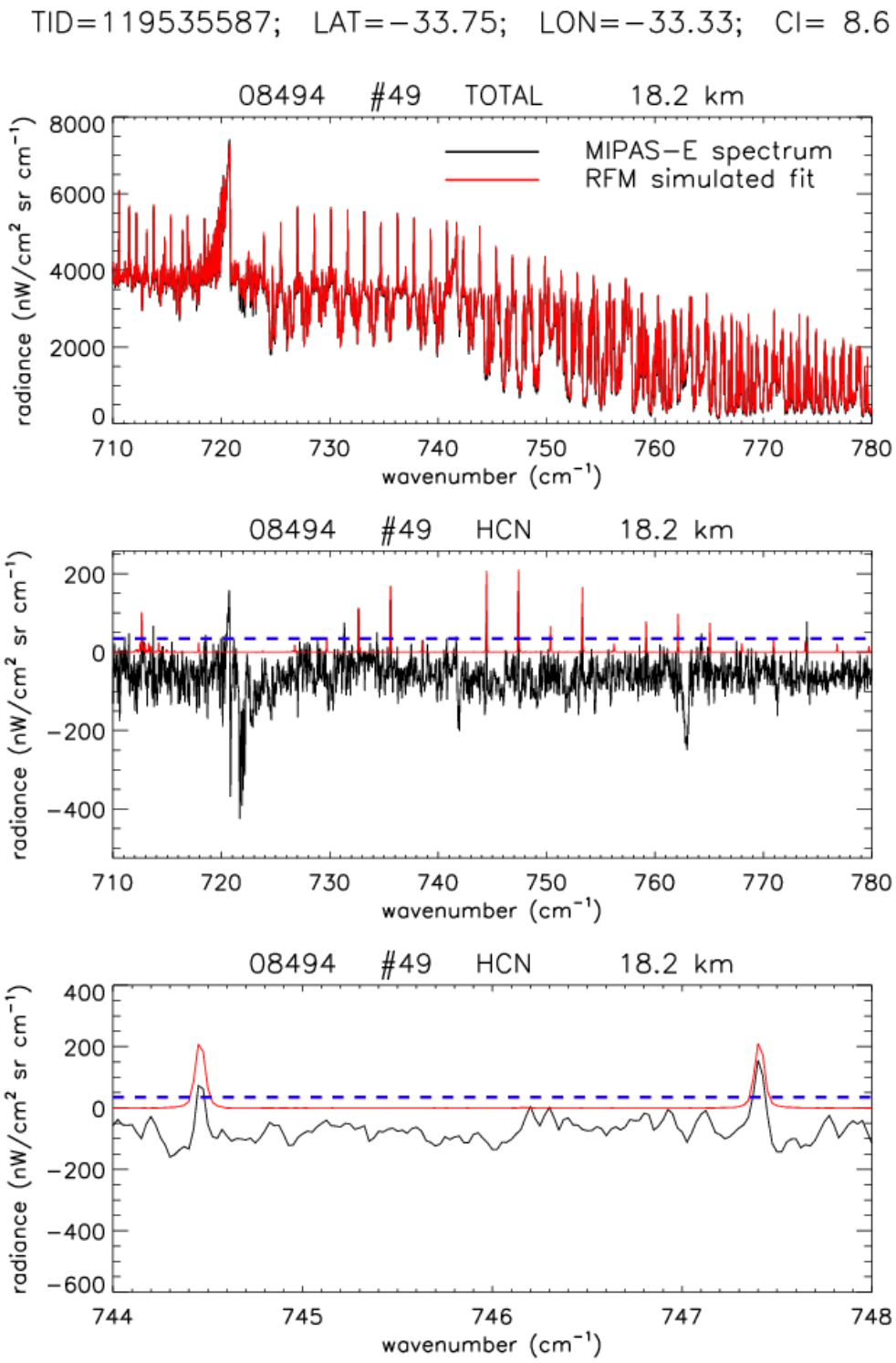

Figure 4.39: Comparison of measured MIPAS-E spectrum with simulated total at 18.2 km tangent altitude (top); measured residual ΔY (black) with reference residual ΔX (red) spectra (middle); and close-up of ΔY and ΔX residual spectra in the 744–748 cm^{-1} region (bottom). The MIPAS-E NESR is 34.9 nW/cm^2 sr cm^{-1} (blue dashed line).

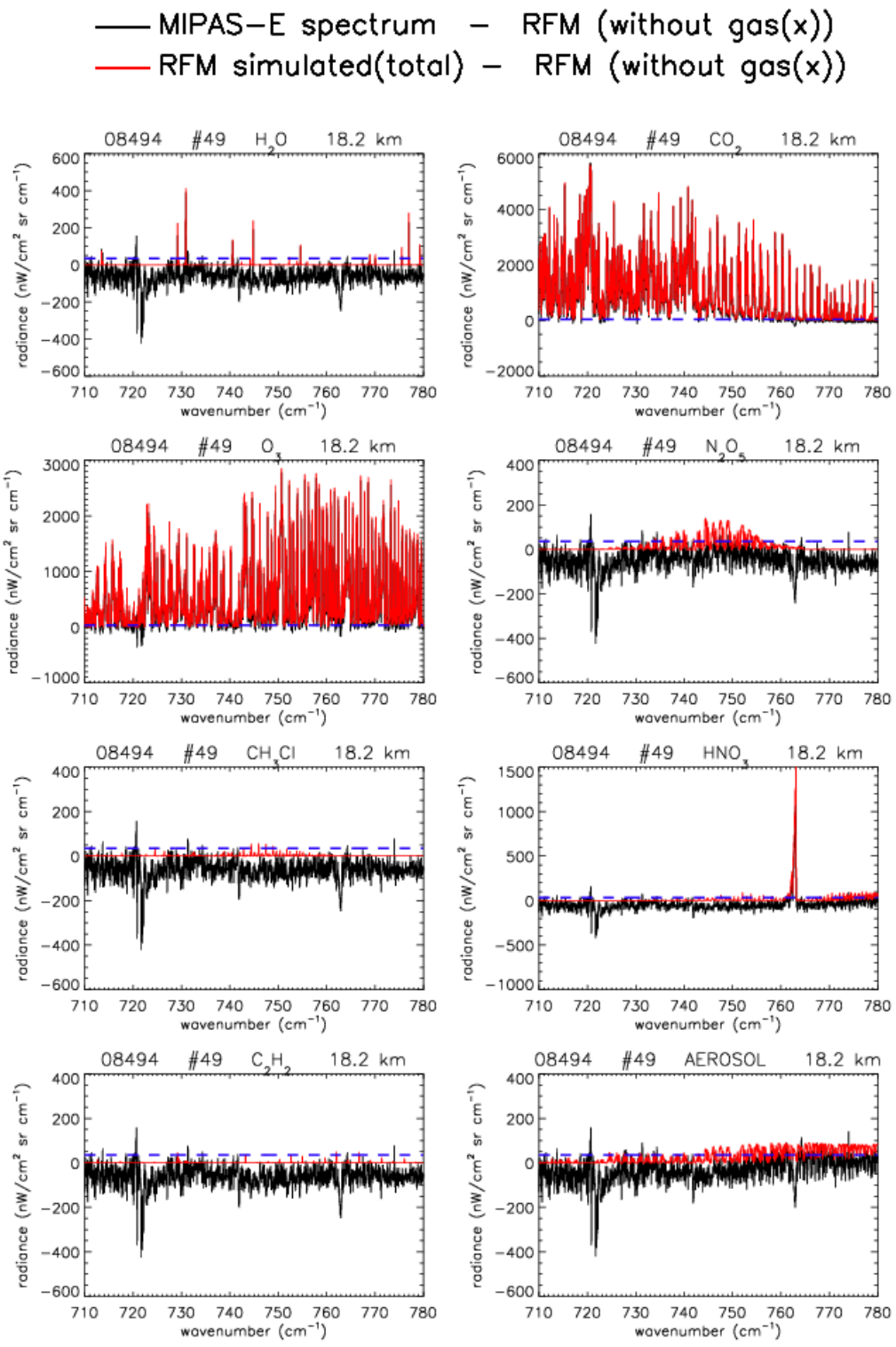

Figure 4.40: Comparison of measured residual ΔY with reference residual ΔX spectra for major interfering gases and aerosol extinction at 18.2 km tangent altitude. The MIPAS-E NESR is 34.9 nW/cm² sr cm⁻¹ (blue dashed line).

4.2.6.3.3 Mid-latitude night: Orbit 08587 scan#16

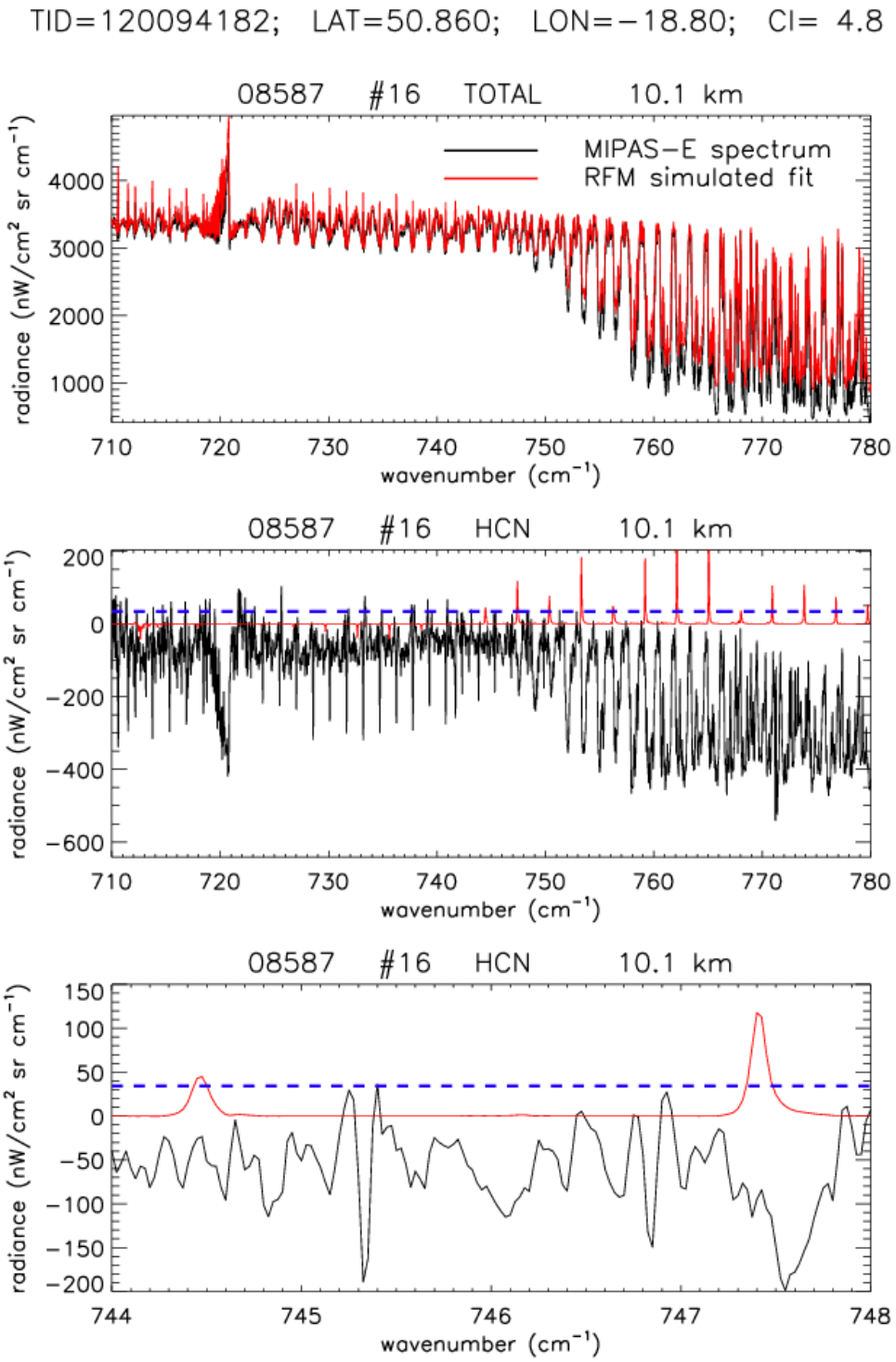

Figure 4.41: Comparison of measured MIPAS-E spectrum with simulated total at 10.1 km tangent altitude (top); measured residual ΔY (black) with reference residual ΔX (red) spectra (middle); and close-up of ΔY and ΔX residual spectra in the 744–748 cm^{-1} region (bottom). The MIPAS-E NESR is 34.0 nW/cm^2 sr cm^{-1} (blue dashed line).

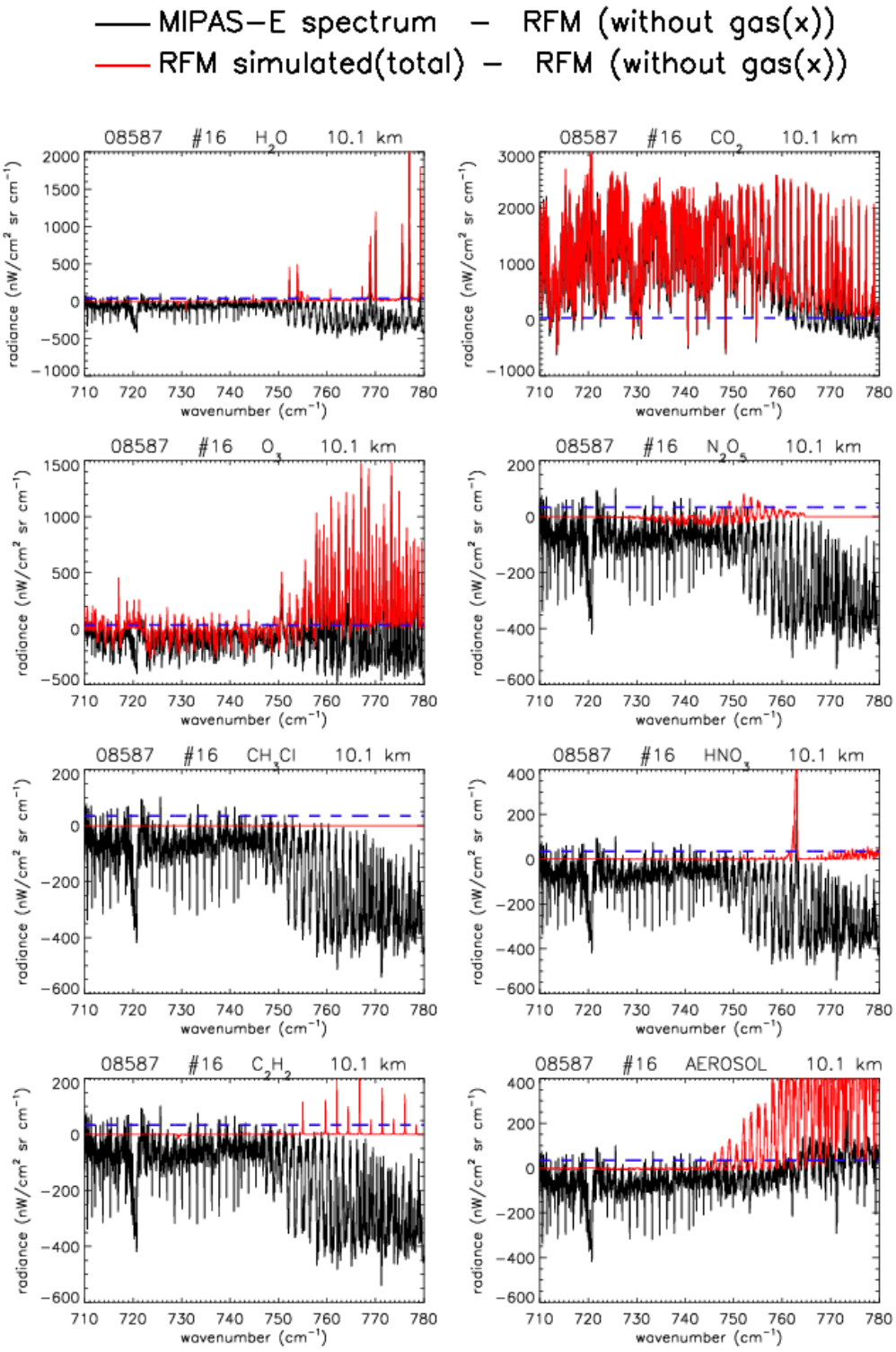

Figure 4.42: Comparison of measured residual ΔY with reference residual ΔX spectra for major interfering gases and aerosol extinction at 10.1 km tangent altitude. The MIPAS-E NESR is 34.0 nW/cm² sr cm⁻¹ (blue dashed line).

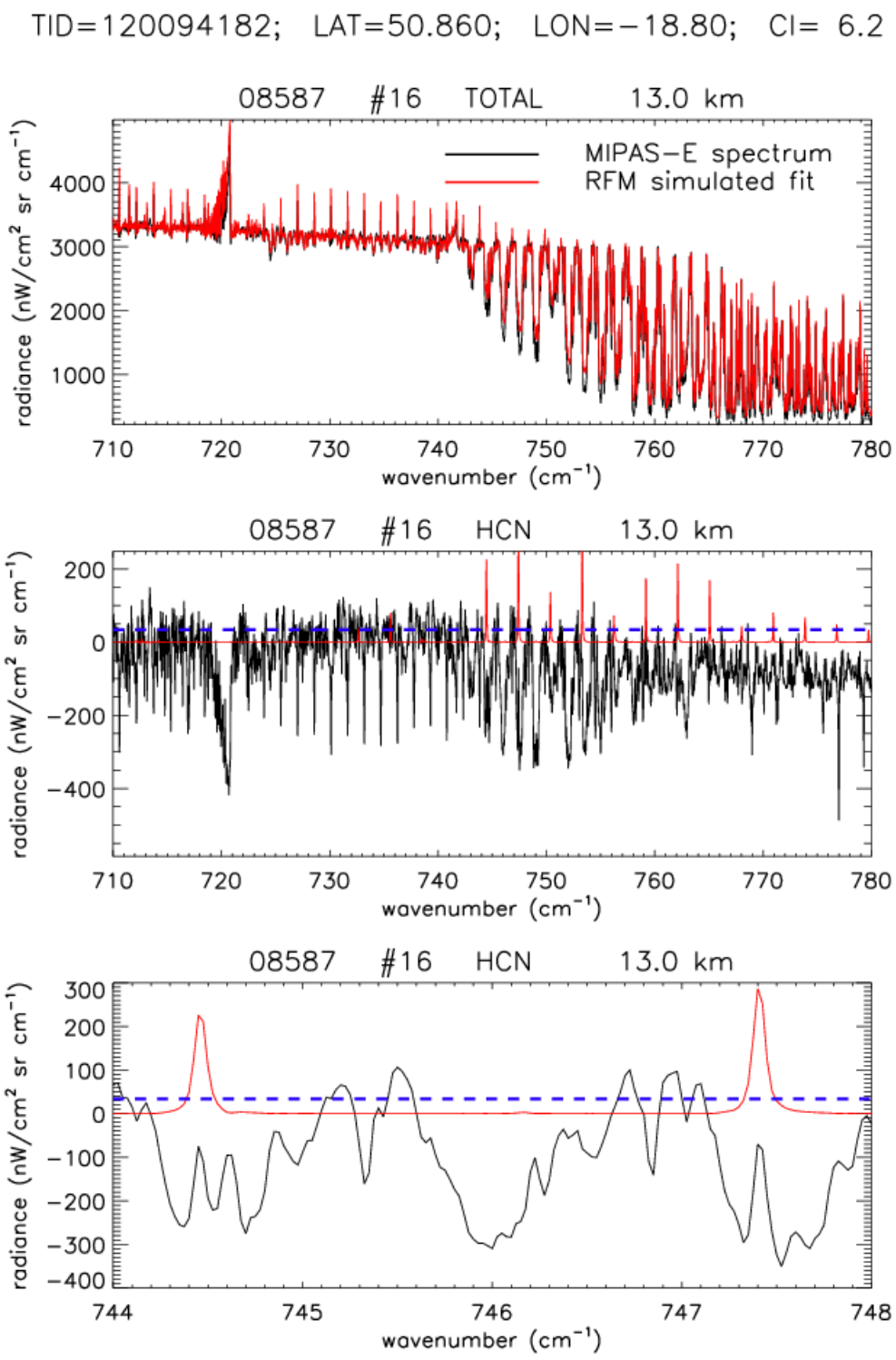

Figure 4.43: Comparison of measured MIPAS-E spectrum with simulated total at 13.0 km tangent altitude (top); measured residual ΔY (black) with reference residual ΔX (red) spectra (middle); and close-up of ΔY and ΔX residual spectra in the 744–748 cm^{-1} region (bottom). The MIPAS-E NESR is 34.2 nW/cm^2 sr cm^{-1} (blue dashed line).

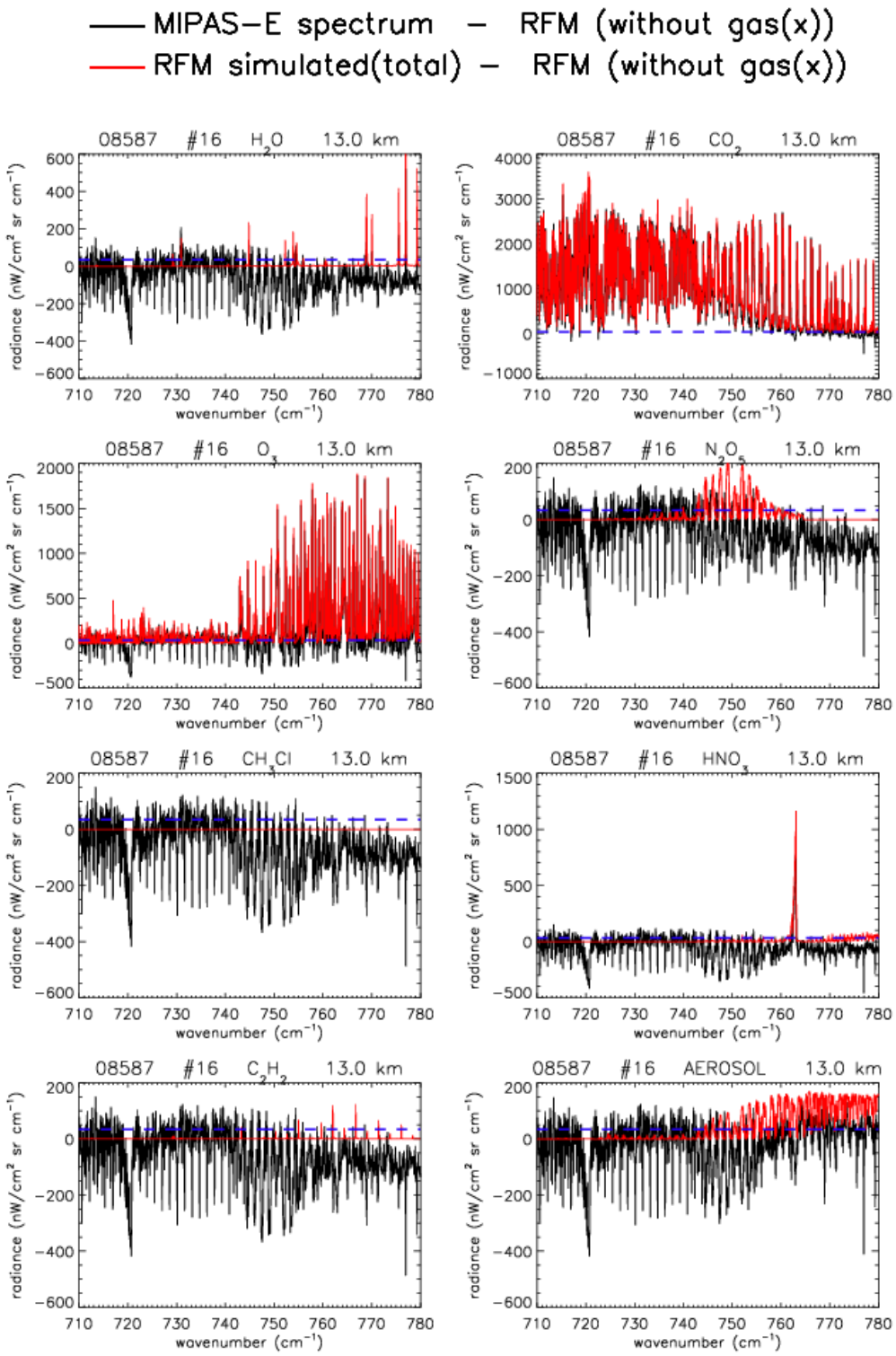

Figure 4.44: Comparison of measured residual ΔY with reference residual ΔX spectra for major interfering gases and aerosol extinction at 13.0 km tangent altitude. The MIPAS-E NESR is 34.2 nW/cm² sr cm⁻¹ (blue dashed line).

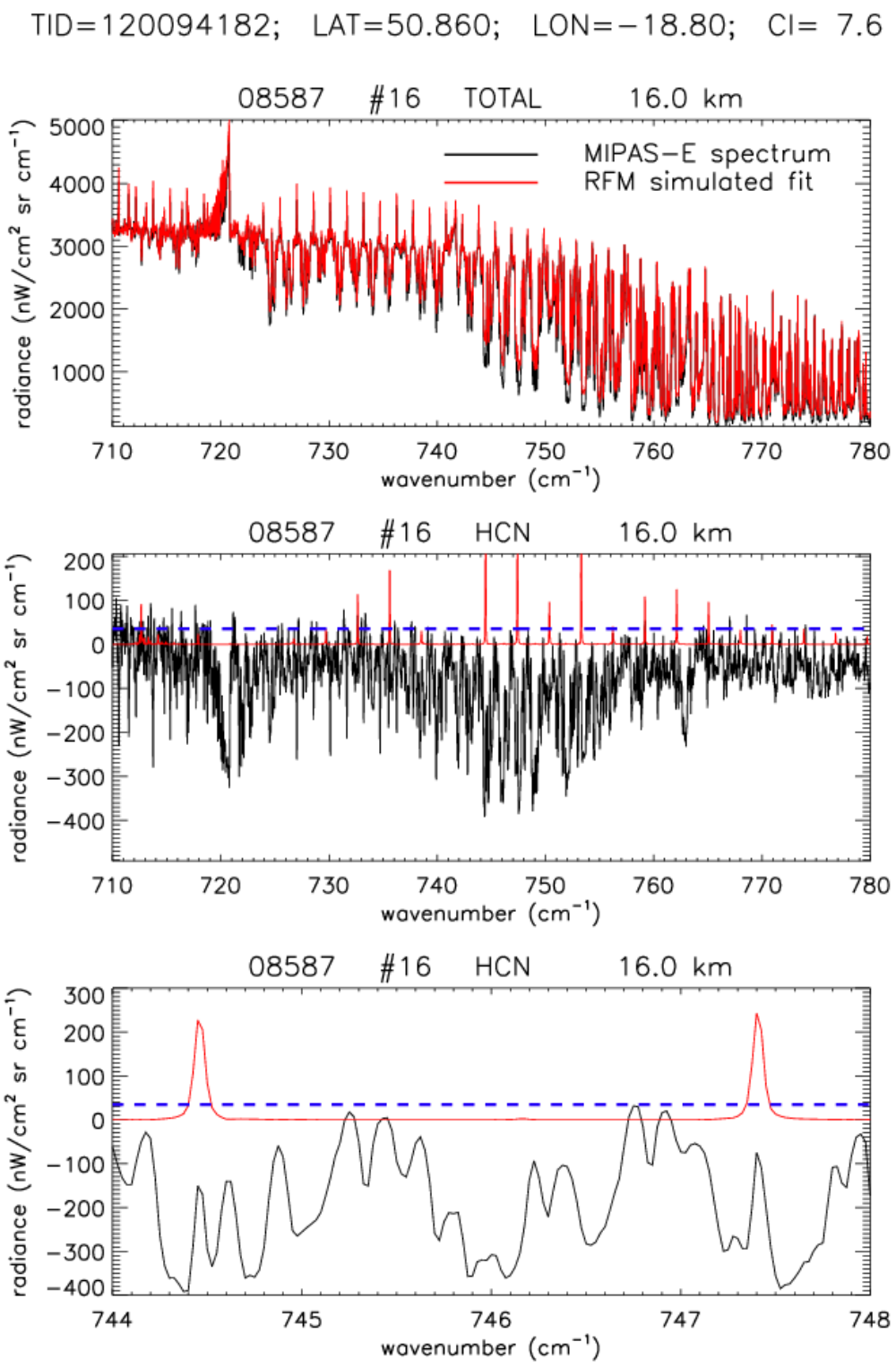

Figure 4.45: Comparison of measured MIPAS-E spectrum with simulated total at 16.0 km tangent altitude (top); measured residual ΔY (black) with reference residual ΔX (red) spectra (middle); and close-up of ΔY and ΔX residual spectra in the 744–748 cm^{-1} region (bottom). The MIPAS-E NESR is 34.9 nW/cm^2 sr cm^{-1} (blue dashed line).

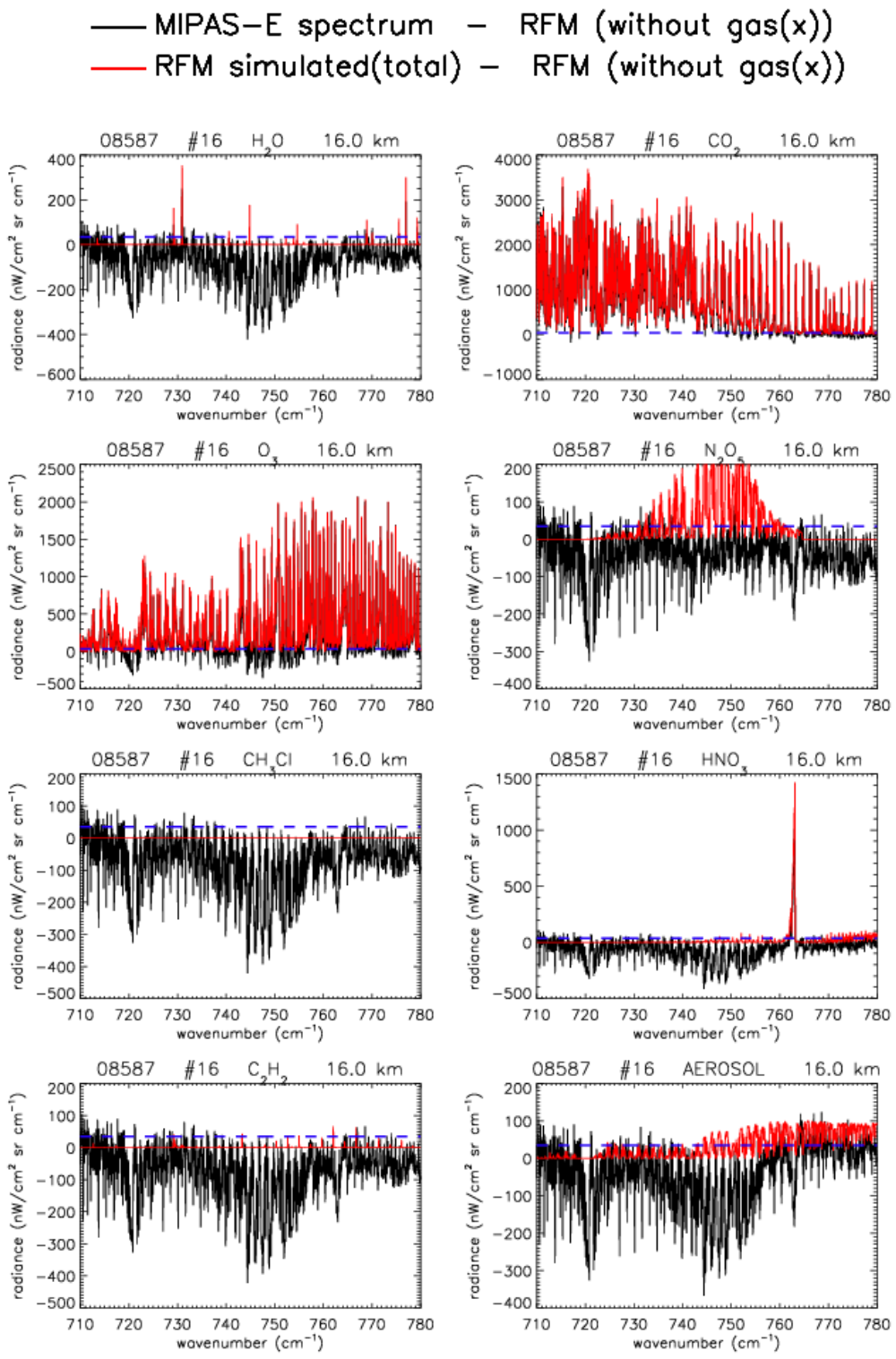

Figure 4.46: Comparison of measured residual ΔY with reference residual ΔX spectra for major interfering gases and aerosol extinction at 16.0 km tangent altitude. The MIPAS-E NESR is 34.9 nW/cm² sr cm⁻¹ (blue dashed line).

4.2.6.3.4 Polar summer: Orbit 08574 scan #25

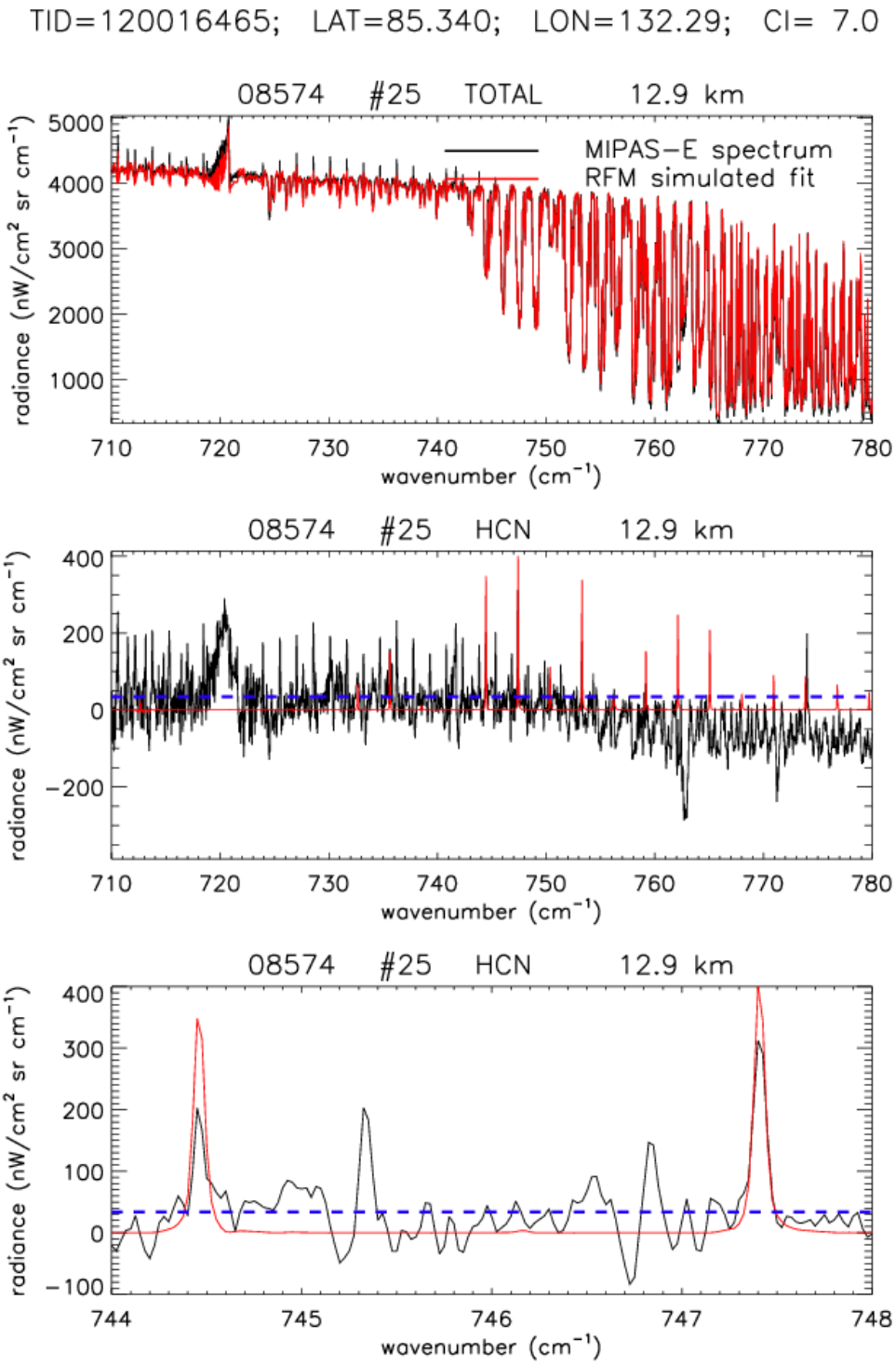

Figure 4.47: Comparison of measured MIPAS-E spectrum with simulated total at 12.9 km tangent altitude (top); measured residual ΔY (black) with reference residual ΔX (red) spectra (middle); and close-up of ΔY and ΔX residual spectra in the 744–748 cm^{-1} region (bottom). The MIPAS-E NESR is 34.2 nW/cm^2 sr cm^{-1} (blue dashed line).

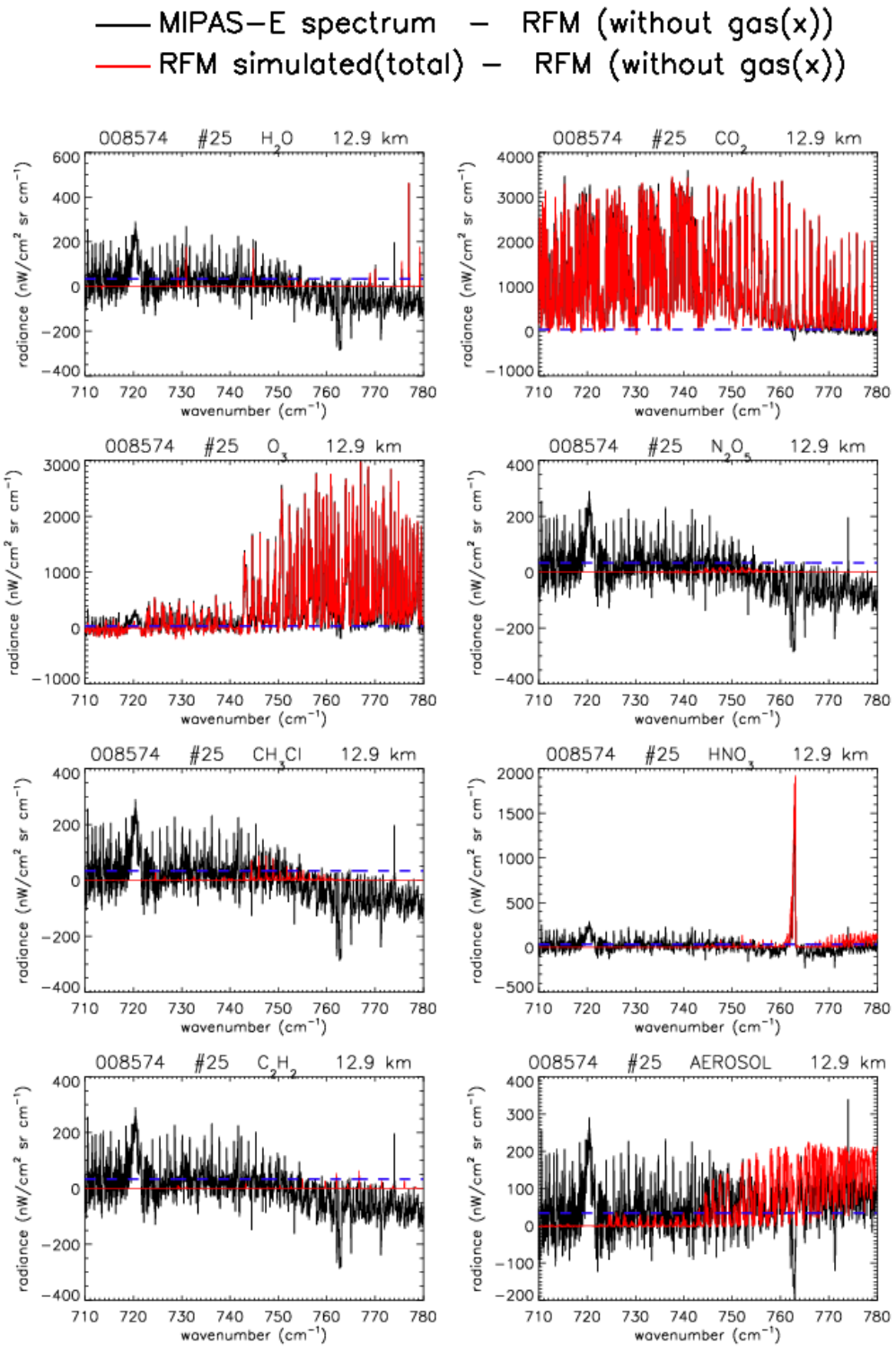

Figure 4.48: Comparison of measured residual ΔY with reference residual ΔX spectra for major interfering gases and aerosol extinction at 12.9 km tangent altitude. The MIPAS-E NESR is 34.2 nW/cm² sr cm⁻¹ (blue dashed line).

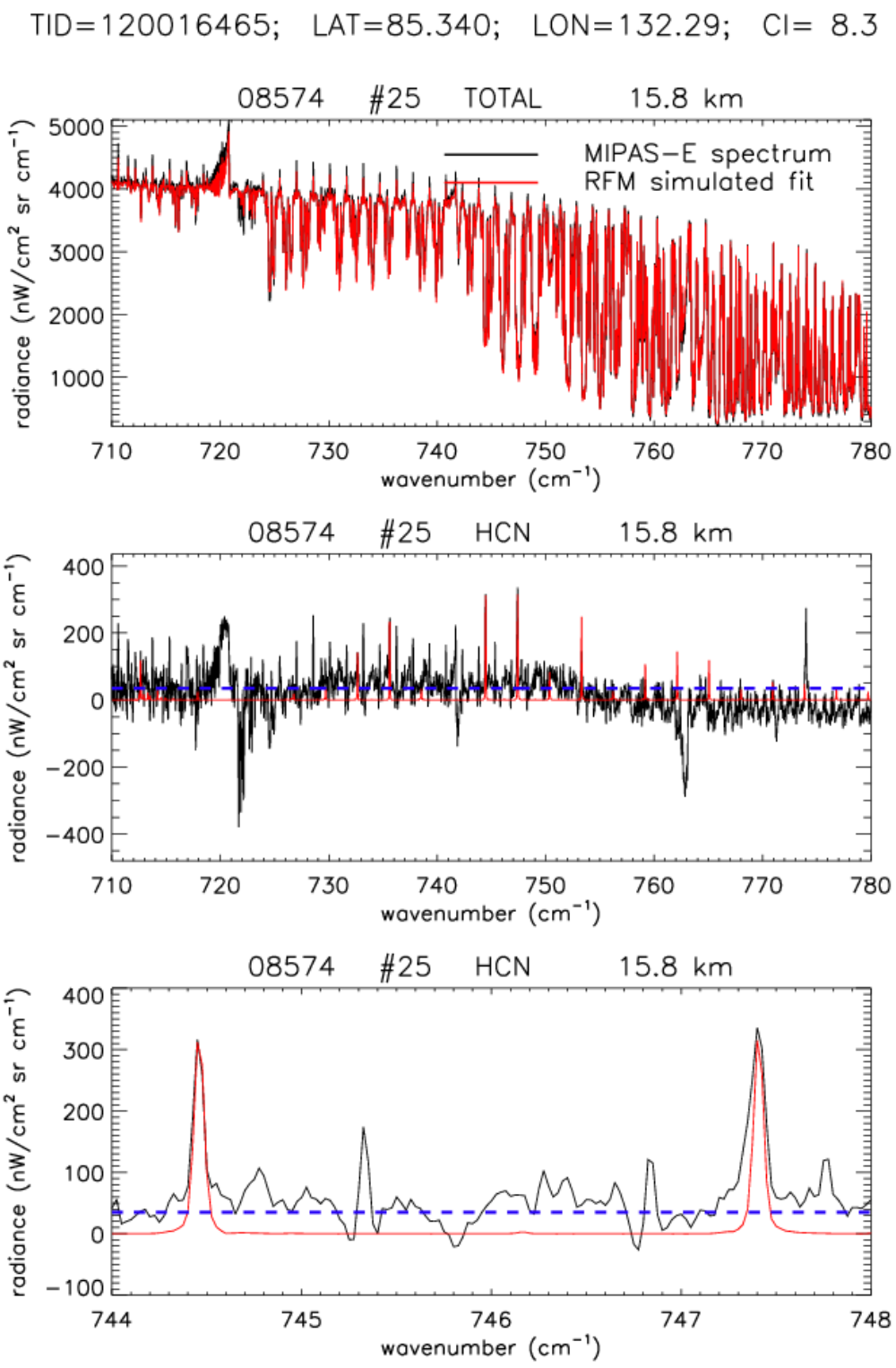

Figure 4.49: Comparison of measured MIPAS-E spectrum with simulated total at 15.8 km tangent altitude (top); measured residual ΔY (black) with reference residual ΔX (red) spectra (middle); and close-up of ΔY and ΔX residual spectra in the 744–748 cm^{-1} region (bottom). The MIPAS-E NESR is 34.9 nW/cm^2 sr cm^{-1} (blue dashed line).

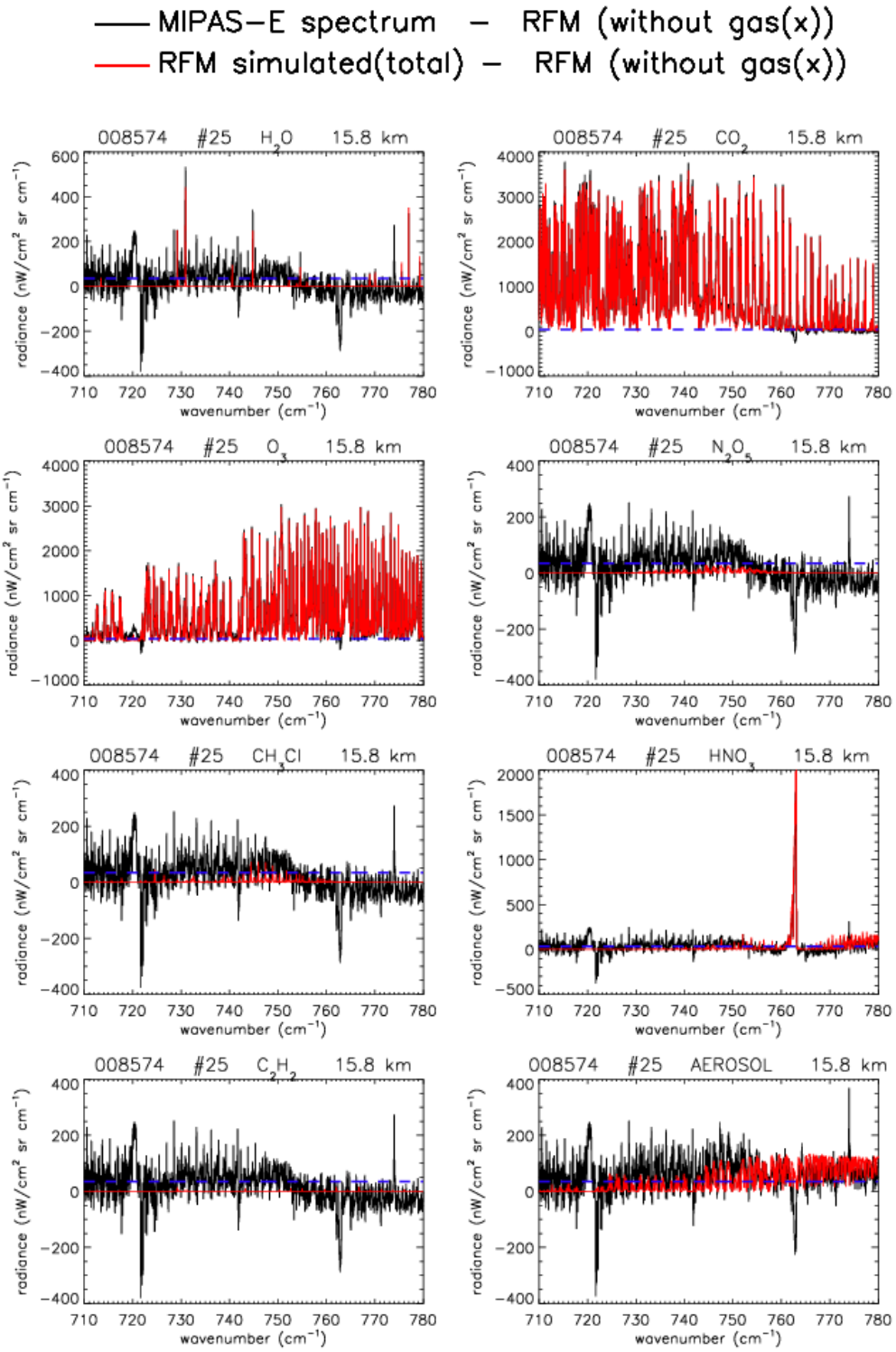

Figure 4.50: Comparison of measured residual ΔY with reference residual ΔX spectra for major interfering gases and aerosol extinction at 15.8 km tangent altitude. The MIPAS-E NESR is 34.9 nW/cm² sr cm⁻¹ (blue dashed line).

4.2.6.3.5 Polar winter: Orbit 08321 scan#65

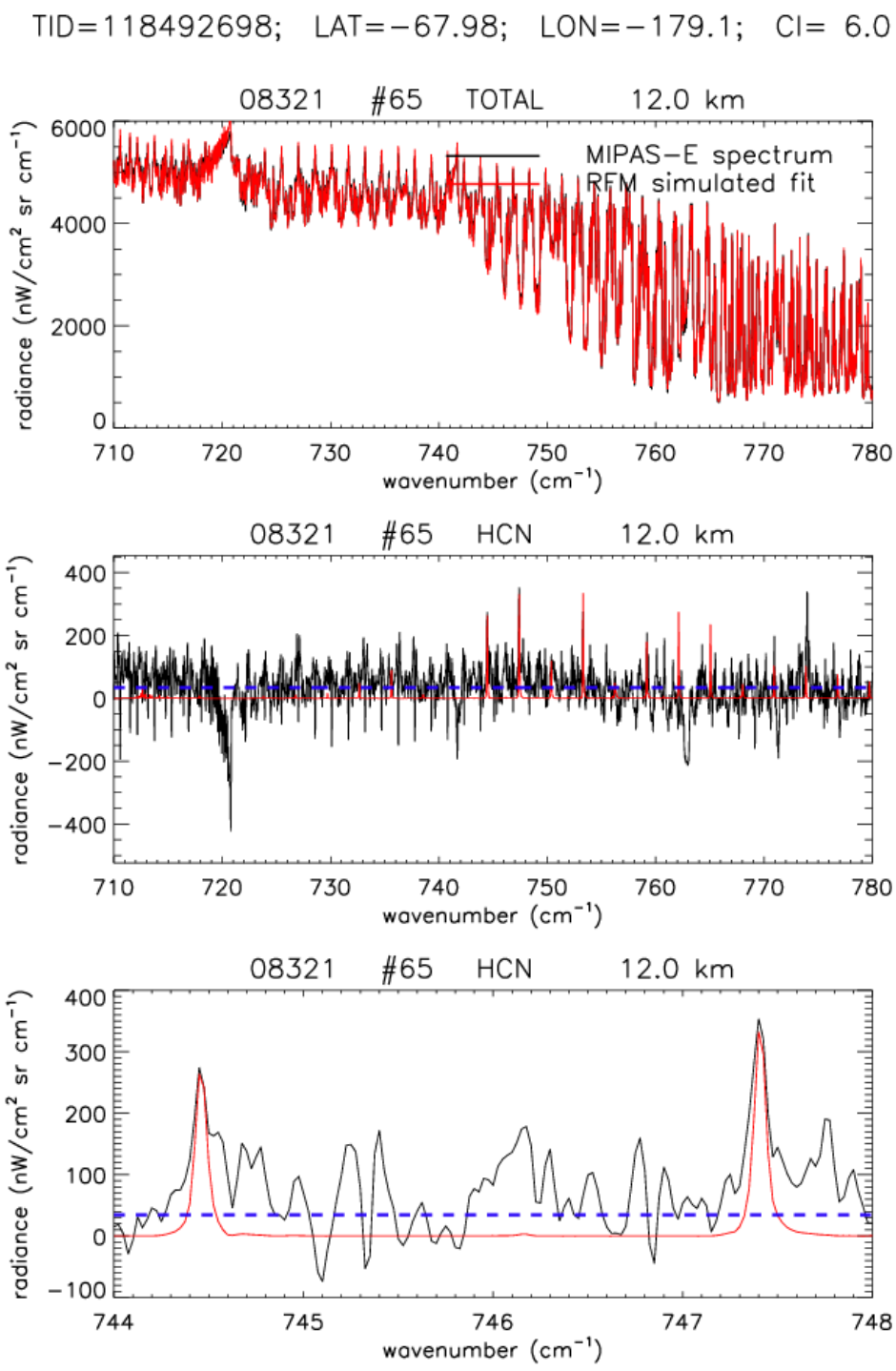

Figure 4.51: Comparison of measured MIPAS-E spectrum with simulated total at 12.0 km tangent altitude (top); measured residual ΔY (black) with reference residual ΔX (red) spectra (middle); and close-up of ΔY and ΔX residual spectra in the 744–748 cm^{-1} region (bottom). The MIPAS-E NESR is 34.0 nW/cm^2 sr cm^{-1} (blue dashed line).

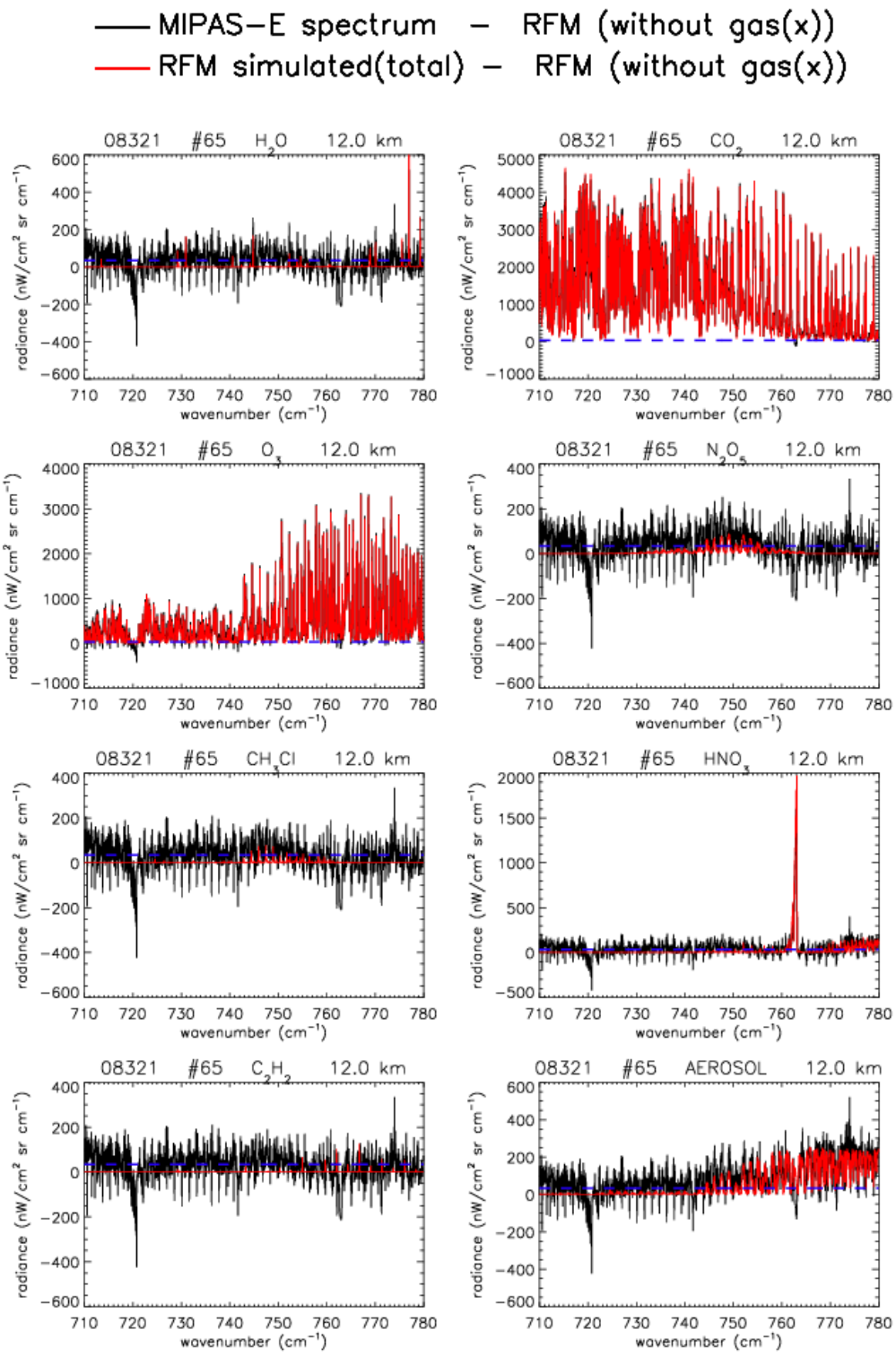

Figure 4.52: Comparison of measured residual ΔY with reference residual ΔX spectra for major interfering gases and aerosol extinction at 12.0 km tangent altitude. The MIPAS-E NESR is 34.0 nW/cm² sr cm⁻¹ (blue dashed line).

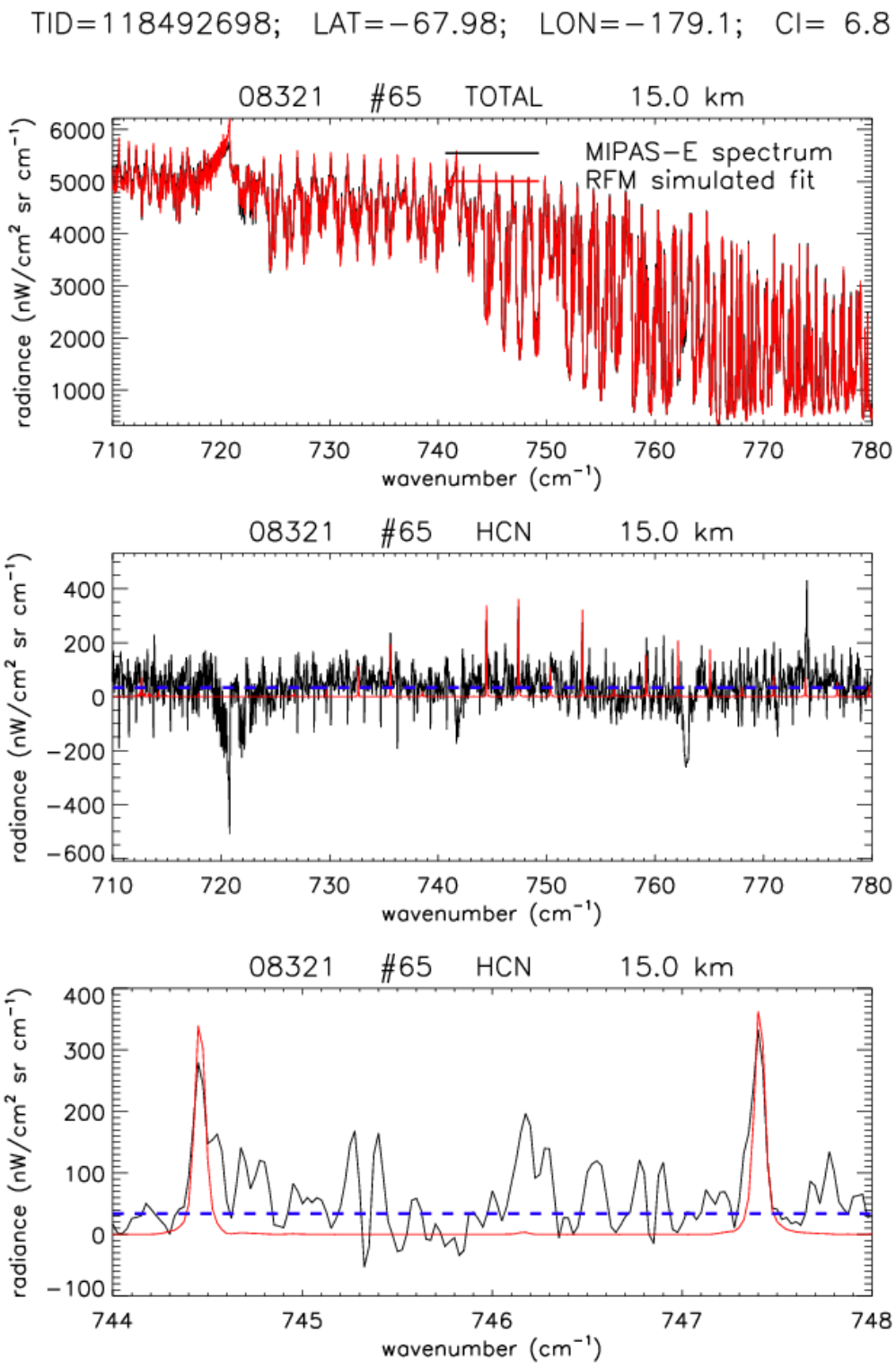

Figure 4.53: Comparison of measured MIPAS-E spectrum with simulated total at 15.0 km tangent altitude (top); measured residual ΔY (black) with reference residual ΔX (red) spectra (middle); and close-up of ΔY and ΔX residual spectra in the 744–748 cm^{-1} region (bottom). The MIPAS-E NESR is 34.2 nW/cm^2 sr cm^{-1} (blue dashed line).

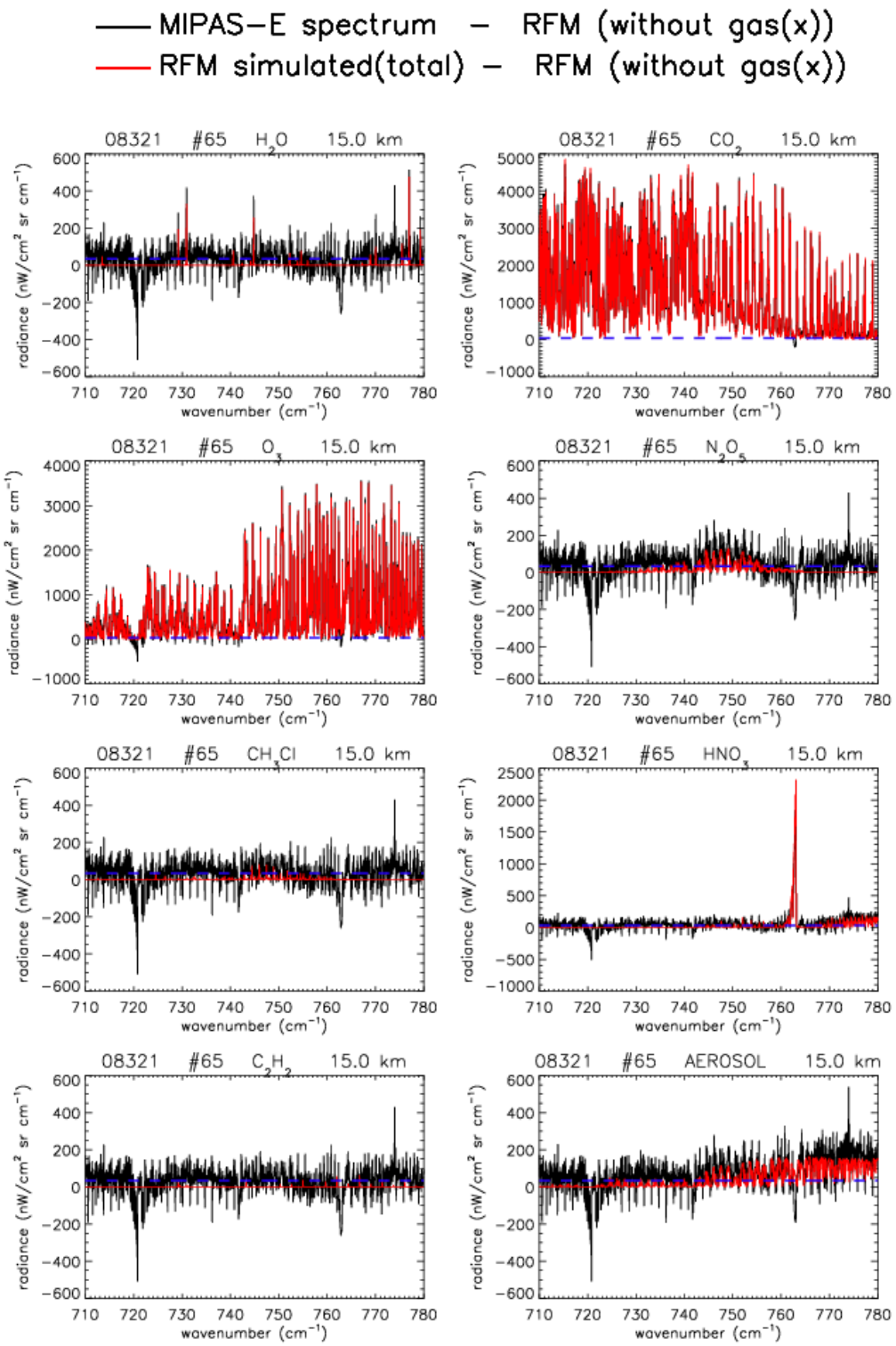

Figure 4.54: Comparison of measured residual ΔY with reference residual ΔX spectra for major interfering gases and aerosol extinction at 15.0 km tangent altitude. The MIPAS-E NESR is 34.2 nW/cm² sr cm⁻¹ (blue dashed line).

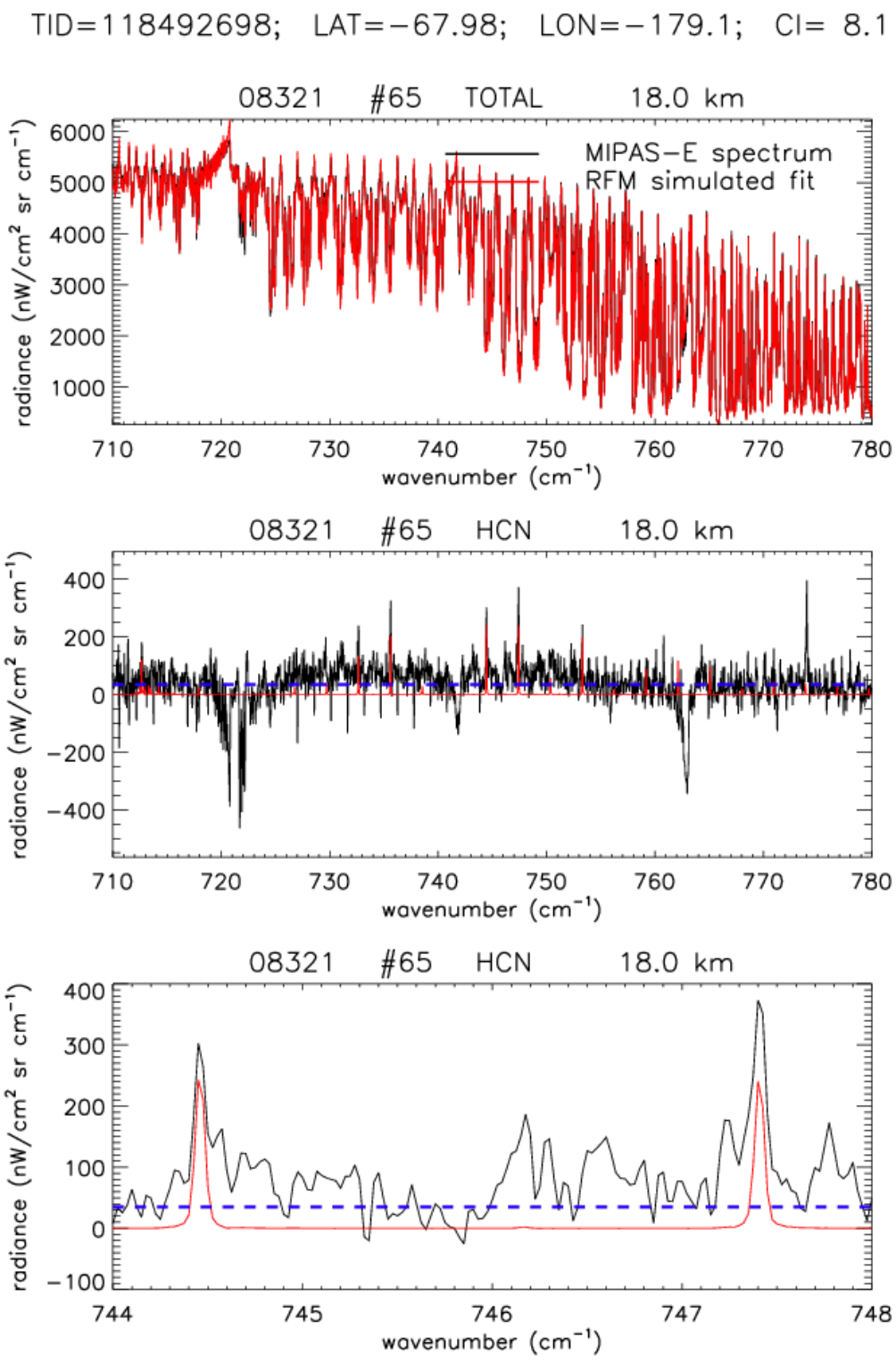

Figure 4.55: Comparison of measured MIPAS-E spectrum with simulated total at 18.0 km tangent altitude (top); measured residual ΔY (black) with reference residual ΔX (red) spectra (middle); and close-up of ΔY and ΔX residual spectra in the 744–748 cm^{-1} region (bottom). The MIPAS-E NESR is 34.9 nW/cm^2 sr cm^{-1} (blue dashed line).

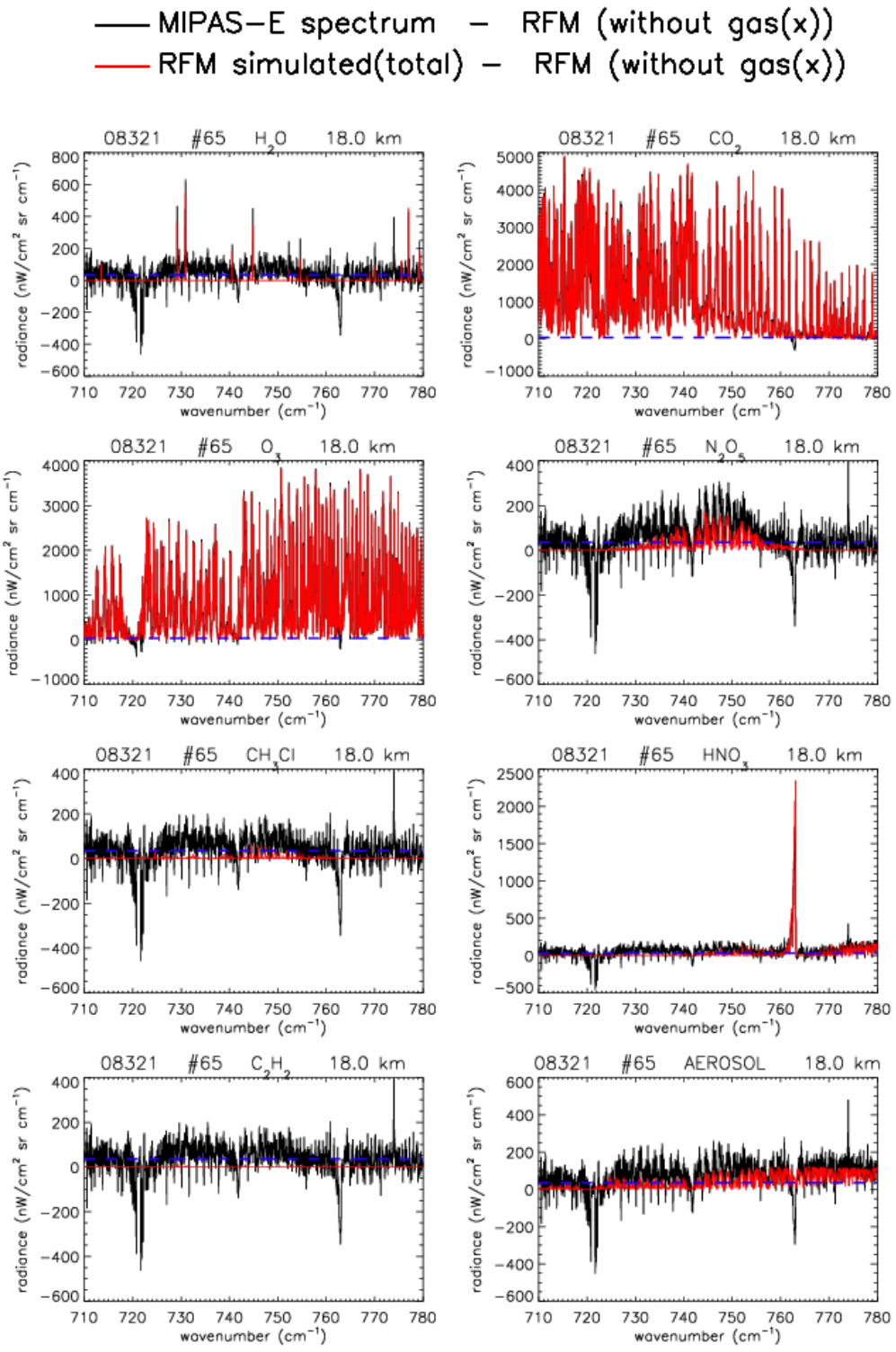

Figure 4.56: Comparison of measured residual ΔY with reference residual ΔX spectra for major interfering gases and aerosol extinction at 18.0 km tangent altitude. The MIPAS-E NESR is 34.9 nW/cm² sr cm⁻¹ (blue dashed line).

4.2.6.4 Comments on the detection results

As a first approximation results shown in the Figure 4.29 to Figure 4.56, the MIPAS-E measured spectrum and simulated RFM fit agree well enough. The ΔY and ΔX residual spectra (central panel) show good agreement within acceptable MIPAS-E NESR levels accept for the spectral region near 720 and 770 cm^{-1} at all altitude levels.

4.2.6.4.1 Tropics: Orbit 08585 scan#2

At 11.5 km [Figure 4.29], with a cloud index value less than 4, the expected HCN residual radiance is below the MIPAS-E NESR (blue dashed) and hence difficult to be detected due to saturation of HCN spectral lines in the region of interest. The radiance increase in the total radiance along with increase in variability of all trace gases and aerosol in the troposphere, make simulations in the atmosphere difficult with the possibility of scattering of radiation at lower altitudes and as a result weak interfering gases such as HCN spectral lines are saturated.

At 14.3 km [Figure 4.31], ΔY and ΔX residual spectra show the presence of HCN spectral signatures in 743–762 cm^{-1} spectral range. The close-up range further shows the matching of the shape of the two residual spectra in the HCN peak regions and confirm the presence of HCN spectral signature in a tropical spectrum measured at 12 km MIPAS-E nominal altitude. The same is true for the 17.2 km altitude level [Figure 4.33].

With an increase in altitude, the residual feature seen near spectral regions 720 and 770 cm^{-1} could possibly indicate the poorly fit temperature profiles and water vapour (H_2O) lines. These sharp line features are a function of pressure, temperature and concentration profiles at a particular altitude. Thus, the importance of use of improved spectral parameters for water vapour with decrease in altitudes increases along with accurate fitting of both temperature and water vapour profiles st such levels.

4.2.6.4.2 Mid-latitude day: Orbit 08494 scan #49

The 12.5 km [Figure 4.35, central panel] residual spectra comparison shows presence of the HCN spectral signatures with HCN spectral intensity greater than

twice the NESR value. Conversely, the blown up region of 744–748 cm^{-1} [Figure 4.35, lower panel] reveals the shape of the two spectral signatures. The left wing of both the HCN spectral features are affected by presence of some other interfering gas and hence there is need to separate the contribution due to the interfering gas from the HCN spectral contribution in order to evidently detect the presence of HCN at this altitude level.

The 15.3 km [Figure 4.37] residual spectra comparison show better match for the HCN spectral signatures with higher intensity compared to lower altitude leve in the spectral region of interest but still there is an influence of another gas contribution in the HCN peak regions. At 18.2 km [Figure 4.39], even though the HCN spectral intensity is well above the NESR limits, the non-peak regions do not agree within the MIPAS-E NESR limits.

4.2.6.4.3 Mid-latitude night: Orbit 08587 scan #16

At 10.1 km [Figure 4.41], ΔY and ΔX do not agree well and hence the HCN spectral signature cannot be detected at this altitude. Similarly at 13.0 km [Figure 4.43] and 16.0 km [Figure 4.45], the residual spectra show no match as the non-HCN peak regions do not agree at all within the MIPAS-E NESR limits. The failure to completely fit the measured spectrum at all atitudes could most likely be due to poorly fitted temperature profiles and water vapour profiles.

4.2.6.4.4 Polar summer: Orbit 08574 scan #25

For this orbit and scan, the lowest level RFM calculations were not performed and hence the results are not included in the study. The residual spectra match well at 12.9 km altitude level.[Figure 4.47] The expected and measured HCN spectral feature in the HCN_0102 MW does not match as well enough when compared to the HCN spectral feature in the HCN_0105 MW region.

At 15.8 km [Figure 4.49], the HCN_0105 MW spectral line is influenced due to presence of other interfering gas as the left wing is slighly broadened than the expected. One can say that the two HCN spectral MWs are not correlated to each other and can have different spectral feature when measured in the same spectrum

[Figure 4.49, lower panel]. The conclusion can be derived once the residual values of ΔY and ΔX are significantly reduced to the acceptable MIPAS-E NESR limits.

4.2.6.4.5 Polar winter: Orbit 08321 scan#65

The central panel in Figure at 12.0 km [Figure 4.51] show presence of HCN lines but the close-up region show no match between ΔY and ΔX. This is true for 15.0 [Figure 4.53] and 18.0 km [Figure 4.55] as well. There is significant influence of other interfering gas and the HCN spectral signature needs to be extracted by fitting the measured spectrum properly, well within the MIPAS-E NESR limits.

At all altitudes, ΔY seems to be in good agreement with ΔX within the noise level of MIPAS-E NESR. The detection method appears to show the presence of HCN spectral lines in all cases except for mid-latitude night-time. This may be due to the particular case chosen and so it was recognised that detection should be performed for a large number of profiles. This is described in section 4.2.7. Sharp spectral lines are seen at all altitudes, with increasing intensity as altitudes decreases are to be noted due to poor fit, most likely poor fitting of the water vapour spectral lines. An improvement over these lines can be made by using the Jacobian fitting analysis and also by using an improved database of spectral parameters for major interfering gases.

The Jacobian perturbation spectra [Section 4.2.4.4] can be calculated along with simulated radiance spectra using the RFM. It may be possible to improve the ΔY spectral fit by adding or subtracting calculated Jacobian spectra to approximate the inaccuracy in parameters and VMR profiles that are used in the simulated atmospheres for the forward modelling of the spectrum. The adding or subtracting of original spectrum will result in new spectrum and such a process can be repeated iteratively to obtain 'best' fit between ΔY and ΔX. The fitting of spectrum can be applied to large spectral region and successively lower tangent altitudes (similar to global fit and onion peeling methods described in Section [2.6.3]) with the exception of convergence criteria.here is based on visual inspection of the spectral residuals.

It is expected that even after such an improvement, failure to completely fit these lines is due to small errors of paremeters such as pressure and temperature

and also due to the limitations to accurately measure spectral parameters in a laboratory.

4.2.7 Step 7: Results of automated detection methodology

In this section, results of the automated detection methodology for the month of October 2003 are shown. This is to understand how well the detection method works for different MIPAS-E spectra and detects HCN in background and enhanced concentration levels. The automated detection method involves the same technique as described in section 4.1 and summary of steps for the comparison of measured and simulated limb emission spectra are covered in section 4.2.6.2, except for few modifications shown in the flowchart to encorporate the use of the MIPAS-E level 1c (L1C) files in the automated detection method. The flowchart shows the steps involved in the automated method.

The automated detection method for the HCN emission feature in HCN_0102 shows successful detection results in comparison with the HCN_0105 detection MW region mainly because there is less interference due to the major gases in the HCN spectral feature in the HCN_0102 MW region. Plots for HCN_0102 MW region are shown in Figure 4.58 and Figure 4.59 and for HCN_0105 region are shown in Figure 4.60 and Figure 4.61.

The automated detection method uses the L1C data that are generated using a utility IDL program written by Anu dudhia, l1c.pro, that extracts the MIPAS-E L1b radiance information based on the MW list generated for either detection or retrieval purpose. This is a necessary step to introduce in global detection of the HCN spectral signature to significantly reduce the computing time. A maximum of 3 cm^{-1} (121 points, MIPAS-E full resolution mode) can be handled per simulation at a specified altitude.

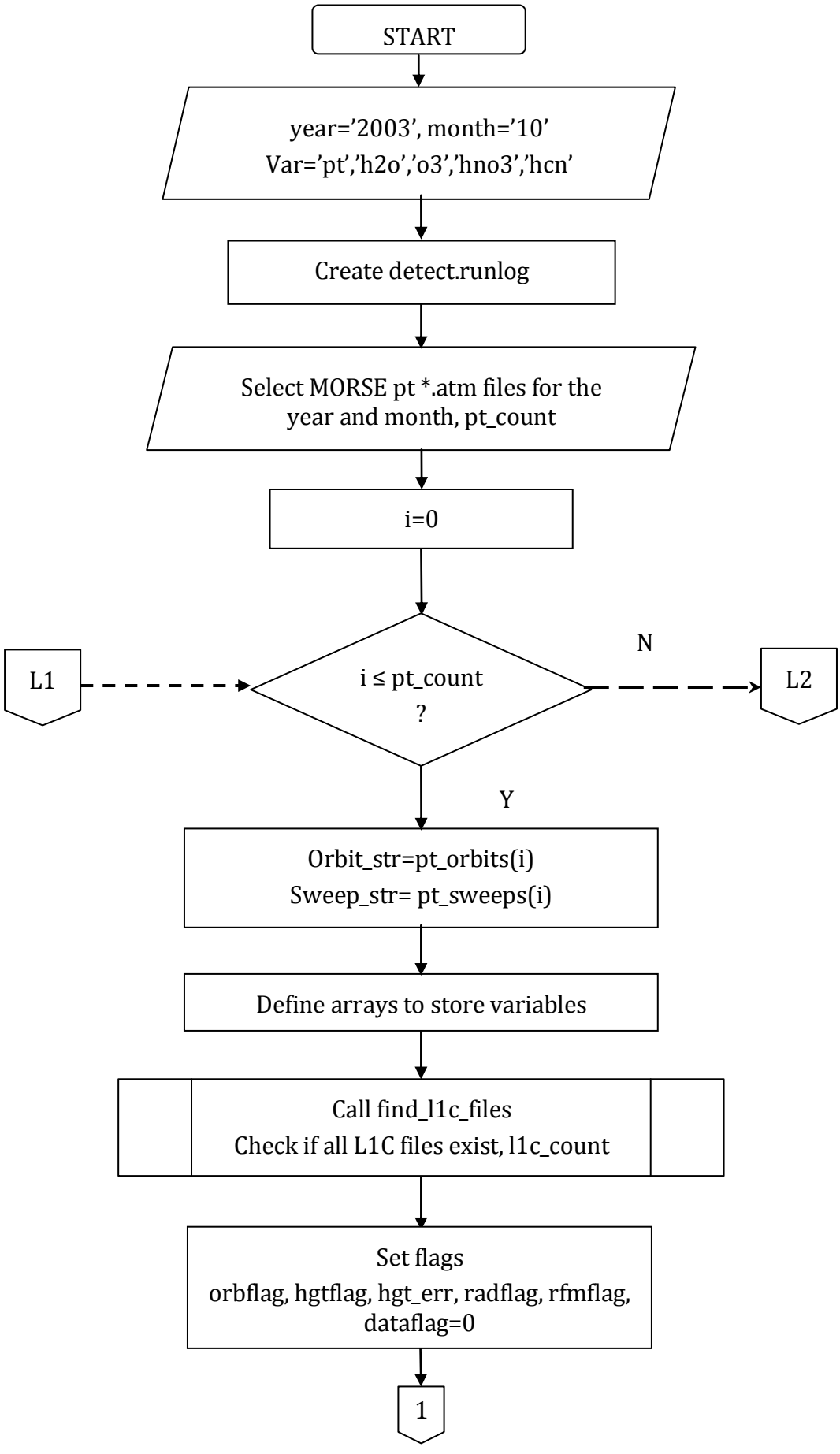
START
year='2003', month='10'
Var='pt','h2o','o3','hno3','hcn'
Create detect.runlog
Select MORSE pt *.atm files for the year and month, pt_count
i=0
L1
i ≤ pt_count ?
N
L2
Y
Orbit_str=pt_orbits(i)
Sweep_str= pt_sweeps(i)
Define arrays to store variables
Call find_l1c_files
Check if all L1C files exist, l1c_count
Set flags
orbflag, hgtflag, hgt_err, radflag, rfmflag, dataflag=0
1

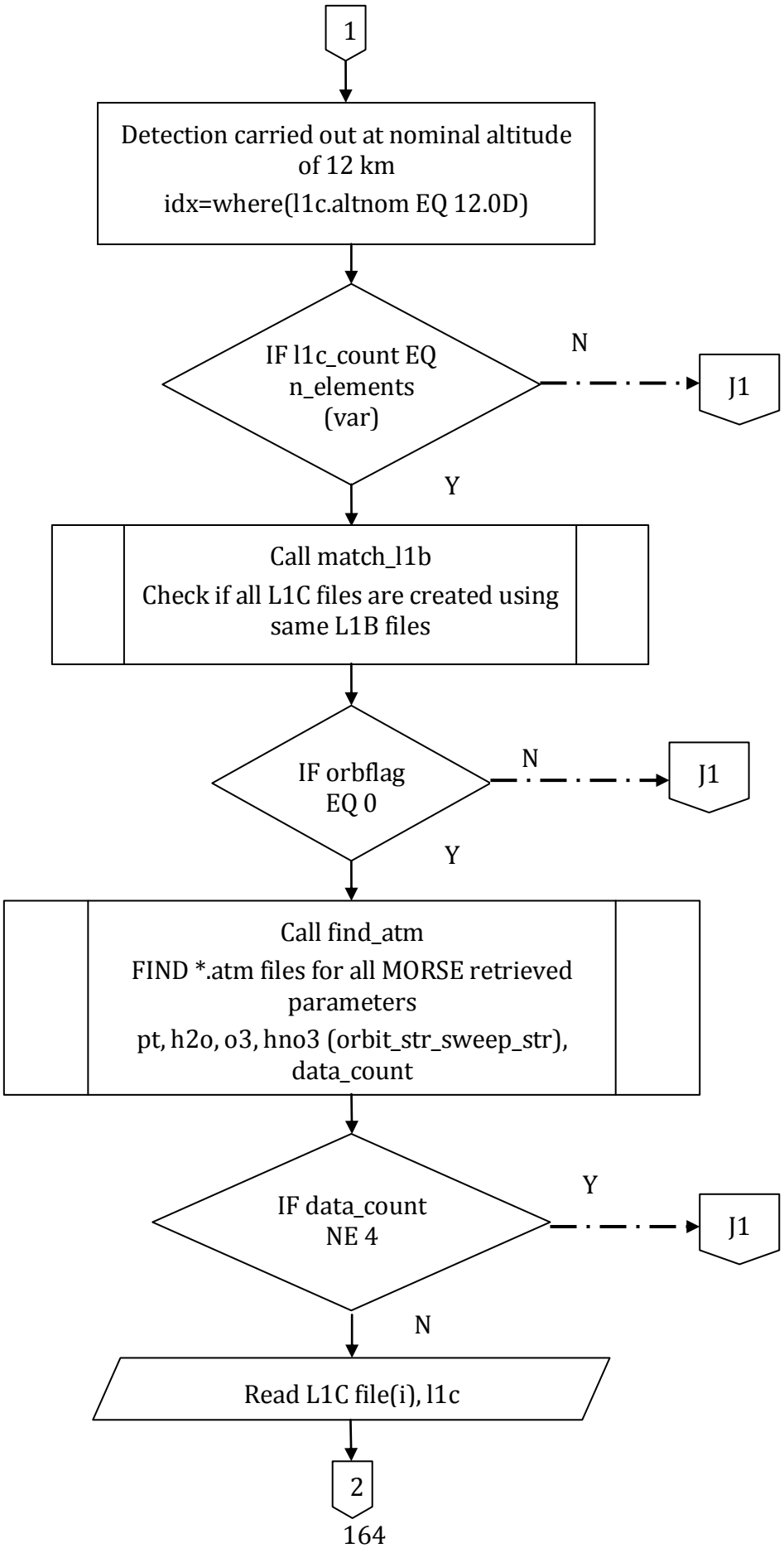
1
Detection carried out at nominal altitude of 12 km
idx=where(l1c.altnom EQ 12.0D)
IF l1c_count EQ n_elements (var)
N
J1
Y
Call match_l1b
Check if all L1C files are created using same L1B files
IF orbflag EQ 0
N
J1
Y
Call find_atm
FIND *.atm files for all MORSE retrieved parameters
pt, h2o, o3, hno3 (orbit_str_sweep_str), data_count
IF data_count NE 4
Y
J1
N
Read L1C file(i), l1c
2

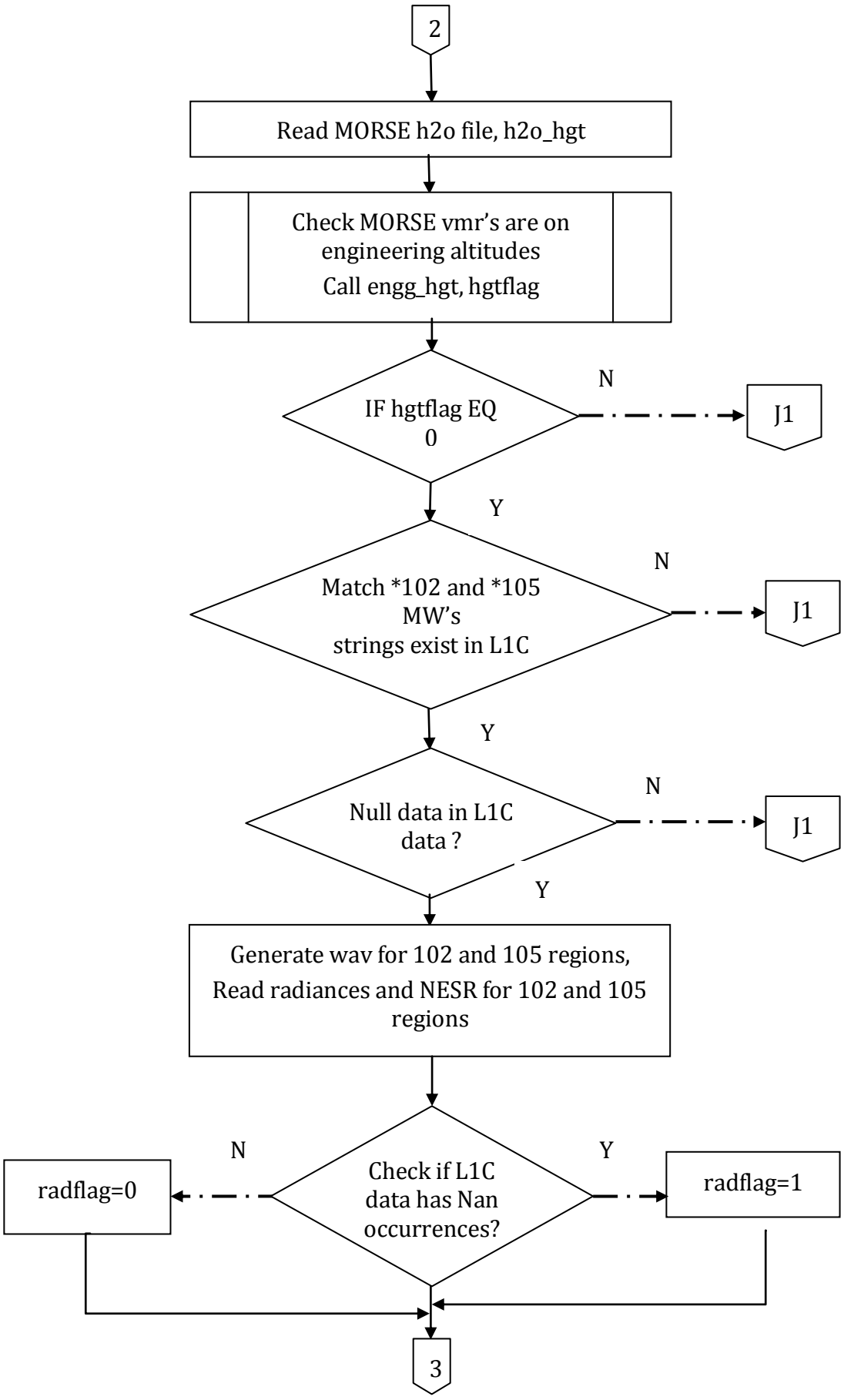
2
Read MORSE h2o file, h2o_hgt
Check MORSE vmr's are on engineering altitudes
Call engg_hgt, hgtflag
IF hgtflag EQ 0
N
J1
Y
Match *102 and *105 MW's strings exist in L1C
N
J1
Y
Null data in L1C data ?
N
J1
Y
Generate wav for 102 and 105 regions,
Read radiances and NESR for 102 and 105 regions
Check if L1C data has Nan occurrences?
N
radflag=0
Y
radflag=1
3

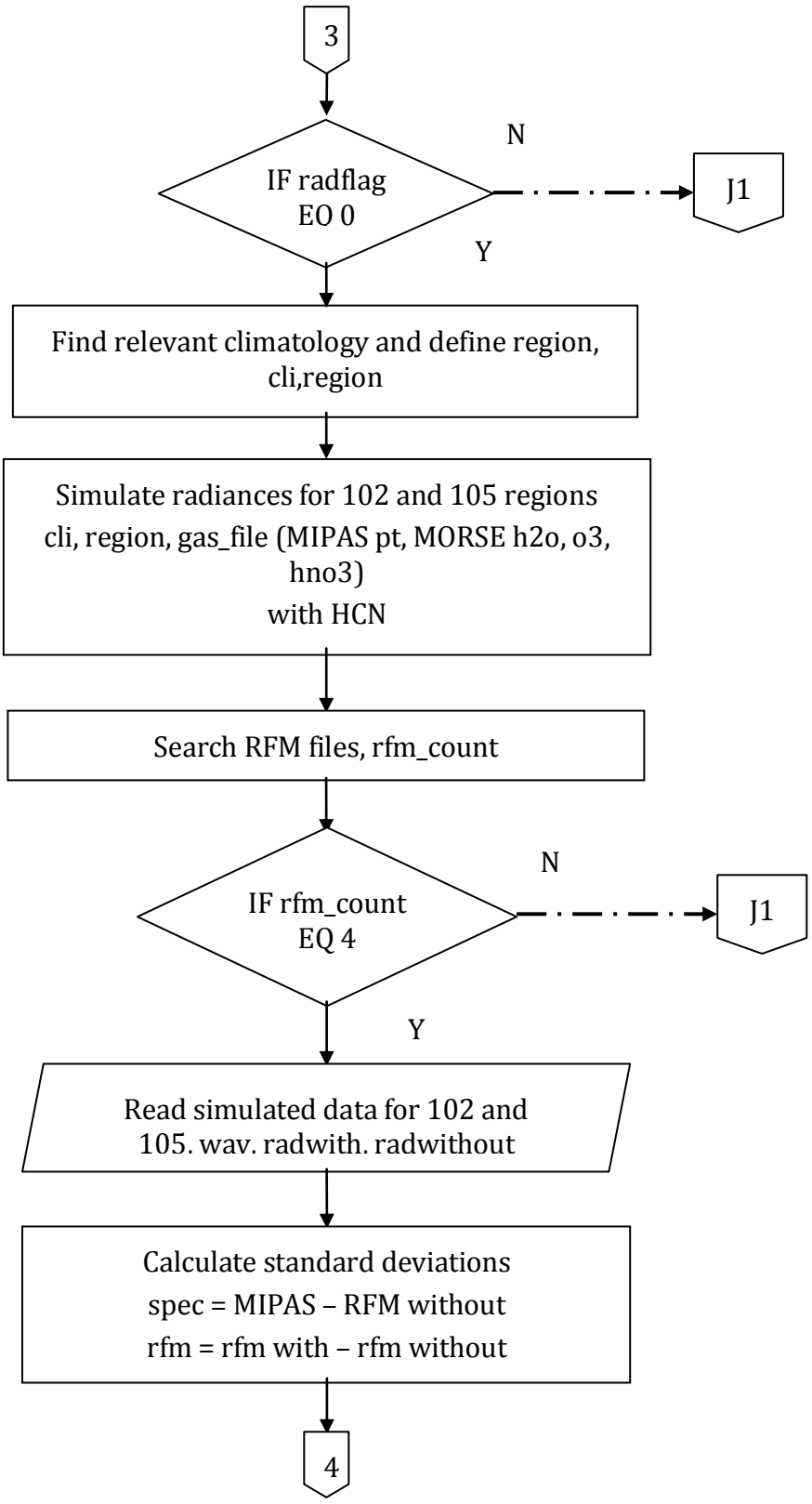
3
IF radflag
EO 0
N
J1
Y
Find relevant climatology and define region,
cli,region
Simulate radiances for 102 and 105 regions
cli, region, gas_file (MIPAS pt, MORSE h2o, o3,
hno3)
with HCN
Search RFM files, rfm_count
IF rfm_count
EQ 4
N
J1
Y
Read simulated data for 102 and
105. wav. radwith. radwithout
Calculate standard deviations
spec = MIPAS – RFM without
rfm = rfm with – rfm without
4

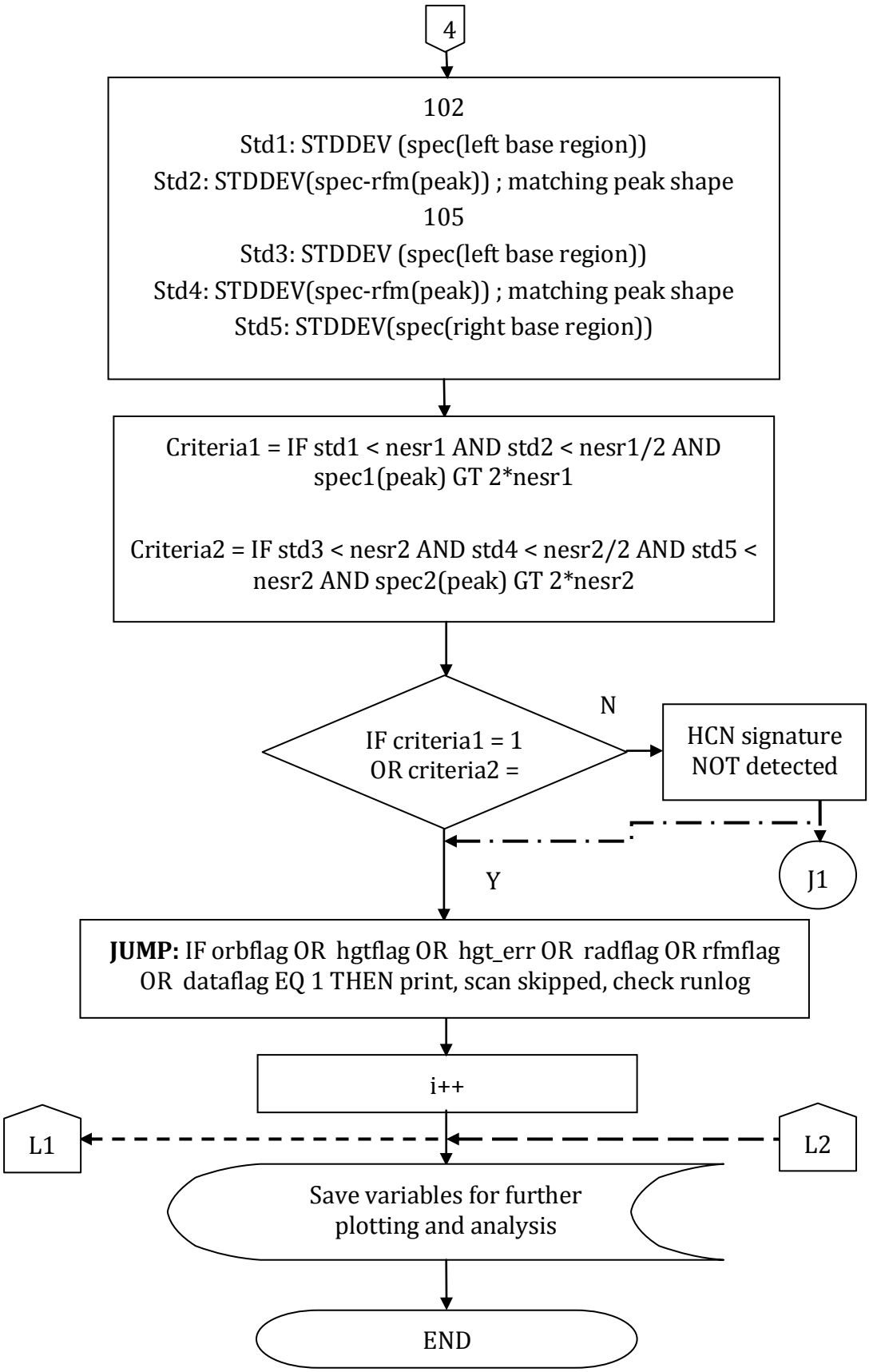

Figure 4.57: Flowchart of automated process to detect HCN emission signature in MIPAS-E level 1b data.

L1c data are apodised spectra for optimised MWs and are obtained using MIPAS-E L1b spectra (full, unapodised spectra) for the automated detection process. The L1c data files for HCN are generated for the month of October 2003 based on HCN MWs listed in Table 4.2.

A summary of the steps involved in the automated process for detecting HCN emission signatures is as follows:

1. The number of L1c data files for pressure and temperature is made to initialise the loop for automated process.
2. For each sweep for a particular orbit:
    i. Find all the L1C data files related to other variables specified such as H_2O, O_3, HNO_3 and HCN.
    ii. Check if all the L1c files are created using the same L1b spectra.
    iii. Find all atmospheric profiles for H_2O, O_3 and HNO_3 based on the MORSE [Chapter 5] retrieval algorithm.
3. Read radiances at the selected nominal altitude range from L1c data for HCN MWs [Table 4.2].
4. Filter data using the cloud index to ignore cloudy profiles.
5. To simulate the measured radiances:
    i. To keep a consistent altitude grid for all parameters used in the detection method, a pressure-temperature atmospheric profile is created based on MIPAS-E l2 data using time ID from l1c data and the pressure-temperature data is filtered using MIPAS-E l2 convergence and quality flag criteria.
    ii. All atmospheric profiles based on MORSE retrieval used in the detection method should be on one defined altitude grid, i.e., engineering altitude grid.
    iii. Find relevant climatology profiles for all other interfering gases.

iv. Simulate radiances for HCN_0102 and HCN_0105 MWs, one with HCN gas included and the other without HCN gas with a spectral resolution of 0.025 cm^{-1}.

v. The residuals ΔY and ΔX [equations (4.1 and (4.2] are calculated.

6. To detect the HCN spectral feature, ΔY and ΔX need to be compared using following criteria:

i. The peak value of the HCN spectral feature must be greater than two sigma NESR value of the instrument.

ii. The standard deviation for ΔY must be less than half the NESR in the base region so that it shows that the calculations did not miss any major interfering gas molecule in the region of interest.

iii. For the shape of the HCN spectral feature, the difference between ΔY and ΔX spectrum should be less than half the NESR in the HCN peak region.

The results based on above detection methodology for the month of October 2003 are shown in Figure 4.58 to Figure 4.61. The results are for HCN_0102 and HCN_105 MW regions at the 12 km nominal altitude. Offset in the MIPAS–RFM spectra fit can be observed as aerosols are not fitted well in the selected MW, but this should not affect the HCN spectral feature. One should note that detection in the mid-latitudes now appears to show the presence of HCN spectral feature in both HCN_0102 and HCN_0105 MW consistently across many spectra.

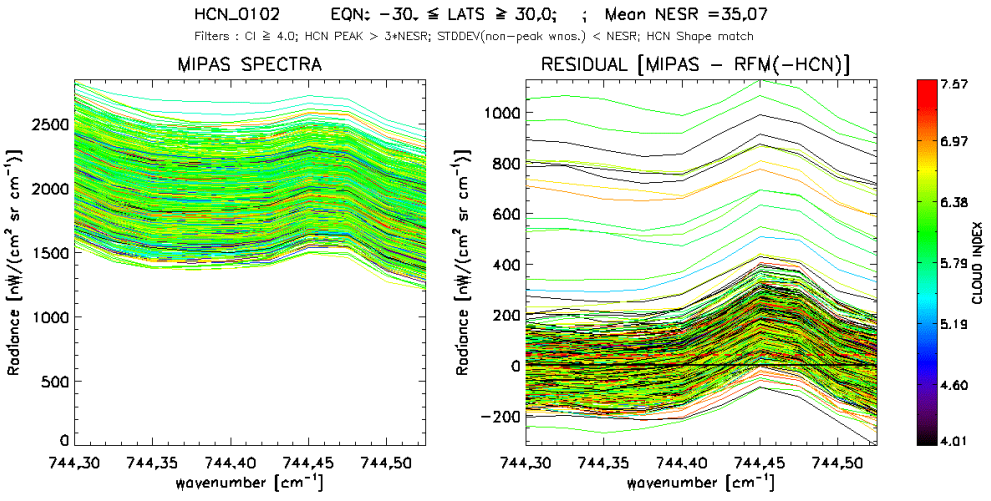

(a)

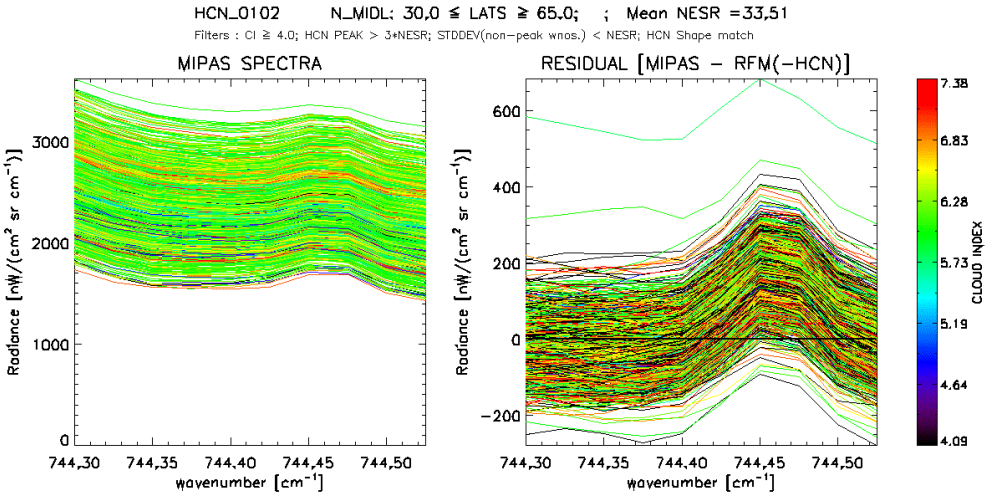

(b)

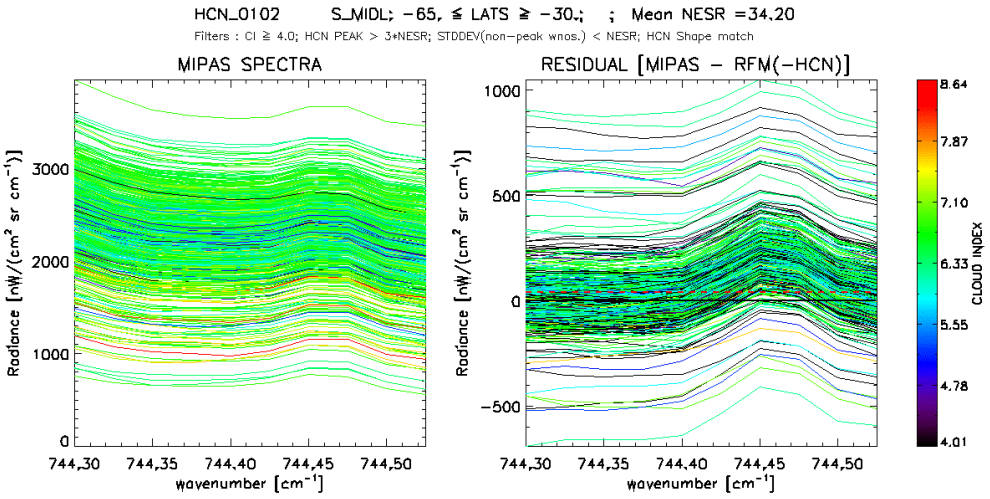

(c)

Figure 4.58: MIPAS-E spectra (left) and measured residual spectra (MIPAS−RFM(−HCN)) (right) in the HCN_0102 MW region. The red dotted line on the plots of residual spectra represents MIPAS noise level in Band A of MIPAS spectrum. The spectra are plotted for (a) tropical, (b) Northern Mid-latitudes and (c) Southern Mid-latitudes and spectra are colour coded using cloud index value.

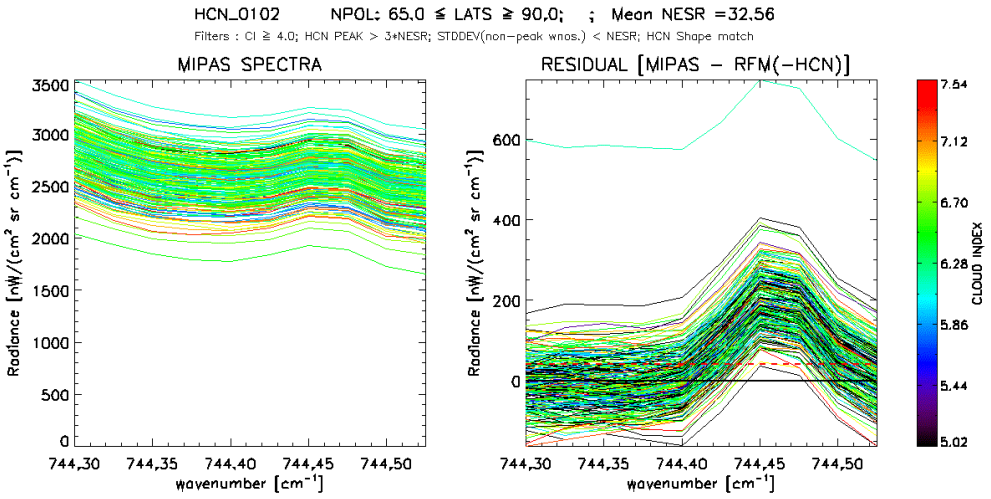

(a)

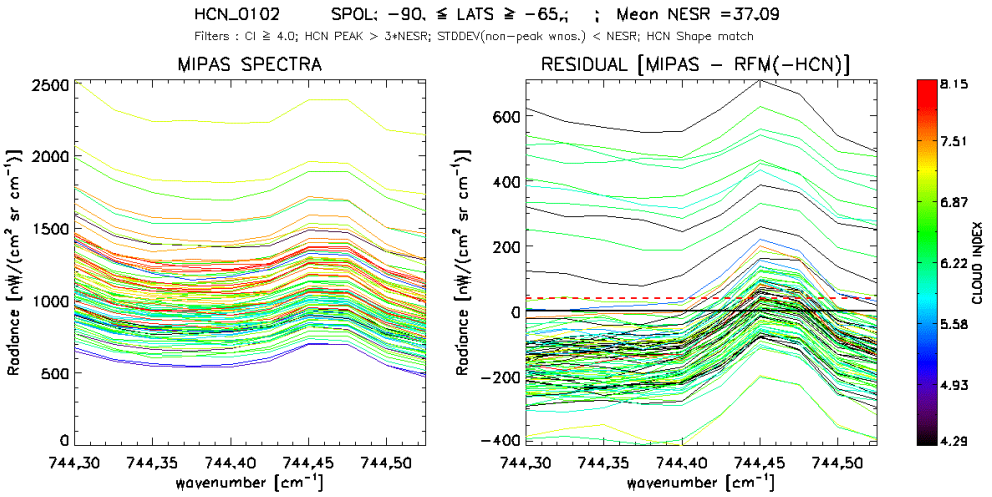

(b)

Figure 4.59: MIPAS-E spectra (left) and measured residual spectra (MIPAS−RFM(−HCN)) (right) in the HCN_0102 MW region. The red dotted line represents noise level in band A of MIPAS-E spectrum. The spectra are plotted for (a) Northern Polar and (b) Southern Polar regions and spectra are colour coded using cloud index value.

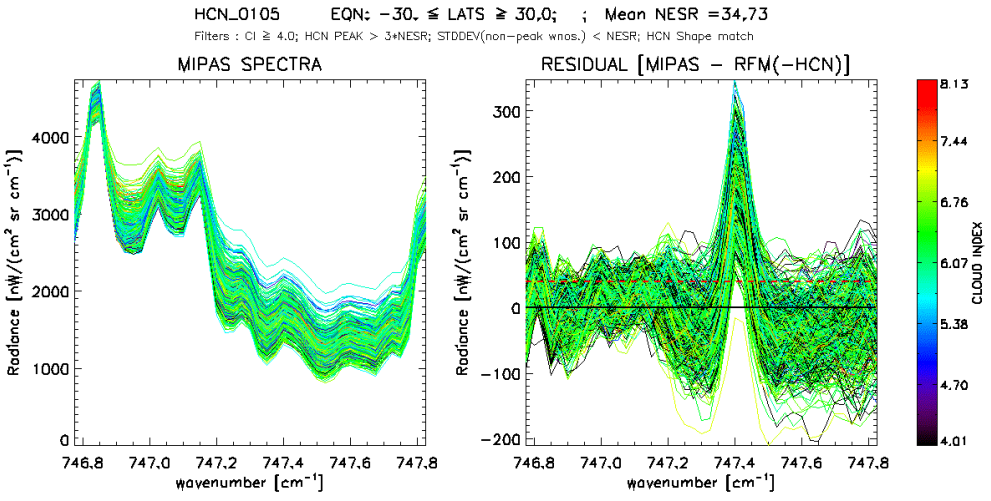

(a)

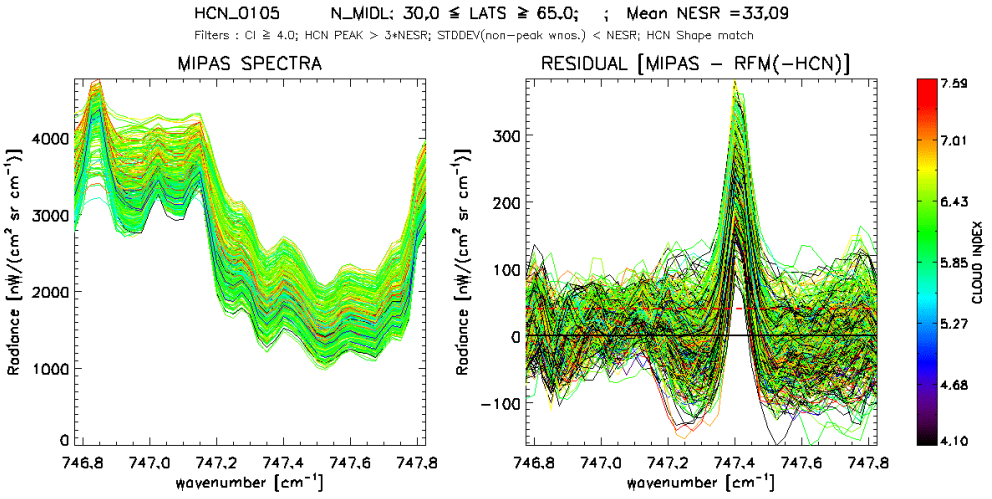

(b)

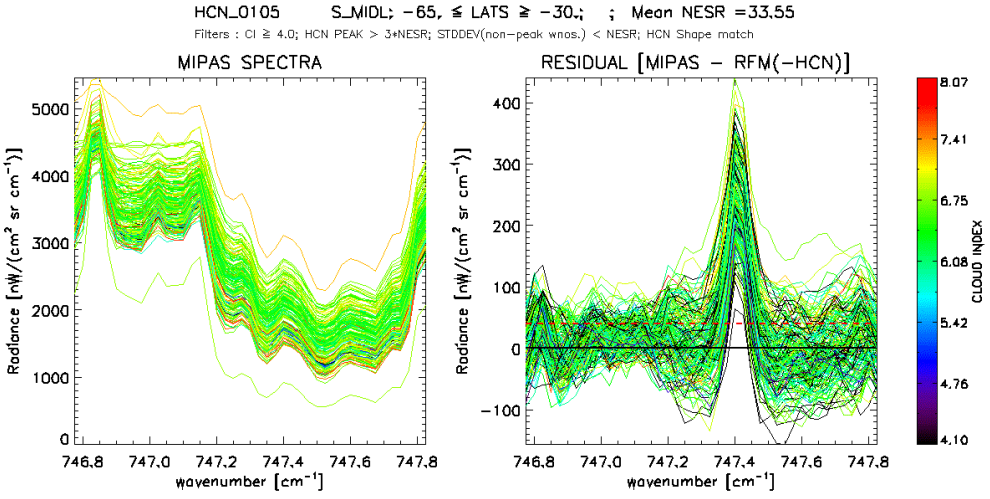

(c)

Figure 4.60: MIPAS-E spectra and measured residual spectra (MIPAS−RFM(−HCN)) in HCN_0105 MW region. The red dotted line on the plots of residual spectra represents MIPAS noise level in Band A of MIPAS spectrum. The spectra are plotted for (a) tropical, (b) Northern Mid-latitudes and (c) Southern Mid-latitudes and spectra are colour coded using cloud index value.

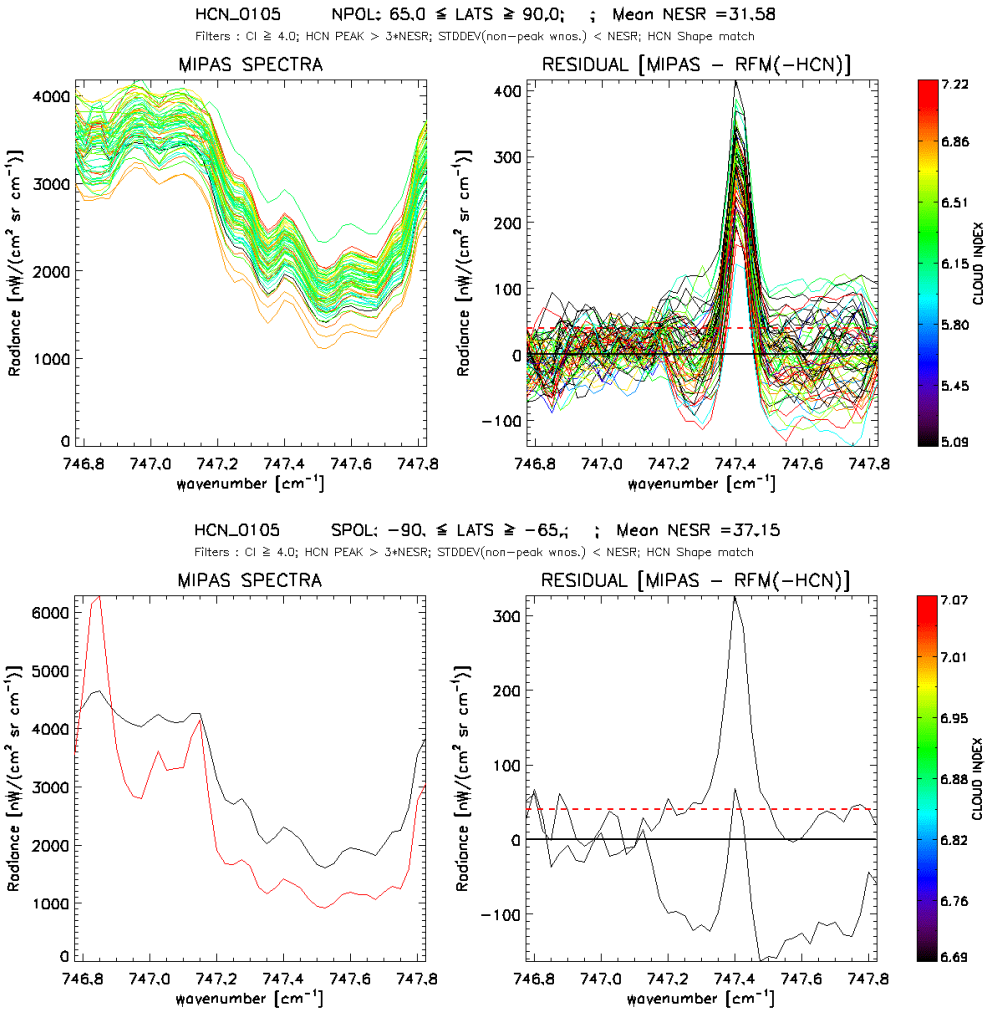

Figure 4.61: MIPAS spectra and measured residual spectra (MIPAS–RFM(–HCN)) in HCN_0105 MW region. The red dotted line represents MIPAS noise level in Band A of MIPAS-E spectrum. The spectra are plotted for (a) Northern Polar and (b) Southern Polar regions and spectra are colour coded using cloud index value.

4.2.8 Step 8: Global detection results

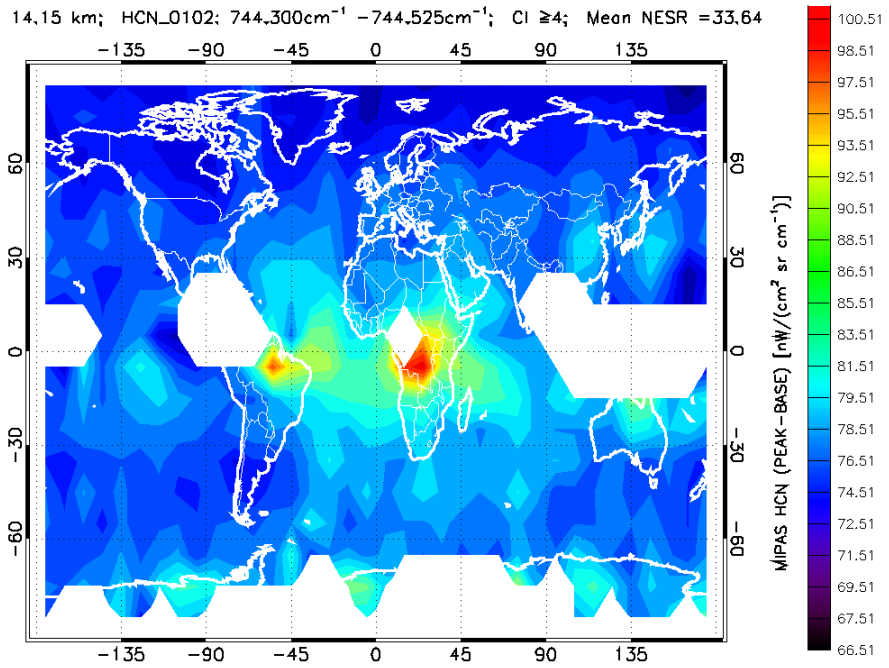

Figure 4.62: Difference in MIPAS-E radiance from peak to base using HCN_0102 MW for the month of October 2003. The white patches represent no detection in the MIPAS-E spectra.

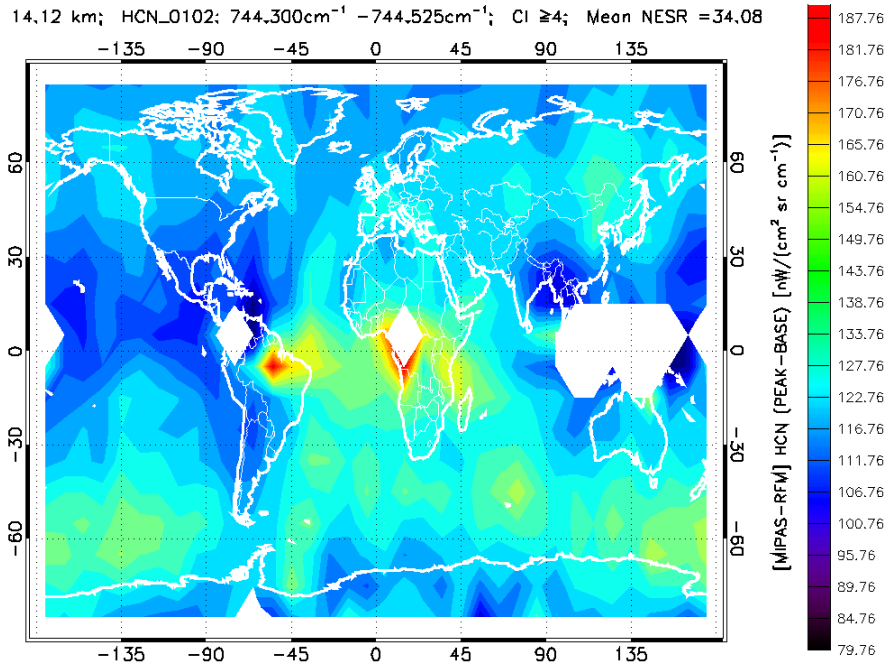

Figure 4.63: Difference in ΔY spectrum (MIPAS−RFM(without HCN)) radiance from peak to base using HCN_0102 MW for the month of October 2003. The white patches represent no detection in the MIPAS-E spectra.

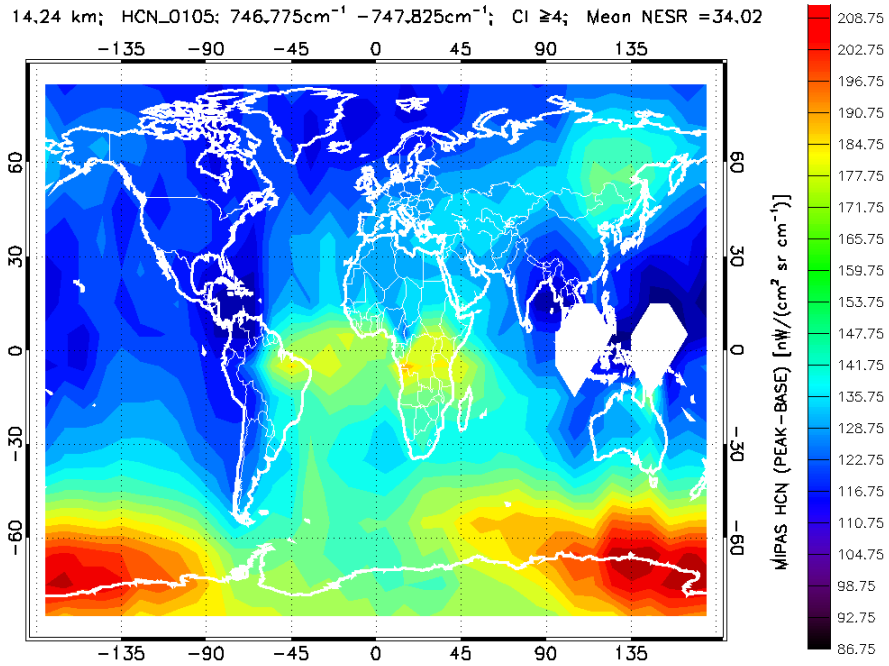

Figure 4.64: Difference in MIPAS-E radiance from peak to base using HCN_0105 MW for the month of October 2003. The white patches represent no detection in the MIPAS-E spectra.

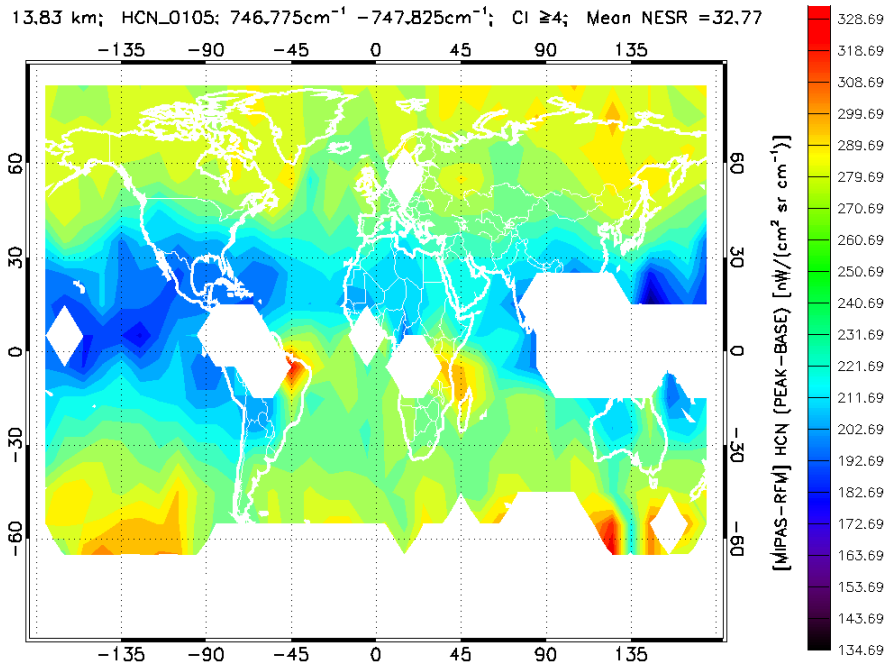

Figure 4.65:Difference in ΔY spectrum (MIPAS–RFM(without HCN)) radiance from peak to base using HCN_0105 MW for the month of October 2003. The white patches represent no detection in the MIPAS-E spectra.

Figure 4.62 to Figure 4.65 represent the global map of MIPAS-E radiance, where the residual of the HCN peak radiance to the baseline value in the HCN_0102 and HCN_0105 MW regions is calculated. The baseline was calculated as the mean value of radiance in the HCN_0102 MW HCN peak region, whereas for HCN_0105 MW, the median value was treated as the baseline value to measure the HCN peak strength. Figure 4.64 andFigure 4.65 represent the global maps of ΔY spectrum (difference between the MIPAS-E and simulated spectra without HCN), where again the difference of the peak radiance to the baseline defined as the minimum value in the HCN peak region for both the MW regions again to measure the strength of HCN peak in the residual spectra. The white patches represent data that does not satisfy the following filtering criteria:

1) The HCN peak strength has to be greater than twice NESR.
2) The standard deviation in the non-peak regions has to be less than the NESR.
3) For the shape of the HCN spectral feature, the difference between the ΔY and ΔX spectrum was calculated and thus, this difference had to be less than half NESR in the HCN peak region.

The presence of the HCN emission feature in MIPAS-E spectral data can be confirmed once these criteria are satisfied. Only the first criterion was used to detect HCN spectral signature in MIPAS-E spectral data assuming that the HCN spectral signature was clear enough to be detected. The third criterion for residual spectra was ignored since a large amount of data remained unfiltered for both the MWs. The automated detection process manages to detect HCN sources and transport with some discrepancies.

The automated detection works well in case of HCN_0102 MW with some inconsistency in the South Polar Regions. By simply using MIPAS-E radiance the detection fails in the HCN_0105 MW for North Eastern and South Polar Regions. Figure 4.63 and Figure 4.65 shows the HCN spectral feature is masked by other interfering gases in both the MW regions. The automated detection for residual analysis works in the HCN_0102 MW region with inconsistency in Polar Regions but fails in the HCN_0105 MW region. Figure 4.62 and Figure 4.64 show the importance

of input parameters used to fit the MIPAS-E spectral data and how well the detection of HCN work.

Thus, it is crucial to understand the atmospheric spectra well enough in the HCN MW regions as well as input parameters used to fit the spectra.

4.3 Summary

The evidence presented in the chapter strongly indicates the presence of a detectable HCN limb emission signature in the MIPAS-E spectral data [Section 4.2.6.3, 4.2.7 and 4.2.8].

As a first approximation, the measured MIPAS-E spectrum and simulated RFM fit agree well enough, as also seen in the comparison of ΔY and ΔX residual spectra. MIPAS-E measured spectra based on five different latitude bands are selected to show the evidence of the presence of HCN line signatures and also where HCN is not detected. At 12 km nominal altitude level, clear evidence of HCN line signature is seen in the tropics and polar winter case, whereas mid-latitude and polar summer case show influence due to presence of other interfering gas. The comparison of ΔY and ΔX residual spectra in case of mid-latitude night show disagreement, hence, no HCN line signature is detected. Sharp lines are seen at all altitudes in all five cases, and hence improvement over these lines is needed. Such an improvement can be achieved by using the Jacobian fitting analysis and by using improved spectral database of major interfering gases.

The HCN_0102 (744.3000–744.5250 cm^{-1}) and HCN_0105 (746.7750–747.8250 cm^{-1}) MW regions are suitable for the detection of the HCN spectral feature as the intensity of the HCN spectral feature is strong [Section 4.2.4.3] and importantly, strength of the interfering species is the lowest.

The detection of the HCN spectral feature becomes increasingly complicated at altitudes less than 9 km [Section 4.2.4.3] due to spectral saturation by high concentrations of stronger infrared absorbers such as water vapour (H_2O), reducing the intensity of HCN spectral signal below the instrument's noise level in preferred HCN MW regions.

Detection at higher altitudes (>21 km for HCN_0102 and >27 km for HCN_0105) has not been made. This is due to the expected low concentrations of HCN at such high altitude, which is expected to give very poor signal-to-noise ratio.

The detection of the HCN spectral feature depends on the accurate fitting of pressure and temperature and can be fitted well using pre-retrieved values based on MIPAS-E operational level 2 or MORSE retrievals [based on Chapter 5]. Similarly, the interference due to major gases in both the MWs such as H_2O, O_3 and C_2H_2 can also be reduced by fitting the spectra using pre-retrieved values.

Sensitivity plots suggest that apart from major interfering gases such as H_2O, O_3 and HNO_3, one needs to consider contributions due to trace gases such as N_2O_5, CH_3Cl and C_2H_2 which are significant enough to overlap with the HCN spectral feature making it difficult to separate from the rest of the trace gas contributions in order to be detected in the HCN_0102 and HCN_0105 MW regions. Recall that in this chapter, climatological values for these gases have been used. It is clear that retrieval of these species is necessary to improve the global detection maps shown in this chapter. This reflects in the global plots of HCN detection as it includes only MIPAS-E operational pressure, temperature, and the MORSE retrieved H_2O, O_3 and HNO_3 to fit the MIPAS-E spectral data.

During the automated detection process [Section 4.2.7]. The global detection of HCN spectral features using HCN_0102 and HCN_0105 MW regions was successful. Further refinement of detection criteria for the HCN_0105 MW region needs to be taken into consideration. Fitting of aerosol extinction and water vapour (H_2O) profiles is necessary below 15 km to separate the HCN spectral signature from the rest of the contributions.

Using an automated detection process, we can reveal the presence of HCN spectral feature at both the North and South Polar Regions. To validate the presence of HCN we need to retrieve the accurate concentration levels and further study the source and variability of HCN at Polar Regions. Higher HCN signals observed in South Polar regions [Figure 4.59(b) and Figure 4.61(b)] could possibly indicate

transport of HCN towards the South Pole or further investigation needs to be carried out by means of in-situ measurements to find any other source of HCN.

Despite the detection of high concentration levels of HCN, the radiance contribution due to the HCN signal is relatively small compared to the total atmospheric radiance. Thus, the detection of the HCN spectral feature requires accurate fitting of many parameters prior to the spectral fitting of HCN. The most important criteria for successful detection of the HCN spectral feature are as follows:

1. Accurate optimized retrievals for pressure and temperature profiles
2. Accurate optimized retrieval profiles of H_2O, O_3, HNO_3, CH_3Cl and N_2O_5 which are very important in chosen spectral MW regions for HCN detection
3. Accurate and precise measurements of spectral parameters related to all interfering gases

Global automated detection maps of HCN reveal the importance of understanding atmospheric spectra and input parameters used to fit the MIPAS-E spectral data in both the HCN MW regions.

CHAPTER 5

5. Retrieval of HCN using the MORSE algorithm

5.1 Retrieval approach

In Chapter 4, the detection of Hydrogen Cyanide (HCN) in HCN_0102 and HCN_0105 MWs is discussed. It was shown that the high spectral resolution of MIPAS-E can be exploited to detect HCN spectral signatures. The retrieval of HCN profiles is complicated by the presence of major radiatively active gases in the selected MWs. Figure 4.10 to Figure 4.15 show the interfering spectral features that mask the HCN spectral signature in the 710–780 cm^{-1} wavenumber region. Even though it is assumed that 744.300–744.525 and 746.775–747.825 cm^{-1} MW regions are the 'best' spectral regions to detect and retrieve HCN profiles, one challenge still lies in the fact that the effects due to CH_3Cl and N_2O_5 may need to be characterised if possible. HCN spectral features that lie between wavenumbers 760–780 cm^{-1} are not significantly affected by the presence of CH_3Cl and N_2O_5, but these spectral features are well below noise levels at altitudes above 12 km at low concentration levels. Thus, it is difficult to retrieve HCN in spectral regions between wavenumbers

760–780 cm^{-1}. The month of October 2003 is chosen to retrieve HCN VMR profiles following the HCN detection results. The success of MORSE HCN retrieval results would further verify the HCN detection results but obviously would quantify the amount of HCN present.

5.1.1 MIPAS Orbital Retrieval using Sequential Estimation (MORSE)

The fine spectral resolution (unapodised, 0.025 cm^{-1}) of the MIPAS-E instrument allows simultaneous measurement of more than 25 trace gas species [Section 3.2]. Thus to invert MIPAS-E observations and retrieve concentration values of species other than operationally retrieved MIPAS-E level 2 data products (pT, H_2O, O_3, HNO_3, CH_4, N_2O and NO_2) a number of retrieval codes have been developed under the AMIL2DA project [Section 3.4.2]. One of the retrieval codes developed is the MIPAS Orbital Retrieval using Sequential Estimation (MORSE) algorithm, a technique implemented at the University of Oxford to retrieve both strong and weak trace gas profiles from MIPAS-E spectral data. The aim of the MORSE project was to either replicate or improve upon the parameters retrieved by using the ESA L2 operational processor.

The key difference between the ESA L2 operational processor and the MORSE is that the former uses a linear least squared global fitting technique whereas the latter uses a sequential estimation method. The MORSE retrieval algorithm steps down vertically from high altitudes, thus reducing upward propagating instabilities. The solution is found within an uncertainty limit by using *a-priori* as a constraint (in this case standard climatology reference atmospheric profiles [Remedios *et al.*, 2007(c)] are used as *a-priori* information). The scheme uses selected MWs, which contain the most information of the target gas and a line-by-line radiative transfer forward model (Oxford's RFM) is used to fit these spectral regions measured by MIPAS-E at each altitude scan in a particular orbit. The solution is found by minimizing the cost function χ^2 through an iterative process [Sections 2.6.2 and 2.6.3].

5.1.1.1 Microwindow selection

The MORSE algorithm can employ any user-defined MWs for trace gas retrievals. One approach to MW selection is to simulate the propagation of random noise through the retrieval and select measurements that maximise the information content or degrees of freedom of the signal [Rodgers, 2000]. The approach developed at the University of Oxford for MIPAS-E by Dudhia*et al.* [2002] selects MWs by simulating one full profile retrieval as a function of increasing number of spectral data points used, including the propagation of systematic error terms. Microwindows are grown in such a manner that the spectral range selected has the maximum information content for the target gas retrieval by minimizing the total error including both systematic and random error components [Section 3.4.2.1]. This also gives a full error analysis for the final retrieval. The final MWs are chosen when the information content cannot increase further (growing MWs) or when the maximum width of 3 cm^{-1} is reached. Microwindow selection can also be prioritised through different criteria, e.g., sensitivity to a particular altitude region.

A list of 10 MWs [Table 5.1] was generated using the 'mwmake.pro' algorithm for HCN. This study focuses on the HCN_0102 and HCN_0105 MW regions both for detection of HCN spectral signatures and retrieval of HCN VMR profiles from the MIPAS-E measurements. MORSE processes *n* number of MWs sequentially for any given parameter in the order specified. Theoretically, there should be no difference in the final retrieved result, but there is always some difference due to non-convergence in any MW for a particular MIPAS-E measurement. The retrieval analysis is based on the detection analysis described in Chapter 4 [Table 4.2]. A subset of these two MWs is used for the retrieval analysis of HCN, in order to fit only the HCN peak region in both the MWs [Table 5.2], thus maximising the HCN information content relative to the baseline region.

Anu Dudhia had previously generated list of MWs for pressure, temperature and the other trace gases in order to carry out the MORSE retrievals required for this work.

Microwindow number	Spectral range (cm^{-1})	Altitude level (km)	Interfering gases in the MW
HCN_0101	711.1250–714.1250	6–60	CO_2, H_2O, O_3, HCN, C_2H_2, CH_3Cl , N_2O, NO_2, NH_3
HCN_0102	744.3000–744.5250	6–18	H_2O, CO_2, O_3, HCN, N_2O_5, CH_3Cl, C_2H_2, HNO_3, NH_3, NO_2, C_2H_6, COF_2
HCN_0103	761.9500–762.2250	9–21	CO_2, H_2O, O_3, HNO_3, C_2H_2, HCN, $ClONO_2$, N_2O_5, CCl_4, COF_2, NO_2, NH_3, CH_3Cl, C_2H_6
HCN_0104	735.4500–735.7750	18–30	O_3, CO_2, N_2O_5, HCN, HNO_3, NO_2, COF_2, CH_3Cl
HCN_0105	746.7750–747.8250	6–27	H_2O, CO_2, O_3, HCN N_2O_5, CH_3Cl, HNO_3, C_2H_2, NH_3, NO_2, COF_2, C_2H_6
HCN_0106	732.3750–732.9750	9–39	O_3, CO_2, H_2O, HCN, N_2O_5, CH_3Cl, C_2H_6, HNO_3, NO_2
HCN_0107	764.9500–765.3250	6–33	H_2O, CO_2, O_3, HCN, $ClONO_2$, N_2O_5, C_2H_2, COF_2, HNO_3, C_2H_6, NO_2, CH_3Cl, NH_3
HCN_0108	1450.3250–1451.9000	6–60	H_20, O_2, HCN, CH_4, O_3
HCN_0109	726.4500–726.8250	12–36	CO_2, O_3, HCN, H_2O, N_2O_5, CH_3Cl, NO_2, HNO_3, N_2O
HCN_0110	738.4500–738.8000	6–21	H_2O, CO_2, O_3, C_2H_2, HCN, N_2O_5, HNO_3, CH_3Cl, NO_2, C_2H_6

Table 5.1: List of MW generated for HCN in the order of expected MW information content from the MIPAS-E spectral measurements.

HCN region	MWs generated by University of Oxford (a)	Updated HCN regions	MW subsets for HCN retrieval analysis (b)
HCN_0102	744.300–744.525	HCN_0115	744.375–744.525
HCN_0105	746.775–747.825	HCN_0112	747.350–747.500

Table 5.2: HCN Microwindows used in this thesis. Column (a) represents the MWs generated by the University of Oxford. A subset of the HCN_0102 and HCN_0105 MWs used for retrievals is listed in column (b).

5.1.1.2 Input spectral data-L1C files

MORSE reads MIPAS-E L1b spectral data in L1C format. A utility l1c.pro, an IDL routine, is used to extract MIPAS-E L1b radiance information based on the MW list generated for retrieval. The program also apodises (using the Norton-Beer 'strong' apodisation function) the MIPAS-E L1b spectra before writing it to L1C files, suitable for input to MORSE. For MORSE version 3, the L1C format v2.0 or later must be used because these files contain an additional record that identifies the viewing geometry and resolution. One L1C file is generated for each scan (each scan contains 17 spectra; 72 scans per orbit-[Section 3.2.1]) of a particular orbit and contains the radiances required for all the MWs listed in the input file at user specified tangent altitudes. L1C files were generated by extracting MIPAS-E radiances for pressure, temperature, aerosol extinction and other trace gases such as H_2O, O_3, HNO_3, C_2H_2 and HCN based on the respective input MW list files and specified tangent altitudes. It is assumed that the respective input parameter has the best information for specified MWs and tangent altitude ranges. No further reduction of MWs is applied to input parameter files. C_2H_2 L1C file information is based on the study done by Parker [2010]. L1C files generated for HCN are based on the HCN_0112 MW list file which has the MIPAS-E radiance information for 6–27 km.

5.1.1.3 *a-priori* covariance

The MIPAS reference atmospheres (RAMSTAN) constructed by Remedios *et al.* [2007(c)] contains standard climatology profiles for the tropics, mid-latitudes and polar regions, which remains the same for HCN [Figure 4.6]. The *a-priori* covariance for HCN assumes an uncertainty of 1000% on the *a-priori* profile as little is known about the expected accuracy of the retrieved HCN profile. A 1000% uncertainty on the *a-priori* profile covers events of HCN concentration levels in both background and biomass burning events. The *a-priori* profile is correlated also through the covariance matrix with a vertical length scale of 3 km. This shows how adjacent layers are related in the atmosphere and, if at any given layer HCN concentration levels are atypically high then it is most likely that the HCN VMR value is higher in layers above and below the retrieved level. This is true for the pre-retrieved parameters as well [Section 5.1.1.6.5]. For, S_a ,a first order auto-regressive model (an exponential function, $e^{\delta z/h}$) with a vertical correlation length (h) of 3 km determined its off-diagonal elements. The off-diagonal elements of S_y were set to zero (assuming no noise correlation between different altitudes).

5.1.1.4 Cloud detection criteria

Clouds are detected using the process described in Section 3.4.2.1 [Spang *et al.*, 2004]. A cloud index value is determined by calculating the ratio between mean radiances in the 788–796 cm^{-1} MW region which remains unaffected by clouds and the 832–834 cm^{-1} MW region which is dominated by aerosols and clouds with a threshold value of 2.0. If the ratio in a profile is found to be below this threshold value, the measurements at this altitude and all the altitudes below are flagged cloudy; otherwise, the retrieval is performed. The quality of data is subsequently filtered based on the cloud index (CI) values greater than or equal to 4.0, to filter cloudy data.

5.1.1.5 Convergence criteria

The MORSE retrieval process is iterative hence it requires minimizing the cost function χ^2 value that is computed followed by evaluation against the convergence criteria.

1) The maximum relative difference of the χ^2 value from the previous iteration to the current χ^2 value must be less than the threshold of 0.2.

2) The minimum value of χ^2 convergence is set to 1.5.

3) The maximum number of allowed iterations is limited is 10 due to general computer time constraints.

The retrieval is stopped if any of the above criteria is satisfied. A typical value of χ^2 equal to 2.0 is used to test the quality of the retrieved data otherwise specified.

5.1.1.6 Retrieval requirements

5.1.1.6.1 Spectroscopic database

For the HCN retrievals using MORSE, HITRAN 2004, a spectroscopic database file (in binary format), is used for all the absorbing molecules for HITRAN IDs less than 50 and cross-section files for HITRAN IDs greater than 50. Details of HITRAN 2004 can be found in Section 4.2.4.5. The dedicated database version for MIPAS-E based on Section 3.4.2 (hitran_mipas_pf3.3_ifort22.bin) that contains updates for C_2H_6 and NO^+ line parameters [Flaud and Ridolfi, 2007] is used.

5.1.1.6.2 Reference climatology profiles

Atmospheric profiles [Section 4.2.4.1.1] are used to specify both *a-priori* for retrieved species and fixed values for un-retrieved species. The order in which the climatology profiles are specified is important as the first file determines the altitude grid on which subsequent files are interpolated and stored. Previously, retrieved profiles within the same scan had to be specified in the *L2P section of the MORSE driver table, thus avoiding unnecessary interpolation. The RAMSTAN climatology profiles are used for all *a-priori* profiles.

5.1.1.6.3 Instrument line shape (ILS) and Field of View (FOV) requirements

An AILS file [Section 4.2.5.1] is needed that covers all the MWs specified in the list. Separate files can be provided for particular spectral regions. MORSE convolves with the MIPAS-E apodised ILS file (a pre-flight ground measurement estimate) similar to the RFM as described in Section 2.5.4. A FOV shape file is needed to represent the MIPAS-E FOV. It is assumed that the FOV does not have any spectral dependence; thus, one single FOV (3 km 5-point; Section 2.5.4) represents all bands of MIPAS-E.

5.1.1.6.4 Retrieval grid

The retrieval grid is defined in terms of four different grid types: altitude (km), pressure (mb), tangent points by specifying sweep indices and tangent points specified by nominal altitudes (km). All the retrievals in this thesis were performed using the last mentioned grid type. The HCN retrievals in the HCN_0112 MW case were set to 9–27 km in terms of MIPAS-E nominal altitudes (km) in an increasing order.

5.1.1.6.5 List of parameters to be retrieved

The total radiance measured by the MIPAS-E is the sum of all the interfering gases in a particular MW at a particular pressure and temperature. Hence, before retrieving HCN VMR profiles, parameters are needed to be retrieved in the following order; Pressure and temperature (pT) (to be retrieved jointly) and major interfering gases such as: water vapour (H_2O), ozone (O_3), nitric acid (HNO_3), acetylene (C_2H_2).

An attempt to retrieve CH_3Cl using the MORSE algorithm failed and needs more detailed analysis by detecting CH_3Cl in the MIPAS-E spectral data in the first place. The same is true for MORSE retrieved N_2O_5 as well. Thus, CH_3Cl and N_2O_5 are not retrieved at this stage, in this study, and only climatology profiles are used for these parameters while fitting the MIPAS-E spectral data. Since CH_3Cl and HCN are both biomass burning trace gases, an assumption is made that even at high concentrations of CH_3Cl and HCN in biomass burning regions, signals due to HCN

contribute more than CH_3Cl in the chosen MWs. Errors due to CH_3Cl in biomass burning events [Figure 5.3; Figure 5.4] are discussed in Section 5.2.

5.2 Retrieval errors

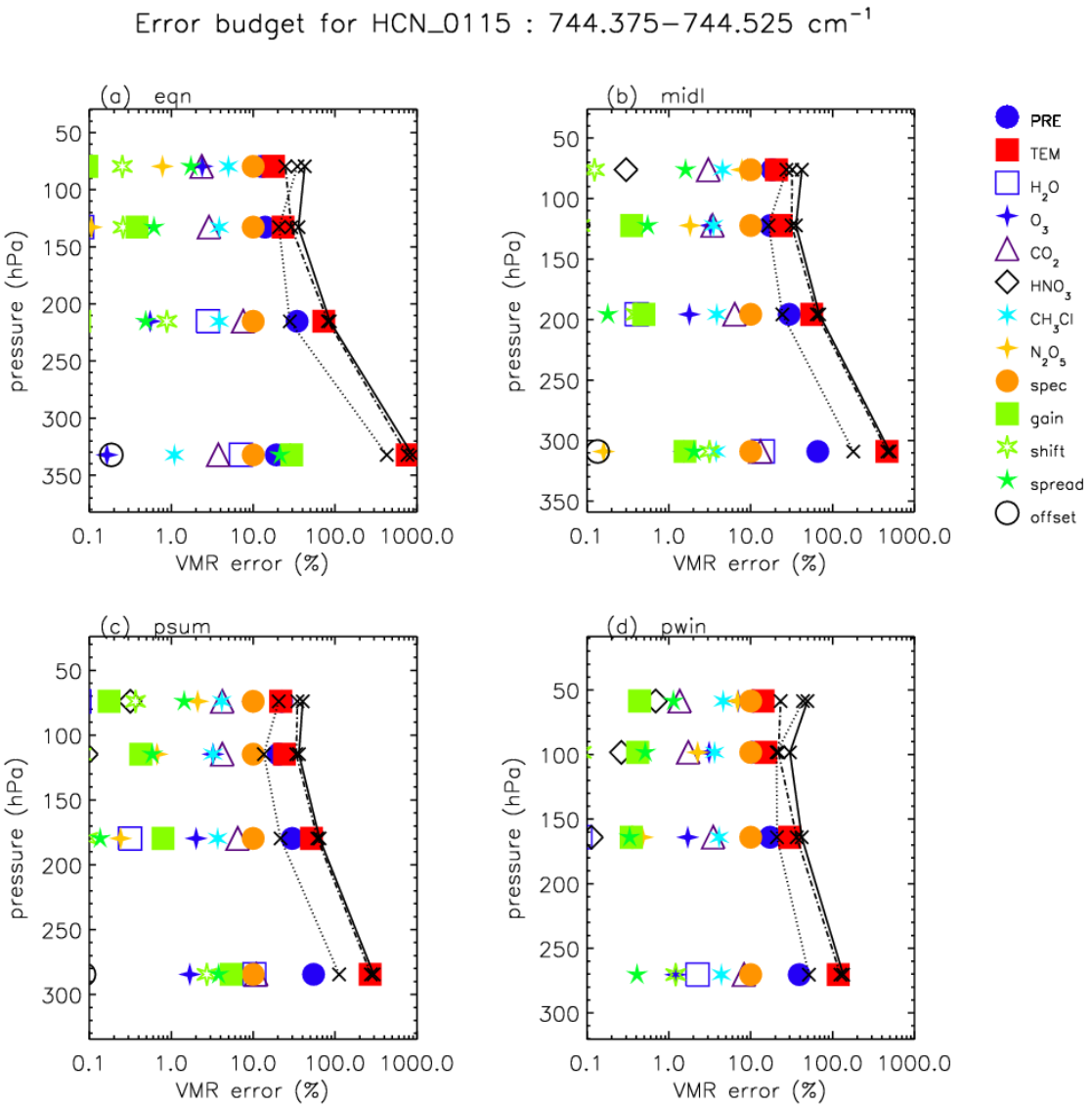

Figure 5.1: Error budget for HCN profile retrievals in HCN_0115: MW-744.375–744.500 cm^{-1}. The data is split into four regions (a) 20°S–20°N: tropical; (b) 20°–65°: mid-latitudes; (c) 65°–90° in summer hemisphere-Polar summer; (d) 65°–90° in winter hemisphere-Polar winter. The solid black lines represent the total error on a single retrieval. The dotted and dashed lines represent the random and systematic components of the total error, respectively. The *a-priori* error is assumed to be 1000%.

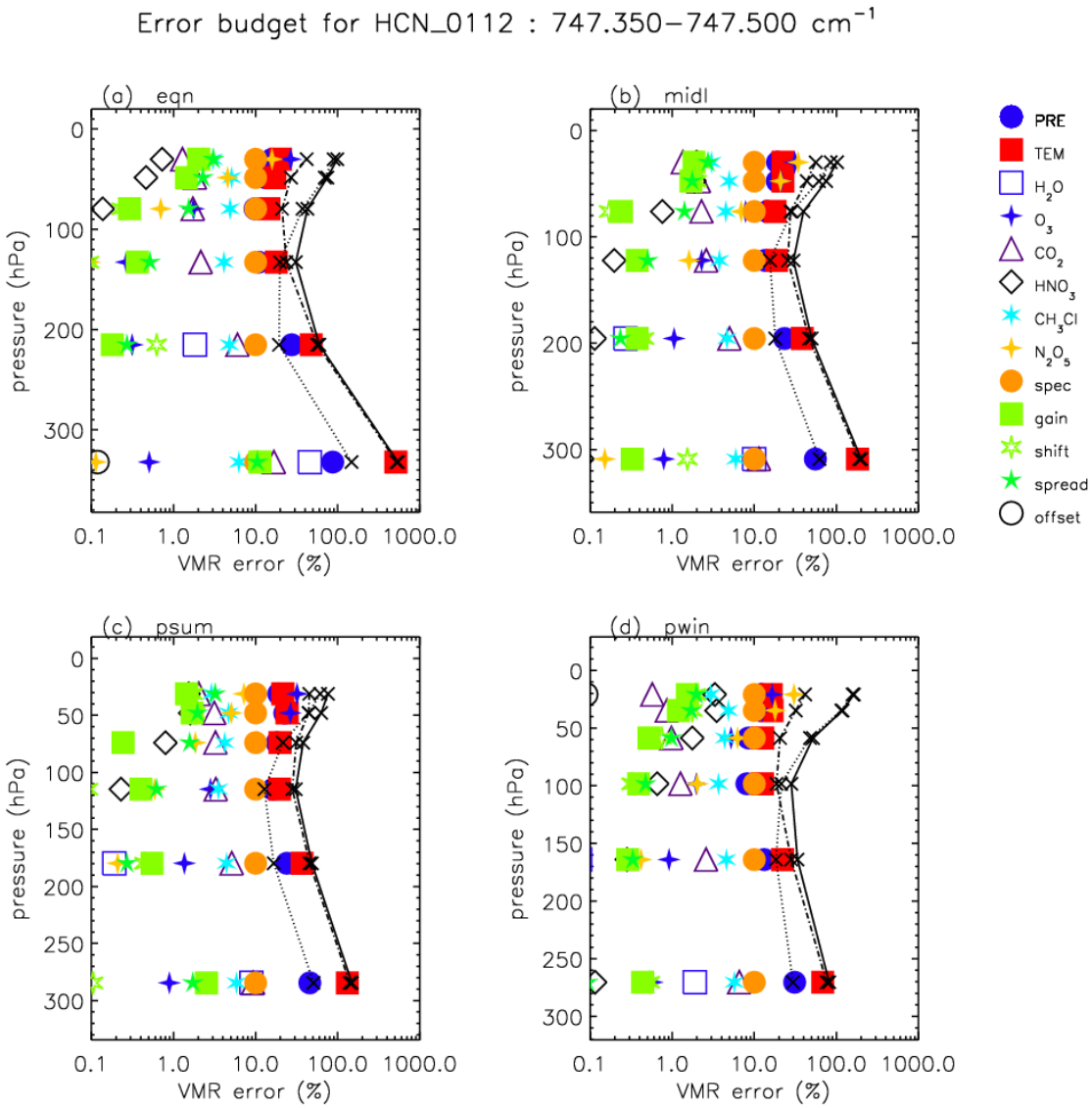

Figure 5.2: Error budget for HCN vmr retrievals in HCN_0112 MW: 747.350–747.500 cm^{-1}. The data is split into four regions (a) 20°S–20°N: tropical; (b) 20°–65°: mid-latitudes; (c) 65°–90° in summer hemisphere-Polar summer; (d) 65°–90° in winter hemisphere-Polar winter. The solid black lines represent the total error on a single retrieval. The dotted and dashed lines represent random and systematic components of the total error, respectively. The *a-priori* error is assumed to be 1000%.

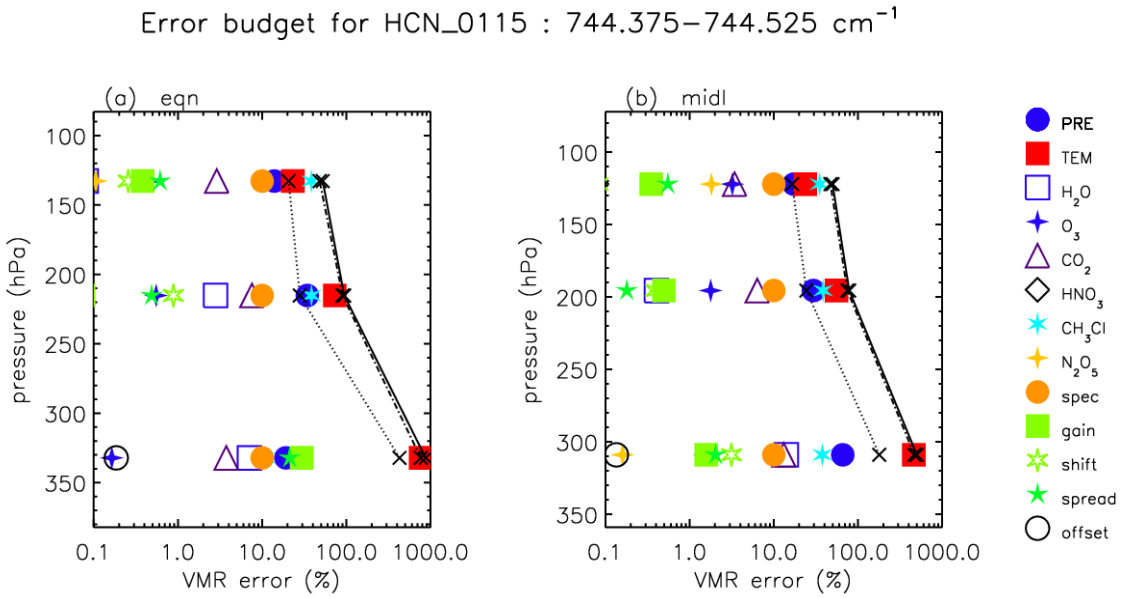

Figure 5.3: Similar error budget for HCN vmr profile as Figure 5.1 (only for tropics and mid-latitudes) with CH_3Cl error increased from 20% to 100% at 9–15 km nominal altitudes (310–120 mb).

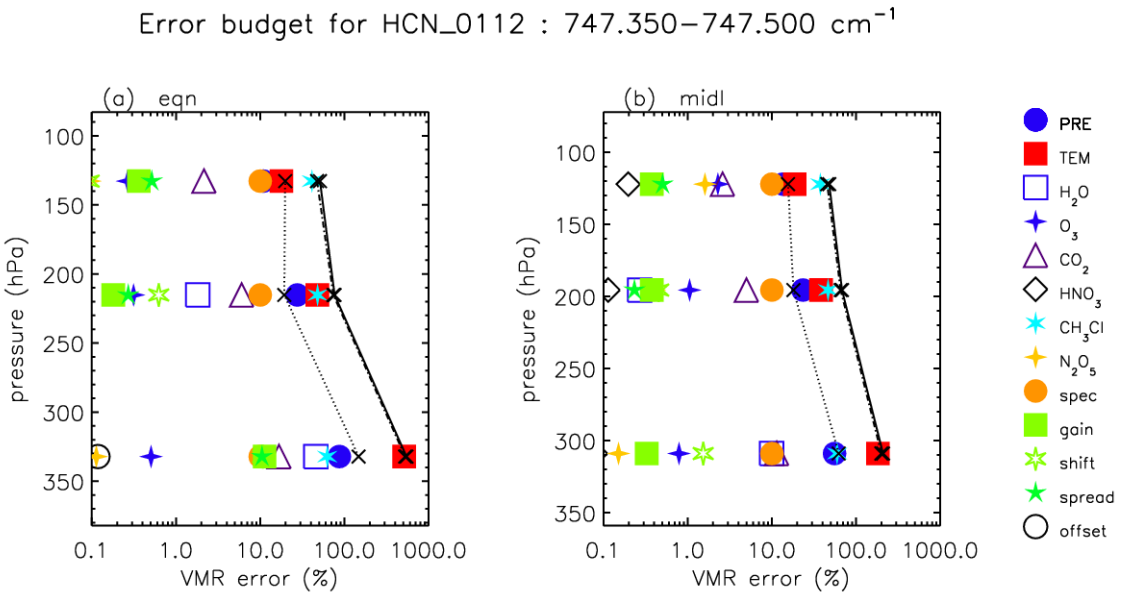

Figure 5.4: Similar error budget for HCN vmr profile as Figure 5.2 (only for tropics and mid-latitudes) with CH_3Cl error increased from 20% to 100% at 9–15 km nominal altitudes (310–120 mb).

Figure 5.1 and Figure 5.3 present the error budget for HCN_0115 MW (744.375–744.500 cm^{-1}) for four different latitude bands: (a) 20°S–20°N: tropical; (b) 20°–65°: mid-latitudes (in each hemisphere); (c) 65°–90° in summer hemisphere - Polar summer; (d) 65°–90° in winter hemisphere - Polar winter. Similarly, Figure 5.2 and Figure 5.4 represent the error budget for HCN_0112 MW (747.350–747.500 cm^{-1}). The figures show random error (instrument noise) and systematic error (model parameter error, gain, ILS and spectroscopy) components of the total error in a single HCN retrieval. The systematic model errors were calculated using the measured biases in MIPAS-E data. An uncertainty of 2 mb [Raspollini *et al.*, 2006] and 1 K [Ridolfi *et al.*, 2007] has been used for pressure and temperature, 20% for H_2O [Lahoz *et al.*, 2004] and 10% for O_3 [Cortesi *et al.*, 2007]. The errors for other contaminants were expected to be small and,therefore, set to 10% and 20% for HNO_3 [Wetzel *et al.*, 2007] and N_2O_5, respectively.

The only difference between Figure 5.1 and Figure 5.3 and similarly Figure 5.2 and Figure 5.4 is the error introduced at the 9–15 km nominal altitude range (310–120 mb) by perturbing CH_3Cl from 20% to 100% uncertainty. By perturbing CH_3Cl from 20% to 100%, one can take into account the background and biomass burning conditions in the tropics and the mid-latitudes, respectively (100% corresponds to a CH_3Cl enhancement of 1.12 ppbv) [Rinsland *et al.*, 2007]. The uncertainty of the instrument gain and offset was set to 2% and 2 $nW/(cm^2\ sr\ cm^{-1})$, respectively [Spang *et al.*, 2005]. For both the HCN_0115 and HCN_0112 MWs, an uncertainty index of 5 was reported in the HITRAN 2004 spectral database [Devi *et al.*, 2005; Rothman *et al.*, 2005] for HCN line position, air pressure-induced line shift, intensity, air pressure and self half-width; whereas no error was reported for temperature-dependence. An uncertainty index of 5 indicates an uncertainty range of ≥5% and <10%. Hence, spectroscopic uncertainties were set to 10% for both (HCN_0115 and HCN_0112) the MW regions.

The *a-priori* error is assumed to be 1000%. The total error is higher than 30% at all altitude ranges, except for a 15 km nominal altitude (120 mb) where the total error is better than 30% for all the latitude bands. The systematic error is dominated by temperature change in all the four latitude regions and for both the MWs. Random error dominates at stratospheric levels in HCN_0112 MW region; in

addition to the temperature, systematic errors are also dominated by ozone (O_3) and N_2O_5. The 9 km HCN retrieval is too sensitive to the temperature changes as a 1K change in temperature causes more than 100% error in both the MWs. At 12 km, a 2 mb change in the pressure reflects a 20% error in the tropical HCN retrievals and up to 60% error outside tropics. At higher altitudes, the errors due to the pressure changes remain under 20%. In the case of biomass burning events (100% CH_3Cl perturbation) at 12 and 15 km, a 100% change in the CH_3Cl introduces a 30–50% error in the mid-latitude and the tropical regions, respectively, and becomes the largest component of error at 120 mb (15 km nominal).

5.3 Data quality

This section details the criteria used to filter the data for the final HCN data values to be 'acceptable'. The quality of data is also tested by setting the threshold values for χ^2 convergence and CI values, and how well the measured spectra are fitted by analysing the residual (Y-F) spectra of the measured (Y) and the modelled spectra (F). The data are retrieved at less constrained values of cloud index values of CI ≥ 2, and are filtered with more stringent cloud filter by using cloud index values of CI ≥ 4. For MORSE retrieved HCN and the C_2H_2 case, only one MW is used to carry out the retrievals; hence, data are filtered with all the MW convergences, unless otherwise specified.

5.3.1 Averaging kernels

The averaging kernel matrix **A** [Rodgers, 2000] is a significant indicator of the retrieval quality [Section 2.6.2.2].

Figure 5.5 shows typical averaging kernels for HCN retrieval in October 2003 for four different latitude bands; tropics, mid-latitudes, North Pole and South Pole. These results are based on HCN_0112 MW retrieval using a 9–27 km altitude grid. The coloured dotted lines represent the data that does not satisfy the data quality filter criteria of the cloud Index ≥ 4, 0 < HCN chi-square (χ^2) ≥ 2, 0 < pT χ^2 ≥ 2 and all the MWs should converge at each altitude level. The HCN radiance signals decrease with an increase in the altitude and therefore, the averaging kernels show

the same effect at the higher altitudes where the averaging kernels have lower peaks where the HCN concentrations are more biased towards the *a-priori* profile. At lower altitudes, the averaging kernels peak between 0.7–0.8, which indicates the retrieval is almost free of *a-priori* bias. The HCN averaging kernels in the tropical and the mid-latitude regions peak beyond 0.8 for the four altitude levels.

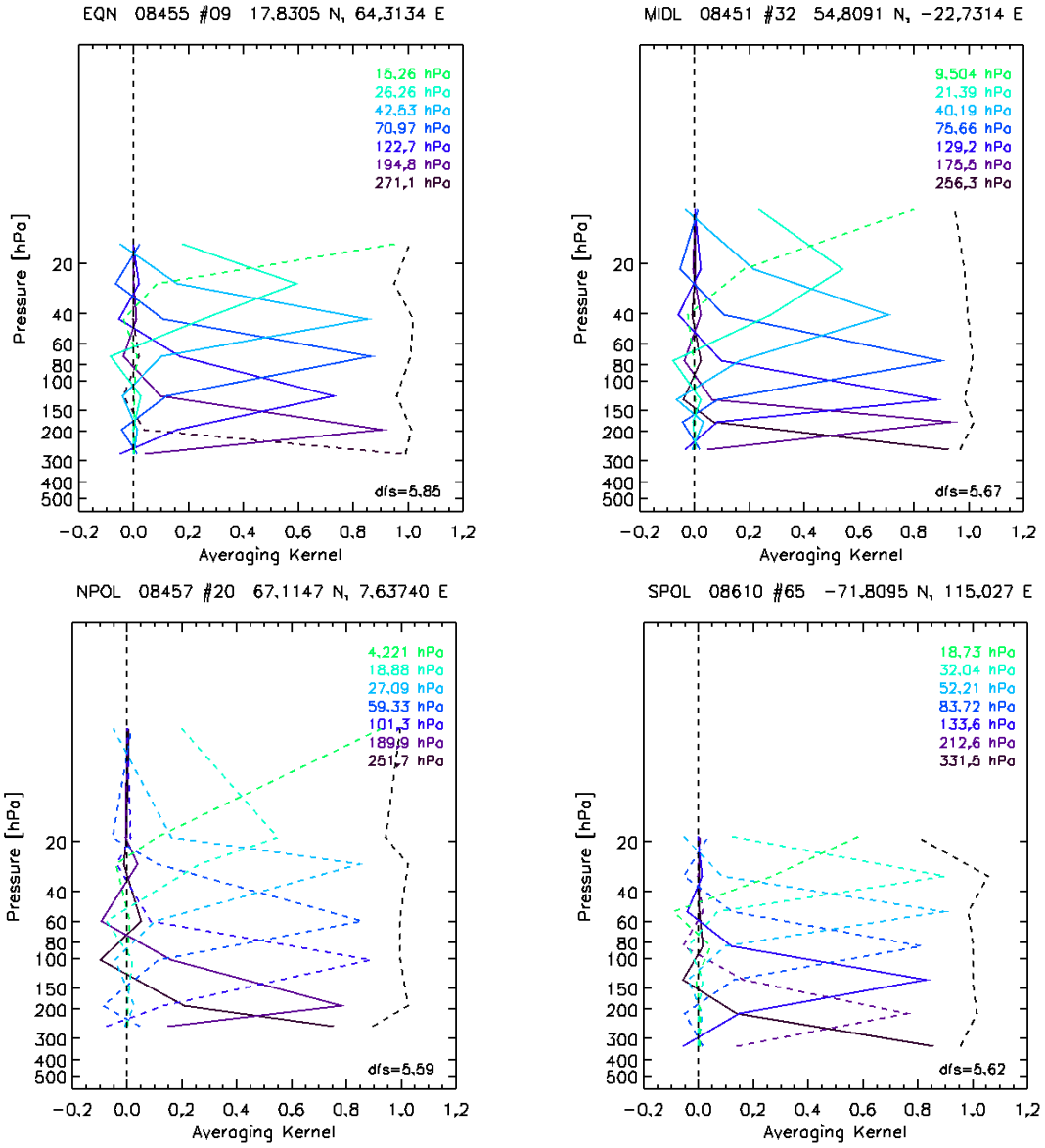

Figure 5.5: Averaging kernels for single HCN retrieval performed using HCN_0112 MW for: (top left) tropics; (top right) mid-latitudes; (bottom left) North Pole; (bottom right) South Pole. The black dotted line represents the sum of the rows of the averaging kernel matrix at each tangent height.

The width of the averaging kernels represents the vertical resolution which is about 3–4 km, gradually increases to 6 km at the highest altitudes (as seen in mid-

latitude case). Out of 7 retrieval levels the degrees of freedom are 5.85, 5.67, 5.59, and 5.62 for the tropics, the mid-latitudes, the North Pole and South Pole regions respectively. The best results are found in the cases of mid-latitude and tropical regions as the averaging kernels peak closer to unity for more than 4 altitude levels where enough data points pass through the data quality filter as well. The polar cases indicate that whilst the good sensitivity is maintained, there are problems with the quality of the data at the higher altitudes.

5.3.2 Chi-square as an indicator of data quality

The density distribution of χ^2 values for MORSE retrieved parameters at 9–27 km MIPAS-E nominal altitudes is shown in the Figure 5.6 for October 2003. The general conclusion for the χ^2 behaviour is that the mean state of all parameters is about 2–6, and these values are accepted as the maximum limit to test the quality of the data retrieved using the MORSE algorithm. A χ^2 value of 0 means either retrieval result did not converge or a cloudy scene is encountered and the retrieval process is skipped. As water vapour (H_2O) retrievals are important in the UTLS regions especially in the tropics and upper tropospheric levels, the H_2O χ^2 values shown in Figure 5.6 suggest that $0 < \chi^2$ values ≥ 2 are chosen to remove the bad quality data in all MORSE retrievals.

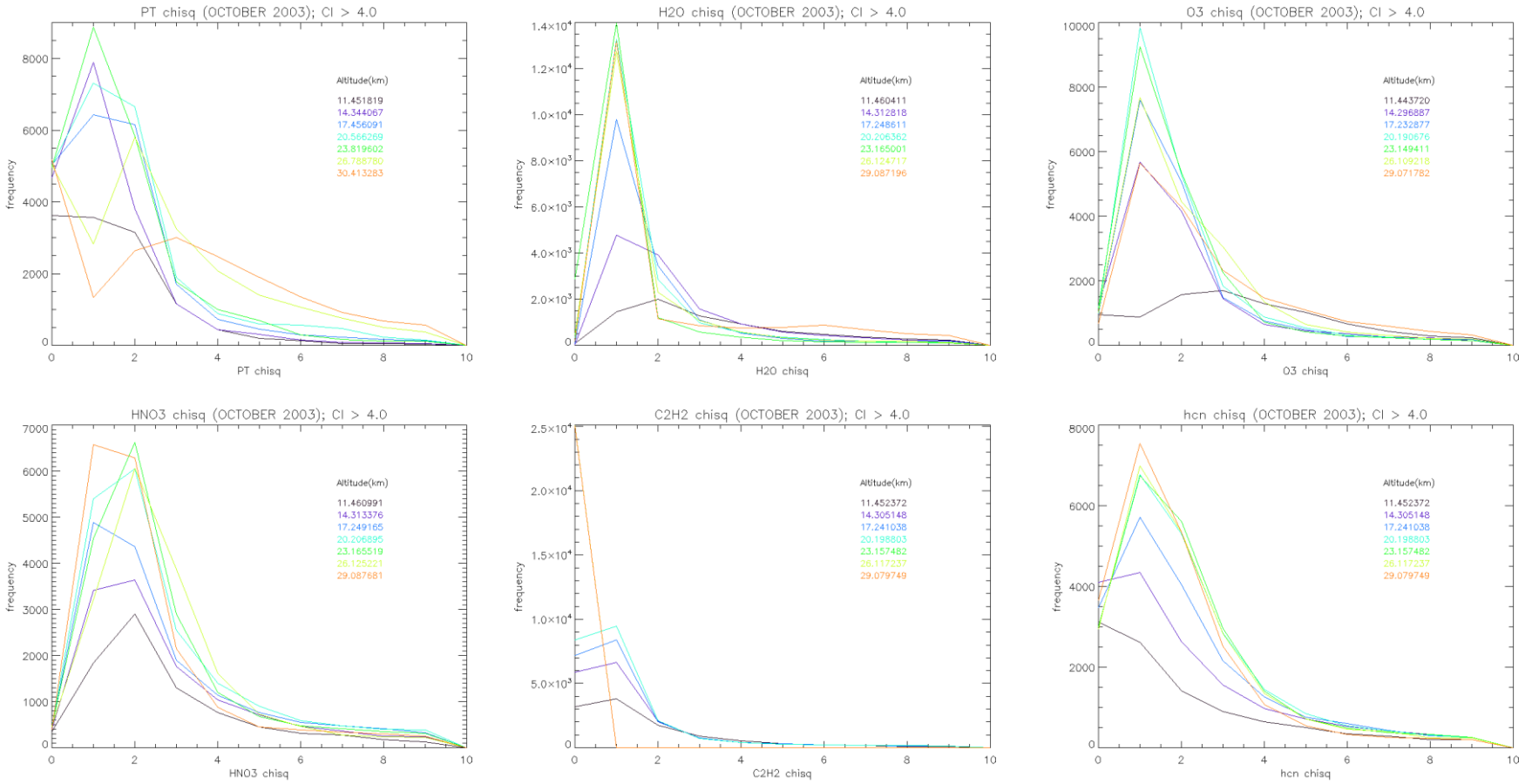

Figure 5.6 : Histogram distribution of χ^2 for the MORSE retrieved parameters.

5.3.3 Y–F residual as indicator of good data

To verify the MORSE retrieved HCN, a residual analysis is carried out, where the difference in measured (Y) and MORSE calculated fit (F) is analysed. This residual information suggests the quality of the MORSE retrieved data. The Figure 5.7 shows the result of this analysis at 9–18 km altitude levels. The data is filtered using the same criteria mentioned above. In general, the residual plots show quite a good agreement and are below the MIPAS-E noise levels. The residual fit shows the MORSE retrieved HCN data in HCN_0112 MW works fairly well and can be accepted as quality tested data. The mean NESR for the different altitudes are based on the NESR distribution from level 1b MIPAS-E data for the 746.775–747.825 cm^{-1} MW region [Figure 3.8]. The mean NESR values are 34.2, 34.0, 34.9, 35.9 nW/cm^2 sr cm^{-1} for 9-, 12-, 15-and 18-km nominal MIPAS-E altitudes.

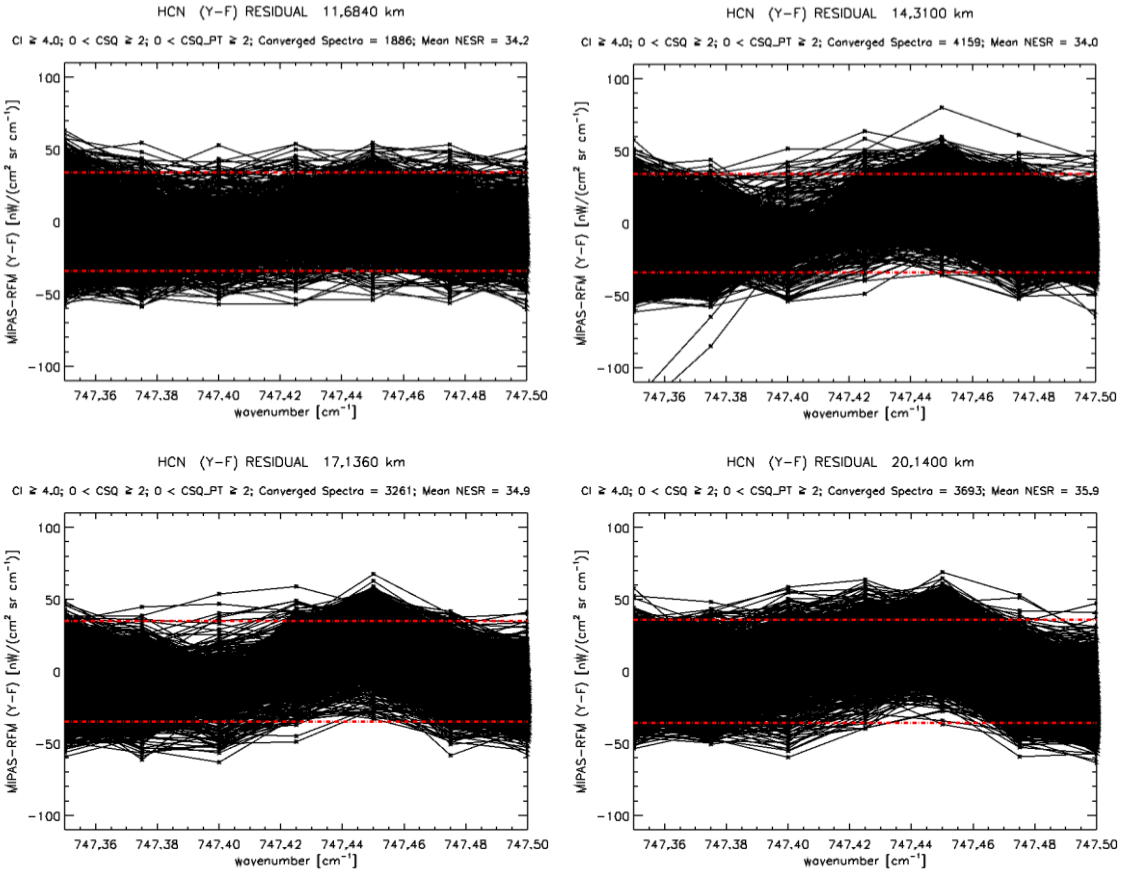

Figure 5.7: Difference in measured (Y) and MORSE calculated fit (F) spectra (black) in the HCN_0112 MW region for 9–18 km MIPAS-E nominal altitudes. The dash-dot (red) line shows the mean NESR at a particular tangent altitude.

5.4 Investigation of the HCN_0112 MW retrieval using MORSE algorithm

Pressure, temperature, and major trace gases such as H_2O, O_3, HNO_3 and C_2H_2 VMR and aerosol extinction retrievals are carried out prior to the HCN concentration retrievals. To minimize the contribution effects due to CH_3Cl and N_2O_5 to the total signal in the HCN_0105 MW, the reduced HCN_0112 MW is chosen. As the HCN concentration level decreases with the increasing altitude, the HCN retrieval grid is between 9–27 km nominal altitude range [Section 4.2.4.1.1]. Due to the presence of clouds, the lowest 6 km nominal altitude level is not considered for the HCN VMR retrieval.

Unfortunately, there was no comparison possible with any HCN model data or with any other retrieval scheme to test the quality of the MORSE retrieved HCN profiles in this study for October 2003. No direct comparisons of the HCN profile data could be made due to the lack of coincident data from the other space based instruments. This study however focuses on how results differ when different sets of input parameters are used prior to the HCN retrieval. It is crucial to understand the part of atmospheric spectrum that has HCN spectral signatures so that one can separate the contributions of various problems that arises while retrieving HCN concentrations using the MIPAS-E radiances. Further study of the MORSE retrieved data is done using non-coincident sample level 1 transmission spectral data obtained using the ACE-FTS instrument. The aim of this study is to understand how the ACE-FTS transmission spectra respond to the difference in pressure, temperature and interfering trace gases in the HCN_0102 and HCN_0105 MWs and ACE-FTS HCN spectral regions.

5.4.1 Analysis of the MORSE retrieved data

The primary objective of this study is to investigate the effects due to the input parameters used to retrieve HCN using the MORSE retrieval algorithm. In this

investigation, HCN is retrieved at the 9–27 km nominal altitude range using two pre-retrieved data sets in HCN_0112 MW. The pre-retrieved data sets includes retrieval of pressure, temperature and H_2O, O_3, HNO_3 and C_2H_2VMR profiles and aerosol extinction profiles. One set is retrieved at 9–27 km altitude range (PRET_A) and the other set at 6–68 km range (PRET_B). For both cases, the HCN VMR profiles are retrieved using the HCN_0112 MW (747.350–747.500 cm^{-1}).

The differences in these pre-retrieved data sets other than the tangent altitude grid are as follows:

1) A subset of MWs is used for HNO_3 retrievals in case of 6–68 km (PRET_B) retrieval grid. In this case, HNO_3 MW list excludes the HNO30022, 23, 24, 27, 28, 43, 47 MWs from the complete list generated from the database by IMKLST.

   http://www.atm.ox.ac.uk/MORSE/MW/hno3_040.lst

2) The C_2H_2 MW database file used in both cases differs in terms of the tangent altitude grid. For 9–27 km (PRET_A), the C_2H_2 tangent altitude grid is defined at 6–30 km and for 6–68 km (PRET_B), the C_2H_2 tangent altitude grid is defined at 6–60 km.

3) Microwindows used for the aerosol retrievals in both cases belong to two different spectral bands of MIPAS-E. The 9–27 km retrieval (PRET_A) uses the band A (833.00–834.00 cm^{-1}) aerosol data whereas, the 6–68 km (PRET_B) retrieval uses the band B (1233.900–1234.100 cm^{-1}) retrieved aerosol data.

4) For 9–27 km retrieval (PRET_A) aerosol uncertainty is set to the default value of $10E^{-3}$*(p/500) where p is the pressure (in mb) and a value of $10E^{-2}$ is set in the case of 6–68 km retrieval (PRET_B).

The MW lists used for pressure, temperature, H_2O and O_3 remains the same in both cases. The correlation length is set to 3 km [Section 5.1.1.3]; default values are used to set *a-priori* uncertainty in pressure (50%), temperature (10K), and remaining gases (100%). A maximum cloud index value of 2 is used to detect the cloudy scenes in the MIPAS-E data, and a cloud radiance threshold test is ignored, i.e., the minimum radiance in a cloud detection channel (960.7cm^{-1}) is set to −1. For

all the pre-retrieved data, the convergence criteria are as those mentioned in Section 5.1.1.5.

5.4.1.1 Global analysis of the MORSE retrieved parameters at 12 km MIPAS-E nominal altitude

This section focuses on the 12 km MIPAS-E nominal altitude level to investigate more closely the global effects of the two different scenarios of the MORSE retrieved input parameters for the HCN retrieval. The global distributions are derived from the 365 orbits of MIPAS-E data plotted at average pressure levels. The data are contoured and gridded at 20° longitude and 10° latitude resolution. The following plots are cloud cleared using a cloud index value of ≥ 4; calculated as per Section 5.1.1.4 [Spang *et al.*, 2004]. Data is also filtered using MW convergence and respective pressure temperature and/or trace gas χ^2 criteria. Ad hoc limits (see details in the following text) were set to both the convergence and χ^2 criteria to obtain enough data points to plot a global picture in order to study the difference between two sets of input data. In global maps, the white regions indicate the cloud-contaminated data, and the retrievals are set to default climatology where no retrieved profiles exist but not likely to be a problem in the case of C_2H_2 which has small contribution in the HCN_0112 MW.

Figure 5.8 (a) and (b) represent the global maps of pT at 12 km MIPAS-E nominal altitude level. The left plot represents the pT retrievals based on PRET_A retrieval grid and the right plot represents the pT retrievals based on PRET_B retrieval grid. A maximum of two pT MWs are allowed not to converge and the pT χ^2 values are constrained to a maximum value of 10. High pressure retrievals near Central America and Central West Africa regions and lower temperature retrievals at North Polar regions can be observed in the case of the 9–27 km retrieval grid. Generally, there is no major difference observed in case of pressure-temperature retrievals at this altitude level except for a ≈10 K difference in the North pole regions which can be significant enough, hence, the MORSE retrieved HCN data in these regions have to be quantified well.

The data used to plot Figure 5.9 are filtered using a cloud index value ≥ 4, a maximum of two H_2O MWs are allowed not to converge and the pT and the H_2O χ^2 values are constrained to a maximum value of 6. Figure 5.9(a) shows the water vapour distribution at the 12 km nominal altitude level. The H_2O distribution is higher in tropical regions by a factor of at least 2 when it is retrieved using PRET_A retrieval grid using the relaxed filters. To verify the two H_2O retrievals, a further residual analysis is performed by plotting the difference (Y−F) between the measured radiance (Y) and the MORSE calculated fit (F). The x-axis in the H_2O (Y−F) residual plots represents the selected MWs used in order to retrieve the final H_2O VMR, i.e., the array of selected H_2O MW spectral ranges are concatenated together to form the x-axis. Figure 5.9(b) shows the two H_2O retrievals agree well enough at 12 km nominal altitude when the pT and H_2O χ^2 are further constrained to 2.

Figure 5.10 (a) shows the ozone (O_3) distribution at the 12 km nominal altitude level. A maximum of 2 O_3 MWs are allowed not to converge and the pT and O_3 χ^2 values are constrained to a maximum value of 6. For the PRET_A retrieval grid, high O_3 concentration levels are retrieved in the North polar regions. Figure 5.10 (b) shows the HNO_3 distribution at 12 km nominal altitude level. A maximum of two HNO_3 MWs are allowed not to converge and the pT and HNO_3 χ^2 values are constrained to a maximum value of 6. For the PRET_A retrieval grid, the HNO_3 data remains unfiltered for the high latitude regions. No significant differences in the HNO_3 retrievals can be observed for rest of the world.

Figure 5.11 shows the C_2H_2 distribution at 12 km nominal altitude level. For Figure 5.11; as only one MW is used to retrieve C_2H_2 all MWs should converge and pT and C_2H_2 χ^2 values are constrained to a maximum value of 10 and 2, respectively. Even though both retrievals show a good agreement in the tropics, a lot of data is missing for the C_2H_2 retrieval in the case of the PRET_A retrieval grid especially in the Polar Regions when the same filtering criteria are applied to both datasets.

The hydrogen cyanide (HCN) distribution at the 12 km nominal altitude is not discussed here as the comparison leads to noisy data in case of the MORSE retrieved HCN at 9–27 km while using the PRET_B pre-retrieved dataset and a lot of data is lost due to stringent filtering criteria. The final retrieved HCN distribution using the PRET_A pre-retrieved dataset is discussed in detail in section 5.6.

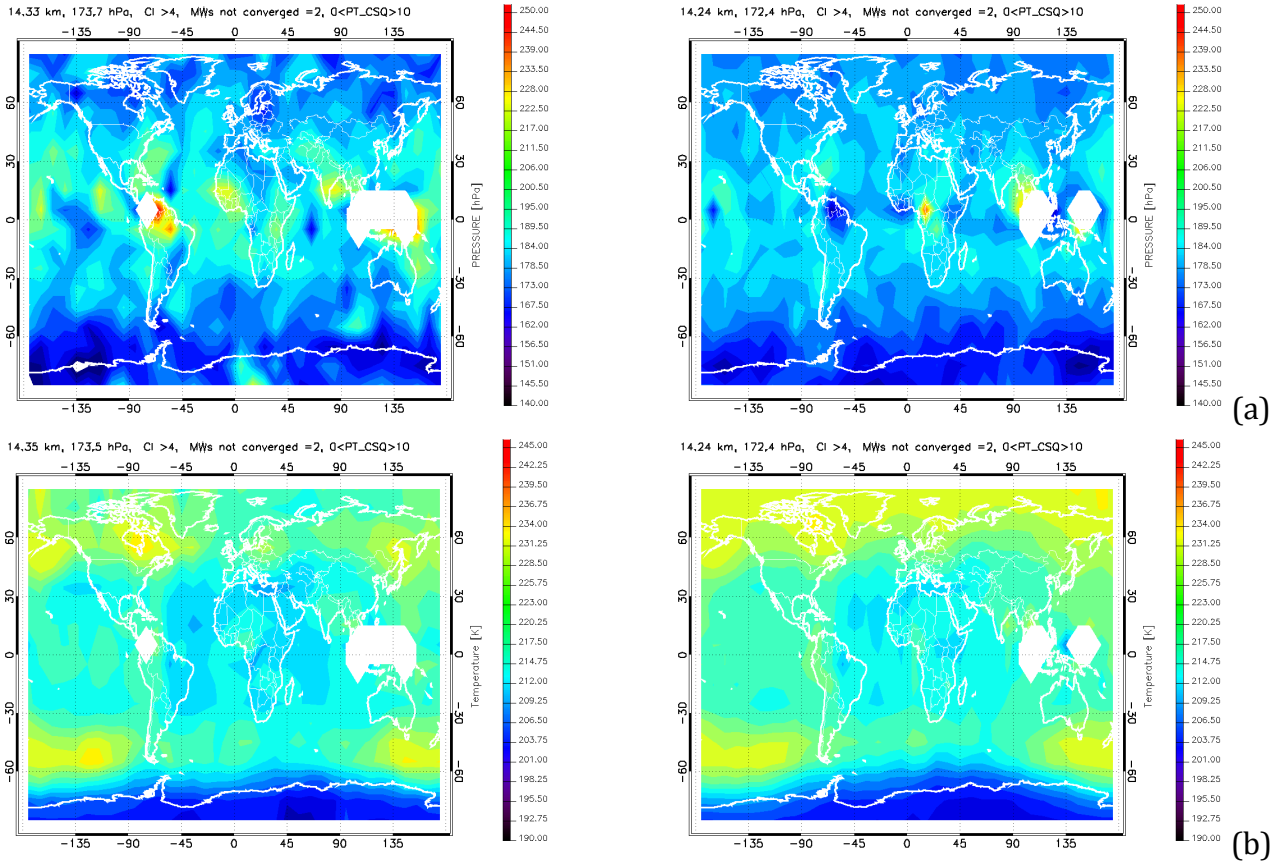

Figure 5.8: Global map of MORSE retrieved (a) pressure and (b) temperature at 12 km nominal altitude level. Global map represents the MORSE retrieved data (left) using PRET_A retrieval grid and (right) using PRET_B retrieval grid.

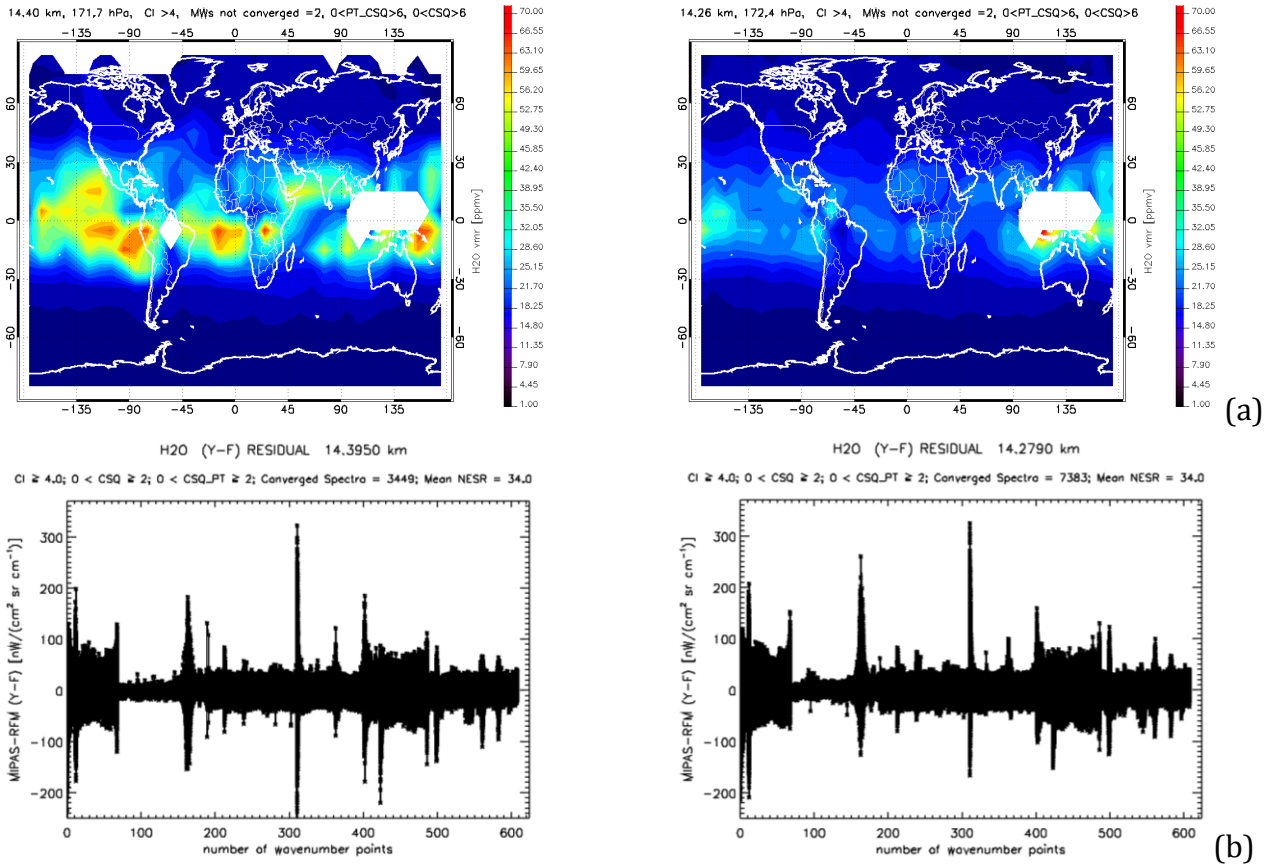

Figure 5.9: (a) Global map of MORSE retrieved H_2O at 12 km nominal altitude level. (b) Residual (Y−F) plots of MORSE retrieved water vapour (H_2O) at 12 km nominal altitude level. H_2O retrieved (left) using PRET_A and (right) using the PRET_B retrieval grid.

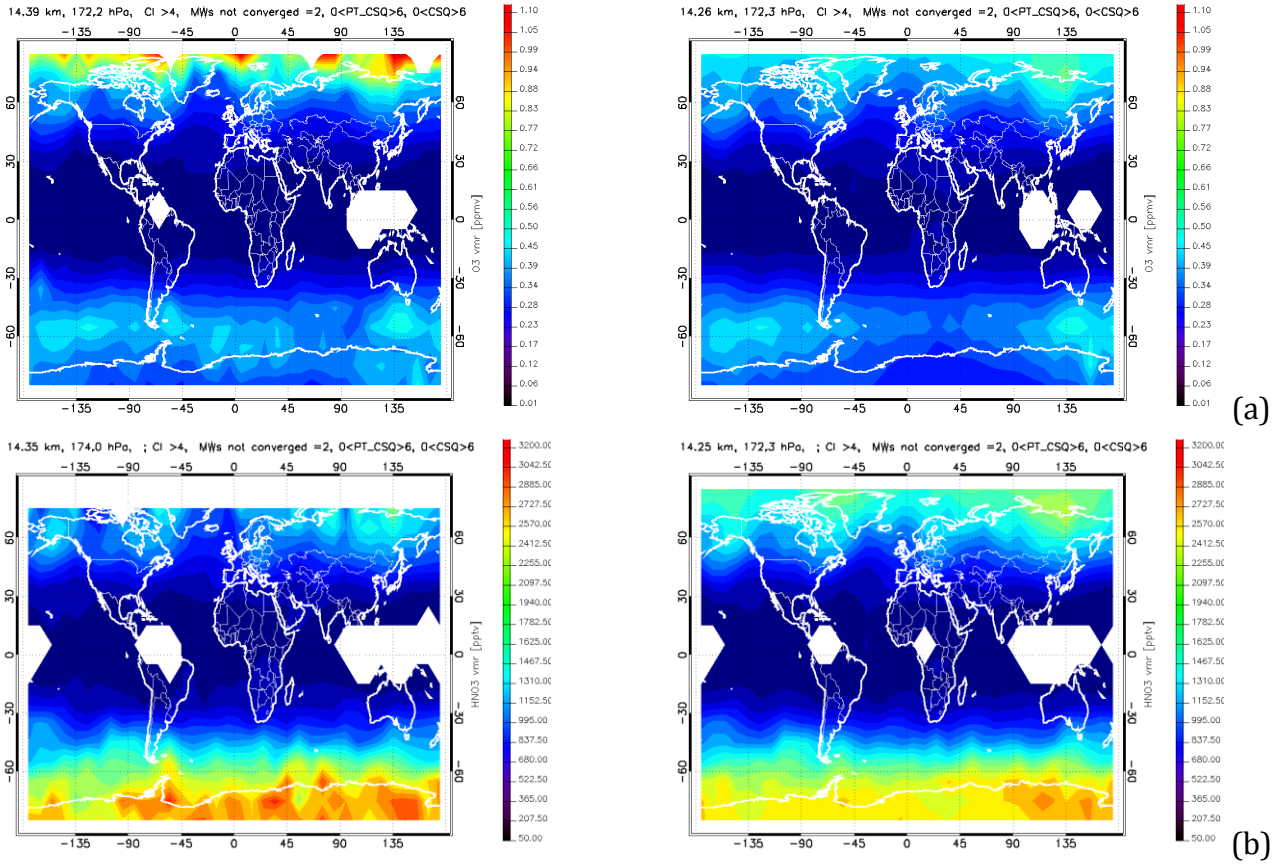

Figure 5.10: Global map of MORSE retrieved (a) O_3 and (b) HNO_3 at 12 km nominal altitude level. Global map represents retrieved data (left) using the PRET_A and (right) using the PRET_B retrieval grid.

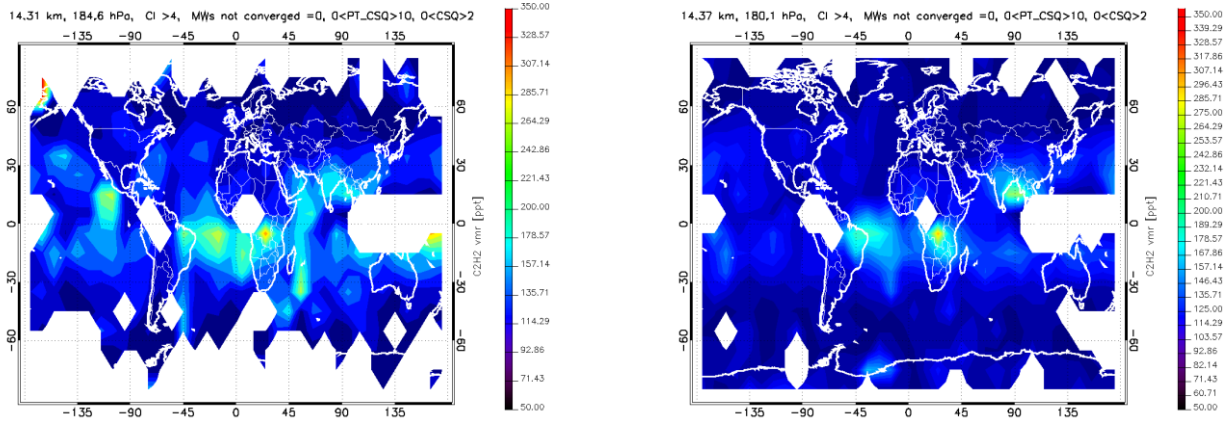

Figure 5.11: Global map of MORSE retrieved C_2H_2 at 12 km nominal altitude level. Global map represents C_2H_2 retrieved (left) using the PRET_A and (right) using the PRET_B retrieval grid.

5.4.1.2 Density distribution of the MORSE retrieved parameters at 12- and 18-km MIPAS-E nominal altitudes

This section investigates the density distribution of the parameters retrieved at the two different altitude grids, i.e., at the 12- and 18-km MIPAS-E nominal altitudes. The two input data sets are quality filtered using respective criteria. Each MIPAS-E scan measurement is time ordered and is assigned a unique time stamp, and to plot the density distribution of each input parameter the two input data sets are further matched with time ID as well. The blue and red curve represents data retrieved using the PRET_B and PRET_A retrieval grids, respectively. The trace gas VMR values are cut-off at a minimum value of 50 pptv. From this histogram, several relevant quantities can be calculated: (1) the mean and median state, (2) the standard deviation and (3) the input parameter maximum value of the histogram distributions.

Figure 5.12 and Figure 5.13 show the density distribution plots for parameters used in HCN_0112 MW retrieval at 9–27 km. The comparison at 12 km nominal altitude shows that the mean and median states show an offset of approximately 15 mb. The pressure distributions show that the data in the PRET_B have a lot lower pressure values compared to the PRET_A data. The density distribution for temperature shows an offset of 4 K in the peak values of the temperature distributions. The H_2O density distribution shows an offset in the VMR distribution in the lower edge of the H_2O distributions.

Figure 5.14 and Figure 5.15 compare the density distribution of the input parameters at the 18 km nominal altitude level. The mean and median states agree well for the two input parameter data sets. The mean and median states of the temperature density distribution have a difference of 2.62 K and 3.60 K, respectively. The HNO_3 density distribution suggests that HNO_3 retrieved at PRET_A data have more low retrieved values in comparison to the 6–68 km retrieval grid.

The blue curve in the Figure 5.13 for the HCN histogram distribution shows that less data qualify to pass through the quality filter. With the increase in altitude,

less data pass through the quality filter in the case of retrieved HCN where the input parameter data is retrieved using PRET_A retrieval grid. The 12 km HCN density distribution plot shows a wider spread when HCN is retrieved using input parameters retrieved uing the PRET_B retrieval grid, whereas an opposite effect is seen in case of the 18 km HCN density distribution [Figure 5.15].

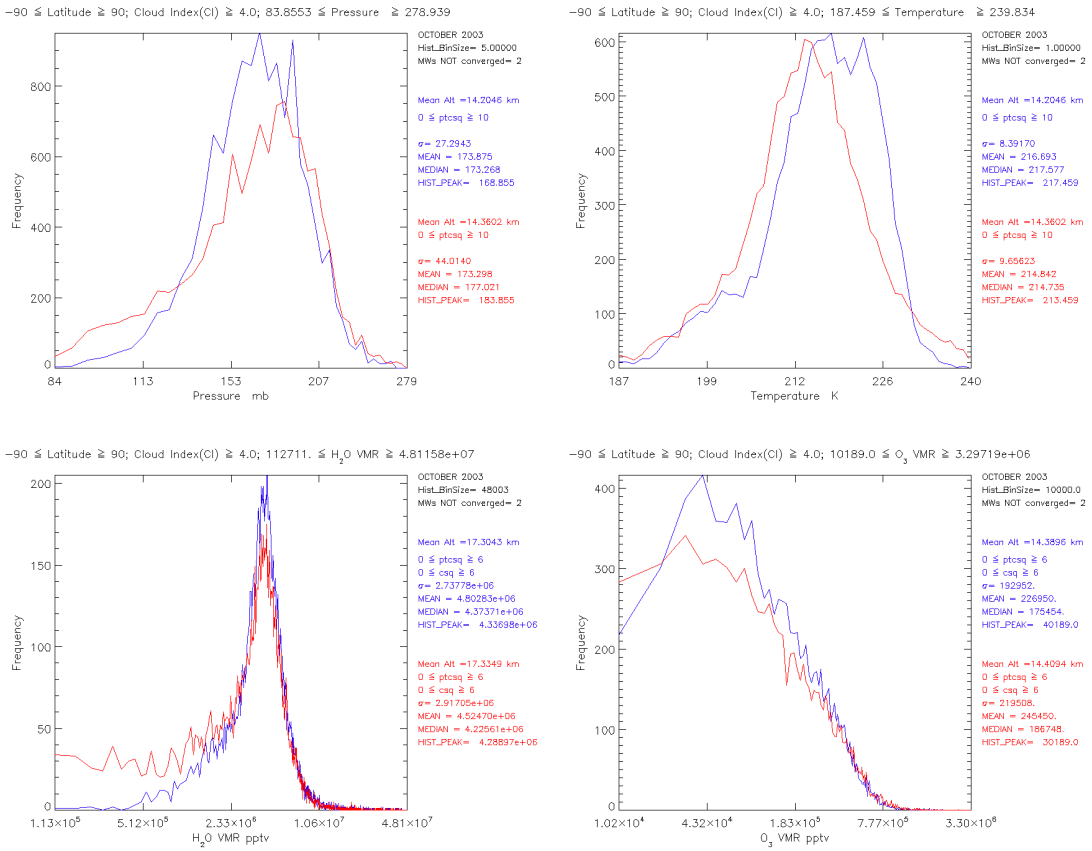

Figure 5.12: Histogram distribution of pressure, temperature, H_2O, O_3 12 km nominal altitude level using global quality filtered data. The plot compares the distribution of particular input parameter using different retrieval grid where blue represents PRET_B and red represents PRET_A retrieval grid data.

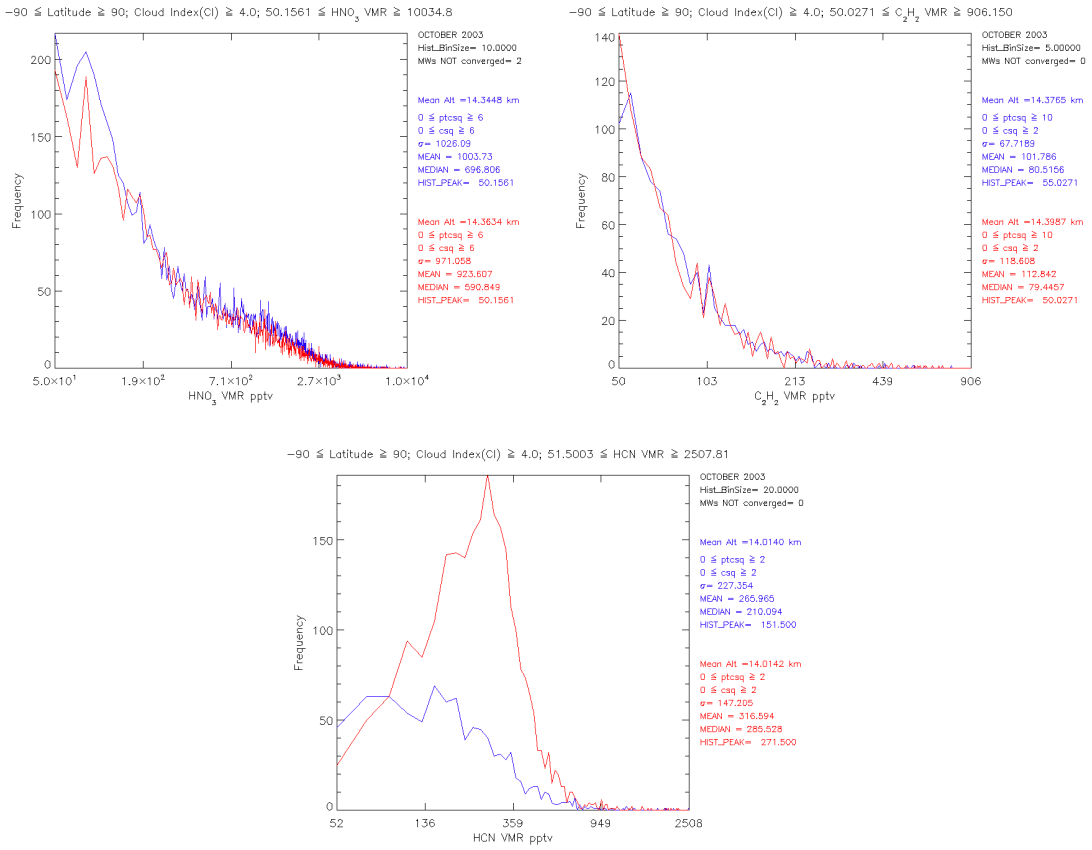

Figure 5.13: Histogram distribution of HNO_3, C_2H_2 and HCN at 12 km nominal altitude level using global quality filtered data. The plot compares the distribution of particular input parameter using different retrieval grid where blue represents PRET_B and red represents PRET_A retrieval grid data.

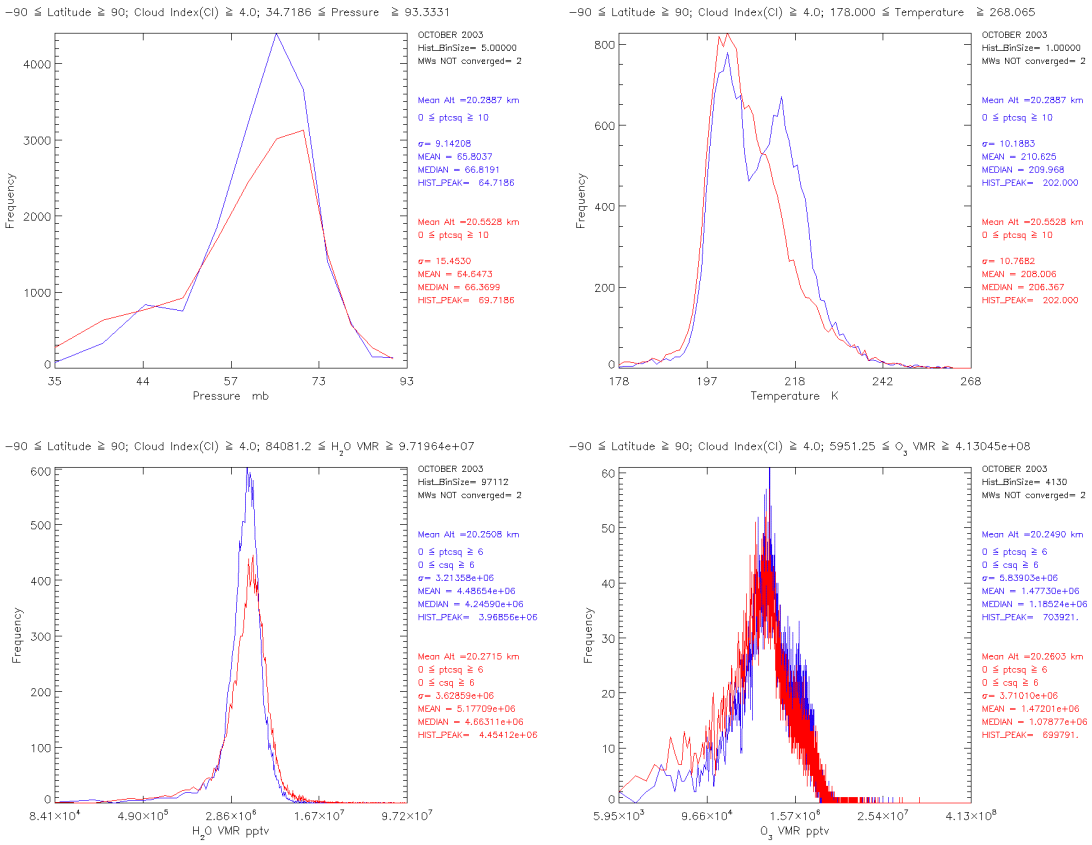

Figure 5.14: Histogram distribution of pressure, temperature, H_2O, O_3 at 18 km nominal altitude level using global quality filtered data. The plot compares the distribution of particular input parameter using different retrieval grid where blue represents PRET_B and red represents PRET_A retrieval grid data.

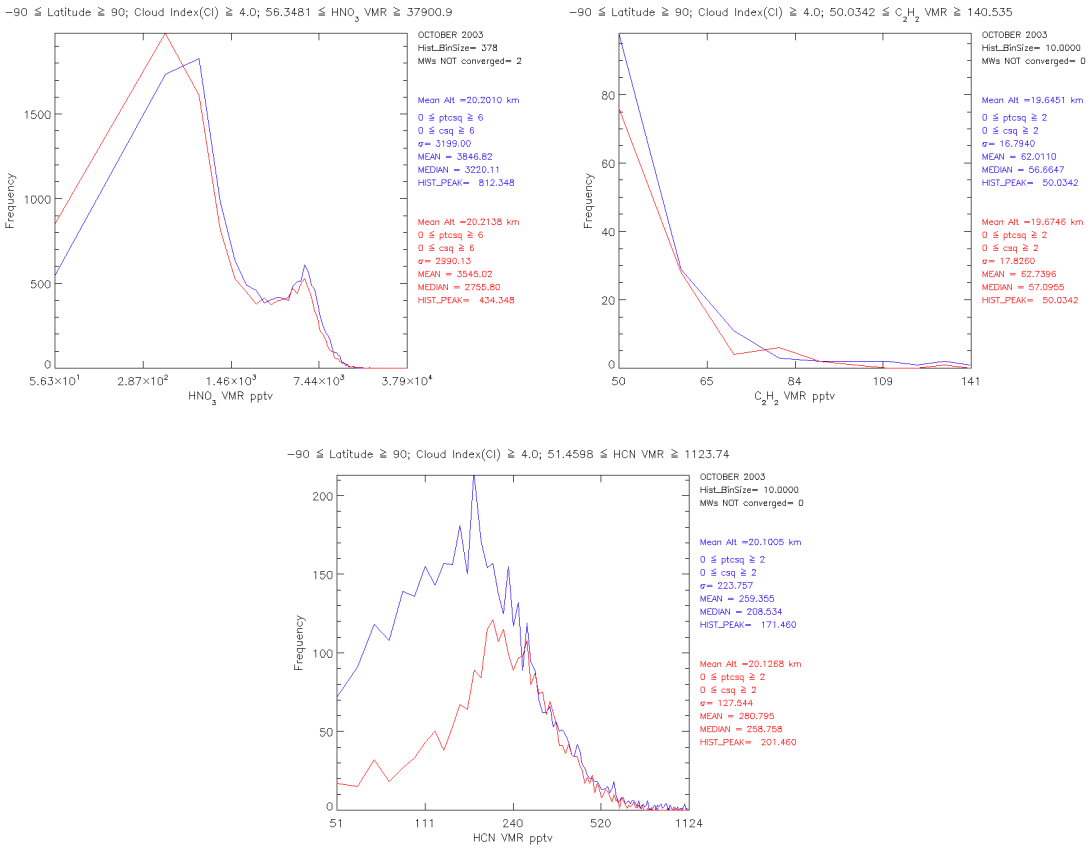

Figure 5.15: Histogram distribution of HNO_3, C_2H_2 and HCN at 18 km nominal altitude level using global quality filtered data. The plot compares the distribution of particular input parameter using different retrieval grid where blue represents PRET_B and red represents PRET_A retrieval grid data.

5.5 Inter-comparison of the MORSE retrieved HCN with ACE-FTS

To inter-compare data sets a certain approach has to be adopted in order to validate the data products under investigation. The two satellite observing systems should retrieve the same quantity x in the same units and be represented on the same vertical grid either in terms of altitude (km) or pressure (mb). If the vertical grid differs, averaging kernels have to be considered [Rodgers and Connor, 2003] in order to compare the data products where the quantity x retrieved using the high-resolution instrument has to be smoothed by applying averaging kernels of the low-resolution instrument. Unfortunately, ACE-FTS averaging kernels are not operationally produced. In this study, it is assumed that both the MIPAS-E and ACE-FTS instruments have the same averaging kernels because (1) the two satellite systems measure the Earth's atmospheric spectra in the limb mode and (2) the FOV of both the instruments is about 3–4 km, which means that the vertical resolution should be similar.

An indirect comparison is made in this section due to lack of co-incident HCN retrieved profiles from any other space based instrument for October 2003. The ACE-FTS measurements are preferred for the inter-comparison study for reasons: (1) solar occultation measurements provide high vertical resolution and low Signal to Noise Ratio (SNR) (2) the instrument has a high spectral resolution and (3) ACE-FTS has cleaner spectral regions near 3000 cm^{-1}. The main aim of this inter-comparison is to understand differences in the profile data retrieved using different retrieval grids and ACE-FTS retrieved data for the same month but different years. A sensitivity test will be carried out in order to test the input parameters used for the HCN_0105 and HCN_0102 MWs with the help of ACE-FTS retrieved profile data. MORSE retrieved profile data are used as the input to model the ACE-FTS transmission data to analyse the MORSE retrieved HCN VMR profiles for different latitude bands: tropics and North and South Pole regions at 12- and 15-km altitude levels.

The inter-comparison study is carried out in three different latitude bands (1) tropics-30°N to 30°S, (2) North Pole-65°N to 90°N, and (3) South Pole-65°S to 90°S. The two MORSE retrieved datasets using the different retrieval grids (PRET_A and PRET_B) for October 2003 along with ACE-FTS sample transmission spectra (available dataset at the time of analysis) and profile data for October 2004, 2005 and 2006 are used in this analysis.

5.5.1 The Atmospheric Chemistry Experiment (ACE-FTS)

The ACE-FTS satellite was launched on 12 August 2003 using a Pegasus-XL rocket. The Atmospheric Chemistry Experiment (ACE) is an infrared Fourier Transform Spectrometer (FTS) with a high spectral resolution of 0.02 cm^{-1}. It is the primary instrument onboard SCISAT-1. It operates in the range of 2–13μm (750–4400 cm^{-1}) to measure the vertical distribution of trace gases and particles and temperature. Aerosols and clouds are monitored using the extinction of solar radiation at 1.02 and 0.525μm as measured by the two filtered images. ACE-FTS/SCISAT-1 is in the 74° inclined orbit, which allows covering 85°N–85°S latitudes. ACE-FTS operates in the solar occultation mode and measures 15 sunrises and 15 sunsets per day. Figure 5.16 represents the latitude coverage of ACE-FTS for one year which shows poor coverage in terms of latitude especially in the tropics.

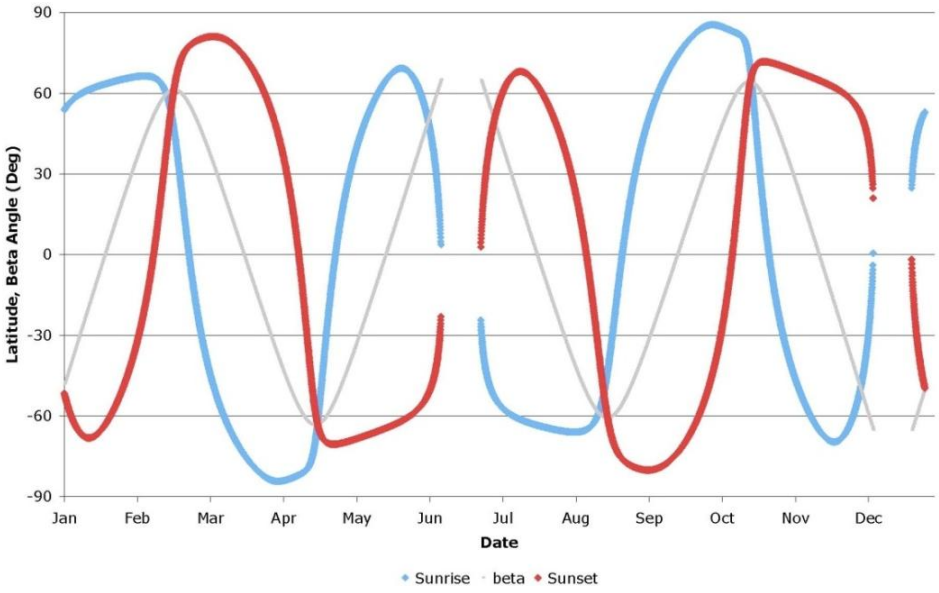

Figure 5.16 : ACE-FTS occultation latitudes throughout one year on orbit.

ACE-FTS instrument's design is based on a Michelson interferometer and measures more than 30 atmospheric constituents by absorption spectroscopy using the Sun as a light source. During an occultation, ACE-FTS instruments observe the Sun with the help of a pointing mirror which is controlled by a sun-tracker servo loop and records a series of atmospheric spectra. For each occultation, measurements are recorded during the time when the Sun rays pass well above the Earth's atmosphere (tangent altitudes of 160–225 km). The spectra are recorded every 2 seconds during the sunrise or the sunset with the help of two mercury-cadmium-telluride (MCT/HgCdTe) photovoltaic detectors to cover the 750–1850 cm^{-1} range and a indium-antimonide (InSb) detector is used for the 1850–4400 cm^{-1} range. The SNR is wavenumber dependant and exceeded the target SNR of 100:1 for the 750–4400 cm^{-1} range except for a small region in the 750–850 cm^{-1} range [Châteauneuf *et al.*, 2004; Nassar, 2006]. The FTS has a circular FOV of 1.25 mrad which translates into a maximum vertical resolution of 3–4 km for a satellite at ≈2700 km from the tangent altitude.

Accurate pointing knowledge cannot be determined as no information from the sensor other than a clock which is used to compute the tangent altitudes. The tangent height *z* is considered as an unknown quantity to be determined during the retrieval process. To retrieve pressure p and temperature T profiles, the ACE-FTS processor first analyses CO_2 spectral lines because CO_2 has a long atmospheric lifetime and is well mixed, typically resulting in an approximate constant VMR for altitudes below ≈80 km, except during the polar winter case. The CO_2 VMR is calculated from an empirical relationship suggested for the Halogen Occultation Experiment (HALOE) on NASA's Upper Atmospheric Research Satellite (UARS) [Russell *et al.*, 1993] which accounts for the increase in CO_2 VMR as a function of time [Boone *et al.*, 2002; 2005].

The VMR retrieval software allows for the retrieval of as many as six molecules simultaneously. A modified global fit approach [Carlotti *et al.*, 1988], is applied in which all parameters are determined simultaneously with the Levenberg-Marqurdt non-linear least-squares method. The weighting factor (square of the SNR) used for least square fitting uses the effective SNR listed in the Table 5.3. The actual SNR performance of the ACE-FTS instrument is typically underestimated by the

effective SNR. For the altitude range of ACE-FTS measurements (5–150 km) it is not possible to obtain sufficiently accurate meteorological data from *a-priori* information [Boone *et al.*, 2005]; the gas spectroscopic information from the HITRAN 2004 spectroscopic database is adopted for the retrieval of atmospheric molecules.

The retrieved results are interpolated onto a 1 km 'grid' using a piecewise quadratic method. For versions 2.2, both the 'retrieval' grid and the '1 km' grid profiles are available. In this study, the 'retrieval' grid data profiles are used as the vertical resolution of the ACE-FTS measurements is 3–4 km which is comparable, hence, no MIPAS-E averaging kernels are applied to the ACE-FTS measured profiles. The ACE-FTS retrieval processor utilises MWs wherein some of the windows may not have any information about the target molecule, but the sole purpose is to improve results for interfering species that contribute to relatively weak spectral features in the target MW.

Wavenumber range (cm^{-1})	**Effective SNR**
< 800	50
800–900	75
900–1000	100
1000–1850	175
1850–2500	200
2500–2750	125
2750–3900	100
3900–4100	70
4100–4200	50
> 4200	35

Table 5.3: SNR for correspoding ACE-FTS wavenumber range.

5.5.1.1 Sources of errors

The ACE-FTS instrument has either good or poor pointing knowledge, where the geometry of the measurements (tangent altitude z) becomes unknown. The ACE-

FTS retrieval processor uses the most appropriate approach to use for imposing the constraint of hydrostatic equilibrium, which depends on the pointing knowledge to retrieve pressure and temperature [Boone *et al.*, 2002]. Algorithms were developed to consider both good and poor pointing knowledge.

Errors for ACE-FTS profiles have not been systematically estimated. A guide to error contributions can be found in Mahieu *et al.* [2008] where pointing uncertainties of 150 m in the target point are considered. The random retrieval errors are available and are provided with the ACE-FTS level 2 profile data files. Further, there is no cloud detection method involved in order to detect cloudy scene at the current stage.

5.5.2 Mean profile comparisons

Ideally, for profile comparison analysis using different data sets for retrieved quantity x, coincidence criteria of ± 300 km and ± 3 h in space and time, respectively, are preferred to validate the reference measurements. However, lack of HCN measurements by any space-based, *in-situ* or air-borne instruments, these criteria indicate that validation must be restricted to more general comparison of MORSE retrieved HCN to ACE-FTS retrieved HCN profiles, but this comparison experiment should reveal major differences in the retrieved profiles.

The MORSE retrieved average profiles are compared with the ACE-FTS level 2 (version 2.2) retrieved average profiles. The MORSE retrieved data cover October 2003, and profile data from the months of September, October and November 2004, 2005 and 2006 are compared since ACE-FTS measurements do not have tropical coverage [Figure 5.17] for the month of October alone. The ACE-FTS measurements are chosen for the inter comparison study because the above mentioned months cover the biomass burning period in the tropical regions, and one can expect high amounts of HCN concentration levels in the biomass burning regions.

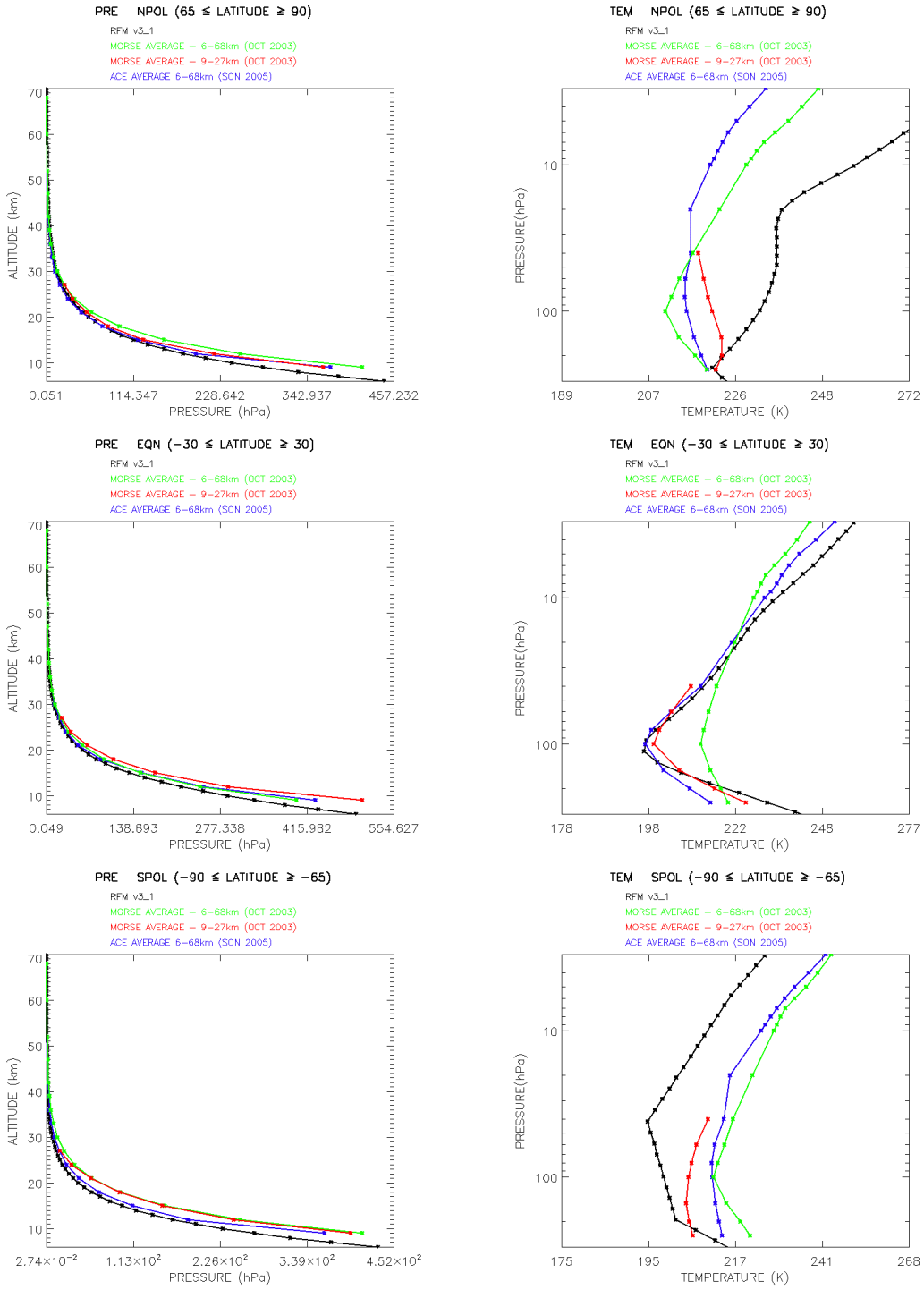

Figure 5.17: Mean ACE-FTS and MORSE retrieved profiles retrieved using two different retrieval grids in North Pole (top), tropical (middle) and South Pole (bottom) regions. The black curve represents standard climatology profiles; the dark blue curve, average ACE-FTS retrieved profiles; green curve, average MORSE retrieved profiles for PRET_B and red curve, average MORSE retrieved profiles using PRET_A.

Figure 5.17 shows the comparison of mean profiles for three different latitude bands: the North Pole (top), the tropics (middle) and the South Pole (bottom). The black profiles represent standard reference atmospheric profiles [Remedios *et al.*, 2007(c)], the green profiles represent the mean state of the MORSE retrieved parameters using PRET_B retrieval grid for October 2003, the red profiles represent the mean state of MORSE retrieved parameters using the PRET_A retrieval grid for October 2003 and the blue profiles represent the ACE-FTS retrieved parameter profiles for September, October and November 2005. For the MORSE retrieved profiles, the general quality criteria are applicable for all retrieved parameters and remain the same for different retrieval grids for thecomparison study. ACE-FTS retrieved profiles have no quality information except for random retrieval errors and T fit values, which indicate whether temperature is retrieved using data or is set to the *a-priori* value [Section 5.4.1]. Also the missing retrieved VMR profile data are assigned with a value of −999 and the VMR statistical errors are flagged using value of −888.

To compare the pressure and temperature profiles, each pressure and temperature profile is quality filtered and interpolated onto a defined altitude (9–27 km in steps of 3 km) and pressure grid (250, 200, 150, 100, 80, 60 and 40 mb) respectively. The most distinguishable observation is that high pressure levels are retrieved and the two different sets of altitude grid used for the MORSE retrievals shows significant offset between retrieved mean pressure profiles when compared to the reference *a-priori* pressure at low altitude levels. Such an offset in the mean MORSE pressure profiles can be explained by the fact that the MIPAS-E engineering altitudes for the month of October 2003 are generally higher by 1.6 km [Kiefer *et al.*, 2007]. Compared to standard reference climatology it is possible that there is a small pointing offset in the ACE-FTS data as well.

The mean temperature profiles for each latitude band follow the respective *a-priori* temperature structure. For the North Pole case, the red curve shows higher temperature retrievals with an increase in altitude. The red curve based on PRET_A and blue curve match closer to the reference atmosphere temperature state profile for tropical case with lower temperature values at lower altitudes. The green curve based on PRET_B show higher temperature values at 15–27 km altitude levels. The

green curve shows that the temperature retrievals are generally higher by 10K at 9–27 km altitude levels for the South Pole regions in comparison with the mean state temperature profiles based on the PRET_A retrieval grid.

5.5.3 Spectral analysis

The ACE-FTS sample transmission data are used to study the MORSE retrieved parameters at the 9–27 km retrieval altitude in both HCN_0102 and HCN_0105 MW regions. The latitude coverage of the ACE-FTS level 1 sample data on a global scale is shown in the Figure 5.18.

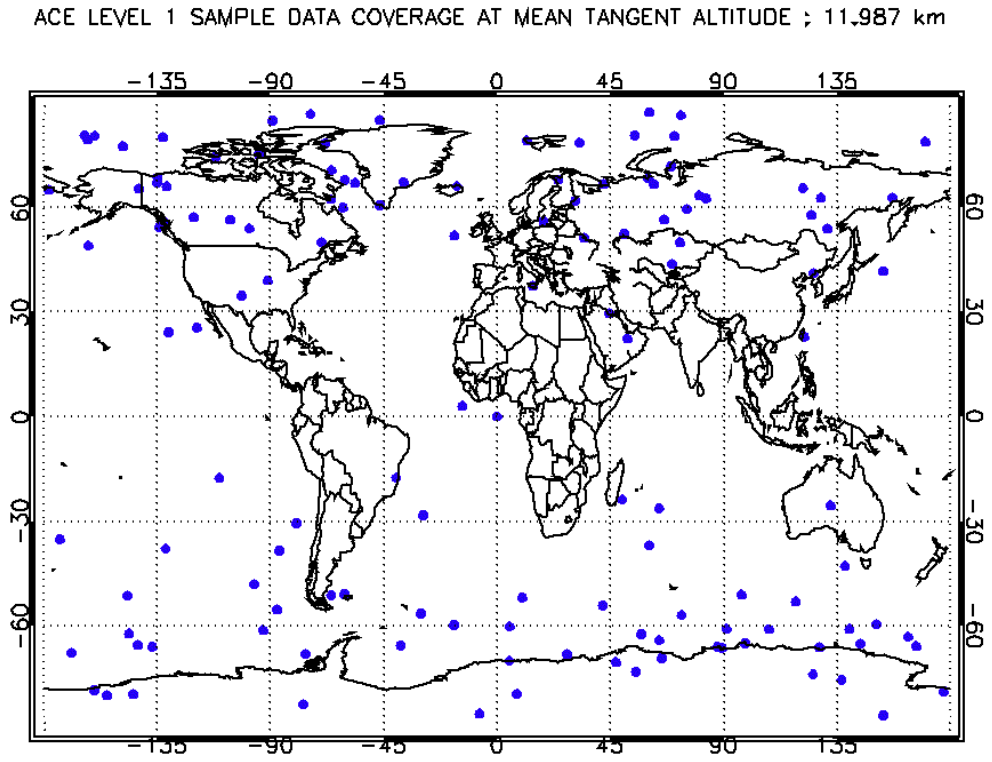

Figure 5.18 : Latitude coverage of ACE-FTS level 1 sample data at mean 12 km altitude.

The RFM is used to model the ACE-FTS transmission data by following the steps required for the forward model driver table:

1. The ACE-FTS retrieval processor uses 12 spectral MWs to retrieve HCN concentration levels out of which 3 MWs (listed in the Table 5.4]) are chosen for the analysis based on the information content of the HCN spectral feature

in the ACE-FTS sample transmission data along with the HCN_0102 and HCN_0105 MW.

2. The ACE-FTS AILS files from the ACE-FTS operational processor are used in this study. The ACE-FTS ILS is wavenumber dependant which is convolved with the simulated transmission data [Genets and Tremblay, 1999].
3. The ACE-FTS FOV response is calculated as a function of elevation angles (in degrees) since the input aperture for the ACE-FTS instrument is a circle of diameter 1.25 mrad (0.07161973°) [Boone *et al.*, 2005]. This roughly translates to 3 to 4 km at the tangent point. Unlike the MIPAS-E instrument, the measuring geometry varies for the ACE-FTS instrument as measurements are based on solar occultation method. So, sometimes ACE-FTS is pointing along the orbit track, and sometimes it is pointing at > 60° off the orbit track to view the sun. The FOV 'footprint' at the tangent point will vary with the viewing geometry and even with the altitude within an occultation when not looking along the orbit track.
4. As the FOV is a function of elevation angles, the forward model needs extra information about the position of the satellite observing system. An altitude of 650 km from the Earth's surface is used in the OBS section of the driver table.
5. The spectroscopic database and cross section data from HITRAN 2004 are used.
6. Standard reference atmospheric data based on standard climatology version 3.1 is used.

HCN MWs	**Wavenumber range (cm^{-1})**	**Altitude grid (km)**	**List of absorbers**
HCN_A101	3296.350–3296.610	10–28	HCN, H_2O, CO_2, C_2H_2, O_3, NH_3, CH_4
HCN_A102	3305.365–3305.715	7–22	
HCN_A103	3328.620–3329.070	20–28	

Table 5.4: List of absorbers in the MW list for HCN based on ACE-FTS selection.

The main aim of this study is to test the response of the transmission signal in ACE-FTS HCN MWs, while using a combination of MORSE and ACE-FTS retrieved parameters. The 'official' wavenumber range for ACE-FTS is 750–4400 cm^{-1} but the SNR is not too good between 4100 and 4400 cm^{-1} [Table 5.3]. The limit at the low wavenumber end is due to the MCT detector and for the upper wavenumber end the problem is actually a coating on the beamsplitter. The study focuses on three main latitude regions of interest: 1) North Pole, 2) Tropics and 3) South Pole; within these latitude bands, spectra were averaged together to give the mean transmission spectra at desired tangent altitudes. The modelled RFM spectra are compared to the mean transmission signal calculated for respective MW regions. It should be possible to compare the simulations and mean spectra both in the ACE-FTS retrievals and HCN_0102 and HCN_0105 MW regions, which have been used for MORSE retrievals. For comparison, the ACE-FTS transmission signal is normalised by dividing each of the spectral data point at a specified tangent altitude to a defined baseline (the transmission signal is close to 1) corresponding to each MW.

5.5.3.1 Sensitivity test

The sensitivity test should help to distinguish errors due to the interfering gases in the HCN retrieval MWs. The primary objective of this study is to investigate whether any input parameter has a direct affect on the HCN retrieval MWs at the 12 km MIPAS-E nominal altitude level. The sensitivity test is carried out in different latitude zones in tropics and both North and South Pole regions.

5.5.3.1.1 The methodology

The ACE-FTS atmospheric transmission signal is simulated using appropriate inputs required for forward model calculations mentioned in Section 5.5.3. In the tests, each mean state MORSE retrieved input parameter or retrieved profiles is segregated and combined with the rest of the ACE-FTS retrieved mean state parameters or profiles. However, differences were only found for pressure. Thus, the transmission signal is simulated using the atmospheric state which is represented by 1) all MORSE retrieved mean state profiles (blue) and 2) MORSE retrieved mean pressure profile replaced with ACE-FTS mean pressure profile (red). The simulated

results are compared to normalised mean ACE-FTS transmission signals at the 12 km nominal altitude only, all three latitude zones and MIPAS-E and ACE-FTS HCN MWs.

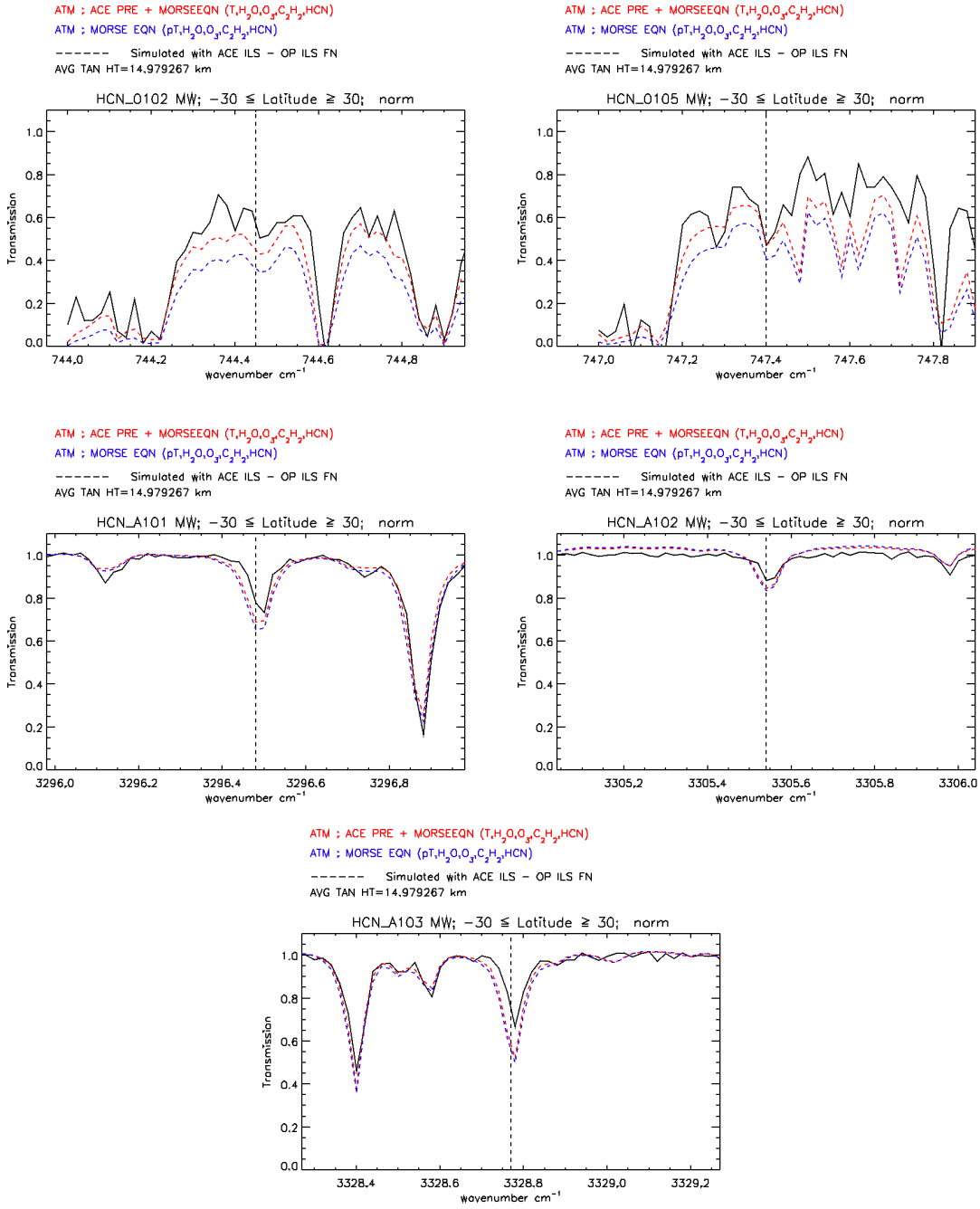

Figure 5.19: Comparison of simulated and normalised mean ACE-FTS transmission signal (black solid) at 12 km nominal altitude for tropical regions (−30° ≤ latitude ≥ 30°). Blue dotted- MORSE retrieved mean profiles, red dotted- MORSE retrieved mean pressure replaced by ACE-FTS mean pressure profile, black dotted- line centre of HCN spectral feature.

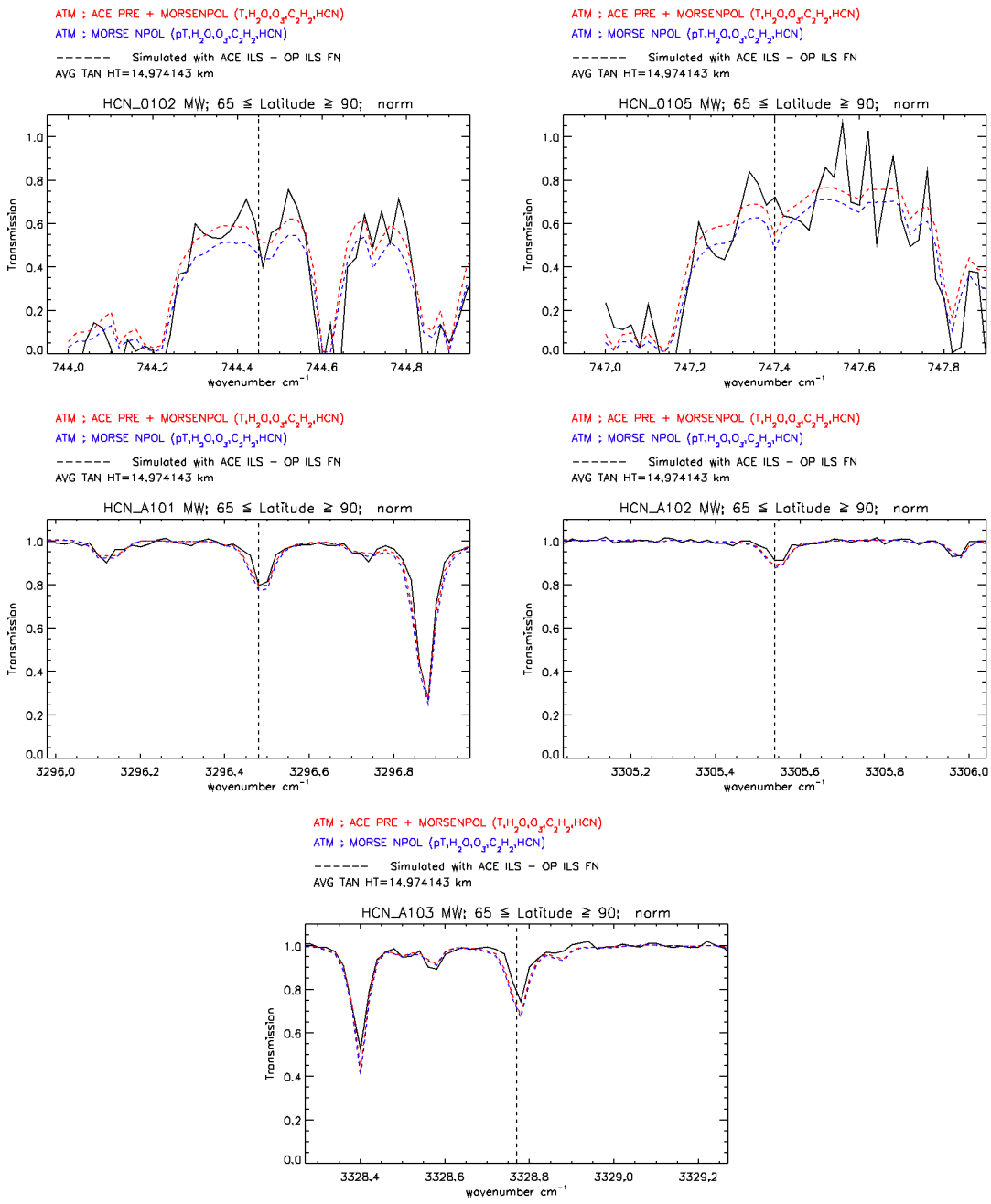

Figure 5.20: Comparison of simulated and normalised mean ACE-FTS transmission signal (black solid) at 12 km nominal altitude for North Pole (65° ≤ latitude ≥ 90°). Blue dotted- MORSE retrieved mean profiles, red dotted- MORSE retrieved mean pressure replaced by ACE-FTS mean pressure profile, black dotted- line centre of HCN spectral feature.

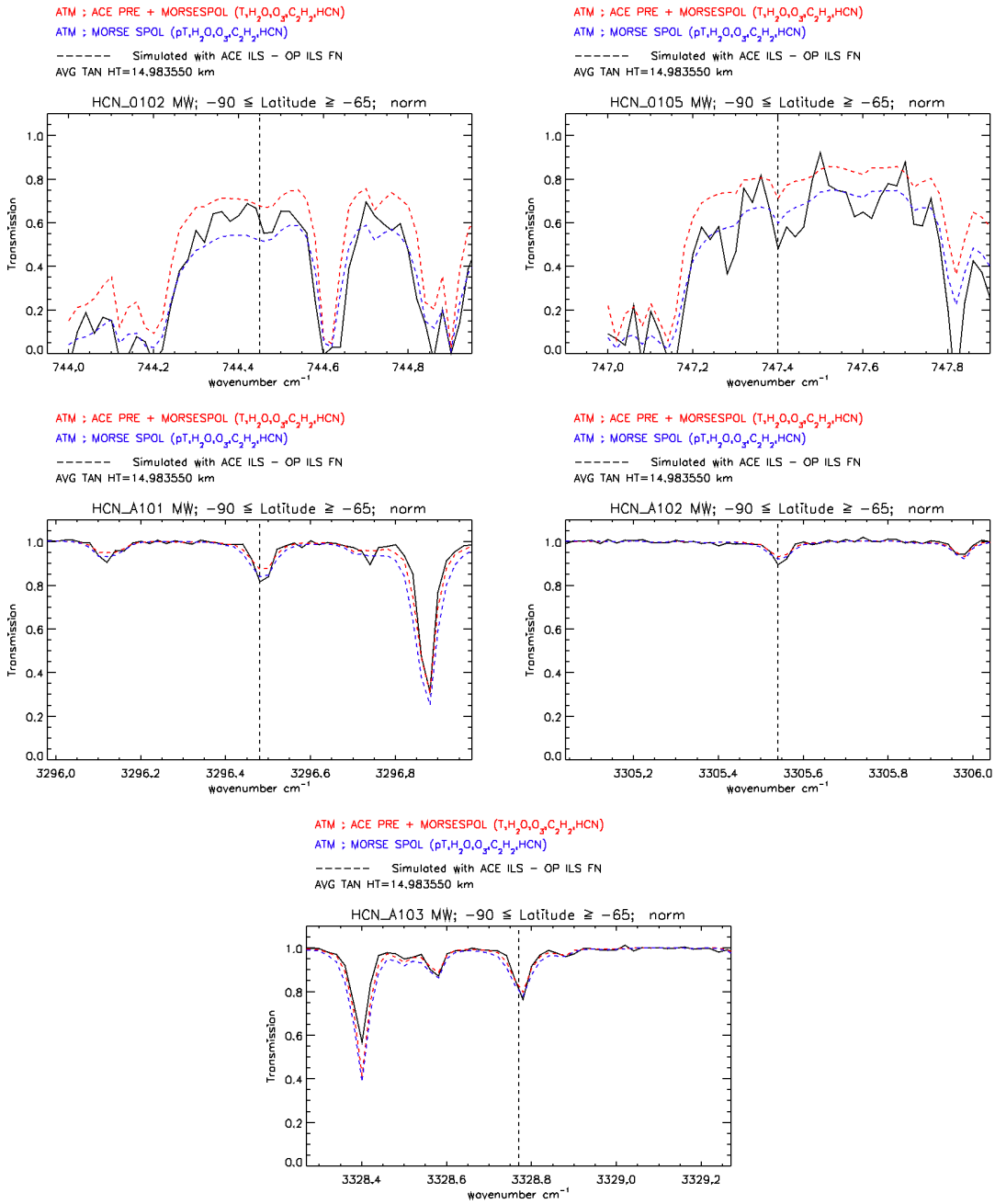

Figure 5.21: Comparison of simulated and normalised mean ACE-FTS transmission signal (black solid) at 12 km nominal altitude for South Pole (−90° ≤ latitude ≥ −65°). Blue dotted- MORSE retrieved mean profiles, red dotted- MORSE retrieved mean pressure replaced by ACE-FTS mean pressure profile, black dotted- line centre of HCN spectral feature.

The sensitivity test is carried out by using the measured MIPAS-E level 1b spectral data from the orbit 08585 scan 03 at the 12 km nominal altitude level. A simulation approach used in this investigation calculates the measured MIPAS-E radiance using the method described below:

1) Simulated radiances are calculated using the MORSE retrieved pressure and the MIPAS-E level 2 retrieved parameters such as temperature and H_2O, O_3, HNO_3 VMR profiles in both the HCN MWs.
2) The simulations are repeated once again but with PRET_A MORSE retrieved pressure state replaced with the MIPAS-E level 2 operational pressure.
3) Steps 1 and 2 are repeated by excluding HCN from the simulation calculations.
4) The difference between measured and simulated radiances with all gases (black) is calculated. It is compared to the difference computed between simulated radiance with all gases and simulated radiance without HCN (red).

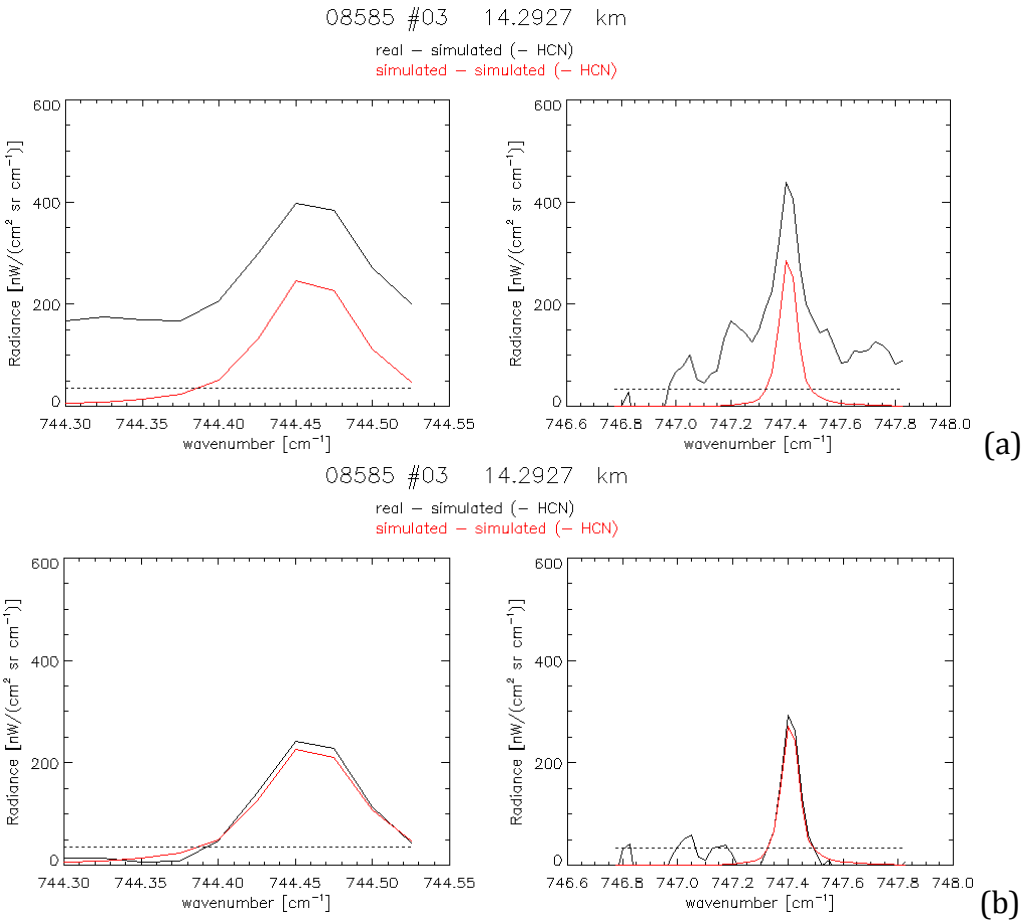

Figure 5.22: Difference between measured spectrum and simulated spectrum without HCN (black) compared to difference between simulated spectrum with all interfering gases and simulated spectrum without HCN (red) in the HCN_0102 MW (left) and HCN_0105 MW (right) at 12 km MIPAS-E nominal altitude (a) MORSE retrieved mean pressure profile is replaced by MIPAS-E level 2 pressure data and (b) MIPAS-E level 2 retrieved parameters.

5.5.3.1.2 Sensitivity test results

Figure 5.19, Figure 5.20, andFigure 5.21 show that the comparison of the difference between pressures in the HCN_0102 and HCN_0105 MWs with the HCN_A101, HCN_A102 and HCN_A103 MWs in the tropics and North and South Pole regions. The profile comparison in the Figure 5.17 shows difference of about 50–60 mb in both the MORSE and ACE-FTS pressure retrievals values at the 12 km nominal altitude level. Figure 5.22 shows the comparison of residual spectral radiances in HCN_0102 and HCN_0105 MW. Part (a) of the figure shows the result when the MORSE retrieved pressure is used in the simulation calculations and part (b) when MIPAS-E level 2 retrieved pressure values is used for orbit 08585 scan 03 at the 12 km nominal altitude.

Results are shown for the MORSE retrieved pressure only, as there is no significant difference observed in the MWs due to temperature and other retrieved profiles. The significant offset seen as a result of the MORSE retrieved mean pressure state used in the simulations to compare the ACE-FTS transmission signal and the difference between the measured MIPAS-E level 1b spectral radiance and simulated spectrum suggests that the two MWs are sensitive to the changes in pressure retrievals. Thus, the MORSE retrieved HCN concentration levels have significant changes in retrieved pressures cause large differences in transmission. Clearly retrievals of HCN are highly sensitive to pressure in both the HCN_0102 and HCN_0105 MWs.

5.5.3.2 Effect of CH_3Cl

The primary sources of methyl chloride (CH_3Cl) are biomass burning, oceans and biogenic emissions located mainly in the tropics and subtropical terrestrial regions [Rinsland *et al.*, 2004]. The major sink of CH_3Cl in the atmosphere is due to reaction with OH and other sinks are oceans and soil sinks.

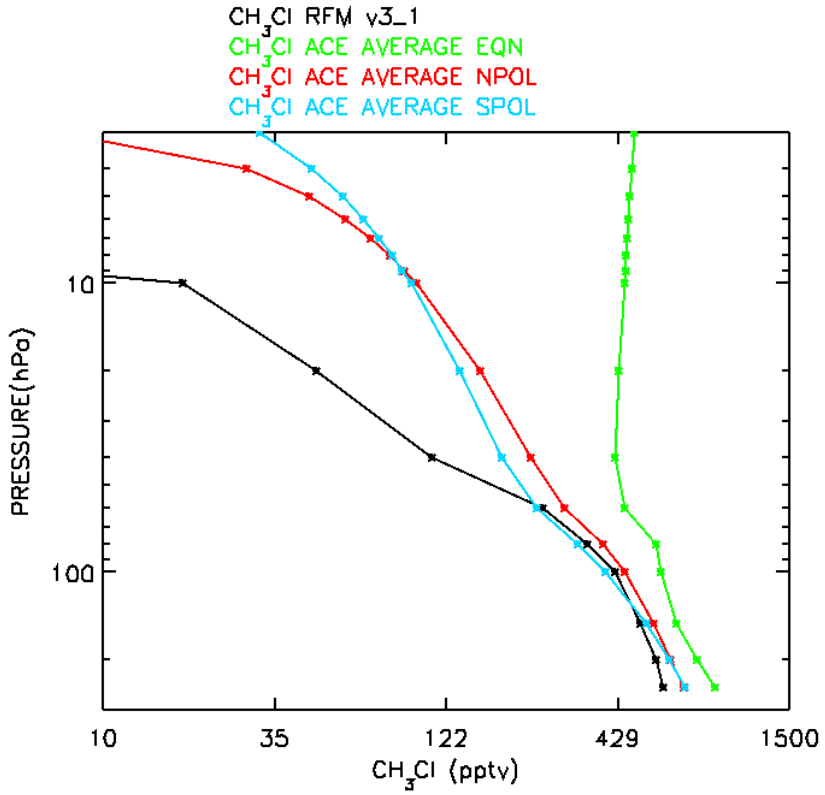

Figure 5.23: ACE-FTS CH_3Cl profiles for tropics (green), North Pole (red) and South Pole (aqua) against CH_3Cl profile based on extra_species_v3_1.dat (black).

The latitudinal distribution of CH_3Cl is the highest in tropics and the lowest in polar regions [Khalil *et al.*, 1999]. The global average mixing ratios of CH_3Cl is about 550 ± 30 pptv [Yazuko *et al.*, 2006]. Mixing ratios of up to 1.12 ppbv and 0.96 ppbv for CH_3Cl were measured in the upper troposphere using ACE-FTS measurements in the boreal forest and East coast of Tanzania respectively. The Figure 5.23 shows mean state profiles for CH_3Cl using the ACE-FTS level 2 data from September, October and November 2005 in tropics and North and South Pole regions. Between 200 and 60 mb the polar mean profiles are closer to background values and tropics show large enhancement due to biomass burning events. The black profile represents the climatology profile based on the extra_species_v3_1.dat file.

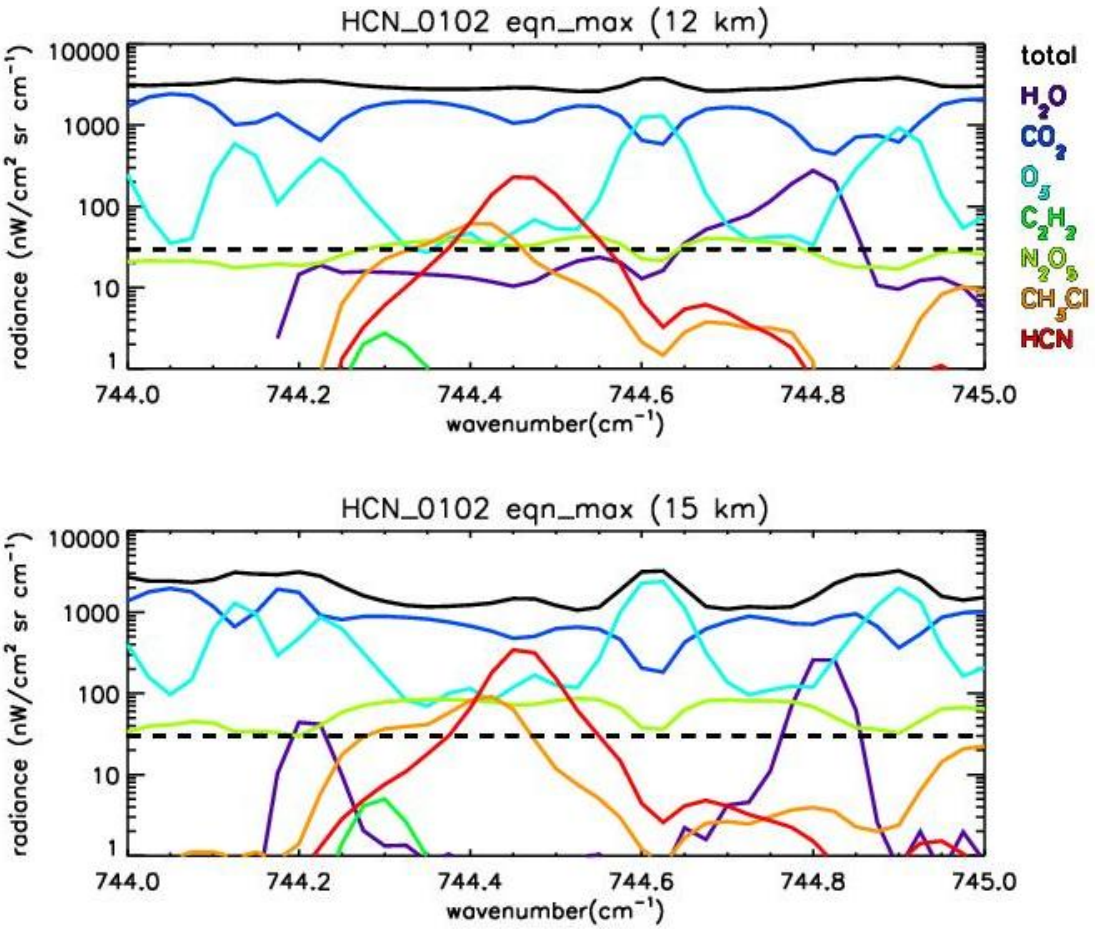

Figure 5.24: Plot of RFM modelled radiances (RFM(all)−RFM(without gas)) for major interfering gases in 744–745 cm^{-1} in tropics (30°N–30°S) using tropical climatology and extreme maximum HCN and CH_3Cl values. The black dotted line represents the expected noise equivalent to spectral radiance (NESR) of the MIPAS-E, which is based on pre-flight estimates of 50 $nW/(cm^2\ sr\ cm^{-1})$ for band A.

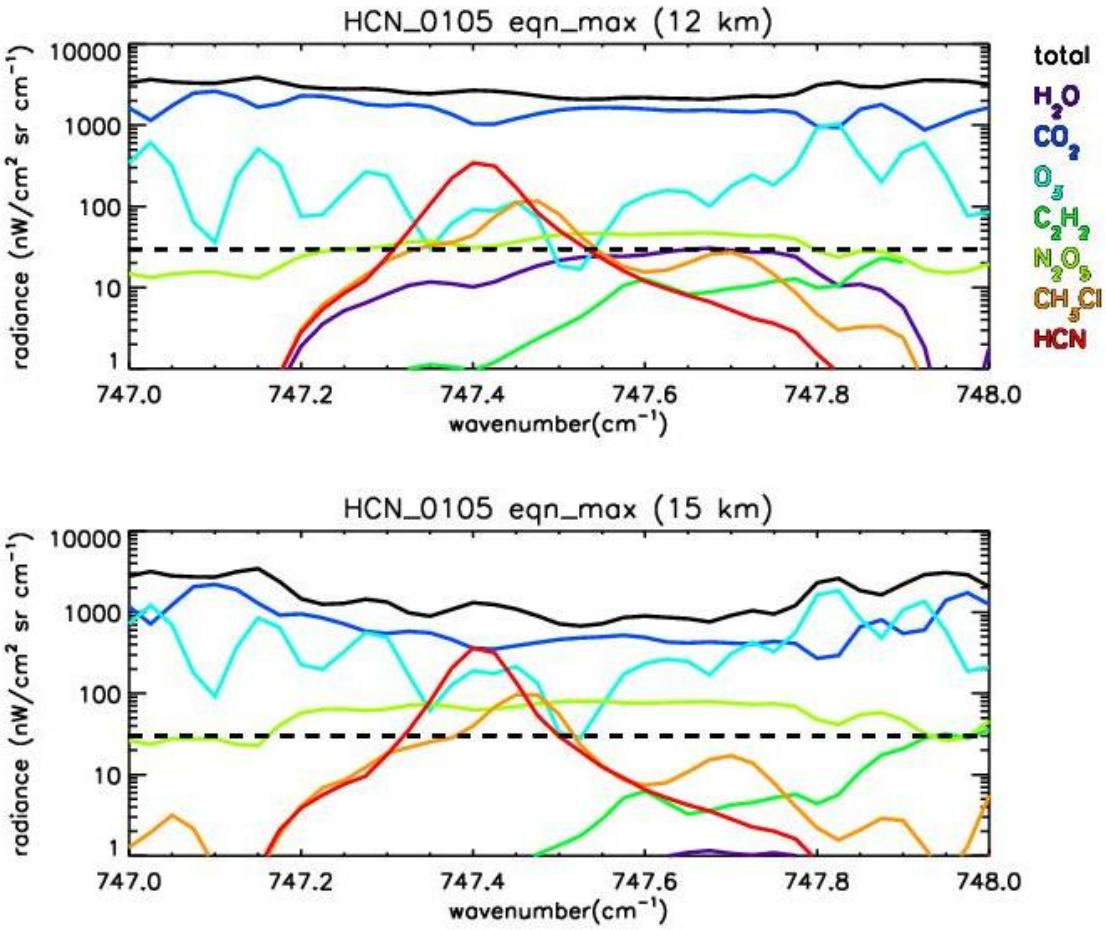

Figure 5.25: Plot of RFM modelled radiances (RFM(all)−RFM(without gas)) for major interfering gases in 747–748 cm^{-1} in tropics (30°N–30°S) using tropical climatology and extreme maximum HCN and CH_3Cl values. The black dotted line represents the expected noise equivalent to spectral radiance (NESR) of the MIPAS-E, which is based on pre-flight estimates of 50 $nW/(cm^2\ sr\ cm^{-1})$ for band A.

Figure 5.24 and Figure 5.25 based on Section 4.2.4.3 show the influence due to the presence of enhanced CH_3Cl in the tropical atmosphere in HCN_0102 and HCN_0105 MW regions at the 12- and 15-km levels. Atmospheric profiles for H_2O, O_3, HNO_3, NO_2 and N_2O_5 are based on standard tropical climatology values and the extreme maximum values for HCN and CH_3Cl [Rinsland *et al.*, 2004] are based on ACE-FTS tropical measurements in the upper troposphere. The HCN spectral feature is significantly masked due to presence of enhanced CH_3Cl in both MW regions at the 12- and 15-km altitude levels. The contribution plots highlight the importance of segregating the CH_3Cl spectral feature in order to retrieve HCN concentration levels with more accuracy and smaller retrieval errors.

5.5.3.2.1 The methodology

Once again, a simulation approach is adopted to confirm the magnitude of effects of the presence of CH_3Cl in the selected [Table 5.2] HCN MWs. The method involves the following steps:

1) The ACE-FTS transmission signals (black solid) are averaged at MIPAS-E 12 km nominal altitude in HCN_0102, HCN_0105 and CH3CL_0101 MWs (ACE-FTS MW) (listed in Table 5.5]) in all the three latitude regions.
2) Firstly, simulated transmission calculations are performed using all MORSE retrieved parameters and CH_3Cl for enhanced cases (red dotted).
3) Secondly, again the transmission signal is simulated with all MORSE retrieved parameters but excluding CH_3Cl in the forward model calculations (blue dotted).
4) The mean ACE-FTS transmission signal is compared to the simulated transmission signals.

CH_3Cl MWs	**Wavenumber range (cm^{-1})**	**Altitude range (km)**	**List of absorbers**
CH3Cl_0101	2966.30–2966.70	9–25	CH_3Cl, H_2O, CH_4, O_3, C_2H_6, NH_3, NO_2
	2966.70–2967.10		
	2966.95–2967.65		

Table 5.5: List of absorbers for CH_3Cl MWs based on ACE-FTS selection.

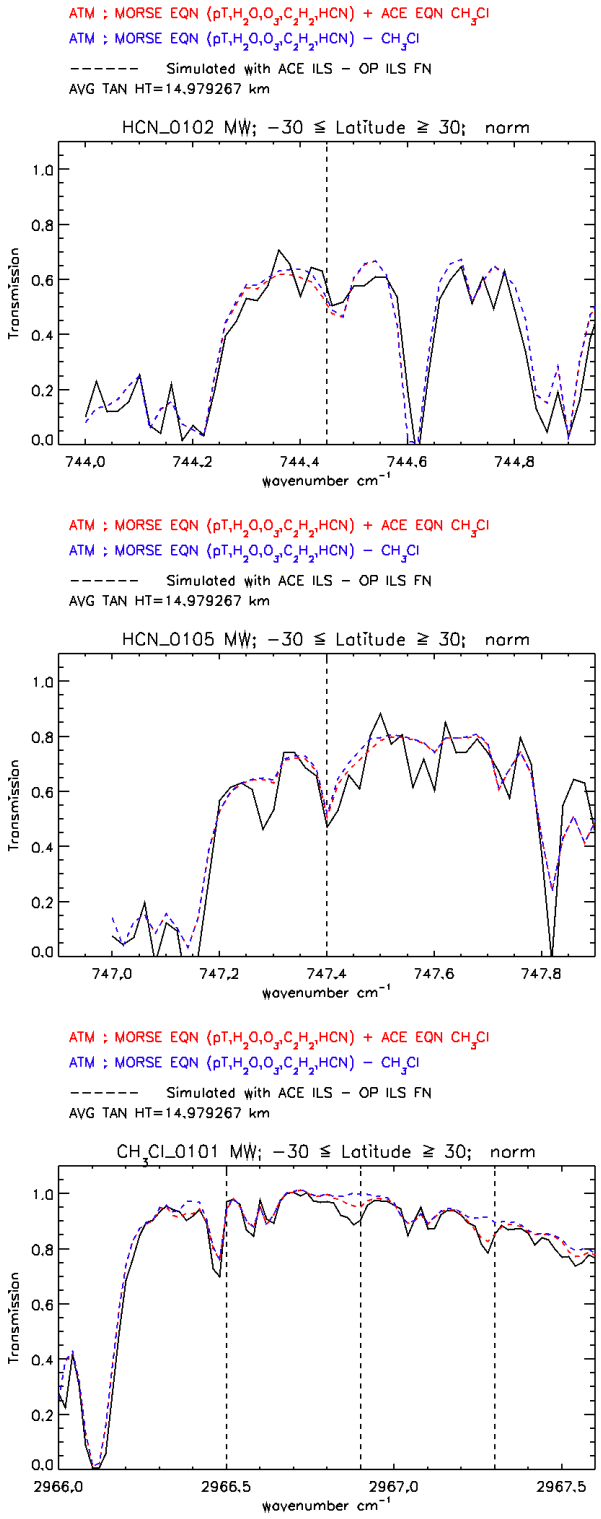

Figure 5.26: Comparison of simulated and normalised mean ACE-FTS transmission signal at 12 km nominal altitude for tropics (−30° ≤ latitude ≥ 30°). The black dotted line represents line centre of the HCN and CH_3Cl spectral features in the respective MW regions, black solid- the ACE-FTS transmission.

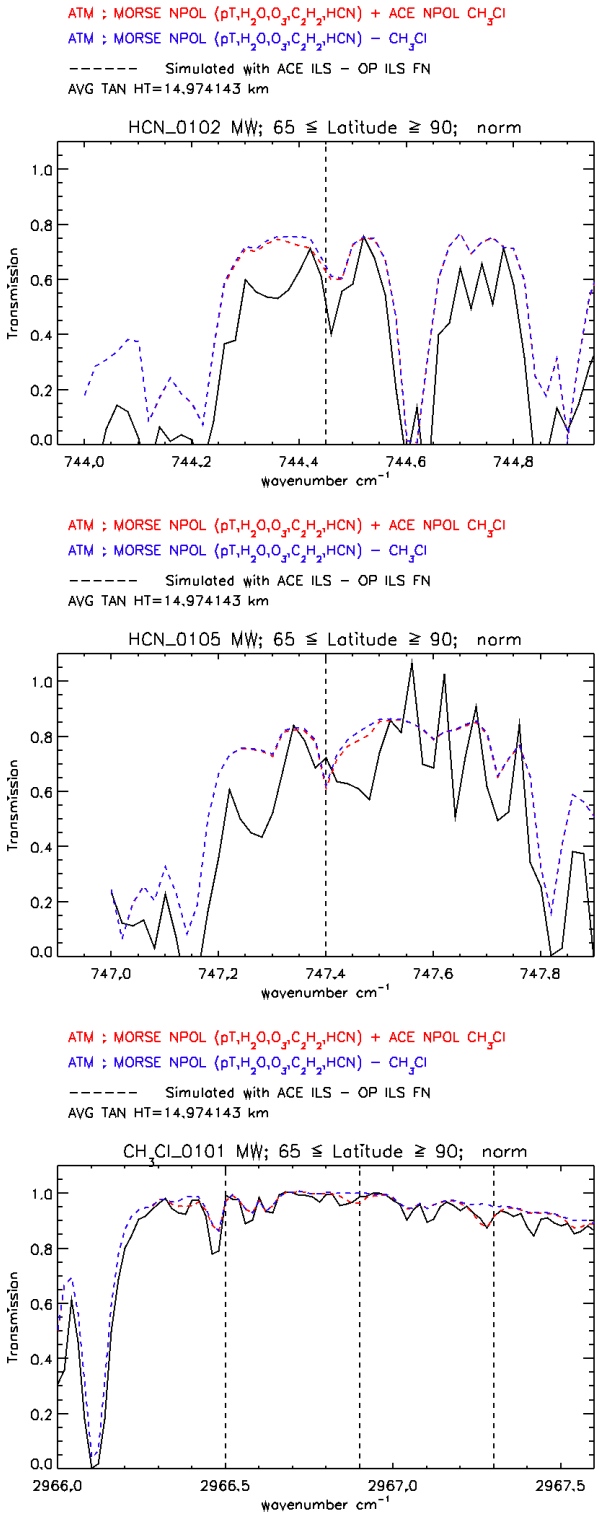

Figure 5.27: Comparison of simulated and normalised mean ACE-FTS transmission signal at 12 km nominal altitude for North Pole (65° ≤ latitude ≥ 90°). The black dotted line represents line centre of the HCN and CH_3Cl spectral features in the respective MW regions, black solid- the ACE-FTS transmission.

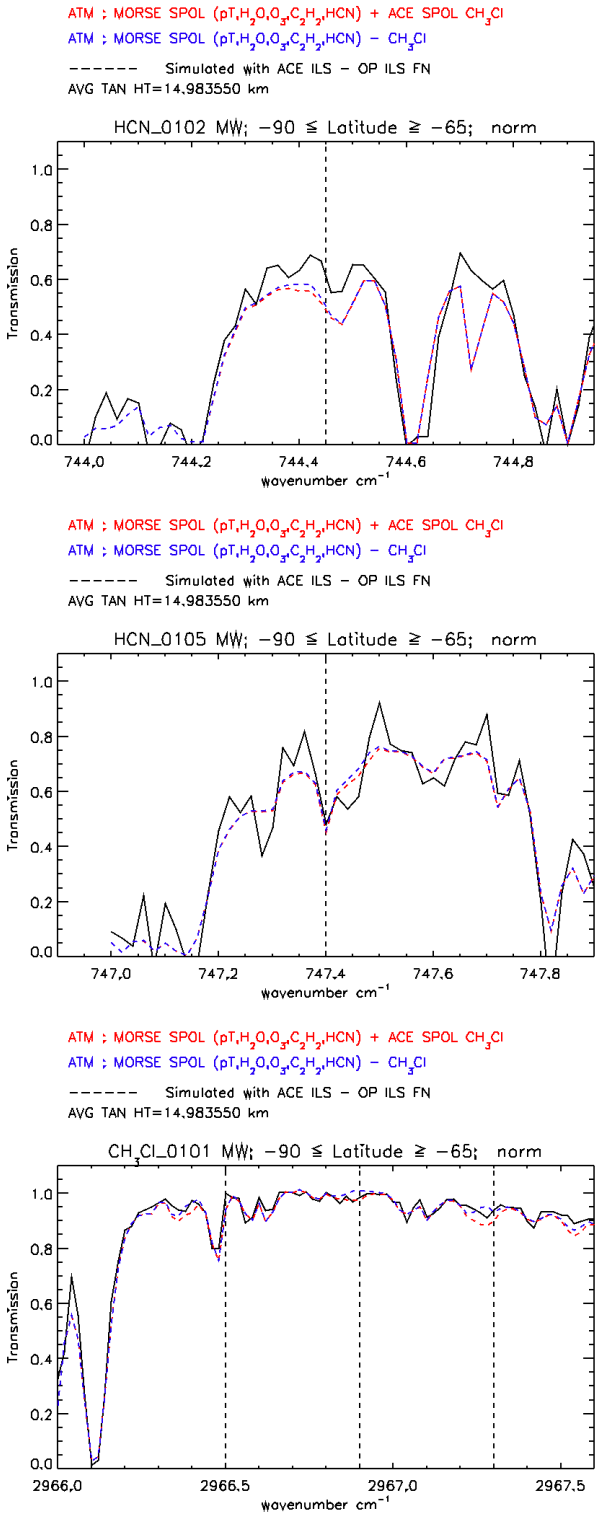

Figure 5.28: Comparison of simulated and normalised mean ACE-FTS transmission signal at 12 km nominal altitude for South Pole (−90° ≤ latitude ≥ −65°). The black dotted line represents line centre of the HCN and CH_3Cl spectral features in the respective MW regions, black solid- the ACE-FTS transmission.

Figure 5.26, Figure 5.27 and Figure 5.28 show the results of the comparison of tropics, North and South Pole regions for enhanced CH_3Cl (right) in the HCN_0102 (top), HCN_0105 (middle) and CH3CL_0101 (bottom) MWs. The line centres for HCN and CH_3Cl in respective MWs are shown by black dotted lines. The 2966.70–2967.10 and 2966.95–2967.65 cm^{-1} regions in CH_3Cl MWs have more information content than the 2966.30–2966.70 cm^{-1} region. No major difference is observed in the HCN_0102 and HCN_0105 MW regions except for a slight difference in the left wing regions if HCN spectral features in the tropics and North Pole regions.

5.5.4 Inter-comparing the MORSE retrieved HCN based on PRET_A pre-retrieved data

The main objective of this investigation is to study the final HCN (PRET_A) retrieved using the MORSE algorithm. The study should lead to the interpretation of the amount of concentration levels retrieved in the tropics and North and South Pole regions. First, a mean transmission signal is calculated in the ACE-FTS HCN retrieval MWs at the 9- and 12-km nominal altitudes. Next, the simulated transmission signals are calculated using all MORSE retrieved parameters as the input.

The comparison results are shown in Figure 5.29, Figure 5.30 and Figure 5.31. The general conclusion is that HCN retrieved using the MORSE algorithm is high in all latitude regions and also at all altitude levels compared to ACE-FTS retrieved HCN concentration levels. The comparison in the tropics can be ignored as poor sampling of ACE-FTS sample transmission data set is available for the tropics [Figure 5.18].

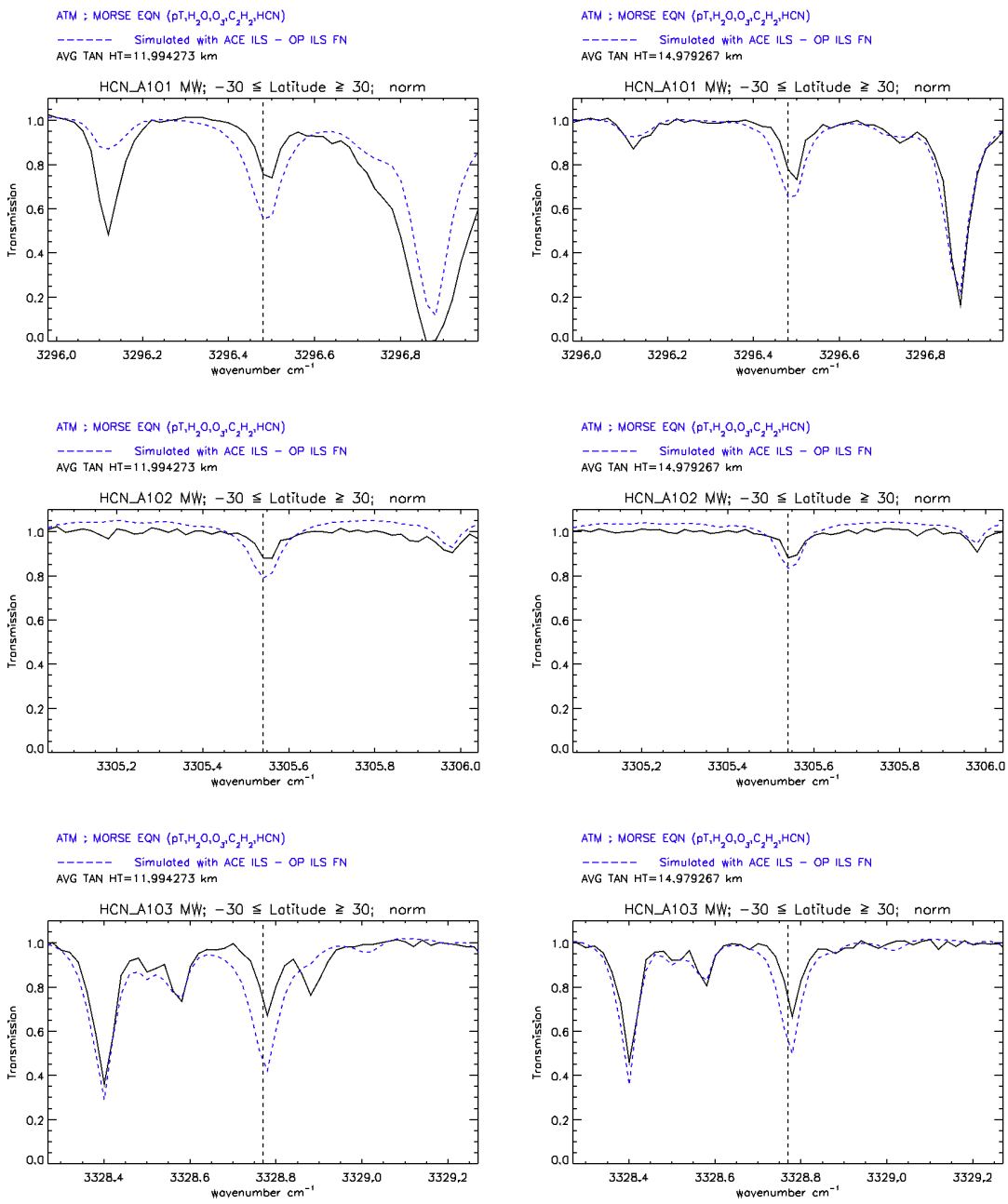

Figure 5.29: Comparison of simulated and normalised mean ACE-FTS transmission signal at 9 km (left) and 12 km (right) nominal altitude for tropics (−30° ≤ latitude ≥ 30°). The black dotted line represents line centre of HCN spectral feature in the respective MW regions, black solid- the ACE-FTS transmission signal.

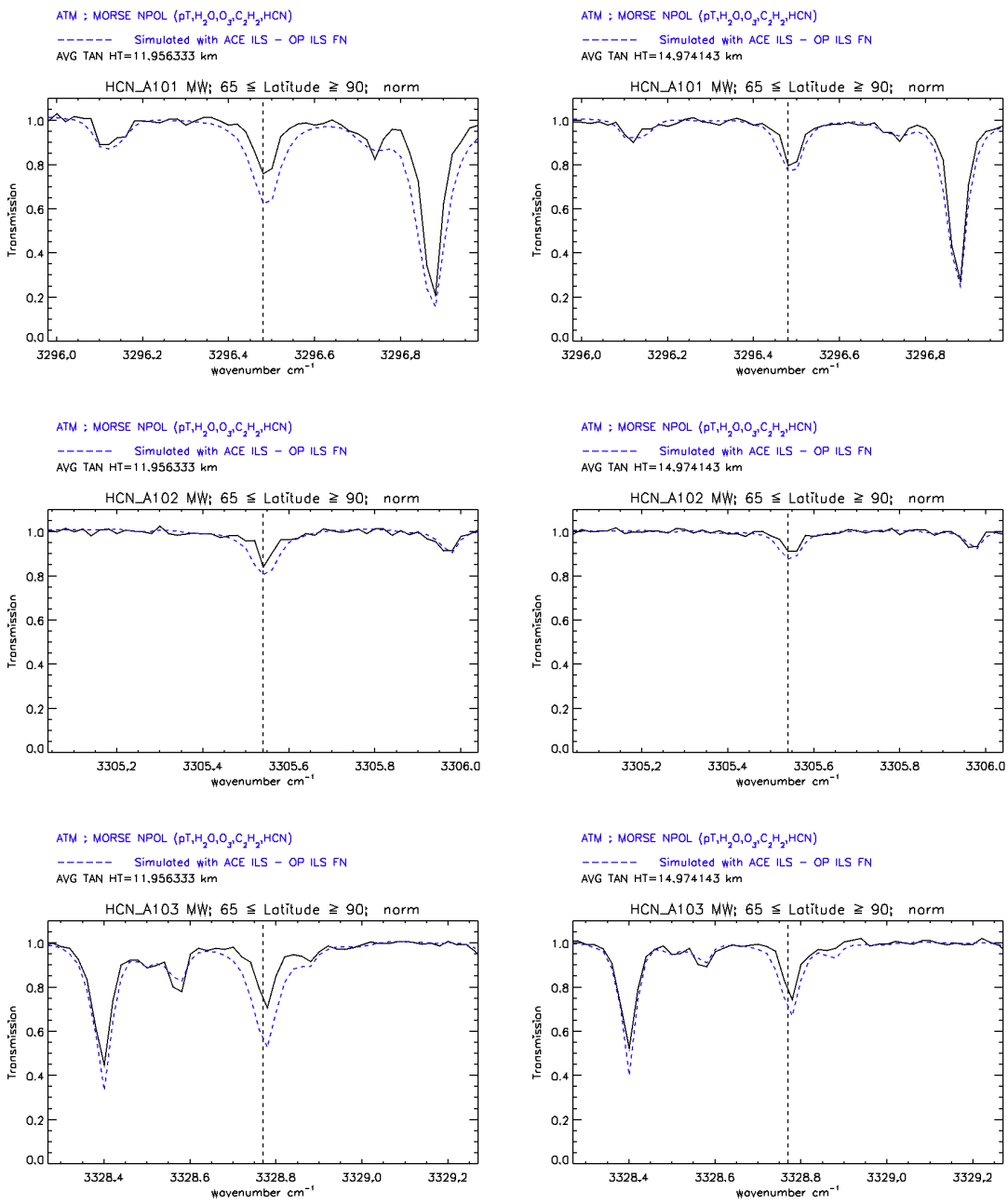

Figure 5.30: Comparison of simulated and normalised mean ACE-FTS transmission signal at 9 km (left) and 12 km (right) nominal altitude for North Pole (65° ≤ latitude ≥ 90°). The black dotted line represents line centre of HCN spectral feature in the respective MW regions, black solid- the ACE-FTS transmission signal.

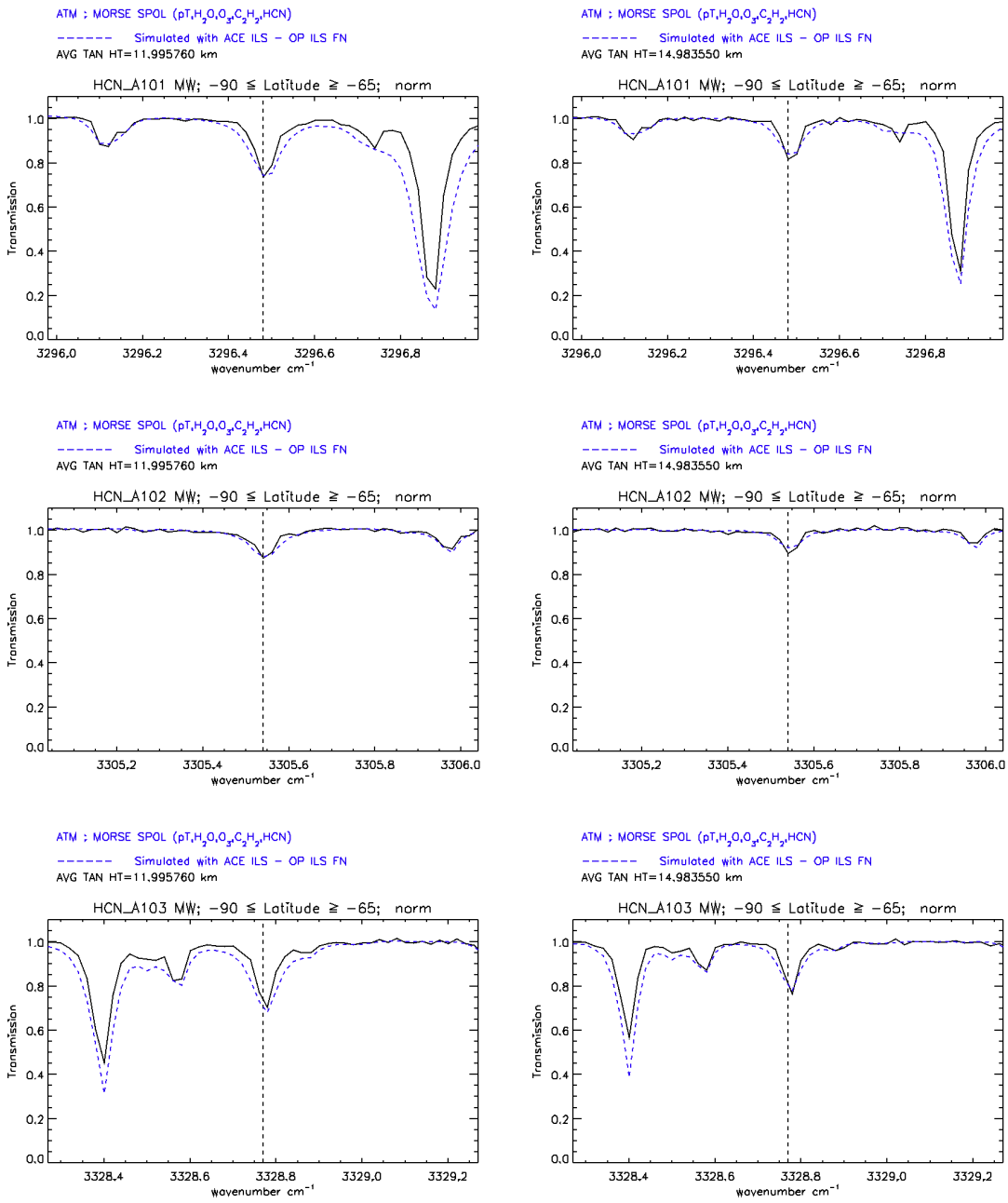

Figure 5.31: Comparison of simulated and normalised mean ACE-FTS transmission signal at 9 km (left) and 12 km (right) nominal altitude for South Pole (−90° ≤ latitude ≥ −65°). The black dotted line represents line centre of HCN spectral feature in the respective MW regions, black solid- the ACE-FTS transmission signal.

5.6 Final HCN retrieval data based on PRET_A

The final MORSE HCN retrieval data chosen for study are based on the 9–27 km pre-retrieved dataset (PRET_A), i.e., all the input parameters or VMR profiles abd extiction profiles are retrieved on 9–27 km retrieval grid. The other retrieval inputs are detailed in Section 5.1.1. Maps of HCN distributions for October 2003 are derived from 365 orbits of MIPAS-E data plotted at average pressure levels. The data are contoured and gridded at 20° longitude and 10° latitude resolution. The data is quality filtered and plotted for the 9–18 km altitude levels. White regions represent cloud contaminated data. The general pressure temperature and HCN χ^2, convergence and cloud filters are applicable. The maximum limit for pT and HCN χ^2 is set to 2 and cloud index should be greater than or equal to 4.

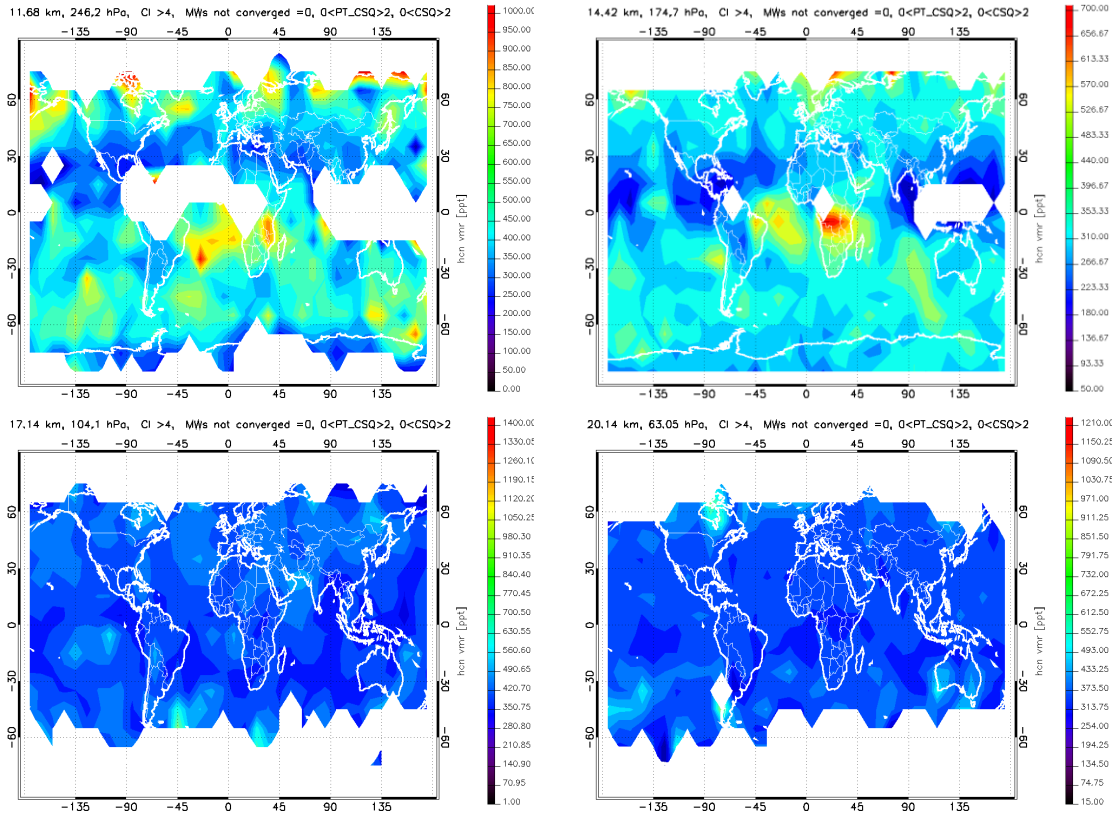

Figure 5.32: Global map of MORSE retrieved HCN at 9–18 km nominal altitude levels using PRET_A retrieval grid.

The data remains unfiltered for the North and South Pole regions as seen in the global maps shown in Figure 5.32. The global HCN map for 9 km (top left) show elevated HCN concentration levels. The retrieval level shows more unstable

retrieved HCN as elevated levels can be seen in different parts of the globe and cannot make any sensible conclusion. Conversely, the 12 km HCN retrieval (top right) show clearly the transport of pollution in both South American and Central African regionsThe HCN concentration levels retrieved at higher altitude levels are higher compared to background levels of 220 pptv, the map show fairly distributed HCN concentration levels.

5.6.1 HCN zonal behaviour

This section investigates the zonal distribution of HCN for October 2003 using the final MORSE retrieved data in the UTLS region. The monthly averaged HCN zonal mean result is inter-compared to the ACE-FTS HCN zonal mean and EOS MLS HCN zonal mean behaviour.

5.6.1.1 MORSE HCN zonal behaviour

Figure 5.33, shows the monthly zonal mean of HCN and how it varies for the month of October 2003. Following can be interpreted from Figure 5.33:

1) Enhanced tropical and mid-latitude HCN concentration levels at lower pressure levels. The enhancements in tropics can be mainly due to biomass burning events Further South mid-latitude HCN enhancement can be due to the transport of pollutants.
2) Strong uplift can be seen higher up in the atmosphere (≈50 mb) in both hemispheres.
3) A strong decrease in HCN concentrations levels can be seen in the tropics at around 150 mb pressure level.
4) An increase in HCN concentration levels is observed at higher altitude levels in tropics.
5) An increase in HCN concentration levels in the North Pole region at 200–100 mb pressure levels is observed.

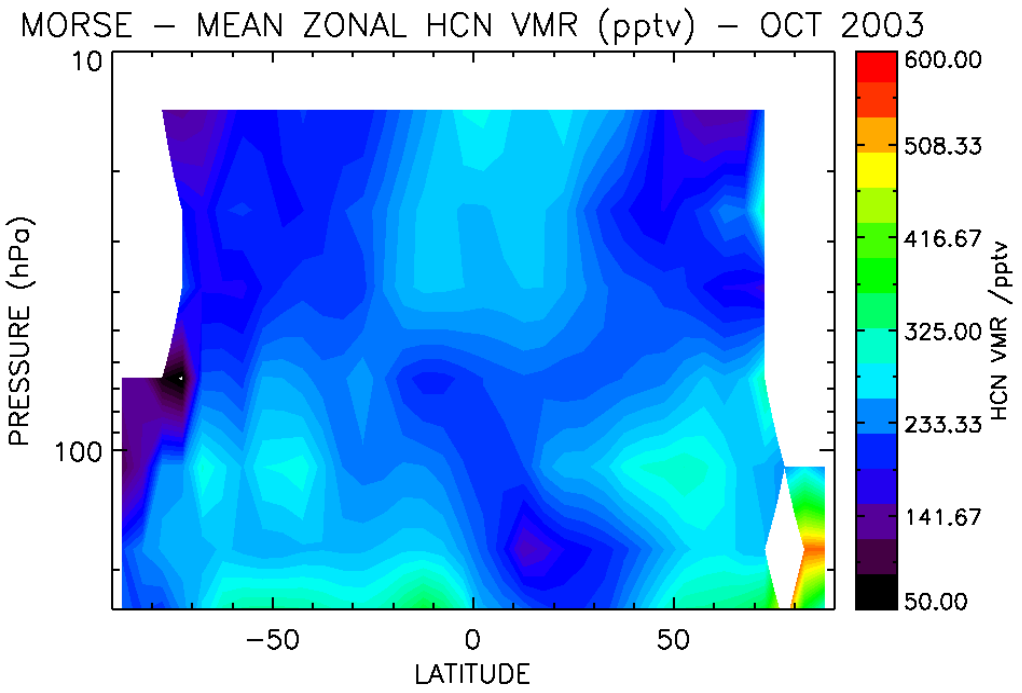

Figure 5.33: Latitudinal HCN distribution (unit: pptv), averaged zonally for October 2003.

5.6.1.2 ACE-FTS HCN zonal behaviour

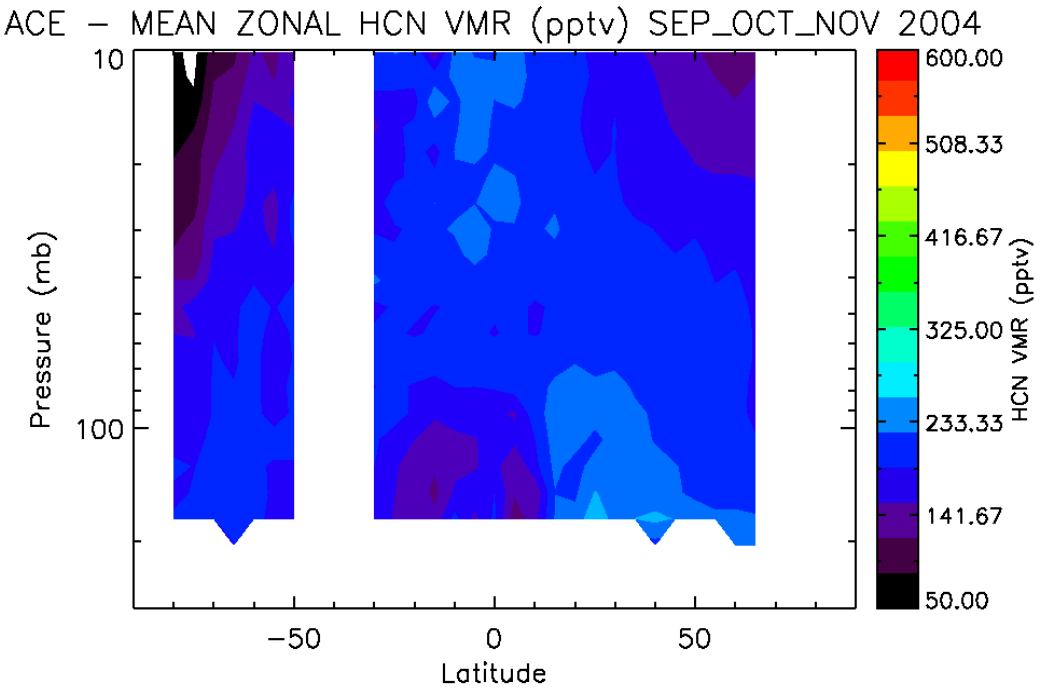

Figure 5.34: Latitudinal cross section using average of ACE-FTS HCN version 2.2 data from September, October and November 2004.

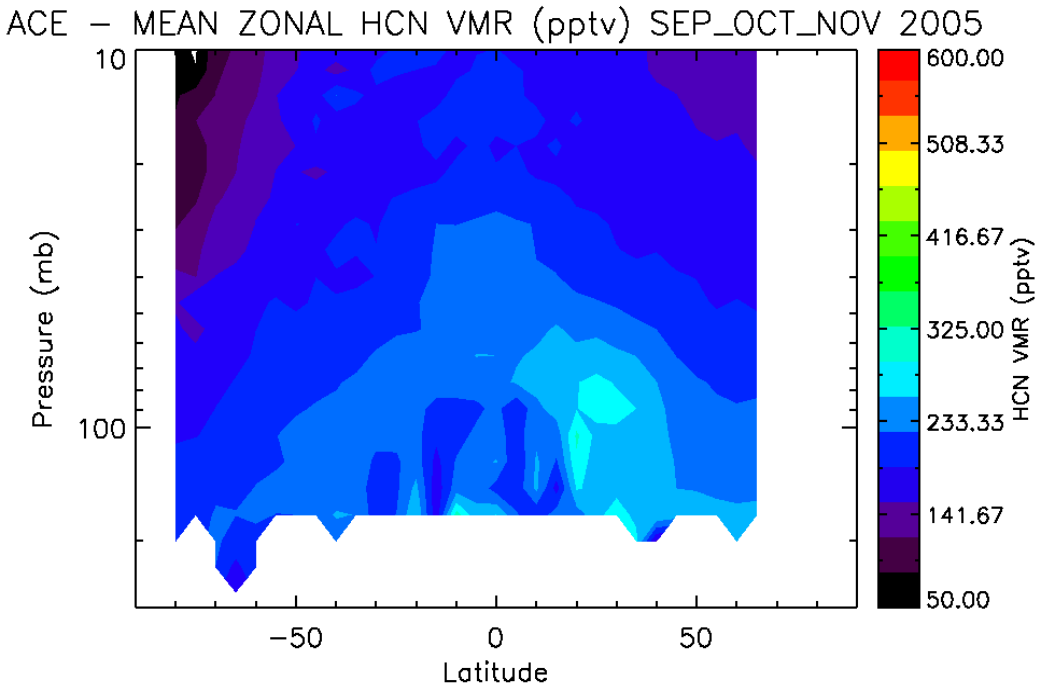

Figure 5.35: Latitudinal cross section using average of ACE-FTS HCN version 2.2 data from September, October and November 2005.

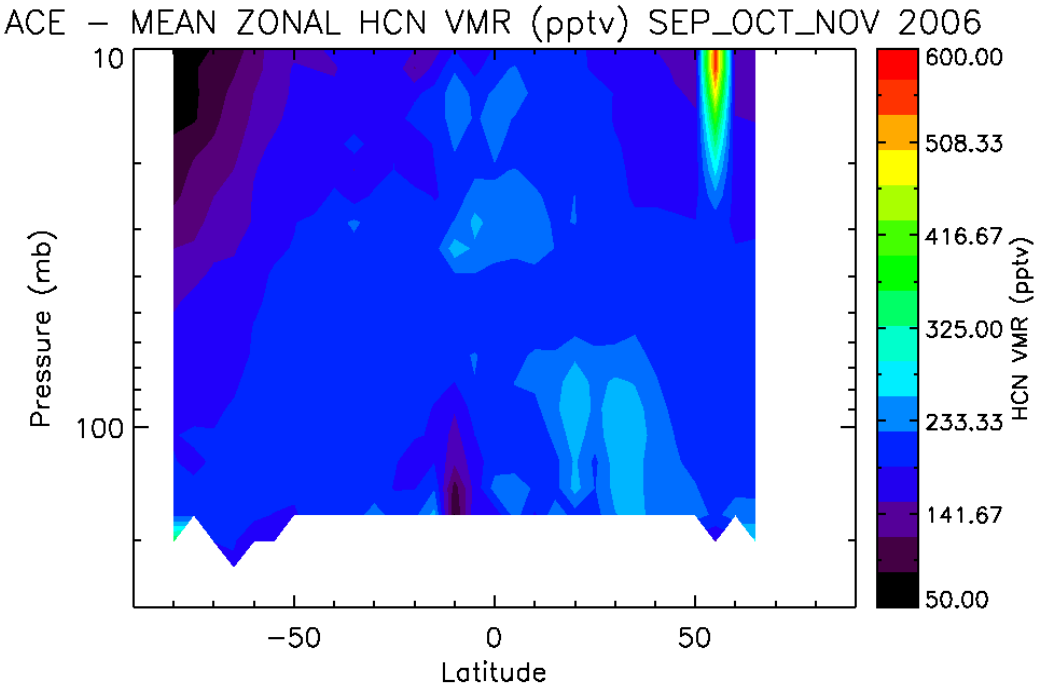

Figure 5.36: Latitudinal cross section using average of ACE-FTS HCN version 2.2 data from September, October and November 2006.

Due to the lack of ACE-FTS data in the tropical regions for the month of October [Figure 5.18], three months worth of data i.e. data from September, October and November are used to plot the zonal cross section for three different years—2004, 2005 and 2006. Figure 5.34, Figure 5.35 and Figure 5.36 show the zonal mean plots for ACE-FTS HCN data for different years. The white areas suggest missing data or T_fit parameter is set to 0 means no retrieval is performed and values set to *a-priori* values. The inter-comparison is limited to the 170–150 mb pressure levels due to the lack of data. All three zonal mean plots suggest highest HCN vmr in the tropics and south mid-latitude regions. The uplift can be seen as far as 10 mb pressure levels in the zonal cross sections. The Polar Regions show background concentration levels of HCN in both hemispheres.

5.6.1.3 EOS MLS experiment

The Earth Observing System Microwave Limb Sounder (EOS MLS) on NASA's EOS Aura satellite is a small radio telescope launched on 15th July 2004 aboard a Delta II 7920-10L, a two stage expendable rocket, from the Vandenberg Western Test Range. Aura was launched into a sun-synchronous, near polar (98.2 degree inclination) orbit. It orbits 705 km (438 miles) above the Earth and provides 82°N–82°S latitude coverage for each orbit. The Aura orbit stays fixed relative to the Sun and gives global coverage with ≈14 orbits per day.

The Earth's atmosphere is measured in the millimetre and sub-millimetre wavelength ranges with the help of a 1.6 m dish antenna as the instrument's FOV scans across the Earth's limb every 24.7 s [Pumphrey *et al.*, 2008] using the passive remote limb sounding technique. The EOS MLS instrument measures globally day and night. The instrument has an advantage of microwave measurements since it can be made even in the presence of ice clouds and aerosols unlike short-wave infrared, visible and ultraviolet measurements.

The radiation received by the dish antenna is converted into lower frequency in several heterodyne mixers (118, 190, 240 and 640 GHz radiometers; the 2.5 THz radiometer has a dedicated telescope and a scanning mirror whose operations are synchronised with the GHz antenna and GHz switching mirror). Four types of

spectrometers with different resolutions and bandwidths are used to cover the different altitude ranges. Lower altitude measurements require more spectral coverage and less resolution than measurements at higher altitudes. In total, 32 spectrometers (28 filter banks and 4 digital autocorrelators) are used to analyse the data. The EOS MLS version 2.2 standard data products are temperature, geopotential height, H_2O, HNO_3, O_3, HCl, ClO, N_2O, OH BrO, CO, HCN, HO_2, HOCl, SO_2, relative humidity (deduced from H_2O and temperature data) and cloud ice water content.

The EOS MLS has two filter banks— band 6F and band 27M— that are affected by the HCN lines. Band 27M was included in the instrument specifically to measure HCN. These filter banks are located such that they cover a frequency range centred on a single spectral line of a target molecule. The filter banks are designed with narrower filters at the band centre as the microwave spectral lines show strong pressure broadening [Pumphrey *et al.*, 2006]. The EOS MLS HCN measurements is produced by the so-called 190 GHz retrieval which includes information from band 27 in which the lower sideband of the radiometer is sensitive to the 177 GHz spectral line [Pumphrey *et al.*, 2006; 2008]. The EOS MLS experiment is making global measurements of HCN since August 2004.

5.6.1.3.1 Sources of errors

The level 2 algorithms adopt an optimal estimation retrieval approach to fit the MLS radiances and constraint with *a-priori* estimates and smoothing of the results are applicable. HCN is retrieved using the bands R2:190.B6F:O3 and R2:190.B27M:HCN. The strength of the HCN signal is not strong and is further masked by the interfering species. The interference due to stronger signals from O_3 and HNO_3 in the upper sideband of band B27M makes the retrieval of HCN difficult in the lower stratosphere [Livesey *et al.*, 2007].

The HCN signal is relatively low and hence a strong smoothing constraint is applied for useful HCN profiles, and thus, usable data lie between 10 hPa (≈32.0 km) and 1 hPa (≈48 km) [Pumphrey *et al.*, 2008].. As a result of retrieval smoothing the observed scatter is smaller compared to the estimated precision. HCN retrievals have extremely large systematic errors in the lower stratosphere and data are not considered useful above 10 hPa (≈ below 32 km).

The resolution, accuracy and estimated precision of EOS MLS HCN version 2.2 data are tabulated in Table 5.6. The accuracy is not less than 50%, precision data flagged negative suggest strong *a-priori* influence and hence these data should be avoided. The status variable stores the quality of the HCN profiles and hence even numbered status is used as a quality check for retrieved HCN profiles.

Given the useful height range of the v2.2 HCN product, it was not useful to compare these MLS data with the MIPAS MORSE retrievals produced in this thesis.

Pressure hPa	**Resolution V × H/km**	**Precision/pptv**	**Accuracy/%**	**Comments**
< 0.1	—	—	—	Unsuitable for scientific use
1–0.1	500 × 12	50	50	
10–1	300 × 10	30	50	
100–10	300 × 10	50	Very poor	Unsuitable for scientific use
> 100	—	—	—	Not retrieved

Table 5.6: Resolution, and accuracy of EOS MLS HCN version 2.2 data product. The precision is estimated precision (L2gpPrecision); the observed scatter is about 80 % of this value. (Table taken from Version 2.2 Level 2 data quality and description document [Livesey *et al.*, 2007]).

5.6.1.3.2 EOS MLS HCN weekly zonal mean behaviour

Averaging the v2.2 level 1 radiances to weekly zonal means can help in retrieving HCN mixing ratios over a greater vertical range since the HCN signal is relatively low in the retrieval MWs. Weekly zonal mean data [Pumphrey *et al.*, 2008] has been produced, using bands 6F, 27M and 1F, and can be used instead of the standard version 2.2 EOS MLS data. At 100 hPa, retrieval is attempted but the resulting values depend mostly on the a priori. Retrieval is not attempted at pressures greater than 100 hPa.]. The vertical resolution of the product is 6 km at an altitude of 32 km, degrading to 8 km at 20 km. The data are useful between 68 hPa

(≈18.7 km) and 0.1 hPa (≈64 km) [Pumphrey *et al.*, 2008] but also show biases with respect to historical measurements.

Given the uncertainties of both MIPAS MORSE and this MLS data at the extremes of the altitude range, and the low vertical resolution, it was decided that unfortunately this MLS product was also not suitable for comparisons for this thesis.

5.7 Comparison of MORSE retrieved HCN with IMK/IAA

HCN is also retrieved by the Institut für Meteorologie und Klimaforschung and Instituto de Astrofísica de Andalucía (IMK/IAA) retrieval processor [Glatthor *et al.*, 2009], where retrievals of HCN are carried out by using selected MIPAS-E measurements and, thus, a further comparison can now be made.

Following are the details of IMK/IAA retrieval set up:

- Retrieval of HCN using IMK/IAA processor is based on non-linear least square fitting using global fit approach [von Clarmann *et al.*, 2003].
- Any *a-priori* influence has been set to zero for HCN and C_2H_6 ; and hence, there is no explicit regularisation effect on the retrieved products.
- The retrieved data products are oversampled where 1 km spacing up to 44 km and 2 km spacing for the 44–70 km altitude grid is used. For other retrievals of MIPAS-E data performed at IMK, Tikhonov's regularisation scheme was used with a first derivative operator as a constraint.
- HCN is retrieved using 10 MWs in the ν_2 band between 715.5 and 782.725 cm^{-1} along with the application of the HITRAN spectroscopic C_2H_6 update of 2007.
- First, spectral shift, temperature profile and tangent heights are fitted, followed by the retrieval of the abundances of H_2O, O3, CH_4, N_2O, HNO_3, $ClONO_2$, ClO, N_2O_5, CFC-11, CFC-12, NO_2, HNO_4 and C_2H_6 in order to retrieve HCN profiles.

- To account for the rest of the interfering gases in the forward radiative transfer model (KOPRA-Karlsruhe Optimized and Precise Radiative Algorithm): CO_2, NH_3, OCS, C_2H_2, COF_2, C_2H_4, CFC-22, CFC-113 and PAN, CH_3Cl, $CH3CCl_3$, CCl_4, HCFC-141a and acetone are all based on climatological profiles.
- Along with the HCN profiles, MW-dependent continuum radiation profiles and MW-dependent, height-independent zero level calibration corrections are jointly fitted.

5.7.1 Comments on IMK/IAA retrieved HCN data

The IMK/IAA selection of MIPAS-E dataset covers 54 days from 8th September 2003 to 25th March 2004; this time period marks the peak and decline of the biomass burning period. The days used for the month of October are 13, 14, 15, 20, 21, 22, 30 and 31. They intend to expand this dataset and also improve poorer coverage in December to March by analyzing additional data. However, no further study has been published or is underway to improve the poorer coverage of data for HCN retrievals at IMK.

The additional interfering species such as, CH_3Cl 732.2 cm^{-1}, Furan 744.5 cm^{-1} and phenol 752.1 cm^{-1} were not fitted because their influence on HCN spectral lines was considered to be too small. IMK/IAA have fitted C_2H_2 at_729 cm^{-1} before retrieving HCN and they make sure that the HCN MWs selected such that there is no influence of C_2H_2 and CH_3Cl. Figures 2 and 3 in the paper by Glatthor *et al.* [2009] shows (Y−F) residual fits for 744 and 747 cm^{-1} HCN lines. However, the analysis of this thesis shows that during biomass burning events CH_3Cl is also emitted in high amounts (up to 1.12 ppbv measured by ACE-FTS) and thus the signal contribution due to CH_3Cl overlaps these HCN spectral lines as shown in the radiance contribution plots [Figure 5.24 andFigure 5.25].

The quality of the IMK/IAA HCN data was checked by the inspection of the RMS-values (should not significantly exceed measurement noise) and of the χ^2 values (should be below 2, ideally close to 1) associated to each individual fit. The residual fits of simulated radiances with and without HCN were compared and the

retrieved HCN values were at least qualitatively compared to the results of other experiments such as comparison with MOPITT CO column data (due to unavailability of any other independent global HCN measurements). The cloud filtering of the retrieved data was performed by using a cloud index threshold value of 4.0 derived from the spectral windows 788.2–796.25 and 832.3–834.4 cm^{-1} [Spang *et al.*, 2004]. This same criterion was applied to the comparison of MORSE global retrieved HCN.

5.7.2 Global retrieved HCN comparison

The MORSE retrieved global HCN data (data analysed consists of complete October 2003 dataset along with filtering criteria to test the quality of retrieved HCN; Section 5.3) at 177.3 mb [Figure 5.37] are compared with IMK/IAA global HCN data at 200 mb [Figure 5.38]. The MORSE retrieved data are generally higher than the IMK retrieved data by a factor of ≈1.4 to 1.5. The biomass burning source of HCN and the transport of HCN plumes at 12 km nominal altitudes agree well except for the North Pole region.

Note that much of the MORSE retrieved HCN data in the polar regions is lost due to stringent conditions applied in order to quality test the HCN retrieved data. The polar MORSE data and the comparisons at the poles should be therefore not over-interpreted.

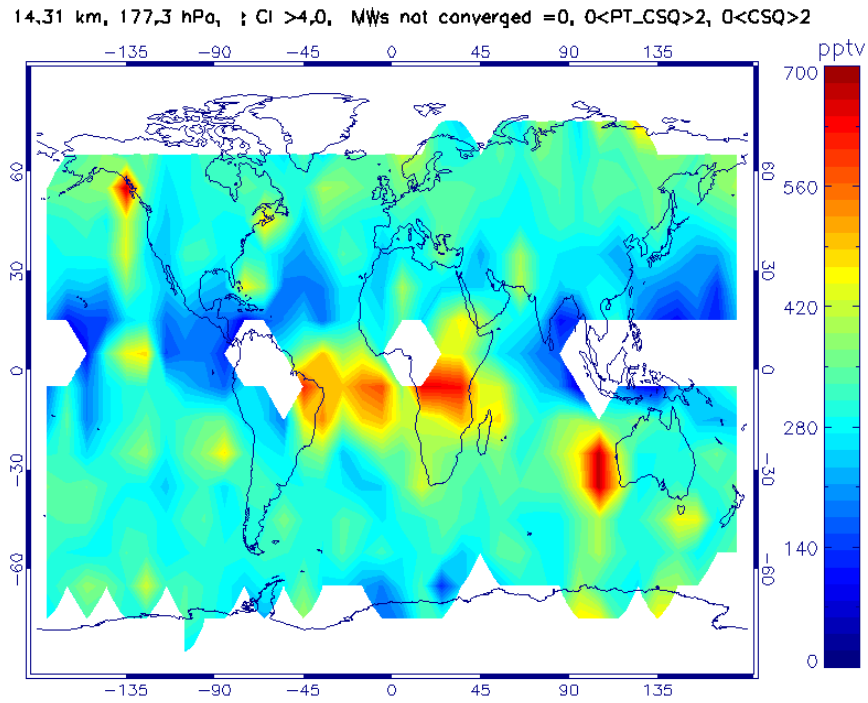

Figure 5.37: Global MORSE retrieved HCN distribution at (177.3 mb) 12 km nominal altitude level using the PRET_A retrieval grid in October 2003. The white areas indicate data gaps due to cloud contamination

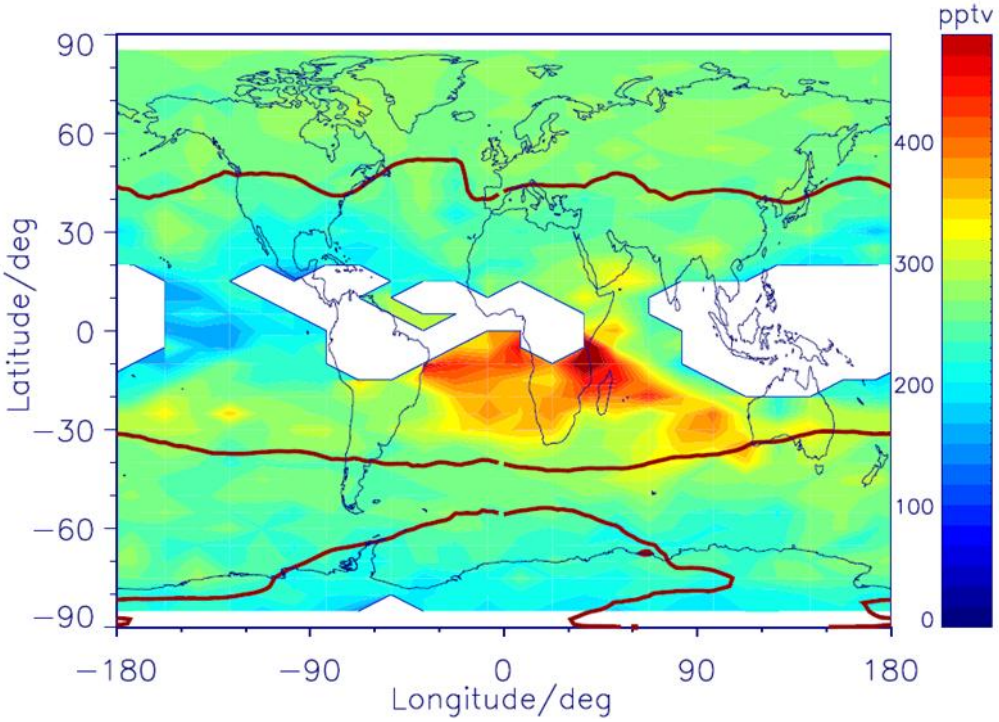

Figure 5.38: Global IMK/IAA HCN distribution at 200 hPa (10.5–12.6 km) in October 2003. The white areas indicate data gaps due to cloud contamination. The red solid lines show the tropopause intersection from the NCEP reanalysis.

5.8 Summary

In this study, an attempt has been made to identify HCN in the MIPAS-E spectra using Oxford's MORSE retrieval algorithm. Based on detection criteria, the HCN_0112 MW, a spectral subset of the HCN_0105 MW, is used to retrieve global HCN concentration levels at 9–27 km altitude levels. The data is quality filtered using the a cloud index ≥ 4 and the convergence criteria 0 <chi-square (χ^2) ≥ chi-square (χ^2)limit set for individual retrieved products. The χ^2 values are based on the histogram distribution plots which show the mean state of the distribution at all the levels for all input parameters is between 2 and 6.

The systematic errors are larger at the lower altitude levels, particularly at 9 km, for both HCN_0115 and HCN_0112 MW regions in the tropics and mid-latitude regions. The total systematic errors are found to be better than 30% at the 15 km altitude level for all latitude bands in both the MWs. An error of 30–50% maybe introduced due to enhanced CH_3Cl in both the HCN MWs in both the tropics and mid-latitude regions.

The averaging kernels in the tropical and mid-latitude regions for MORSE retrieved HCN using the PRET_A retrieval grid peak beyond 0.8 for four altitude levels suggest that the MORSE HCN retrievals have significant information from 300–60 mb.

The MORSE retrieved input parameters are investigated in detail at the 12 km nominal altitude level leading to a conclusion that higher O_3 is retrieved in the North Pole region in the case of PRET_A retrieval grid. Further, a lot of missing data is found in the case of C_2H_2 retrieved data when same filters are applied to both PRET_B and PRET_A retrieval grid datasets. The density distribution plots for HCN show a wider spread of HCN data at the 12 km nominal altitude in the case of PRET_A retrieval grid when compared to the 18 km nominal altitude.

The inter-comparison study is based on the MORSE retrieved parameters, ACE-FTS level 2 profiles and ACE-FTS level 1 sample spectral data. A significant difference can be seen in the mean pressure profile data inter-comparison plots for all three latitude bands. The results of sensitivity test further suggest differences of

50–60 mb pressure retrievals at the 12 km nominal altitude showing a significant offset in the HCN_0102 and HCN_0105 MW regions compared to the ACE-FTS MW regions. The presence of enhanced CH_3Cl does not show significant differences in the simulated transmission signals calculated in both MIPAS-E and ACE-FTS MW regions. The inter comparison results for examining the final MORSE retrieved HCN leads to a general conclusion that HCN concentration levels are generally higher than ACE-FTS retrieved HCN concentration levels.

The final MORSE retrieved HCN results are presented in this chapter based on the PRET_A retrieval grid in the HCN_0112 MW region. The 'best' result can be seen at the 12 km nominal altitude. The 9 km nominal altitude show unstable retrieved HCN data and higher altitude levels show higher HCN concentration levels compared to background concentration values. The residual of measured (Y) and MORSE calculated fit (F) suggest that the data are acceptable at all altitudes as the differences lie with in the MIPAS-E NESR levels in the HCN_0112 MW region.

The MORSE zonal mean HCN data show enhancements in the tropics and mid-latitude regions. The enhancements can be due to biomass burning events and transport of pollutants. A strong uplift of HCN plumes can be seen reaching altitudes above 50 mb. The MORSE retrieved HCN zonal mean data for October 2003 are inter-compared with ACE-FTS HCN zonal mean data for October 2004 to 2006. The inter-comparison results are limited as the satellite measurements are sparse in the tropics and lower altitude levels. High concentration levels are seen in the tropics and the south mid-latitude regions. The ACE-FTS HCN zonal mean plots show background concentration levels in the polar regions in both hemispheres whereas MORSE HCN show enhancements in the North Pole region at lower altitude level. From MORSE and EOS MLS (weekly) zonal mean plots one interesting feature can be seen in the tropics at higher altitudes where an increase in the HCN concentration levels is apparently observed. The EOS MLS weekly zonal mean HCN data is not useful for comparison as, unfortunately, it is valid only at altitudes greater than 68 mb and comparisons indicate possible systematic biases. Hence no comparison study is made with MORSE retrieved HCN zonal mean data.

The MORSE retrieved HCN at 177.3 mb is compared with IMK/IAA retrieved HCN at 200 mb, which is generally higher by a factor of ≈1.4–1.5 with a general

agreement of source and the transport of biomass burning events. Note that much of the MORSE retrieved HCN data is lost in the polar regions due to strict filtering criteria set in order to test the quality of retrieved HCN and, hence, should not be over-interpreted.

CHAPTER 6

6. Conclusions and Future Work

The primary aim of the work presented in this thesis is to investigate pollution-events using satellite instrument measurements and to separate the two sources of pollution, industrial transport or non-coal emissions and biomass burning, by examining molecules which provide unique markers. In this work investigations of the HCN molecule in the spectral regions are carried out using the measurements made by the MIPAS-E instrument onboard the ENVISAT satellite that show maximum information content of the HCN spectral signatures. The HCN investigation is led as follows:

- Use of the MIPAS-E level 1b spectral data measured in band A (685–970 cm^{-1}) and level 2 operational processor data products (pressure, temperature, H_2O, O_3, HNO_3, CH_4, NO_2 and N_2O VMRs).
- Measured spectra are simulated using Oxford's RFM.
- The Oxford's MORSE algorithm is used to invert the MIPAS-E limb measurements and retrieve accurate HCN VMR profiles.

- Use of the ACE-FTS level 1 data (sample transmission spectral data) and level 2 data (September to November 2004, 2005 and 2006) at 12 km MIPAS-E nominal altitude level.
- Finally, comparisons with zonal mean HCN concentrations determined from averaged radiances measured by the EOS MLS instrument for the months of October (2004–2006).

This chapter summarises the work and lists possible future work related to detection and retrieval of HCN and other organic trace gases using infrared remote sounding techniques.

6.1 Detection of HCN in MIPAS-E spectral data

A cloud-free dataset for October 2003 obtained by using the Michelson Interferometer for Passive Atmospheric Sounding on ENVISAT (MIPAS-E) is used. The dataset covers the biomass burning period in South Africa and Madagascar and, thus, the data is useful for the detection of HCN. The HCN spectral lines in HCN_0102 (744.300–744.525 cm^{-1}) and HCN_0105 (746.7750–747.8250 cm^{-1}) MWs are selected.

First, a detection procedure is carried out in a single scan #2 of orbit 08585 measured by MIPAS-E on 21 October 2003. The same procedure is followed for four selected MIPAS-E spectra from different latitude bands to show evidence of the presence of HCN in the MIPAS-E level 1b spectra. The detection method appears to show presence of HCN spectral lines in all cases except for mid-latitude night.. At 12 km nominal altitude level, clear evidence of HCN line signature is seen in the tropics and polar winter case, whereas mid-latitude and polar summer case show influence due to presence of other interfering gas. Sharp lines are seen at all altitudes in all five cases, and hence improvement over these lines is needed. Such an improvement can be achieved by using the Jacobian fitting analysis and by using improved spectral database of major interfering gases.

The whole months data is analysed at 12 km nominal altitude in HCN_0102 and HCN_0105 MW for the global analysis of HCN spectral signature. The results using automated detection method in the mid-latitude night now appears to show

the presence of HCN spectral feature in both HCN_0102 and HCN_0105 MW consistently over many spectra.. The HCN spectral lines in 760–780 cm^{-1} are not analysed as at low concentration levels, the spectral features are well below the MIPAS-E instrument noise levels at 12 km nominal altitudes and therefore undetectable.

The HITRAN and GEISA spectral databases show distinct differences in the HCN line parameter measurements. The two versions of the HITRAN database, HITRAN 2004 and HITRAN 2008 HCN spectral data lines do not show any significant difference. In this study, HITRAN 2004 spectral data are used in both the forward model calculation and MORSE inverse model algorithm.

Detection in both MWs is limited to levels above 9 km as strong absorbers such as water vapour (H_2O) saturate the HCN detection MWs by reducing the HCN spectral signatures. The HCN concentration levels decrease with an increase in altitude where the HCN radiance contribution signals are well below the instrument's measurement limit; therefore, an upper limit of 15 km (MIPAS-E nominal altitude level) is set for HCN_0102 MW and HCN_0105 MW.

The analysis of spectral fits calculated using the RFM at 11.5-, 14.3- and 17.2-km strongly indicates the presence of a detectable HCN limb emission signature in the MIPAS-E spectral data. The automated detection method used to investigate global HCN was successful in both MWs which revealed the presence of HCN spectral features in Polar Regions, both hemispheres at a 12 km nominal altitude.

The HCN spectral feature shows a relatively smaller radiance contribution to the total radiance measured by the MIPAS-E instrument in both spectral regions; hence, the accurate knowledge of many other parameters are needed for both the detection of HCN spectral signatures and the retrieval of accurate and reliable HCN VMR profiles globally.

6.2 Retrieval of HCN VMR using the MIPAS-E limb measurements

The MORSE retrieval algorithm based on an optimal estimation approach is used to invert the MIPAS-E limb measurements [Rodgers, 2000]. The HCN_0112 spectral region (747.350–747.500 cm^{-1}, a subset of HCN_0105 MW) is used in order to maximise the information content of the HCN radiance contributions. A very high *a-priori* covariance of uncertainty 1000% is used to retrieve HCN VMR profiles. The data is retrieved using a cloud index value of greater than or equal to 2. The retrieval convergence criteria are set to threshold values defined in Section 5.1.1.4 and the number of iterations is limited to a maximum of 10. The parameters such as pressure, temperature, H_2O, O_3, HNO_3, C_2H_2 and aerosol are retrieved in order, prior to HCN VMR profile retrievals. The remaining interfering gases in the MW are modelled based on climatology values.

The response of the MORSE algorithm is tested while retrieving HCN VMR profiles where two different pre-retrieved datasets (PRET_A and PRET_B), are used. The results obtained using these two different input parameters show significant differences and only HCN retrieval based on input parameters retrieved using PRET_A is used in the final analysis and compared with the ACE-FTS (level 1 and 2) and EOS MLS (level 2) HCN data.

The data used in the analysis is quality tested using retrieval output parameters such as χ^2, averaging kernels, convergence, difference in measured (Y) and MORSE calculated fit (F). As the MORSE retrieved H_2O profiles are significant, the mean H_2O χ^2s at all altitude levels suggest χ^2 values of 2 as an indicator to filter good quality HCN retrieved data. The data is further cloud cleared using a cloud index value of greater than or equal to 4. The Y–F residual is a good measure of data quality as it shows how well the measured spectrum is fitted.

In the inter-comparison experiment using non-coincident datasets, the mean pressure profiles suggest a significant offset compared to the standard climatology pressure profile (*a-priori*). Both MORSE retrieved pressure values are higher at the 12 km nominal altitude and the sensitivity plots suggest that in the HCN

transmission signal in both HCN_0102 and HCN_0105 MW regions are sensitive to pressure differences. Thus, the accurate retrieval of pressure is important in order to fit the measured spectrum and retrieve HCN VMR profiles. The effects of CH_3Cl present either in background or in enhanced scenarios is not significant in the transmission signals in both the HCN_0102 and HCN_0105 MW regions. The general conclusion is that HCN retrieved data are generally higher at all altitude levels compared to the ACE-FTS measurements.

The MORSE retrieved HCN zonal mean data in October 2003 is compared to the ACE-FTS zonal data measurements (mean state from September to November) for 2004, 2005 and 2006. The EOS MLS weekly zonal mean HCN data is not useful for comparison as, unfortunately, it is valid only at altitudes greater than 68 mb and comparisons indicate possible systematic biases. Hence no comparison study is made with MORSE retrieved HCN zonal mean data.

The MORSE retrieved HCN at 177.3 mb is compared with IMK/IAA retrieved HCN at 200 mb, is generally higher by a factor of ≈1.4–1.5 with a general agreement of source and the transport of biomass burning events. The polar region data are missing due to strict filtering criteria set in order to test the quality of retrieved HCN and, hence, should not be over-interpreted.

6.3 Future Work

There are some interesting areas of work that could be explored in future.

6.3.1 Working towards more accurate detection of HCN signature and retrievals of HCN profiles

- In order to retrieve more accurate HCN profiles in the HCN_0102 and HCN_0105 MW regions, CH_3Cl and N_2O_5 need to be fitted well enough by either using data from model, *in-situ* or air-borne or space based measurements or retrieve them using MIPAS-E measurements. The radiance contributions due to these gases have to be accounted in the HCN_0112 MW in order to segregate the HCN radiance contributions. This is true for the detection method as well.

- In case of CH_3Cl retrievals from the MIPAS-E measurements, a detailed study has to be carried out by investigating the detection and retrieval of CH_3Cl. Figure 6.1 shows simulated radiance where only CH_3Cl is present in the atmosphere. The CH_3Cl MWs can be chosen such that maximum information content is available for the MIPAS-E spectral bands. Figure 6.2 shows the simulated radiance contribution due CH_3Cl for MIPAS-E spectral band A.

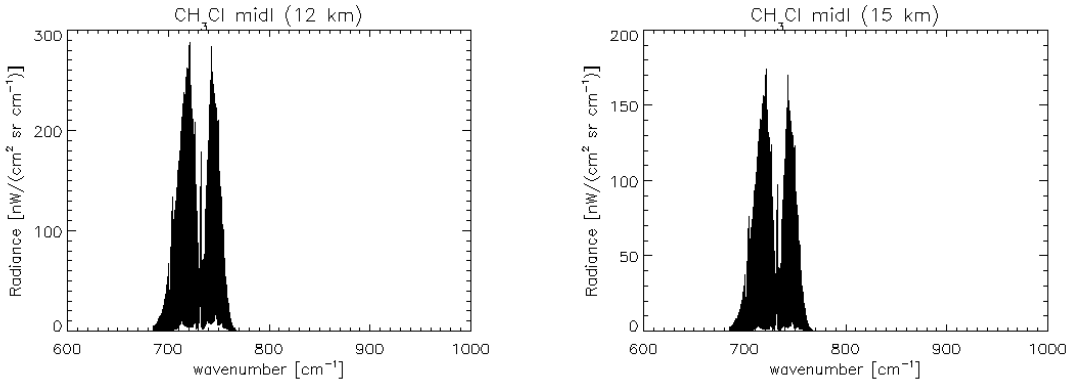

Figure 6.1: Simulated CH_3Cl MIPAS-E band A (685–970 cm^{-1}) limb emission spectrum where CH_3Cl concentration was set to a value of 566 pptv for 12 and 15 km (Only CH_3Cl).

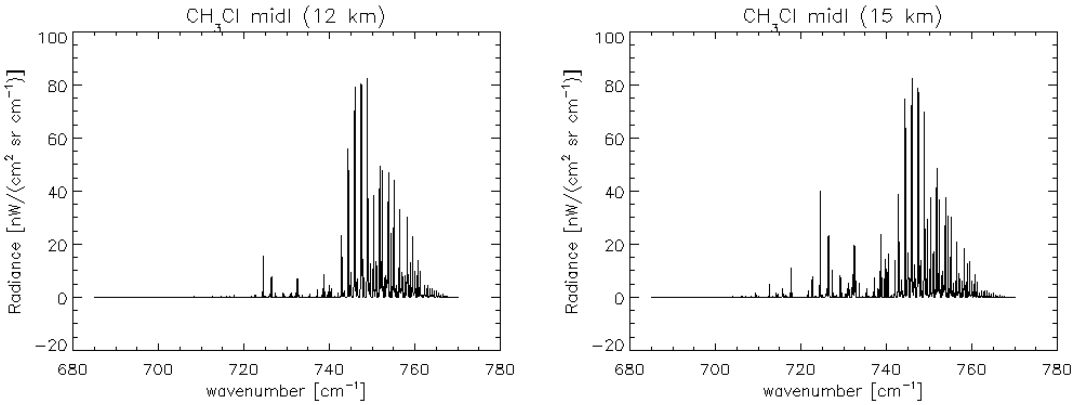

Figure 6.2: Simulated residual (simulated with all gases−simulated with all gases without CH_3Cl) CH_3Cl radiance contribution in MIPAS-E band A (685–780 cm^{-1}) emission spectrum, with CH_3Cl concentrations set at 566 pptv at 12 and 15 km.

- The response of MORSE retrieved HCN can also be tested by changing the *a-priori* covariance uncertainty and different climatology profile data using modelled HCN or HCN profiles measured by different instruments on a local scale to account for biomass burning and background case.

- The offset seen in the mean pressure profiles with respect to the standard pressure profile needs to be corrected as seen in Chapter 5 that HCN_0102 and HCN_0105 MW are sensitive to pressure changes.
- The detection method can be developed further by using Jacobian calculations in order to fit the measured spectra as a necessary step in order to weight the radiance contributions due to the interfering species in the HCN MWs.
- The detection of HCN and retrieval of HCN VMR profiles can be carried out in different months to cover different seasons and thus quantify the seasonal behaviour of HCN on a global scale.
- Different HCN MW regions can be tested as well, for example, the 761.950–762.225 cm^{-1} region.
    - The main absorbers in this MW region are H_2O, O_3, HNO_3 and C_2H_2.
    - With the success of C_2H_2 retrievals [Parker, 2010], the retrieval of HCN using this MW can be tested.

However, there is one drawback: the signal strength starts decreasing rapidly with a decrease in HCN concentrations and none is left above MIPAS-E noise levels, as seen in Figure 6.3.

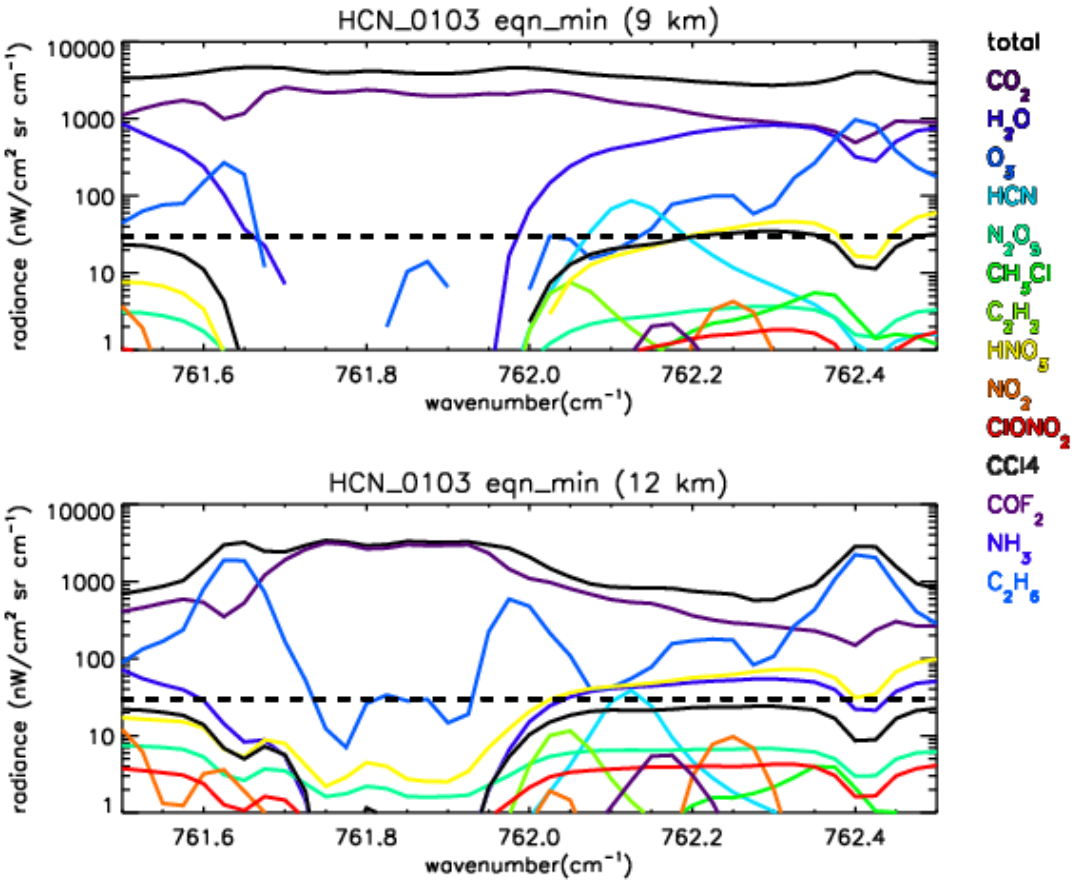

Figure 6.3: Plot of RFM modelled radiances (RFM(all)–RFM(without gas)) for major interfering gases in 761.5–762.5 cm^{-1} in the tropics (30°N–30°S) using tropical climatology values and HCN background concentration levels. The black dotted line represents expected noise equivalent to the spectral radiance (NESR) of the MIPAS-E, which is based on pre-flight estimates of 50 $nW/(cm^2\ sr\ cm^{-1})$ for band A.

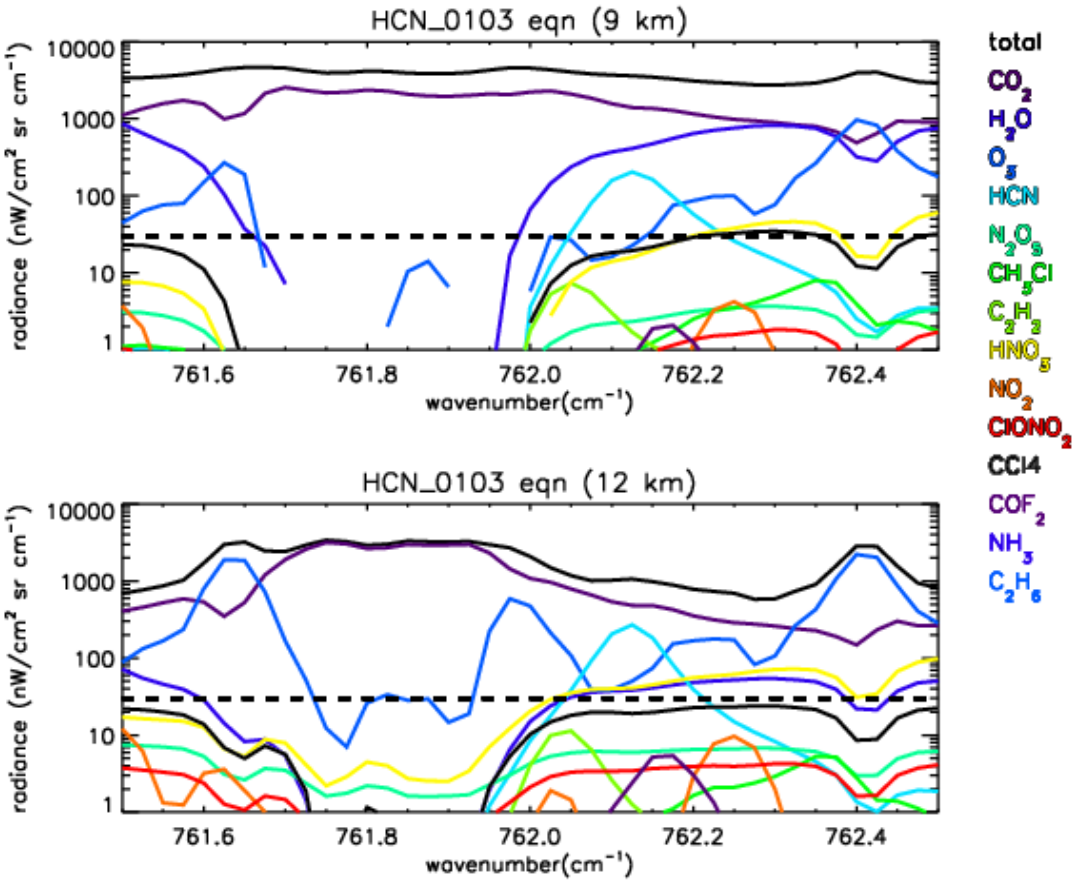

Figure 6.4: Plot of RFM modelled radiances (RFM(all)−RFM(without gas)) for major interfering gases in 761.5–762.5 cm^{-1} in the tropics (30°N–30°S) using tropical standard climatology values. HCN concentration levels are set to 550 pptv at 9- and 12-km levels. The black dotted line represents the expected noise equivalent to spectral radiance (NESR) of the MIPAS-E which is based n pre-flight estimates of 50 $nW/(cm^2\ sr\ cm^{-1})$ for band A.

- To investigate the 2004 to 2006 MIPAS-E optimised resolution data, it is viable to detect the presence of HCN in the MIPAS-E optimised resolution spectrum and provide evidence to retrieve the HCN profiles.

6.3.2 Comparison study

If the HCN data obtained using MORSE retrievals are improved, then the following comparison study can be carried out:

- The MORSE retrieved HCN data can be correlated to MORSE retrieved C_2H_2, C_2H_6 and MOPITT CO data, as previous study using ACE-FTS measurements show a good correlation [Coheur *et al.*, 2007] between these gases in the biomass burning plumes [Figure 6.5].

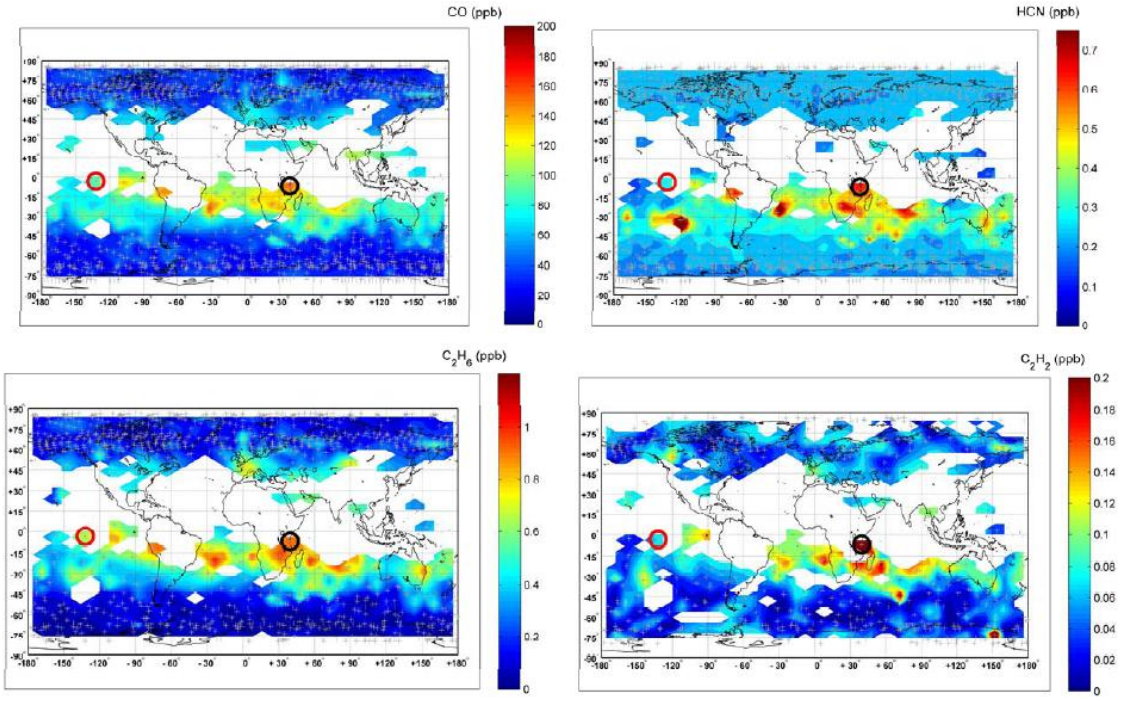

Figure 6.5: Zonal distributions of CO, HCN, C_2H_6 and C_2H_2 using ACE-FTS level 2 data (September to November 2005) at 11.5 km. Data is averaged over the 4° latitude × 8° longitude grid. The crosses indicate the ACE-FTS measurements locations while the black and red circles show the location of the fire occultation (ss11607 measured on 8 October 2005 on the East coast of Tanzania), and the background occultation (ss11615 measured on 9 October 2005, at a similar latitude). The ss notation refers to sunset [Coheur *et al.*, 2007].

- HCN shows a tape recorder effect, with the air entering the stratosphere being preserved and carried upwards by the Brewer-Dobson (meridional) circulation. Between 2003 and 2007, the HCN mixing ratio of air entering the stratosphere varied by ±10% with a predominant timescale of two years. Pumphrey *et al.* [2008] used HCN data from EOS MLS and ACE-FTS HCN [Figure 6.6] to show this tape recorder effect. A similar work can be carried out using MIPAS-E data that covers different seasons and different years.

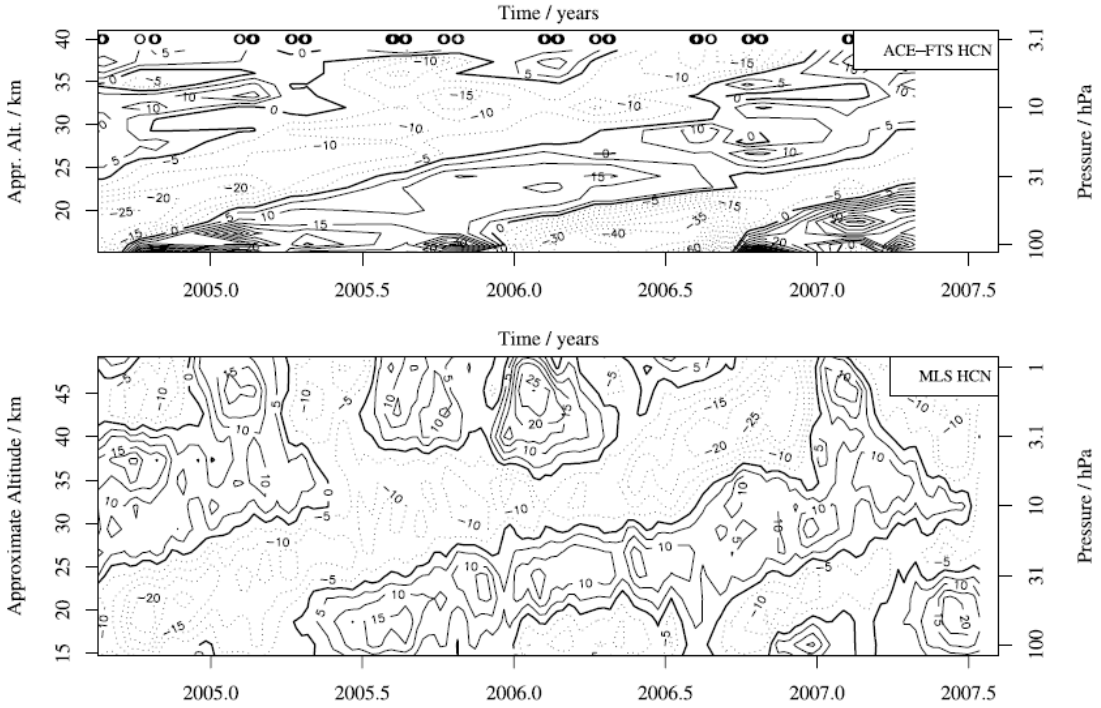

Figure 6.6: Contour plots of ACE-FTS HCN and MLS HCN (units in pptv; all data within 15° of the equator). Negative contours are dashed, and the zero contours are shown by a heavier line. Circles in the ACE-FTS panel indicate the time of the ACE-FTS measurements within 15° of the equator. ACE-FTS data are smoothed in time using a Gaussian filter with a width of 30 days. [Pumphrey *et al.*, 2008]

6.3.3 Validation

In order to estimate the accuracy of the detection of HCN and retrieved HCN VMR profile data can be compared with results from independent co-incident measurements of HCN in the atmosphere. This can be achieved by analysing MIPAS-E data within certain thresholds set for spatial and temporal dimensions. Such

validation would provide greater confidence in the accuracy of inferred concentrations.

- The ACE-FTS sample transmission data used in this analysis is sparse in tropical regions and thus, inter-comparison experiment was limited. The detection and retrieval of HCN can now be carried out due to the availability of more ACE-FTS transmission data in the months of March 2004 and October 2004 to 2006. The March 2004 ACE-FTS data overlaps the MIPAS-E limb measurements in the full spectral resolution mode (0.025 cm^{-1}). The 2004 to 2006 ACE-FTS data overlaps with the MIPAS-E data in the optimised resolution mode (0.0625 cm^{-1}).
- The IMK/IAA retrieved HCN data used for the comparison study in section 5.7 was limited to 10 days worth of data from the month of October 2003 at the time of analysis. In future, the availability of the IMK/IAA retrieved HCN data along with the HCN averaging kernels for the entire month of October 2003 can further validate the MORSE retrieved HCN data product.

Bibliography

ABBAS, M., GUO, J., CARLI, B., MENCARAGLIA, F. and CARLOTTI, M., 1987. Stratospheric distribution of HCN from far infrared observations. *Geophysical Research Letters,* **14**, 531-534.

ALLEN, G., 2005. The infrared remote sensing of peroxyacetyl nitrate in the upper troposphere, Ph.D. Thesis, *University of Leicester*.

ANDREAE, M., 1991. Biomass burning- Its history, use, and distribution and its impact on environmental quality and global climate. *Global biomass burning-Atmospheric, climatic, and biospheric implications (A 92-37626 15-42). Cambridge, MA, MIT Press, 1991.*

ANDREAE, M.O. and MERLET, P., 2001. Emission of trace gases and aerosols from biomass burning. *Global Biogeochemical Cycles,* **15**(4), 955-966.

BANWELL, C.N. and MCCASH, E.M., 1966. Fundamentals of molecular spectroscopy. *McGraw-Hill London*.

BERNATH, P.F., MCELROY, C., ABRAMS, M., BOONE, C.D., BUTLER, M., CAMY-PEYRET, C., CARLEER, M., CLERBAUX, C., COHEUR, P.F. and COLIN, R., 2005.

Atmospheric chemistry experiment (ACE): mission overview. *Geophysical Research Letters,* **32**, (L15S01).

BOONE, C.D. and BERNATH, P.F., 2002(a). Pressure/temperature and volume mixing ratio retrievals for the Atmospheric Chemistry Experiment (ACE), *Proceedings of SPIE,* 2002, pp50-61.

BOONE, C.D., MCLEOD, S.D. and BERNATH, P.F., 2002(b). Apodization effects in the retrieval of volume mixing ratio profiles. *Applied Optics,* **41**, 1029-1034.

BOONE, C.D., NASSAR, R., WALKER, K.A., ROCHON, Y., MCLEOD, S.D., RINSLAND, C.P. and BERNATH, P.F., 2005. Retrievals for the atmospheric chemistry experiment Fourier-transform spectrometer. *Applied Optics,* **44**(33), 7218-7231.

BOUANICH, J.P., BOULET, C., PREDOI-CROSS, A., SHARPE, S.W., SAMS, R.L., SMITH, M.A.H., RINSLAND, C.P., BENNER, D.C. and DEVI, V.M., 2005. A multispectrum analysis of the ν_2 band of $H^{12}C^{14}N$: Part II. Theoretical calculations of self-broadening, self-induced shifts, and their temperature dependences. *Journal of Molecular Spectroscopy,* **231**(1), 85-95.

CARLOTTI, M., 1988. Global-fit approach to the analysis of limb-scanning atmospheric measurements. *Applied Optics,* **27**(15), 3250-3254.

CARLOTTI, M., DINELLI, B.M., RASPOLLINI, P. and RIDOLFI, M., 2001. Geo-fit approach to the analysis of limb-scanning satellite measurements. *Applied Optics,* **40**(12), 1872-1885.

CARLOTTI, M. and RIDOLFI, M., 1999. Derivation of temperature and pressure from submillimetric limb observations. *Applied Optics,* **38**, 2398-2409.

CHÂTEAUNEUF, F., FORTIN, S., BUIJS, H., SOUCY, M., A., 2004. On-orbit performance of the ACE-FTS Instrument, in Proceedings of SPIE-The International Society for Optical Engineering, vol. 5542, Earth Observing systems IX, 166-175, edited by William L. Barnes (Bellingham, WA).

CICERONE, R. and ZELLNER, R., 1983. Atmospheric chemistry of hydrogen cyanide (HCN). *J.GEOPHYS.RES.(C OCEANS ATMOS.).,* **88**, 10689-10696.

CLARMANN, T., HÖPFNER, M., FUNKE, B., LÓPEZ-PUERTAS, M., DUDHIA, A., JAY, V., SCHREIER, F., RIDOLFI, M., CECCHERINI, S. and KERRIDGE, B.J., 2003. Modelling of atmospheric mid-infrared radiative transfer: the AMIL2DA algorithm intercomparison experiment. *Journal of Quantitative Spectroscopy and Radiative Transfer,* **78**(3-4), 381-407

COFFEY, M., MANKIN, W. and CICERONE, R., 1981. Spectroscopic detection of stratospheric hydrogen cyanide. *Science,* **214**(4518), 333.

COHEUR, P., HERBIN, H., CLERBAUX, C., HURTMANS, D., WESPES, C., CARLEER, M., TURQUETY, S., RINSLAND, C., REMEDIOS, J. and HAUGLUSTAINE, D., 2007. ACE-FTS observation of a young biomass burning plume: first reported measurements of C_2H_4, C_3H_6O, H_2CO and PAN by infrared occultation from space. *Atmospheric Chemistry Physics,* **7**, 5437–5446.

CROS, B., DELMAS, R., NGANGA, D., CLAIRAC, B. and FONTAN, J., 1988. Seasonal trends of ozone in equatorial Africa- Experimental evidence of photochemical formation. *Journal of Geophysical Research,* **93**, 8355-8366.

DEVI, V.M., BENNER, D.C., SMITH, M.A.H., RINSLAND, C.P., PREDOI-CROSS, A., SHARPE, S.W., SAMS, R.L., BOULET, C. and BOUANICH, J.P., 2005. A multispectrum analysis of the ν_2 band of $H^{12}C^{14}N$: Part I. Intensities, broadening, and shift coefficients. *Journal of Molecular Spectroscopy,* **231**(1), 66-84.

DEVI, V.M., BENNER, D.C., SMITH, M.A.H., RINSLAND, C.P., SHARPE, S.W. and SAMS, R.L., 2004. A multispectrum analysis of the $2\nu_2$ spectral region of $H^{12}C^{14}N$: intensities, broadening and pressure-shift coefficients. *Journal of Quantitative Spectroscopy and Radiative Transfer,* **87**(3-4), 339-366.

DUDHIA, A., JAY, V.L. and RODGERS, C.D., 2002(a). Microwindow selection for high-spectral-resolution sounders. *Applied Optics,* **41**(18), 3665-3673.

DUDHIA, A., MORRIS, P.E. and WELLS, R.J., 2002(b). Fast monochromatic radiative transfer calculations for limb sounding. *Journal of Quantitative Spectroscopy and Radiative Transfer,* **74**(6), 745-756.

DUFOUR, G., BOONE, C.D., RINSLAND, C.P. and BERNATH, P.F., 2006. First space-borne measurements of methanol inside aged tropical biomass burning plumes using the ACE-FTS instrument. *Atmospheric Chemistry Physics.Discuss,* **6**, 3945–3963.

ENDEMANN, M., 1999. MIPAS instrument concept and performance, *Proceedings of the European Symposium on Atmospheric Measurements from Space,* 1999, pp29-43.

ENDEMANN, M., GARE, P., LANGEN, J., NETT, H. and READINGS, C.J., 2000. MIPAS-An Envisat Instrument for Atmospheric Chemistry and Climate Research. *ESA Bulletin,* **101**, 0276-4265.

FINLAYSON-PITTS, B.J. and PITTS, J.N., 2000. Chemistry of the upper and lower atmosphere. *Academic press, San Diego*.

FISCHER, H., BIRK, M., BLOM, C., CARLI, B., CARLOTTI, M., VON CLARMANN, T., DELBOUILLE, L., DUDHIA, A., EHHALT, D. and ENDEMANN, M., 2007. MIPAS: an instrument for atmospheric and climate research. *Atmospheric Chemistry and Physics Discussions,* **7**(3), 8795-8893.

FISHMAN, J. and SEILER, W., 1983. Correlative nature of ozone and carbon monoxide in the troposphere: Implications for the tropospheric ozone budget. *Journal of Geophysical Research,* **88**(C6), 3662-3670.

FLAUD, J.M., BRIZZI, G., CARLOTTI, M., PERRIN, A. and RIDOLFI, M., 2006. MIPAS database: Validation of HNO_3 line parameters using MIPAS satellite measurements. *Atmospheric Chemistry Physics,* **6**, 5037–5048.

FLAUD, J.M., PICCOLO, C., CARLI, B., PERRIN, A., COUDERT, L.H., TEFFO, J.L. and BROWN, L.R., 2003. Molecular line parameters for the MIPAS (Michelson

Interferometer for Passive Atmospheric Sounding) experiment, Atmos. *Oceanic Opt,* **16**(3), 172–182.

FRITZ, B., LORENZ, K., STEINERT, W. and ZELLNER, R., 1984. Rate of oxidation of HCN by OH radicals at lower temperatures. *Oxid.Commun,* **6**, 363–370.

FROIDEVAUX, L., LIVESEY, N., READ, W., JIANG, Y., JIMENEZ, C., FILIPIAK, M., SCHWARTZ, M., SANTEE, M., PUMPHREY, H. and JIANG, J., 2006. Early validation analyses of atmospheric profiles from EOS MLS on the Aura satellite. *IEEE Transactions on Geoscience and Remote Sensing,* **44**(5), 1106-1121.

GLATTHOR, N., VON CLARMANN, T., FISCHER, H., FUNKE, B., GRABOWSKI, U., HÖPFNER, M., KELLMANN, S., KIEFER, M., LINDEN, A. and MILZ, M., 2007. Global peroxyacetyl nitrate (PAN) retrieval in the upper troposphere from limb emission spectra of the Michelson Interferometer for Passive Atmospheric Sounding (MIPAS). *Atmospheric Chemistry and Physics,* **7**(11), 2775-2787.

GLATTHOR, N., VON CLARMANN, T., STILLER, G.P., FUNKE, B., KOUKOULI, M.E., FISCHER, H., GRABOWSKI, U., HÖPFNER, M., KELLMANN, S. and LINDEN, A., 2009. Large-scale upper tropospheric pollution observed by MIPAS HCN and C_2H_6 global distributions. *Atmospheric Chemistry Physics,* **9**, pp. 9619-9634.

GOODE, J.G., YOKELSON, R.J., WARD, D.E., SUSOTT, R.A., BABBITT, R.E., DAVIES, M.A. and HAO, W.M., 2000. Measurements of excess O_3, CO, CO, CH, CH, CH, HCN, NO, NH, HCOOH, CHCOOH, HCHO, and CHOH in 1997 Alaskan biomass burning plumes by airborne Fourier transform infrared spectroscopy (AFTIR). *Journal of Geophysical Research*. **105**(D17), pp. 22,147–22,166.

GOODY, R., WEST, R., CHEN, L. and CRISP, D., 1989. The correlated-k method for radiation calculations in nonhomogeneous atmospheres. *Journal of Quantitative Spectroscopy and Radiative Transfer,* **42**(6), 539-550.

GREENHOUGH, J., REMEDIOS, J.J., SEMBHI, H. and KRAMER, L.J., 2005. Towards cloud detection and cloud frequency distributions from MIPAS infra-red observations. *Advances in Space Research,* **36**(5), 800-806.

HEIKES, B.G., CHANG, W., PILSON, M.E.Q., SWIFT, E., SINGH, H.B., GUENTHER, A., JACOB, D.J., FIELD, B.D., FALL, R. and RIEMER, D., 2002. Atmospheric methanol budget and ocean implication. *Global Biogeochemical Cycles,* **16**(4), 1133.

HOLTON, J. R., HAYNES, P. H., MCINTYRE, M. E., DOUGLASS, A. R., ROOD, R. B., AND PFISTER, L., 1995 Stratosphere-Troposphere Exchange, *Rev. Geophys.*, 33, pp. 403-439.

HOLZINGER, R., WARNEKE, C., HANSEL, A., JORDAN, A., LINDINGER, W., SCHARFFE, D.H., SCHADE, G. and CRUTZEN, P.J., 1999. Biomass burning as a source of formaldehyde, acetaldehyde, methanol, acetone, acetonitrile, and hydrogen cyanide. *Geophysical Research Letters,* **26**(8), pp. 1161-1164.

HOLZINGER, R., JORDAN, A., HANSEL, A. and LINDINGER, W., 2001. Automobile emissions of acetonitrile: Assessment of its contribution to the global source. *Journal of Atmospheric Chemistry,* **38**(2), pp. 187-193.

HOLZINGER, R., WILLIAMS, J., SALISBURY, G., KLÜPFEL, T., DE REUS, M., TRAUB, M., CRUTZEN, P. and LELIEVELD, J., 2004. Oxygenated compounds in aged biomass burning plumes over the Eastern Mediterranean: evidence for strong secondary production of methanol and acetone. *Atmospheric Chemistry and Physics Discussions,* **4**(5), 6321-6340.

JACQUINET-HUSSON, N., SCOTT, N.A., CHÉDIN, A., CRÉPEAU, L., ARMANTE, R., CAPELLE, V., ORPHAL, J., COUSTENIS, A., BOONNE, C. and POULET-CROVISIER, N., 2008. The GEISA spectroscopic database: Current and future archive for Earth and planetary atmosphere studies. *Journal of Quantitative Spectroscopy and Radiative Transfer,* **109**(6), 1043-1059.

KASAI, Y.J., KAGAWA, A., JONES, N., FUJIWARA, A., SEKI, K., MURAYAMA, Y. and MURCRAY, F., 2005. Seasonal variations of CO and HCN in the troposphere measured by solar absorption spectroscopy over Poker Flat, Alaska. *Geophysical Research Letters,* **32,** (L19812).

KEEDY, C.R., 1992. The rotational-vibrational spectra of HCN and DCN: A physical chemistry experiment. *Journal of chemical education,* **69**(11), 296.

KHALIL, M. and RASMUSSEN, R., 1999. Atmospheric methyl chloride. *Atmospheric Environment,* **33**(8), 1305-1321.

KIEFER, M., VON CLARMANN, T., GRABOWSKI, U., DE LAURENTIS, M., MANTOVANI, R., MILZ, M. and RIDOLFI, M., 2007. Characterization of MIPAS elevation pointing. *Atmospheric Chemistry Physics,* **7**, 1615–1628.

KIEHL, J. and TRENBERTH, K.E., 1997. Earth's annual global mean energy budget. *Bulletin of the American Meteorological Society,* **78**(2), 197-208.

KLEINBOHL, A., TOON, G.C., SEN, B., BLAVIER, J.F.L., WEISENSTEIN, D.K., STREKOWSKI, R.S., NICOVICH, J.M., WINE, P.H. and WENNBERG, P.O., 2006. On the stratospheric chemistry of hydrogen cyanide. *Geophysical Research Letters,* **33**, (L11806).

KLEINERT, A., AUBERTIN, G., PERRON, G., BIRK, M., WAGNER, G., HASE, F., NETT, H. and POULIN, R., 2007. MIPAS Level 1B algorithms overview: operational processing and characterization. *Atmospheric Chemistry Physics,* **7**, 1395–1406.

KOPP, E., 1990. Hydrogen constituents of the mesosphere inferred from positive ions: H_2O, CH_4, H_2CO, H_2O_2, and HCN. *Journal of Geophysical Research,* **95**(D5), pp. 5613-5630.

KOPPMANN, R., KHEDIM, A., RUDOLPH, J., POPPE, D., ANDREAE, M.O., HELAS, G., WELLING, M. and ZENKER, T., 1997. Emissions of organic trace gases from savanna fires in southern Africa during the 1992 Southern African Fire Atmosphere Research

Initiative and their impact on the formation of tropospheric ozone. *Journal of Geophysical Research,* **102**(D15), pp. 18879-18888.

KOPPMANN, R., VON CZAPIEWSKI, K. and REID, J., 2005. A review of biomass burning emissions, part I: gaseous emissions of carbon monoxide, methane, volatile organic compounds, and nitrogen containing compounds. *Atmospheric Chemistry and Physics Discussions,* **5**(5), 10455-10516.

LEMAIRE, V., BABAY, A., LEMOINE, B., ROHART, F. and BOUANICH, J., 1996. Self-and Foreign-Gas-Broadening and Shifting of Lines in the ν_2 Band of HCN. *Journal of Molecular Spectroscopy,* **177**(1), 40-45.

LEVINE, J.S., 1991. Global biomass burning: atmospheric, climatic, and biospheric implications. *The MIT Press*.

LEVINE, J., 1990. Global biomass burning: Atmospheric, climatic and biospheric implications. *Eos Trans. AGU,* **71**(36), 1075.

LI, Q., JACOB, D.J., BEY, I., YANTOSCA, R.M., ZHAO, Y., KONDO, Y. and NOTHOLT, J., 2000. Atmospheric hydrogen cyanide(HCN): Biomass burning source, ocean sink? *Geophysical Research Letters,* **27**(3), 357-360.

LI, Q., JACOB, D.J., YANTOSCA, R.M., HEALD, C.L., SINGH, H.B., KOIKE, M., ZHAO, Y., SACHSE, G.W. and STREETS, D.G., 2003. A global three dimensional model analysis of the atmospheric budgets of HCN and CH_3CN: Constraints from aircraft and ground measurements. *Journal of Geophysical Research,* **108**(D21), 8827.

LI, Q., PALMER, P., PUMPHREY, H., BERNATH, P. and MAHIEU, E., 2009. What drives the observed variability of HCN in the troposphere and lower stratosphere? *Atmospheric Chemistry Physics,* **9**, 8531-8543.

LIE, G., PEYERIMHOFF, S.D. and BUENKER, R.J., 1982. Theoretical integrated intensities for the $2\nu_2$ and $2\nu_2$-ν_2 bands of HCN and DCN. *Journal of Molecular Spectroscopy,* **93**(1), 74-82.

LIOU, K.N., YEH, H., CHEN, F., HUTCHISON, K. and ASTLING, E., 1980. Development of Infrared and Microwave Techniques for Cloud Parameter Inference from Satellite Imagery and Sounder Data. *Utah university salt lake city dept. of meteorology,* A295790.

LIU, H., JACOB, D.J., BEY, I., YANTOSCA, R.M., DUNCAN, B.N. and SACHSE, G.W., 2003. Transport pathways for Asian pollution outflow over the Pacific: Interannual and seasonal variations. *Journal of Geophysical Research,* **108**(D20), pp. 8786.

LOBERT, J., SCHARFFE, D. and HAO, W.E.I.M.I., 1991. Experimental evaluation of biomass burning emissions- Nitrogen and carbon containing compounds. *Global biomass burning- Atmospheric, climatic, and biospheric implications(A 92-37626 15-42).Cambridge, MA, MIT Press, 1991,* , 289-304.

LOBERT, J.M., SCHARFFE, D.H., HAO, W.M. and CRUTZEN, P.J., 1990. Importance of biomass burning in the atmospheric budgets of nitrogen-containing gases. *Letters to Nature,* **346**, pp. 552-554.

LUPU, A., KAMINSKI, J.W., NEARY, L., MCCONNELL, J.C., TOYOTA, K., RINSLAND, C.P., BERNATH, P.F., WALKER, K.A., BOONE, C.D. and NAGAHAMA, Y., 2009. Hydrogen cyanide in the upper troposphere: GEM-AQ simulation and comparison with ACE-FTS observations. *Atmospheric Chemistry and Physics,* **9**,4301-4313.

MAHIEU, E., DUCHATELET, P., DEMOULIN, P., WALKER, K.A., DUPUY, E., FROIDEVAUX, L., RANDALL, C., CATOIRE, V., STRONG, K. and BOONE, C.D., 2008. Validation of ACE-FTS v2. 2 measurements of HCl, HF, CCl_3F and CCl_2F_2 using space-, balloon-and ground-based instrument observations. *Atmospheric Chemistry Physics,* **8**, 6199-6221.

MAHIEU, E., RINSLAND, C., ZANDER, R., DEMOULIN, P., DELBOUILLE, L. and ROLAND, G., 1995. Vertical column abundances of HCN deduced from ground-based infrared solar spectra: Long-term trend and variability. *Journal of Atmospheric Chemistry,* **20**(3), 299-310.

MAKI, A., QUAPP, W. and KLEE, S., 1995(a). Intensities of hot-band transitions: HCN hot bands. *Journal of Molecular Spectroscopy,* **171**(2), 420-434.

MAKI, A., QUAPP, W., KLEE, S., MELLAU, G.C. and ALBERT, S., 1996. Infrared Transitions of $H^{12}C^{14}N$ and $H^{12}C^{15}N$ between 500 and 10000 cm^{-1}. *Journal of Molecular Spectroscopy,* **180**, 323-336.

MAKI, A., QUAPP, W., KLEE, S., MELLAU, G.C. and ALBERT, S., 1995(b). The CN Mode of HCN: A Comparative Study of the Variation of the Transition Dipole and Herman-Wallis Constants for Seven Isotopomers and the Influence of Vibration-Rotation Interaction. *Journal of Molecular Spectroscopy,* **174**(2), 365-378.

MAKI, A., MELLAU, G.C., KLEE, S., WINNEWISSER, M. and QUAPP, W., 2000. High-temperature infrared measurements in the region of the bending fundamental of $H^{12}C^{14}N$, $H^{12}C^{15}N$, and $H^{13}C^{14}N$. *Journal of Molecular Spectroscopy,* **202**(1), 67-82.

MALATHY DEVI, V., BENNER, D.C., SMITH, M.A.H., RINSLAND, C.P., SHARPE, S.W. and SAMS, R.L., 2003. A multispectrum analysis of the ν_1 band of $H^{12}C^{14}N$: Part I. Intensities, self-broadening and self-shift coefficients. *Journal of Quantitative Spectroscopy and Radiative Transfer,* **82**(1-4), 319-341.

MARQUARDT, D.W., 1963. An algorithm for least-squares estimation of nonlinear inequalities. *Siam J.Appl.Math,* **11**, 431-441.

MCELROY, C.T., NOWLAN, C.R., DRUMMOND, J.R., BERNATH, P.F., BARTON, D.V., DUFOUR, D.G., MIDWINTER, C., HALL, R.B., OGYU, A. and ULLBERG, A., 2007. The ACE-MAESTRO instrument on SCISAT: description, performance, and preliminary results. *Applied Optics,* **46**(20), 4341-4356.

MENCARAGLIA, F., BIANCHINI, G., BOSCALERI, A., CARLI, B., CECCHERINI, S., RASPOLLINI, P., PERRIN, A. and FLAUD, J.M., 2006. Validation of MIPAS satellite measurements of HNO_3 using comparison of rotational and vibrational spectroscopy. *Journal of Geophysical Research,* **111,** (D19305).

MONKS, P.S., 2005. Gas-phase radical chemistry in the troposphere. *Chemical Society Reviews,* **34**(5), 376-395.

MOORE, D.P., 2005. Measurements of HCFC-22 in the upper troposphere and lower stratosphere from the MIPAS-E instrument. Ph.D. Thesis, *University of Leicester*.

NAGAHAMA, Y. and SUZUKI, K., 2007. The influence of forest fires on CO, HCN, C_2H_6, and C_2H_2 over northern Japan measured by infrared solar spectroscopy. *Atmospheric Environment,* **41**(40), 9570-9579.

PARK, M., RANDEL, W., EMMONS, L., BERNATH, P., WALKER, K. and BOONE, C., 2008. Chemical isolation in the Asian monsoon anticyclone observed in Atmospheric Chemistry Experiment (ACE-FTS) data. *Atmospheric Chemistry and Physics,* **8**(3), 757-764.

PARKER, R.J., 2010. Satellite Observations of C_2H_2 and C_2H_6 in the Upper Troposphere, Ph.D. Thesis, *University of Leicester*.

PATON-WALSH, C., JONES, N.B., WILSON, S.R., HAVERD, V., MEIER, A., GRIFFITH, D.W.T. and RINSLAND, C.P., 2005. *Journal of Geophysical Research,* **110**, (D24305).

PUMPHREY, H.C., BOONE, C., WALKER, K.A., BERNATH, P. and LIVESEY, N.J., 2008. Tropical tape recorder observed in HCN. *Geophysical Research Letters,* **35**, (L05801).

PUMPHREY, H.C., JIMENEZ, C.J. and WATERS, J.W., 2006. Measurement of HCN in the middle atmosphere by EOS MLS. *Geophysical Research Letters,* **33,** (L08804).

RASPOLLINI, P., BELOTTI, C., BURGESS, A., CARLI, B., CARLOTTI, M., CECCHERINI, S., DINELLI, B.M., DUDHIA, A., FLAUD, J.M. and FUNKE, B., 2006. MIPAS level 2 operational analysis. *Atmospheric Chemistry and Physics,* **6**(12), 5630.

REMEDIOS, J.J., 1999. Extreme atmospheric constituent profiles for MIPAS, *Proceedings of the European Symposium on atmospheric measurements from space,* 1999, pp20-22.

REMEDIOS, J.J., LEIGH, R.J., SEMBHI, H. and WATERFALL, A.M., ESA SP-636, July 2007(a). New IG2 seasonal climatologies for MIPAS, *Proceedings of Envisat Symposium 2007,* 23–27 April 2007, ESA SP-636, July 2007.

REMEDIOS, J.J., ALLEN, G., WATERFALL, A.M., OELHAF, H., KLEINERT, A. and MOORE, D.P., 2007(b). Detection of organic compound signatures in infra-red, limb emission spectra observed by the MIPAS-B2 balloon instrument. *Atmospheric Chemistry Physics,* **7**, pp. 1599-1613.

REMEDIOS, J.J., LEIGH, R.J., WATERFALL, A.M., MOORE, D.P., SEMBHI, H., PARKES, I., GREENHOUGH, J., CHIPPERFIELD, M.P. and HAUGLUSTAINE, D., 2007(c). MIPAS reference atmospheres and comparisons to V4. 61/V4. 62 MIPAS level 2 geophysical data sets. *Atmospheric Chemistry and Physics Discussions,* **7**(4), pp. 9973-10017.

RINSLAND, C.P., BOONE, C.D., BERNATH, P.F., MAHIEU, E., ZANDER, R., DUFOUR, G., CLERBAUX, C., TURQUETY, S., CHIOU, L. and MC-CONNELL, J.C., 2006. First space-based observations of formic acid (HCOOH): Atmospheric Chemistry Experiment austral spring 2004 and 2005 Southern Hemisphere tropical-mid-latitude upper tropospheric measurements. *Geophysical Research Letters,* **33**, (L23804).

RINSLAND, C.P., DUFOUR, G., BOONE, C.D., BERNATH, P.F. and CHIOU, L., 2005. Atmospheric Chemistry Experiment (ACE) measurements of elevated Southern Hemisphere upper tropospheric CO, C_2H_6, HCN, and C_2H_2 mixing ratios from biomass burning emissions and long-range transport. *Geophysical Research Letters,* **32**, (L20803).

RINSLAND, C.P., DUFOUR, G., BOONE, C.D., BERNATH, P.F., CHIOU, L., COHEUR, P., TURQUETY, S. and CLERBAUX, C., 2007(a). Satellite boreal measurements over Alaska and Canada during June-July 2004: Simultaneous measurements of upper

tropospheric CO, C_2H_6, HCN, CH_3Cl, CH_4, C_2H_2, CH_3OH, HCOOH, OCS, and SF_6 mixing ratios. *Global Biogeochemical Cycles,* **21**(GB3008).

RINSLAND, C.P., GOLDMAN, A., HANNIGAN, J.W., WOOD, S.W., CHIOU, L.S. and MAHIEU, E., 2007(b). Long-term trends of tropospheric carbon monoxide and hydrogen cyanide from analysis of high resolution infrared solar spectra. *Journal of Quantitative Spectroscopy and Radiative Transfer,* **104**(1), 40-51.

RINSLAND, C.P., MALATHY DEVI, V., SMITH, M.A.H., CHRIS BENNER, D., W. SHARPE, S. and L. SAMS, R., 2003. A multispectrum analysis of the ν_1 band of $H^{12}C^{14}N$: Part II. Air-and N_2-broadening, shifts and their temperature dependences. *Journal of Quantitative Spectroscopy and Radiative Transfer,* **82**(1-4), 343-362.

RINSLAND, C.P., MEIER, A., GRIFFITH, D.W.T. and CHIOU, L.S., 2001. Ground-based measurements of tropospheric CO, C_2H_6, and HCN from Australia at 34°S latitude during 1997–1998. *Journal of geophysical research,* **106**(D18), 20913.

RINSLAND, C.P., GOLDMAN, A., MURCRAY, F.J., STEPHEN, T.M., POUGATCHEV, N.S., FISHMAN, J., DAVID, S.J., BLATHERWICK, R.D., NOVELLI, P.C. and JONES, N.B., 1999. Infrared solar spectroscopic measurements of free tropospheric CO, C_2H_6, and HCN above Mauna Loa, Hawaii: Seasonal variations and evidence for enhanced emissions from the Southeast Asian tropical fires of 1997–1998. *Journal of Geophysical Research,* **104**(D15), pp. 18667-18680.

RINSLAND, C.P., JONES, N.B., CONNOR, B.J., LOGAN, J.A., POUGATCHEV, N.S., GOLDMAN, A., MURCRAY, F.J., STEPHEN, T.M., PINE, A.S. and ZANDER, R., 1998. Northern and southern hemisphere ground-based infrared spectroscopic measurements of tropospheric carbon monoxide and ethane. *Journal of Geophysical Research,* **103**(D21), pp. 28197.

RINSLAND, C.P., MAHIEU, E., ZANDER, R., DEMOULIN, P., FORRER, J. and BUCHMANN, B., 2000. Free tropospheric CO, C_2H_6, and HCN above central Europe: Recent measurements from the Jungfraujoch station including the detection of

elevated columns during 1998. *Journal of geophysical research,* **105**(D19), pp. 24,235-24,249.

RINSLAND, C.P., MAHIEU, E., ZANDER, R., GUNSON, M.R., SALAWITCH, R.J., CHANG, A.Y., GOLDMAN, A., ABRAMS, M.C., ABBAS, M.M. and NEWCHURCH, M.J., 1996. Trends of OCS, HCN, SF_6, $CHClF_2$ (HCFC-22) in the lower stratosphere from 1985 and 1994 Atmospheric Trace Molecule Spectroscopy Experiment measurements near 30° N latitude. *Geophysical Research Letters,* **23**(17), pp. 2349-2352.

RINSLAND, C.P., MALATHY DEVI, V., SMITH, M.A.H., CHRIS BENNER, D., W. SHARPE, S. and L. SAMS, R., 2003. A multispectrum analysis of the ν_1 band of $H^{12}C^{14}N$: Part II. Air-and N2-broadening, shifts and their temperature dependences. *Journal of Quantitative Spectroscopy and Radiative Transfer,* **82**(1-4), pp. 343-362.

RINSLAND, C.P., MEIER, A., GRIFFITH, D.W.T. and CHIOU, L.S., 2001. Ground-based measurements of tropospheric CO, C_2H_6, and HCN from Australia at 34°S latitude during 1997–1998. *Journal of Geophysical research,* **106**(D18), pp. 20913.

RINSLAND, C., SMITH, M., RINSLAND, P., GOLDMAN, A., BRAULT, J. and STOKES, G., 1982. Ground-based infrared spectroscopic measurements of atmospheric hydrogen cyanide. *Journal of Geophysical Research,* **87**, 11119-11125.

RODGERS, C.D. and CONNOR, B.J., 2003. Intercomparison of remote sounding instruments. *Journal of Geophysical Research,* **108**(D3), 4116-4229.

ROTHMAN, L., GORDON, I., BARBE, A., BENNER, D.C., BERNATH, P., BIRK, M., BOUDON, V., BROWN, L., CAMPARGUE, A. and CHAMPION, J.P., 2009. The HITRAN 2008 molecular spectroscopic database. *Journal of Quantitative Spectroscopy and Radiative Transfer,* **110**(9-10), 533-572.

ROTHMAN, L., JACQUEMART, D., BARBE, A., CHRIS BENNER, D., BIRK, M., BROWN, L., CARLEER, M. and CHACKERIAN, C., 2005. The HITRAN 2004 molecular spectroscopic database. *Journal of Quantitative Spectroscopy and Radiative Transfer,* **96**(2), 139-204.

SCHNEIDER, J., BÜRGER, V. and ARNOLD, F., 1997. Methyl cyanide and hydrogen cyanide measurements in the lower stratosphere: Implications for methyl cyanide sources and sinks. *Journal of Geophysical Research,* **102**(D21), pp. 25,501-25,506.

SEILER, G. and FISHMAN, J., 1981. The distribution of carbon monoxide and ozone in the free troposphere. *Journal of Geophysical Research,* **86**, 7255-7265.

SEILER, W. and CRUTZEN, P.J., 1980. Estimates of gross and net fluxes of carbon between the biosphere and the atmosphere from biomass burning. *Climatic Change,* **2**(3), 207-247.

SHIM, C., WANG, Y., SINGH, H.B., BLAKE, D.R. and GUENTHER, A.B., 2007. Source characteristics of oxygenated volatile organic compounds and hydrogen cyanide. *Journal of Geophysical Research,* **112**(D20).

SINGH, H.B., SALAS, L., HERLTH, D., KOLYER, R., CZECH, E., VIEZEE, W., LI, Q., JACOB, D.J., BLAKE, D. and SACHSE, G., 2003. In situ measurements of HCN and CH_3CN over the Pacific Ocean: Sources, sinks, and budgets. *Journal of Geophysical Research,* **108**, pp. 8795.

SINHA, P., HOBBS, P.V., YOKELSON, R.J., BERTSCHI, I.T., BLAKE, D.R., SIMPSON, I.J., GAO, S., KIRCHSTETTER, T.W. and NOVAKOV, T., 2003. Emissions of trace gases and particles from savanna fires in southern Africa. *Journal of Geophysical Research,* **108**(D13), pp. 8487.

SMITH, H.J.P., DUBE, D.J., GARDNER, M.E., CLOUGH, S.A. and KNEIZYS, F.X., 1978. FASCODE: Fast Atmospheric Signature CODE (spectral transmittance and radiance). *AFGL-TR-0081. Air Force Geophysics Laboratory, Hanscom AFB MA 01731.*

SMITH, M.A.H., MALATHY DEVI, V., BENNER, D.C., BLAKE, T.A., SAMS, R.L. and RINSLAND, C.P., 2006. Measurements of HCN at 14 μm Broadened by Nitrogen at Low Temperatures, *American Astronomical Society, DPS meeting# 38,# 62.18; Bulletin of the American Astronomical Society*.

SOLOMON, S., QIN, D., MANNING, M., CHEN, Z., MARQUIS, M., AVERYT, K., TIGNOR, M. and MILLER, H., 2008. Climate change 2007: the physical science basis. Cambridge University Press Cambridge and New York.

SPANG, R., EIDMANN, G., RIESE, M., OFFERMANN, D., PREUSSE, P., PFISTER, L. and WANG, P.H., 2002. CRISTA observations of cirrus clouds around the tropopause. *Journal of Geophysical Research-Atmospheres,* **107**(D23), pp. 8174.

SPANG, R., REMEDIOS, J.J. and BARKLEY, M.P., 2004. Colour indices for the detection and differentiation of cloud types in infra-red limb emission spectra. *Advances in Space Research,* **33**(7), 1041-1047.

SPRENG, S. and ARNOLD, F., 1994. Balloon-borne mass spectrometer measurements of HNO_3 and HCN in the winter Arctic stratosphere—Evidence for HNO_3-processing by aerosols. *Geophysical Research Letters,* **21**(13), 1251-1254.

STEPHENS, G.L., 1994. Remote sensing of the lower atmosphere. Oxford University Press.

TANG, Y., CARMICHAEL, G.R., UNO, I., WOO, J.H., KURATA, G., LEFER, B., SHETTER, R.E., HUANG, H., ANDERSON, B.E. and AVERY, M.A., 2003. Influences of biomass burning during the Transport and Chemical Evolution Over the Pacific (TRACE-P) experiment identified by the regional chemical transport model. *Journal of Geophysical Research,* **108**(D21), pp. 8824.

TYNDALL, G.S., ORLANDO, J.J., WALLINGTON, T.J. and HURLEY, M.D., 2001. Products of the chlorine atom and hydroxyl radical initiated oxidation of CH_3CN. *J.Phys.Chem.A,* **105**(22), pp. 5380-5384.

VARGHESE, P.L. and HANSON, R.K., 1984. Tunable diode laser measurements of spectral parameters of HCN at room temperature. *Journal of Quantitative Spectroscopy and Radiative Transfer,* **31**(6), 545-559.

VIGGIANO, A.A., HUNTON, D.E., MILLER, T.M. and BALLENTHIN, J.O., 2003. In situ measurements of hydrogen cyanide in the upper troposphere/lower stratosphere during Arctic spring 2000. *Journal of Geophysical Research,* **108**(D5), pp. 8304.

VON CLARMANN, T., CECCHERINI, S., DOICU, A., DUDHIA, A., FUNKE, B., GRABOWSKI, U., HILGERS, S., JAY, V., LINDEN, A. and LÓPEZ-PUERTAS, M., 2003. A blind test retrieval experiment for infrared limb emission spectrometry. *Journal of Geophysical Research,* **108**(D23), pp. 4746.

VON CLARMANN, T., GLATTHOR, N., GRABOWSKI, U., HÖPFNER, M., KELLMANN, S., KIEFER, M., LINDEN, A., TSIDU, G.M., MILZ, M. and STECK, T., 2003. Retrieval of temperature and tangent altitude pointing from limb emission spectra recorded from space by the Michelson Interferometer for Passive Atmospheric Sounding (MIPAS). *Journal of Geophysical Research-Atmospheres,* **108**(D23), pp. 4736.

WATERS, J.W., FROIDEVAUX, L., HARWOOD, R.S., JARNOT, R.F., PICKETT, H.M., READ, W.G., SIEGEL, P.H., COFIELD, R.E., FILIPIAK, M.J. and FLOWER, D.A., 2006. The Earth Observing System Microwave Limb Sounder (EOS MLS) on the Aura Satellite. *IEEE Transactions on geoscience and remote sensing,* **44**(5).

WAYNE, R.P., 2000. Chemistry of atmospheres. *Oxford University Press Oxford*.

WINE, P.H., STREKOWSKI, R.S., NICOVICH, J., MCKEE, M.L., CHEN, G. and DAVIS, D.D., 2002. Atmospheric chemistry of HCN, paper PHYS 134 presented at the 224th ACS National Meeting, 2002.

YANG, C., BULDYREVA, J., GORDON, I.E., ROHART, F., CUISSET, A., MOURET, G., BOCQUET, R. and HINDLE, F., 2008. Oxygen, nitrogen and air broadening of HCN spectral lines at terahertz frequencies. *Journal of Quantitative Spectroscopy and Radiative Transfer,* **109**(17-18), pp. 2857-2868.

YEVICH, R. and LOGAN, J.A., 2003. An assessment of biofuel use and burning of agricultural waste in the developing world. *Global Biogeochemical Cycles,* **17**(4), pp. 1095.

YOKELSON, R.J., BERTSCHI, I.T., CHRISTIAN, T.J., HOBBS, P.V., WARD, D.E. and HAO, W.M., 2003. Trace gas measurements in nascent, aged, and cloud-processed smoke from African savanna fires by airborne Fourier transform infrared spectroscopy (AFTIR). *Journal of Geophysical Research,* **108**(D13), pp. 8478.

YOKELSON, R.J., SUSOTT, R., WARD, D.E., REARDON, J. and GRIFFITH, D.W.T., 1997. Emissions from smoldering combustion of biomass measured by open-path Fourier transform infrared spectroscopy. *Journal of Geophysical Research,* **102**(D15), pp. 18,865-18,877.

YOSHIDA, Y., WANG, Y., SHIM, C., CUNNOLD, D., BLAKE, D.R., AND DUTTON, G.S., 2005. Inverse modeling of the global methyl chloride sources. *Journal of Geophysical Research,* **111**(D16307).

YOSHIDA, Y., WANG, Y., ZENG, T. and YANTOSCA, R., 2004. A threedimensional global model study of atmospheric methyl chloride budget and distributions. *Journal of Geophysical Research,* **109**(D24309).

ZHAO, Y., KONDO, Y., MURCRAY, F., LIU, X., KOIKE, M., IRIE, H., STRONG, K., SUZUKI, K., SERA, M. and IKEGAMI, Y., 2000. Seasonal variations of HCN over northern Japan measured by ground-based infrared solar spectroscopy. *Geophysical Research Letters,* **27**(14), pp. 2085-2088.

ZHAO, Y., STRONG, K., KONDO, Y., KOIKE, M., MATSUMI, Y., IRIE, H., RINSLAND, C., JONES, N., SUZUKI, K. and NAKAJIMA, H., 2002. Spectroscopic measurements of tropospheric CO, C_2H6, C_2H_2, and HCN in northern Japan. *Journal of Geophysical Research,* **107**, pp. 4343.